PhD School in Chemical Science

CHARACTERIZING THE HYGROSCOPIC PROPERTIES OF AEROSOLS:

FROM BINARY AQUEOUS SYSTEMS TO ATMOSPHERIC AEROSOLS

PhD dissertation by
Grazia Rovelli

Supervisor
Prof. Ezio Bolzacchini

Academic year 2014/2015

Contents

List of Figures ii

List of Tables v

Abstract vi

Chapter 1 Introduction 1
1.1 Atmospheric Aerosols: Properties and Sources 1
1.1.1 Chemical Composition and Sources of Atmospheric Aerosols 3
1.1.2 Physical State and Hygroscopic Properties of an Aerosol 4
1.1.3 Optical Properties 6
1.2 Effects of Atmospheric Aerosols 8
1.2.1 Climate Effects of Atmospheric Aerosols 8
1.2.2 Health Effects of Inhaled Particles 10
1.2.3 Contamination of Materials by Deposited Aerosol Particles 11
1.3 Hygroscopicity Measurement Techniques 12
1.4 Aims and Thesis Outline 14

Chapter 2 Thermodynamic Properties of Aerosols and Water Evaporation Kinetics from Droplets 17
2.1 Thermodynamic Properties of Aerosols 17
2.1.1 Phase Transitions within the Condensed Phase of Aerosols 18
2.1.2 The Liquid-Vapour Partitioning of Water in Aerosols 21
2.1.3 The Kelvin Effect 23
2.1.4 Activation of Aerosol Droplets 25
2.1.5 Representing the Hygroscopic Properties of a Compound 26
2.2 Modelling the Hygroscopic Properties of Aerosols 28
2.3 Aerosol Evaporation and Condensation Kinetics 32
2.4 Summary 35
Chapter 3 Electrical Conductance Measurements in the Aerosol Exposure Chamber 37
3.1 Determining DRH and CRH with Conductivity Measurements 37
3.1.1 Conductivity Measurements on Aerosols in the Literature 38

3.2 The Aerosol Exposure Chamber 40
3.2.1 Measurement of the Conductance of Deposited Aerosol Samples during RH Cycles 42
3.3 Sampling of Atmospheric Aerosols 45
3.4 Laboratory Generated Aerosol Samples 45
3.5 Ionic Fraction Characterisation with Ion Chromatography Analysis 48
3.6 Development of the Conductivity Method in the AEC 49
3.6.1 Response Time of the Electrical Signal 50
3.6.2 Lowering the Minimum Aerosol Loading on Filters 51
3.6.3 The Effect of the Filtration Membrane on Conductivity Measurements 53
3.6.4 Comparison of the Electrical Conductance Method with a Gravimetric Method 55
3.7 Summary 59

Chapter 4 Measurements of DRH and CRH of Atmospheric Aerosol Smples 61
4.1 DRH and CRH Seasonal Variations 62
4.1.1 The Dependency of Seasonal Trends on Seasonally-Modulated Chemical Composition of Samples 64
4.2 Comparison with Model Predictions of DRH and CRH 70
4.2.1 DRH 70
4.2.2 CRH 75
4.3 Effect of the Physical State of Atmospheric Aerosols in Various Fields of Application 76
4.3.1 Implications for DFC Data Centers 77
4.3.2 Effect of the Carbonaceous Components on the Conductance Properties of Deposited Aerosols 81
4.3.3 Implications in Heritage Climatology 90
4.3.4 Implications for Remote Sensing Techniques 93
4.4 Summary and Conclusions 96

Chapter 5 The Cylindrical Electrodynamic Balance 99
5.1 Hystorical Development of EDBs 100
5.2 Cylindrical EDB Experimental Setup and Operations 101
5.2.1 Generating and Trapping Droplets in the C-EDB 102
5.2.2 Sizing Trapped Droplets 105
5.2.3 Accounting for Variable Refractive Index in Evaporating Droplets 109
5.2.4 Temperature and RH Control in the C-EDB 112
5.3 Summary 113

Chapter 6 Measuring Aerosol Hygroscopic Properties over a Wide Range of RH with Comparative Kinetics Experiments 115
6.1 Comparative Kinetics Measurements 116
6.1.1 Retrieving the RH from Probe Droplets 118
6.1.2 Calculating Hygroscopic Growth Curves for Sample Aerosol Droplets 120
6.1.3 Experimental Uncertainties, Reproducibility and Averaging Data from Multiple Droplets 122
6.2 Effect of the Temperature Depression of Droplets during Evaporation 125
6.3 Full Hygroscopicity Curves from Droplets Evaporating into Different RHs 129
6.4 Testing the Experimental Method with Well Characterised Aerosol Systems 131
6.4.1 Binary Mixtures of Inorganics 132
6.4.2 Ternary Inorganic Mixtures 135
6.5 Sensitivity to the Value of the Mass Accommodation Coefficient 137
6.6 Summary and Conclusions 139

Chapter 7 Hygroscopic Properties of Aminium Sulphates 141
7.1 Aminium Sulphates 141
7.1.1 Preparation of the Solutions 143
7.1.2 Density and Refractive Index of Aminium Sulphates 145
7.1.3 Hygroscopic Properties of Aminium Sulphates 149
7.1.4 Reproducibility of Measurements 160
7.1.5 Sensitivity to Density Parameterization 162
7.1.6 Vapour Pressures of Amines over Aminium Sulphate Solutions 165
7.2 Summary and Conclusions 170

Chapter 8 Summary and conclusions 173

Bibliography 177

Acknowledgments 193

List of Figures

Figure 1.1: Heterogeneous chemical composition of atmospheric aerosols. 2
Figure 1.2: Deliquescence and water abstorption by a saline aerosl particle. 5
Figure 1.3: Angular dependence of scattered light of three with different radii. 7
Figure 1.4: Direct and indirect radiative forcing of atmospheric aerosols..... 9
Figure 1.5: Evolution of the estimation of radiative forcing (RF) due to aerosols..... 10
Figure 2.1: Radial growth factor vs. RH for a generic pure inorganic salt. 20
Figure 2.2: The solute effect for NaCl, (NH4)2SO4 and glutaric acid. 22
Figure 2.3: Effect of the surface curvature of droplets compared to a flat surface. 23
Figure 2.4: Difference in the Gibbs free energy (ΔG) between a droplet and a vapour as a function of the droplet radius. 24
Figure 2.5: Köhler equation plot for two droplets with different dry size..... 26
Figure 2.6: Development and refinement of current aerosol thermodynamic models..... 31
Figure 2.7: Water evaporation dynamics from a non-equilibrium state..... 33
Figure 3.1: Frontal view of the Aerosol Exposure Chamber (AEC). 40
Figure 3.2: Scheme of the experimental setup, representing a top view of the AEC. 41
Figure 3.3: Electrical conductance measurements during a humidity cycle in the AEC.. 44
Figure 3.4: Gradual increase in conductance with increasing RH..... 44
Figure 3.5: Generation of mixed saline and soot aerosol samples in the laboratory..... 47
Figure 3.6: Test of the electrical signal response time..... 50
Figure 3.7: Conductance curves measures at different times. 51
Figure 3.8: Humidification curves of two samples collected simultaneously but with different surficial mass distribution..... 53
Figure 3.9: Average normalised conductance curves for samples collected on PTFE and on quartz fibre filtration membranes. 55
Figure 3.10: Comparison of conductance and GF_m as a function of RH. 56
Figure 3.11: Correlation of DRH and CRH values obtained with the conductance and gravimetric method..... 57
Figure 3.12: DRH values for pure salts ($(NH_4)_2SO_4$, NH_4NO_3, Na_2SO_4) and $(NH_4)_2SO_4/NH_4NO_3$ mixtures..... 58
Figure 4.1: Frequency distributions the DRH and CRH. 63
Figure 4.2: Ionic fraction relative percentage mass composition..... 65
Figure 4.3: Correlation plot between of the charge equivalents..... 67

Figure 4.4: DRH frequency distribution with an highlight on chemical composition.....69
Figure 4.5: Comparison of the experimental and E-AIM DRH frequency distributions. . 71
Figure 4.6: Correlation of experimental and E-AIM Model DRH values. 73
Figure 4.7: Correlation of the measured and modelled mass of absorbed H_2O. 74
Figure 4.8: Psycrometric chart representing the operating conditions in the ENI DC. ... 80
Figure 4.9: Surficial mass distributions for MI-TS and OB samples..... 87
Figure 4.10: Interpretation of electrical conductance measurements on pure saline samples and mixed saline and soot samples. 89
Figure 4.11: 64x enlargement of a mixed $(NH_4)_2SO_4$ and soot laboratory generated sample, before and after a RH cycle in the AEC..... 90
Figure 4.12: Ncy and TOW monthly values. 92
Figure 5.1:The cylindrical electrodynamic balance (C-EDB) setup. 101
Figure 5.2: Operations for the generation and trapping of single droplets..... 102
Figure 5.3: Electrical field strength for cylindrical ring electrodes EDB setups..... 105
Figure 5.4: Interference pattern of the light generated by a spherical droplet when illuminated by plane-wave light. 106
Figure 5.5: Density and refractive index parameterisations of $(NH_4)_2SO_4$ NaCl. 110
Figure 5.6: Effect of the variable refractive index correction on the evaporation plots of two NaCl droplets evaporating into different RH values..... 111
Figure 6.1: Probe (water) and sample droplets in a comparative kinetics experiment. . 116
Figure 6.2: Modelled evaporation profiles for pure water and for NaCl solution droplets at variable surrounding RH..... 118
Figure 6.3: Error on RH calculated for water and NaCl solution used as a probe..... 120
Figure 6.4: Retrieval of hygroscopic growth curves from evaporation profiles..... 121
Figure 6.5: Reproducibility of NaCl growth curves. 124
Figure 6.6: $(NH_4)_2SO_4$ solution droplets evaporating into different RHs. 126
Figure 6.7: Comparison of the experimental and modelled evaporation profiles of two $(NH_4)_2SO_4$ droplets at RH=85% nd RH=55%. 127
Figure 6.8: *mfs*, $T_{droplet}-T_{gas}$ and error on a_w vs. a_w from the evaporation kinetics of 10 $(NH_4)_2SO_4$ droplets (RH=58%). 128
Figure 6.9: full *mfs* vs. a_w curve of from measurements into different RHs.. 129
Figure 6.10: GF_r, n_{water}/n_{solute} and *mfs* for a_w values between 0.88 and 1 for $(NH_4)_2SO_4$. 131
Figure 6.11: Measured *mfs* vs. a_w plots for $(NH_4)_2SO_4$, $NaNO_3$, Na_2SO_4 and NaCl. 133
Figure 6.12: Measured molar osmotic coefficients (ϕ_{st}) vs. square-rooted solute molality plots for $(NH_4)_2SO_4$, $NaNO_3$, Na_2SO_4 and NaCl.. 133
Figure 6.13: Correlation of measured and E-AIM predicted values for n_{water}/n_{solute}. 134
Figure 6.14: *mfs*, GF_r vs. and n_{water}/n_{solute} vs. a_w for mixtures with different $(NH_4)_2SO_4$/NaCl mass ratios.. 136
Figure 6.15: n_{water}/n_{solute} vs. a_w NaCl obtained with α_M =1 and α_M =0.1..... 138
Figure 7.1: Chemical formulas of the six studied aminium sulphates. 143

Figure 7.2: Hygroscopic properties of ammonium sulphate obtained from the reaction between NH_3 and H_2SO_4. 145
Figure 7.3: Densities and refractive indices of aminium sulphate solutions. 147
Figure 7.4: ρ_{melt} of the six aminium sulphates from this work and from the literature. 148
Figure 7.5: Refractive indices of molten or crystalline aminium sulphates obtained in this work and from the literature. 149
Figure 7.6: GF_r vs a_w hygroscopic growth of the six aminium sulphates. 150
Figure 7.7: n_{water}/n_{solute} vs a_w hygroscopic growth of the six aminium sulphates. 151
Figure 7.8: Moles of salt (n_{salt}) in a 1 µm radius particle as a function of the molecular weight (M_w) of each aminium sulphate. 152
Figure 7.9: Aminium sulphates n_{water}/n_{solute} vs a_w from C-EDB comparative kinetics measurements and from Sauerwein et al. (2015)[73] 155
Figure 7.10: Aminium sulphates osmotic coefficients vs. $m(SO_4^{2-})^{0.5}$ from C-EDB comparative kinetics measurements and from Sauerwein et al. (2015)[73] 156
Figure 7.11: kg of H_2O per mole of solute as a function of the degree of neutralisation of sulphuric acid by amine. 158
Figure 7.12: Reproducibility of the measured hygroscopic properties of DMAS. 161
Figure 7.13: DMAS density measurements. 163
Figure 7.14: Effect of different density and refractive indices parameterisations on th obtained hygroscopic properties of DMAS. 164
Figure 7.15: Equilibria between a methyaminium sulphate droplet and the gas phase. 166
Figure 7.16: Long trapping measurement in a C-EDB. 168

List of Tables

Table 4.1: Measured DRH and CRH and ionic content in the different seasons. 63
Table 4.2: Seasonal percentage mass of the main inorganic ions, other inorganic ions and carboxylic acids for samples collected at MI-TS. 66
Table 4.3: Experimental CRH and calculated values obtained with the paramteric model by Martin et al. (2003)[136]. 75
Table 4.4: Measured outdoor and simulated indoor particles concentrations compared with recommended limits from ASHRAE. 78
Table 4.5: Outdoor and simulated indoor concentrations of PM_1 and $PM_{2.5}$ and average DRH values obtained with E-AIM Model simulations. 79
Table 4.6: Highest, lowest and average measured conductance values. 83
Table 4.7: Surficial concentrations for the overall $PM_{2.5}$ content and of the analysed inorganic and carbonaceous fractions. 85
Table 4.8: EC and OC mass percentages for the two sampling sites (MI-TS and OB) in the four seasons. 85
Table 6.1: Uncertainties on calculation of hygroscopic properties from comparative kinetics measurements in the C-EDB. 123
Table 7.1: Physical properties of ammonia, methyl and ethyl amines. 142
Table 7.2: Fitting parameters of density and the refractive index measured for aminium sulphates solutions. 147
Table 7.3: Fitting parameters of density and the refractive index of DMAS. 163
Table 7.4: Parameters used for the calculations of D_{TMA} and D_{TEA}. 167
Table 7.5: Measured radii gradient after complete water evaporation of TMAS and TEAS solutions at variable RH and the corresponding p_{TMA} and p_{TEA}. 169

Abstract

The quantification of the hygroscopic properties of atmospheric aerosols is important to understand several processes they are involved in, such as clouds formation, their interaction with solar radiation and the penetration of particles in the human respiratory track. In addition, the interaction of deposited aerosols with surfaces depends on their physical state, too; thus, characterizing their phase transitions as a function of their chemical composition is key to understanding the effects they have on materials (e.g. printed circuits, cultural heritage artifacts).

In order to investigate the hygroscopic properties of aerosols, an electrical conductance method in an Aerosol Exposure Chamber was developed for the determination of the phase transitions of $PM_{2.5}$ aerosol samples during relative humidity cycles. The obtained Deliquescence and Crystallization Relative Humidity (DRH and CRH) were put in relation with the ionic chemical composition of the analyzed samples: it was found that seasonal chemical variations result in seasonal trends for DRH and CRH, too. The implications of these results for Free-Cooled Data Centers, for the understanding of the role of particles in stone-decay processes of cultural heritage artifacts and for the common algorithms used in the remote sensing of particulate matter concentrations were evaluated.

The ionic fraction characterisation was also used as an input for a state-of-the-art equilibrium aerosol model (E-AIM) to simulate the DRH of the samples. Some discrepancies were evidenced in the comparison of experimental and modelled values, because the hygroscopic properties of the organic components need to be included too. In order to effectively account for their contribute, current aerosol models need to be refined with accurate hygroscopicity measurements on organic compounds of increasing molecular complexity and their mixtures with common electrolytes. Such measurements are essential for understanding and modelling the microphysical properties that determine the partitioning of water between the gas and the aerosol phases in chemically complex systems.

In this context, an experimental technique based on evaporation kinetics measurements in an Cylindrical Electrodynamic Balance was developed for the measurement of

hygroscopic properties on single confined droplets from aqueous solutions with known chemical composition. To expand the range of applicability of a previously developed technique to water activities from 0.5 to values close to saturation (>0.99), well-characterized binary and ternary inorganic mixtures were considered. The obtained results were used to successfully validate this technique by comparing them with calculations from E-AIM Model and to assess the sensitivity of this technique to small changes in chemical composition. The first class of atmospherically relevant compounds that was considered was aminium sulphates, which are the products of the neutralization reactions of sulphuric acid and short-chained alkylamines (methyl- and ethylamines). They have been detected in atmospheric aerosols up to hundreds of pg m^{-3}, but their hygroscopic behaviour was less characterized than their inorganic equivalent, ammonium sulphate, even if they can promote cloud droplets formation and particle growth.

Chapter 1 Introduction

This work is focused on the characterisation of the hygroscopic properties and phase transitions of aerosols. In this Chapter, an overview of the chemico-physical properties of atmospheric aerosols is given, with particular reference to their chemical composition, size distributions, origin and evolution processes in the atmosphere. A particular highlight is put on the hygroscopic properties of aerosols, which define how particles interact with water and depend on their chemical composition. The various measurement techniques applied in the literature for the determination of the hygroscopic properties of both atmospheric aerosols and simpler systems are discussed. The phase state of particles and the amount of absorbed water directly influence their size and determine the role of aerosols in a number of processes that aerosols are involved in, which are presented in this Chapter, as well. Finally, a general overview of this thesis is presented together with its motivation and aims.

1.1 Atmospheric Aerosols: Properties and Sources

Aerosols are part of everyday life since they are widely used in cosmetic and health care products, for the application of paint and coatings, for drug delivery and in many industrial processes. In addition, atmospheric aerosols influence our lives because of their effect on climate and on the formation of clouds[1–3], and the negative health effects of inhaled particles have been increasingly recognised and studied in the last decades[2,4–6].

From a chemico-physical point of view, aerosols are colloidal systems composed of a particle phase, which can be solid, liquid or both, suspended within a gaseous medium. When atmospheric aerosols are considered, the term Particulate Matter (PM) is widely used to define the particle condensed phase.

The size of atmospheric aerosol particles covers several orders of magnitude, from very few nanometers (3-20 nm) up to several hundreds of micrometers[2,3]. A commonly used classification of aerosol particles according to their size is the one that distinguishes between the *coarse* fraction (d>1 µm), the *fine* fraction (diameter between 0.1 and 1 µm) and the *ultrafine* fraction (d<0.1 µm).

Atmospheric aerosols are ubiquitous and characterised by heterogeneous chemical composition that includes both organic and inorganic components (Section 1.1.1). The concentrations and the chemical composition of atmospheric particles can vary in time and in space. Daily, seasonal, annual and inter-annual trends in particles composition and concentrations are observed[7,8] because of the variability of atmospheric conditions and of the intensity of emission sources. Moreover, different types of environment (e.g. urban, rural, marine, remote, etc.) are characterised by different climatic conditions and by different sources of aerosol particles that result in a spatial variability of the concentrations and of the chemical composition of aerosols[2]. A further heterogeneity can also be found along vertical profiles within the troposphere[9,10] and among particles with different sizes[2,3]. Finally, the climatic conditions (temperature and humidity) of the gas phase in which particles are suspended determine the physical state of aerosols (Section 1.1.2) and the various chemical species they are composed of can partition between solid, liquid and gaseous phases. The chemical complexity of atmospheric aerosols together with the temporal, spatial and climatic factors that influence their variability are summarised in Figure 1.1 and discussed in detail in the following Sections.

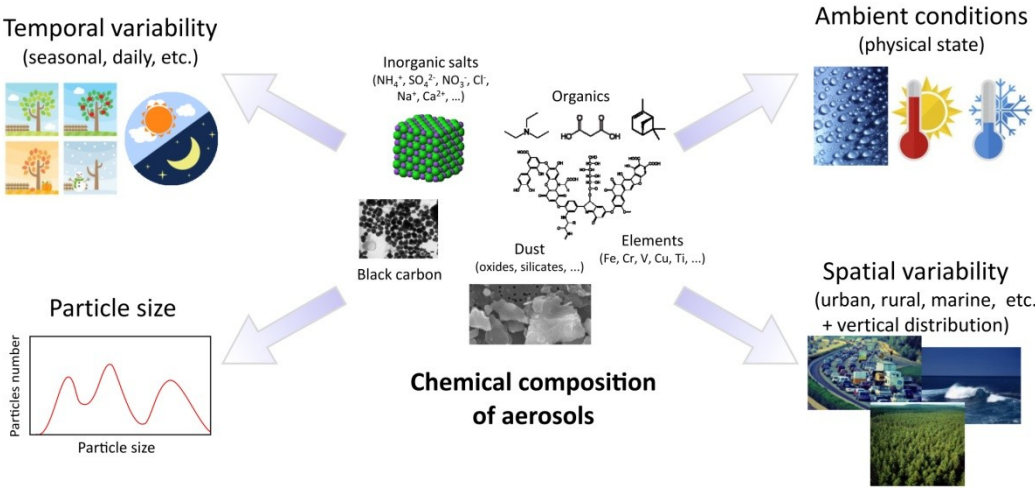

Figure 1.1: Aerosol are characterised by an heterogeneous chemical composition (centre) which is dependent on seasonal and spatial variability and on the particle size. and which also influences the physical state of aerosols, depending on the surrounding climatic conditions.

1.1.1 Chemical Composition and Sources of Atmospheric Aerosols

Atmospheric aerosol particles can originate from a great number of different sources. Primary particles are emitted directly in the atmosphere both by natural (e.g. volcanoes, sea spray, forests and biological activity, dust resuspension, etc.) and anthropogenic sources (e.g. combustion of fossil fuels, biomass burning, domestic heating, cooking, husbandry, etc.). Particles can also originate from reactivity of gaseous components in the atmosphere, from the nucleation processes of new particles from gas molecules and from the modification of primary particles components. Aerosols deriving from such mechanisms are defined secondary.

As anticipated in the previous Section, the chemical composition of atmospheric aerosol particles can be extremely diverse, including both inorganic and organic chemical species, characterized by different water-solubility and volatility and by variable optical and hygroscopic properties (see Sections 1.1.2 1.1.3).

If the inorganic fraction of aerosol particles is considered, it can be divided into water-soluble ionic compounds and insoluble components. With respect to the water-soluble components, the most common ionic compounds are ammonium, nitrates and sulphates, which are mainly secondary components deriving from the reactivity of their gaseous precursors (NH_4, NO_x and SO_2). Other inorganic ionic species in aerosols derive from sea salt (composed mainly by NaCl, but also SO_4^{2-}, Mg^{2+}, Ca^{2+} and K^+)[3] and crustal components (Mg^{2+}, Ca^{2+}, K^+, Na^+, F^-, Cl^-). The insoluble inorganic fraction in aerosols derives mostly from 'mineral dust' and 'road dust'[3], which include metal oxides and trace elements (Al, Si, Ca, Mg, Fe, Ti, Sc, Na, K, Cu, Pb, V, etc.)[11].

Elemental carbon (EC) can represent up to 20-30% of the overall aerosol mass[2] in environments that are strongly impacted by anthropogenic activities, because it mainly derives from incomplete combustion processes. Its structure is mainly amorphous, even though graphitic-like structures are also found[12]. In the literature, EC is usually referred to in different ways, depending on the specific field of application, on the characteristic that needs to be highlighted or on the analytical technique used for its quantification. Frequently the elemental carbonaceous fraction of aerosols is termed 'soot' in order to put the accent on its provenience from incomplete combustion processes. Soot usually can contain a variable amount of heteroatoms (mainly O and N), that depending on the combustion conditions can represent up to 50% of the overall soot mass[12]. Because of the strongly light absorbing properties of EC components, these are often referred to as black carbon (BC), in particular when its quantification is performed by means of optical absorption techniques[2].

Organic components represent probably represent the most heterogeneous fraction in atmospheric aerosol particles, with hundreds of different chemical molecules that have been detected in atmospheric aerosol samples[13,14]. The organic carbon (OC) fraction includes carboxylic acids, hydrocarbons, fatty acids, amines, alcohols, proteins and amino acids, aromatic compounds, cellulose, levoglucosan and multifunctional compounds, as well. The primary emission sources of organic compounds are both natural and anthropogenic and the class of Secondary Organic Compounds (SOA) originates from nucleation of gaseous compounds, gas-particle partitioning of VOCs (volatile organic compounds) and SVOCs (semi volatile organic compounds) and multiphase reactivity[2]. Even if many of the organic species in atmospheric aerosols are just trace compounds, they can be of great interest since their negative health effect can be significant even if present in very small amounts. This is the case, for example, of PAHs (polycyclic aromatic hydrocarbons, concentration ranges from <0.1 to 100 ng m^{-3})[15] that are recognized as carcinogenic, mutagenic or as synergists agents in carcinogenic processes[13,15]. Primary biogenic organic components such as pollen, plant and animal debris, spores, viruses and bacteria represent a consistent portion of the overall organic fraction of atmospheric aerosols (up to 25% of the global aerosol mass[16]).

Because of the chemical heterogeneity of particles, the characterization of the chemical composition of aerosols can be challenging. The characterization of compounds with different chemico-physical properties would also require the application of a number of different analytical techniques, which could be problematic because of the usually small amounts particles collected and because of the presence of hundreds of trace constituents[2].

1.1.2 Physical State and Hygroscopic Properties of an Aerosol

Hygroscopicity is the ability of a substance to absorb water molecules. Atmospheric aerosol particles can interact with gaseous water molecules in the atmosphere and they are characterised by variable hygroscopic properties depending on their chemical composition. The amount of water in the gas phase is usually described in terms of Relative Humidity (RH), which is defined as the ratio of the partial pressure of water (p_w) in the gas phase and the saturation vapour pressure (p_w^0) at the considered temperature:

$$RH(\%) = \frac{p_w}{p_w^0} \cdot 100 = S_{w,\infty} \cdot 100 \qquad 1.1$$

Figure 1.2 is a schematic representation of the interaction of water gaseous molecules with a simple hygroscopic aerosol systems, containing only pure saline particles (NaCl, for example). At low relative humidities, the salt is present in its crystalline solid form. With increasing RH, the water content in the gas phase increases and when a certain critical RH value is exceeded the solid NaCl particle spontaneously absorbs water thus forming an electrolytic solution. This solid-liquid phase transition is termed deliquescence and the thermodynamics behind it are fully described in Section 2.1.1. After deliquescence has occurred, further increase in RH cause more water molecules to partition from the gas phase to the particle phase and to condense on the solution originated from the deliquescence process, which results increasingly diluted. This equilibrium process is usually referred to as 'hygroscopic growth' because the particle increases its radius (and mass) because of absorption of water molecules (see Section 2.1.2). Whenever an aerosol system is not in equilibrium with the surrounding gas phase RH, it responds with evaporation or condensation of water molecules. The kinetics of the dynamic processes of non-equilibrated aerosol systems are described in Section 2.3.

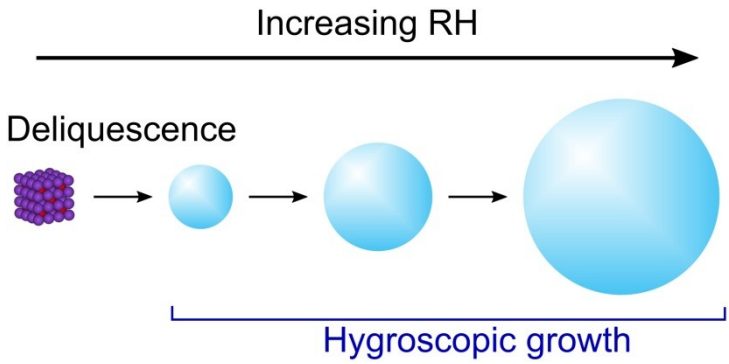

Figure 1.2: With increasing RH, a saline aerosol particle deliquesces at DRH and continuously absorbs water thereafter increasing its size (hygroscopic growth).

If more complex systems like actual atmospheric aerosol particles are considered their overall hygroscopic results from the hygroscopic properties of the different components. In addition, other factors can influence the partitioning of water between the gas and the condensed phase. For example, kinetic limitations to water diffusion from the bulk to the surface of a droplet can be observed in highly viscous or glassy aerosols or when surface-active compounds create hydrophobic films on the surface of droplets[17–20]. Mixed organic and inorganic aerosols can undergo phase separation with the formation of an aqueous phase and an organic hydrophobic, which influences the water uptake by particles[21–23]. In addition, the gas-particle partitioning of VOCs and SVOCs and their co-condensation with water influences the growth of atmospheric aerosol particles and their activity in clod formation processes[24,25].

At a fundamental level, both the thermodynamic factors governing hygroscopic growth and the kinetics of condensation must be better quantified in order to represent the aerosol microphysics under-pinning the partitioning of water between the gas and particle phases. Quantifying the hygroscopic growth of aerosols is important for understanding the liquid water content and size distributions of atmospheric aerosols and for modelling their optical properties (Section 1.1.3), for predicting cloud droplet number and size distribution following the activation of cloud condensation nuclei (CCN, Section 1.2.1) and for determining the partitioning of semi-volatile organic compounds in the condensed aerosol phase[25,26]. The capacity for aerosols to absorb water can also influence their deposition in the respiratory track on inhalation, potentially influencing the impact of aerosols on health[27] (Section 1.2.2).

The thermodynamic properties that describe the equilibrium partitioning of water to the condensed phase of atmospheric aerosols are presented in Chapter 2, together with the current literature modelling approaches. In addition, the kinetics of water evaporation and condensation are

1.1.3 Optical Properties

The interaction between aerosol droplets and light can occur according to different processes, i.e. absorptions, elastic and inelastic scattering, reflection, refraction and diffraction. For a single aerosol particle, its interaction with light depends on size, shape and refractive index of the material. Note also that all these processes are dependent on the wavelength (λ) of the incident light.

When light travels through a bulk medium, its speed is attenuated and the extent of this attenuation depends on the density of the material and on the polarizability of its molecules. If the energy of the incident light is conserved the scattering is elastic, whereas if absorption occurs and the energy of light is attenuated the scattering is defined inelastic. One of the parameters used to describe the propagation of light through a medium is the complex refractive index ($\tilde{m}$):

$$\tilde{m} = m + ik \qquad 1.2$$

In the expression of the complex refractive index, m represents the real part of the refractive index, which describes the elastic scattering of the medium, whereas k describes the attenuation of light through the medium because of absorption processes and is called extinction coefficient.

Maxwell's equations describe the scattering of an incident electromagnetic radiation by aerosol particles[28]. A solution of these equations for spherical, heterogeneous droplets illuminated by monochromatic plane wave light is provided by Mie Theory[29], which evaluates the behaviour of the electric and magnetic components of light before hitting a particle, within its medium and thus calculating how they are scattered by the particle. A description of Mie Theory is beyond the purpose of this work, and can be found in the literature[30]. However, Mie Theory and simplified approaches basing on Mie Theory were used in the literature to interpret the light scattering of single levitated aerosol particles and infer their size and/or refractive index[31,32] (see also Section 5.2.2).

An example of the dependence of light scattering as a function of the scattering angle (being 0° the incident angle of light) simulated with Mie Theory is given in Figure 1.1. The simulation was performed with the software 'Mie Plot', which uses the Mie scattering algorithm by Bohren and Huffmann (1987)[28]. The calculation was done considering a constant refractive index value (1.4) and at a wavelength of λ=532 nm. The polar plot shows the angularly-resolved scattered light intensity (on arbitrary units) generated by three homogeneous spherical droplet with different radius (black – 10 µm; pink – 1 µm; blue – 0.2 µm). The generated scattering pattern consists in a series of light intensity peaks and valleys that originates from the interference of reflected and refracted light by the droplet surface. This pattern is also referred to as phase function and depends on the radius and refractive index of the droplet and on the incident wavelength.

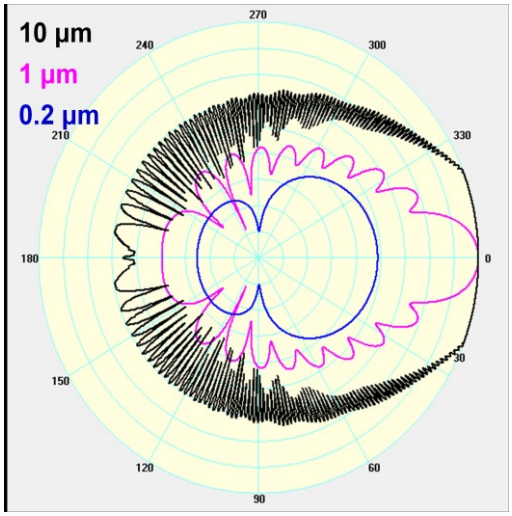

Figure 1.3: Simulation of the angular dependence of scattered light of three droplets with constant m value, but variable radii. Different colours indicate different droplet radii (black – 10 µm; pink – 1 µm; blue – 0.2 µm).

1.2 Effects of Atmospheric Aerosols

After discussing the chemical composition of atmospheric aerosols, their phase state and size distribution, in this Section an overview of the effects of the climatic (1.2.1) and health effects (1.2.2) of aerosols in the atmosphere is given. In addition, a few considerations on the interactions of deposited aerosol particles with deposition surfaces with different chemical physical properties are presented in Section 1.2.3.

1.2.1 Climate Effects of Atmospheric Aerosols

One of the most relevant effects of atmospheric aerosols is that they can impact the radiative balance of the atmosphere, thus playing a role in climate change[3].

The Earth's radiative balance (or energy budget) is the difference between the incoming energy form solar radiation and the outgoing energy from Earth. If these two quantities are equal, the global temperature is constant but there can be factors that perturb the Earth's radiative balance. This perturbation is generally described in terms of Radiative Forcing (RF), which is defined by the Intergovernmental Panel on Climate Change (IPCC)[33] as "a measure of the influence a factor has in altering the balance of incoming and outgoing energy in the Earth-atmosphere system and is an index of the importance of the factor as a potential climate change mechanism". In IPCC reports, RF values are reported as "changes relative to pre-industrial conditions defined at 1750 and are expressed in watts per square metre (W/m^2)". A positive radiative forcing means a warming effect, whereas a negative radiative forcing implies a cooling effect.

The radiative forcing of greenhouse gases (CO_2, CH_4, N_2O and halocarbons) has the highest contribution to the total positive anthropogenic radiative forcing effect[1], which is overall of 3.03 ± 0.58 W m^{-2}, and the level of confidence attributed to the RF of these gaseous species is either 'high' or 'very high'.

Atmospheric aerosols have two different effects on the Earth's radiative balance[34], which are summarised in Figure 1.4. The first effect is defined *direct* and includes the scattering or absorption of the incoming solar radiation by aerosol particles in the atmosphere (Section 1.1.3). The scattering effect results in a cooling effect, whereas absorption of the solar radiation is associated to warming effects. In addition, aerosols also have *indirect* radiative forcing effects, which are related to the role of particles as cloud condensation nuclei (CCN, Section 2.1.4) in the clouds formation processes in the atmosphere. The chemico-physical properties of precursor particles influence the droplets size distribution

in clouds, the optical properties, thickness and lifetime of clouds, and changes to the clouds properties from pre-industrial conditions led to an overall negative indirect radiative forcing effect of atmospheric aerosol particles.

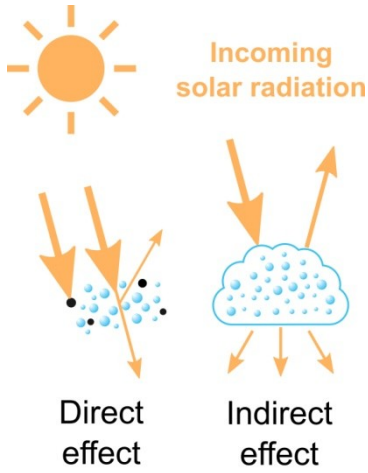

Figure 1.4: Direct and indirect radiative forcing of atmospheric aerosols.

If compared to the good level of confidence IPCC associates to the positive RF of greenhouse gases, the understanding of the magnitude of direct and indirect radiative forcing of aerosols is still affected by significant uncertainties.

Figure 1.5 shows the different estimates of the direct (Panel A) and indirect (Panel B) radiative forcing of atmospheric aerosols from IPCC reports from 1995 to 2013[1,35–37]. RF values are calculated between the year indicated on the x axis and 1750, taken as a relative reference of the pre-industrial situation. In Figure 1.5-A, the black points indicate the overall RF average of all the different chemical species in aerosols together with its uncertainty, whereas different colours in the bars correspond to different components of atmospheric aerosols (dark grey – black carbon; light grey – organic carbon; green – biomass burning; red – sulphates; blue – nitrates; brown – mineral dust). Note the variability of error bars: for the first time with the 2013 report[1], IPCC attributed a 'high' level of confidence to the direct radiative forcing effects, which were overall estimated of -0.27(-0.77 to 0.23) W m^{-2}. With respect to aerosols indirect effects a similar temporal trend is shown in Figure 1.5-B (note that for years 1992 and 2000 only a range of possible values was estimated). The latest reported RF value due to aerosol-cloud interaction was -0.55(-1.33 to -0.06) W m^{-2} and its level of understanding was indicated as 'low' by IPCC[1]. It is then clear that some effort is still needed for a better understanding of the effects of aerosols on the Earth's radiative balance and on climate, especially with respect to the indirect effects of atmospheric aerosol particles. The

uncertainties in understanding these processes provide an incentive to improve the characterisation of aerosol hygroscopicity.

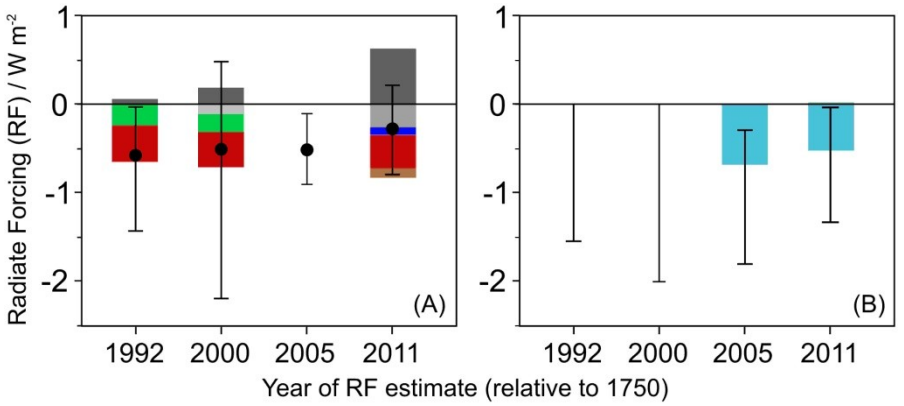

Figure 1.5: Evolution of the radiative forcing (RF) due to the aerosols direct (Panel A) and indirect effects (Panel B) from the last four IPCC reports[1,35-37]. Colours in Panel A: dark grey – black carbon; light grey – organic carbon; green – biomass burning; red – sulphates; blue – nitrates; brown – mineral dust.

1.2.2 Health Effects of Inhaled Particles

Several epidemiological studies have shown the correlation between high concentrations of atmospheric aerosols, especially fine particles, and increase in pathologies and death rates[5,38,39]. The main factors that determine the effects on atmospheric aerosol particles on human health are their size and their chemical composition.

The penetration of aerosol particles in the human respiratory tract and in which regions particles are going to deposit depend on their size. Depending on the penetration ability of particles in the respiratory tract, aerosol particles can be divided in four different fractions[40]: *inhalable*, all the particles that are inhaled thought the mouth and the nose; *extra-thoracic*, inhaled particles that do not penetrate beyond the larynx; *thoracic*, particles that manage to penetrate beyond the larynx; *respirable*, particles that reach the alveolar region and penetrate the blood-air barrier. The standardised PM_{10} and $PM_{2.5}$ sampling fractions were originally defined to represent the inhalable and the thoracic fractions respectively. With respect to the chemical composition of particles, the highest risk for human health is associated to trace heavy elements[41,42] (V, Ni, Cu, Zn, As, Cr, etc.) and to some classes of carcinogenic organic compounds, such as PAHs[15] (Section 1.1.1) and polychlorinated byphenils[13]. Unfortunately, these dangerous chemical species in atmospheric aerosol particles are mainly concentrated in the fine (d<1 µm) and

ultrafine (d<0.1 µm) fractions that can reach the alveoli and penetrate into the peripheral circulation and eventually into the brain and other organs[43].

Besides the negative health effects of inhaled atmospheric aerosol particles, aerosols are also used for the delivery of pharmaceutical active compounds directly to the lungs[44]. The use of pharmaceutical aerosols has the advantage of reducing the dose of active ingredient that has to be administrated to the patient and of decrease the time of action because of rapid transport into the circulatory system. An important aspect for the inhalation of both atmospheric aerosol particles and pharmaceutical aerosols is that the size distribution of the inhaled particles modifies once the aerosol enters the respiratory tract, because of water uptake from the surrounding enviroments[27]. Variations in the size of inhaled particles should be considered for example to target the drug-delivery of pharmaceutical aerosols to a specific region of interest within the respiratory tract[45].

1.2.3 Contamination of Materials by Deposited Aerosol Particles

So far, atmospheric aerosols have been considered when suspended in the atmosphere. However, after a certain lifetime in the atmosphere (ranging from minutes to several days or weeks[2]), they are removed from the atmosphere by a number of different processes (e.g. dry and wet deposition, sedimentation, impaction[3]). In particular, they can undergo dry deposition and accumulate over surfaces they can interact with, according to different interaction patterns that depend on the chemico-physical properties of the surface, on the chemical composition and on the physical state of the deposited particles. The understanding of the hazard represented by deposited atmospheric aerosol particles is important in different application fields, such as building materials damage evaluation[46,47], corrosion of metals[48–50], cultural heritage conservation[51–53], contamination of electronics[54–57].

An example is represented by the contamination of electric circuits by deposited atmospheric aerosol particles, which represent a potential danger for the installed electronic components, as a function of their physical state but especially when hydrated[58–61]. In fact, particulate contaminants can cause different electrical and electrochemical effects on electronics[62]. First of all, electrochemical corrosion can occur and the impact of the deposited aerosols can be different if ionic species are in the solid state or are dissolved in an aqueous solution[48,63,64]. In addition, particles deposited on electronics can have mechanical effects, such as heat accumulation on electronic circuitry, or electrical effects. For example, electrical bridging phenomena could be caused by

particles deposited between components that would normally be electrically insulated in a printed circuit, leading to short-circuiting and electrical failure mechanisms[54,57]. These electrical effects of aerosol particles deposited on electronics can represent a potential danger in particular for Data Centers[58,65,66], where a high density of electronic components is present. Implication for particles contamination in Data Centers are discussed in Section 4.3.1.

Atmospheric aerosol particles also contaminate stone porous materials of cultural heritage importance and assessing the decay-hazard associated to particulate contaminants is extremely relevant for the conservation of cultural heritage stone artefacts. Also in this case, the chemical composition, the physical state of deposited aerosols and their phase transitions of contaminant particles represent important factors to determine the effects on the contaminated stone surfaces. In fact, the presence of liquid water adsorbed on a stone surface can trigger a wide number of different 'chemical' decay processes (such as solid-liquid reactions, acid attack, penetration of salts solutions in the porosity of materials and biofilms formation)[46,67–70]. Besides, "mechanical" decay-mechanisms can be induced by the physical stress associated to the crystallization of dissolved saline components, due to the ambient RH variations[71].

1.3 Hygroscopicity Measurement Techniques

An overview of the most common experimental techniques applied in literature studies for the investigation of the hygroscopic properties of aerosols, both on the field and in the laboratory, is proposed in this Section.

A first distinction has to be made between hygroscopicity bulk measurement techniques[72,73], employed for the characterisation of thermodynamic properties of solutions, and measurements in the aerosol phase. In fact, in contrast to bulk solution analysis, studying levitated particles gives easy access to the supersaturated (i.e. metastable) concentration range as no surfaces for heterogeneous crystallisation are available (see Section 2.1.1). The supersaturated concentration range is of prime importance for atmospheric studies since atmospheric aerosol particles are often in a metastable state[19]. In addition, bulk studies are not able to provide any information for values close to saturation or for RH>100%, which is vital for a correct understanding of the activation of atmospheric aerosol particles in cloud formation processes[74,75] (Section 2.1.4).

One of the most common instruments to characterise the hygroscopicity of aerosol ensembles is the H-TDMA (hygroscopicity tandem differential mobility analyser). DMAs

are able to classify charged aerosol particles as a function of their electrical mobility (i.e. their ability of moving within an electrical field), which is related to the particle size. In the H-TDMA setup, two DMAs are employed: the first is used to select dry particles with a specific size range, then particles are humidified in a humidifying chamber kept at a fixed RH and the second DMA is used to determine the size distribution of the particles after umidification. The comparison of the initial dry size and the final size distribution after water uptake allows the determination of the hygroscopic growth and of the phase transitions of the analysed aerosol. H-TDMA have been applied in literature works both online to atmospheric aerosols[76–79] and to laboratory generated aerosols[79–81]. The RH range usually covered by H-TDMA is ~10-90%, because of the difficulty of accurately measure RH above 90%.

Other used ensemble techniques for the characterisation of hygroscopic properties of aerosols include Nephelometry[82,83], which consists in the measurement of the light scattering of aerosol particles that varies depending on the physical state of aerosol particles, and DAASS[84,85] (dry and ambient aerosol size spectrometry), which measures and compares the dry and ambient size distribution of atmospheric aerosol particles to determine their water uptake.

In recent years, electrical conductance methods were developed in the literature to measure indirectly the phase transitions of aerosol particles, by taking advantage of the different electrical properties of solid particles and of the electrolytic solutions that are formed as a consequence of deliquescence and water absorption by particles. Note that a review of these methods is proposed in Section 3.1.1, where they are discussed in detail and compared to the electrical conductance technique applied in Chapters 3 and 4.

Besides ensemble measurements, single particles techniques allow the characterisation of fundamental thermodynamic properties and kinetic processes in absence of inter-particle interactions. In addition, the same particle can be observed over long periods of time and subjected to variable controlled RH and temperature conditions. With single particle techniques the size and chemical composition of the analysed particle can be measured by non-intrusive techniques (such as light scattering or Raman spectroscopy). A review of the commonly applied single particles techniques that include electrodynamic trapping (see Section 5.1), optical tweezers, acoustic trap and microscopy observations, can be found in the work of Krieger et al. (2012)[21].

1.4 Aims and Thesis Outline

The equilibrium hygroscopic properties and the phase transitions of atmospheric aerosols are of great interest for the understanding of their effects on climate, on health and on contaminated materials (Section 1.2). The hygroscopic properties represent the subject of research of this thesis and they have been investigated with two different but complementary approaches. As envisaged by the title of this work, the investigated aerosol systems are characterised by variable chemical complexity and both atmospheric aerosols and simpler 'model' systems were considered.

On one side, the phase transitions of ensemble atmospheric aerosol samples were investigated, allowing the observation of an overall behaviour of heterogeneous and chemically complex atmospheric aerosol systems. Direct measurements of atmospheric aerosols phase transitions are extremely important if one wants to directly observe and characterise the behaviour of particles in the various chemico-physical processes they are involved in, both on the atmosphere and when deposited on surfaces. However, the rationalisation of ensemble measurements can be difficult and challenging, because of the number of different chemical components in atmospheric aerosol particles.

A completely opposite approach was applied for the development of a single particle technique for the investigation of simplified atmospherically-relevant aerosol systems. The aim of this part of the work was proposing a methodology for a systematic characterisation of the hygroscopic properties of aerosols with increasing chemical complexity (i.e. contanining multifunctional organic molecules, mixtures of organic and inorganic components) over a wide range of RH (above 50% RH) and for values close to saturation (>99%). The broader objective of this research was providing a tool for the reliable quantification of the hygroscopic properties of atmospherically-relevant aerosol systems to refine current aerosol thermodynamic models. In particular, this thesis was focused on the first steps of this broader research: the proposed experimental technique was validated by measuring the hygroscopic properties of well-characterised binary and ternary mixtures of water and inorganic compounds and then applied for the characterisation of the hygroscopicity of a first class of ternary water-inorganic-organic mixtures.

Before presenting the techniques used in this work and the obtained results, Chapter 2 discusses the thermodynamic principles that govern the partitioning of water between the gas and the condensed phases, together with the current thermodynamic modelling approaches applied in literature aerosol models. In addition, a kinetics theoretical framework for the description of the dynamics of water evaporation and condensation from and to aerosol particles is presented. Chapter 3 focuses on the electrical

conductance experimental method that was developed for the characterisation of the phase transitions of atmospheric aerosol samples in an Aerosol Exposure Chamber (AEC). Results from the direct measurements of the deliquescence and crystallisation processes of atmospheric aerosol samples are presented and discussed with reference to their ionic composition in Chapter 4, where the implications of these measurements in different fields of research are addressed, as well. In the second part of this work, the focus is on a single particle experimental technique. Chapter 5 describes the Cylindrical Electrodynamic Balance (C-EDB) experimental setup and all the operations for the generation and the trapping of single charged aerosol droplets in an electrodynamic field. Chapter 6 focuses on how the equilibrium hygroscopic properties of a droplet are measured using comparative kinetics experiments on single levitated droplets and validates the proposed method with measurements of the hygroscopic properties of well-characterised atmospherically-relevant inorganic compounds and their mixtures. The characterisation of a first ternary inorganic-organic systems is presented in Chapter 7, which focuses on the class of aminium sulphates.

Chapter 2 Thermodynamic Properties of Aerosols and Water Evaporation Kinetics from Droplets

In this Chapter, the thermodynamic properties that determine the equilibrium physical state of aerosol particles and their water content are presented. Aerosol thermodynamics is discussed in relation to the different factors that influence the physical state of aerosol particles, which are both dependent on external conditions (i.e. relative humidity, temperature and pressure of the surrounding gas phase) and on the chemical composition of particles. In addition, situations where aerosol systems are far from the thermodynamic equilibrium state are considered, as well. A theoretical kinetic framework for the modelling of the condensation and evaporation of volatile species to and from the aerosol condensed phase is presented and it is going to be applied in Chapters 6 and 7 for the determination of aerosol hygroscopic properties on single levitated droplets.

2.1 Thermodynamic Properties of Aerosols

In Section 1.1, aerosols were described as colloidal systems composed of a condensed phase (liquid and/or solid) within a gaseous phase. The chemical species that compose atmospheric aerosols can partition between the solid, liquid and gaseous phases, depending on their chemico-physical properties (such as solubility, volatility, etc.) and on the ambient condition that they experience, mainly temperature and RH.

Water represents an important fraction of the overall mass of aerosol particles and it is mostly present in the condensed phase of aerosols as 'unbound' water rather than 'bound' water, which is chemically-bound to the crystal form of the saline components in the particles)[3,86]. As anticipated in Section 1.1.2, water in the gas phase is usually described in terms of relative humidity (RH), which is defined as the ratio of the partial

pressure of water (p_w) in the gas phase and the saturation vapour pressure (p_w^0) at the considered temperature:

$$RH(\%) = \frac{p_w}{p_w^0} \cdot 100 = S_{w,\infty} \cdot 100 \qquad 2.1$$

In Eq. 2.1, $S_{w,\infty}$ is the saturation ratio of water in the gas phase, expressed as the ratio of p_w and p_w^0.

The saturation vapour pressure of water is strongly dependent on temperature and its temperature dependence is given by the Clausius-Clapeyron relation, reported in Eq.2.2 in its integrated form and with reference to a standard $p_w^0(T_0)$ at a specific temperature (T_0):

$$p_w^0(T) = p_w^0(T_0) exp\left[\frac{\Delta H_{\text{vap}}}{R}\left(\frac{T - T_0}{T \cdot T_0}\right)\right] \qquad 2.2$$

where ΔH_{vap} is the enthalpy of vaporisation of water and R is the universal gas constant.

In sub-saturated conditions, the RH covers values from 0 (no water in the gas phase) to 100% (saturated gas phase). Super-saturation (RH>100%) can also occur, for example when a mass of air experiences a decrease in temperature, the saturation vapour pressure decreases (according to Eq. 2.2) and the RH consequently increases to values that can exceed 100%, since partial pressure of water stays constant.

In the following Sections and the equilibrium the thermodynamic principles that underlie the equilibrium between the three different phases of an aerosol (solid, liquid and gaseous) are presented. Note that the following discussion specifically refers to aerosol systems where the only volatile chemical species that partitions to the gas phase is water.

2.1.1 Phase Transitions within the Condensed Phase of Aerosols

There are chemical species that can be found in aerosol particles both in the solid or in the aqueous phase, such as inorganic and water-soluble organic species (Section 1.1.2). The physical state that is actually observed for these chemical species in correspondence to fixed T and RH conditions depends on which one is the energetically favoured state.

If a pure salt aerosol system is considered, a typical diagram showing the phase transitions and the hygroscopic behaviour of a single particle is reported in Figure 2.1,

where the size variations of the particle due to water absorption is represented in terms of radial growth factor (GF_r):

$$GF_r = \frac{a(RH)}{a_{dry}} \quad 2.1$$

where $a(RH)$ is the radius of the particle at a certain RH, where a_{dry} is the radius of the dry particle. The radial growth factor is equal to 1 when a particle is in the dry state and no water is absorbed onto it (because $a(RH)=a_{dry}$), whereas it is $GF_r>1$ when some water is condensed to the liquid phase. Note that the GF_r is only one of the possible parameters that can be used to represent the hygroscopic properties of aerosol particles. Other representations are discussed in Section 2.1.5.

In Figure 2.1, at to low RH values, the Gibbs free energy of the solid salt (which is constant at fixed T and p) is lower than the Gibbs free energy of the corresponding aqueous solution, and therefore the salt remains in its solid phase. With increasing RH values, the Gibbs free energy of the solution decreases until it eventually becomes equal to that of the solid salt. A further increase in RH brings to a situation where the solution is the lower energy state for the saline particle and in correspondence to a certain critical RH, which is specific for each chemical species and depends on temperature[3], the salt spontaneously absorbs water, thus suddenly increasing its size (and mass) and forming a saturated solution. This spontaneous process is called deliquescence and the critical RH at which this process occurs is termed Deliquescence Relative Humidity (DRH). After deliquescence has occurred, any other increase in the gas phase RH results in more water condensing to the aqueous phase, according to the thermodynamic principles described in Section 2.1.2. Because of water condensation, the size of the droplet increases and the radial growth factor assumes higher values with increasing RH.

If the RH is successively decreased, water evaporates from the liquid to the gas phase. When the DRH is reached again, no prompt crystallisation is observed, even though the solid would be thermodynamically favoured. This happens because for crystallisation to happen a critical germ of nucleation has to be formed[87]. In fact, on a microscopic scale, within a disordered liquid phase small aggregates of ions are dynamically formed and quickly dissociate, because the release of energy associated to the dissolution of the cluster is bigger than the energy that would be release by the formation of a crystal. For crystallisation to occur, a sufficiently large cluster of ions needs to be formed so that the growth of a crystal is energetically favourable if compared to the dissolution of the cluster[88]. Even though crystallisation would be thermodynamically favoured, it does not happen in correspondence to the DRH because of the kinetic barrier of the critical germ nucleation. The formation of a critical germ of crystallisation occurs in supersaturated conditions and therefore the RH needs to be decreased below DRH (in correspondence of

which the solution is saturated) before the salt in solution can crystallise again. The RH at which crystallisation occurs is referred to as Crystallisation Relative Humidity (CRH) and it can be significantly lower that the DRH.

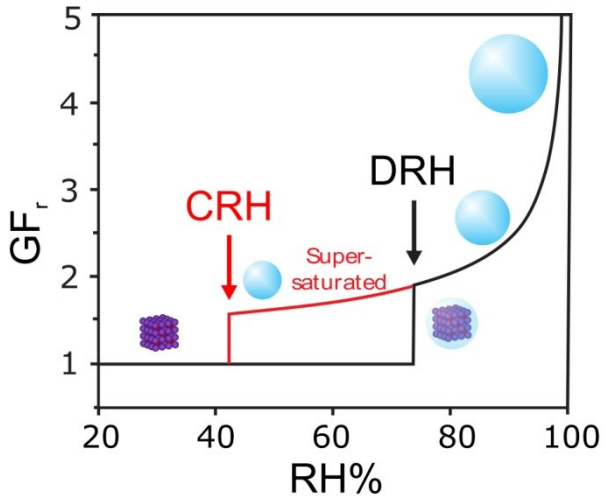

Figure 2.1: Radial growth factor as a function of the gas phase RH for a generic pure inorganic salt. The two phase transition RHs are indicated (DRH and CRH) and the hygroscopic growth of the solution droplet after deliquescence is also represented.

Since DRH and CRH do not coincide, GF_r diagrams as the one in Figure 2.1 present an hysteresis behaviour. Generally speaking, the term hysteresis describes a system whose properties are defined by the current conditions but also by the past conditions experienced by the system. In the case of the hydration state of an aerosol particle, this depends not only on the current RH conditions of the gas phase that surround it, but also from the previous RH history, i.e. the increasing or decreasing RH trend.

As a final remark on the phase transitions of simple hygroscopic saline systems, if a multicomponent aerosol is considered, deliquescence and crystallisation of the saline components occur at the Multual DRH (MDRH) and at the Mutual CRH (MCRH). MDRH and MCRH are always lower than their single-component equivalent of each of the chemical species that are present in the mixture and full deliquescence and crystallisation of all the saline components can occur over a range of RH, rather than as a single-step phase changes[89]. In addition, a number of literature studies investigated the phase transitions and hygroscopic properties of mixed inorganic and organic aerosol systems, demonstrating the influence of organic molecules to determine the overall water uptake of the studied aerosol systems[23,90–94].

2.1.2 The Liquid-Vapour Partitioning of Water in Aerosols

The Section 2.1.1 focused on the phase transitions of aerosol components in the condensed phase in correspondence to DRH and CRH, whereas in this Section the hygroscopic growth of particles due to the water absorption after deliquescence is discussed. In the atmosphere, the partitioning of water between the gas phase and the condensed phase is key for the determination of the size of aerosol particles and its understanding is essential because the amount of water in aerosol particles determine their activation and the formation of cloud droplets (Section 2.1.4).

The principles that govern the hygroscopic growth of aerosol particles after the deliquescence of their saline components are based on the thermodynamic equilibrium that is established between the gas and the condensed phase ($H_2O_{(gas)} \rightleftarrows H_2O_{(aq)}$). When this equilibrium is established, the chemical potential (μ) of water in the gas and in the condensed phases is equal:

$$\mu_{H_2O_{(gas)}} = \mu_{H_2O_{(aq)}} \qquad 2.3$$

Substituting the expressions of the two chemical potential in the gas phase and in the liquid phase:

$$\mu^0_{H_2O} + RTln(p_w) = \mu^*_{H_2O} + RTln(a_w) \qquad 2.4$$

where $\mu^0_{H_2O}$ is the standard chemical potential of water at a pressure of 1 atm, p_w is the vapour pressure of water in the gas phase, $\mu^*_{H_2O}$ is the chemical potential of pure liquid water and a_w is water activity. For pure H_2O in equilibrium with its liquid, since $a_w = 1$ and $p_w = p^0_w$(which is the saturation vapour pressure pressure at the considered T), one can write:

$$\mu^*_{H_2O} - \mu^0_{H_2O} = RTln(p^0_w) \qquad 2.5$$

Consequently, using Eq. 2.5 in Eq. 2.4 it results:

$$a_w = \frac{p_w}{p^0_w} = S_{w,\infty} = \frac{RH}{100} \qquad 2.6$$

Eq. 2.6 implies that water activity in the condensed phase of atmospheric aerosols is equal to the fractional RH of the gas phase, when the aerosol system is in equilibrium with the surrounding gas phase. The relation in Eq. 2.6 is valid for large droplets that can be assimilated to flat surfaces and for which the saturation vapour pressure at the

surface of the droplet ($S_{w,a}$) can be assumed equal to the water activity in solution ($S_{w,a} \approx a_w$). This assumption is valid for the droplet sizes (radius >100 nm) considered in Chapters 5, 6 and 7, but deviations from this assumption for small droplets are discussed in Section 2.1.3.

According to Eq. 2.6, when a droplet exists in equilibrium with the surrounding gas phase, the concentration of solute in it depends on the gas phase RH and on the hygroscopic properties of the solute. When RH assumes values close to saturation, the water activity within a droplet tends to unity, water condenses on it and the solution gets increasingly more dilute. On the contrary, if the RH is decreased, water evaporates to satisfy the relation between a_w and RH in Eq. 2.6 and the solute gets more concentrated in solution. The decrease in the water activity of the solution that is caused by the presence of solutes is referred to as the solute effect. As shown in Figure 2.2, the solute effect is different for different chemical species.

In the aerosol literature, the relation between water activity and solute concentration can be expressed with different, depending on what is the physical aspect that one wants to highlight (e.g. the increase in size due to water absorption with increasing RH, the same increase but on mass or molar basis, etc.). The different representation of the hygroscopic properties of a chemical species are discussed in details in Section 2.1.5.

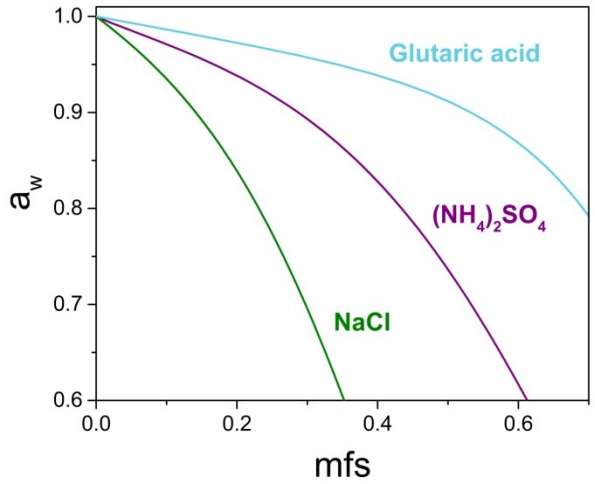

Figure 2.2: The solute effect expressed in terms of water activity (a_w) decrease with respect to the solute mass fraction (mfs). Data calculated for NaCl, $(NH_4)_2SO_4$ and glutaric acid with E-AIM Model (Section 2.2).

2.1.3 The Kelvin Effect

So far, the description of the thermodynamics that govern the partitioning of water between the gas and the condensed phase was performed assimilating aerosol droplets to a liquid flat surface. However, this assumption is valid for large droplets, whereas it fails to correctly describe smaller droplets with radii <100 nm. The reason for this is simply illustrated in Figure 2.3, where a flat surface and the surfaces of two droplets with different size are compared and where the little grey circles represent water molecules. If the arrangement of H_2O molecules at the three different interfaces is considered, a different disposition of water molecules is observed. The surface curvature that characterises droplets results in less neighbouring molecules around an H_2O molecule at the surface of a small droplet, if compared with a water molecule at a flat surface. Because of this arrangement of molecules at the gas-liquid interface, each molecule in a small droplet is subjected to fewer inter-molecular forces than a molecule on a flat surface and consequently it is easier for it to pass into the gas phase. Since the vapour pressure of a substance is related to the energy that is needed to overcome such inter-molecular forces exerted by neighbouring molecules, the vapour pressure at a curved interface is always higher than the vapour pressure for the same chemical species but at a flat surface and this is termed the Kelvin effect[3].

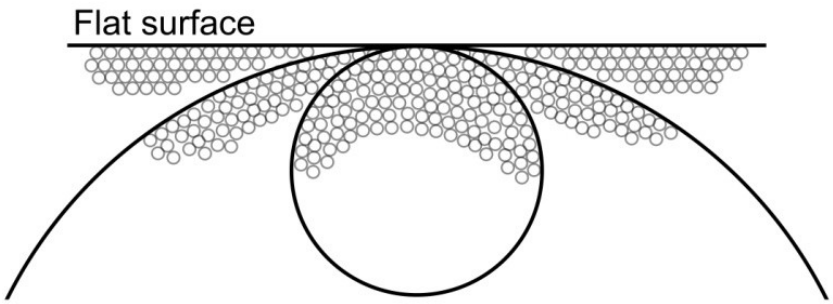

Figure 2.3: Effect of the surface curvature of droplets compared to a flat surface. The little grey circles represent water molecules. (Reproduced from Senfield and Pandis (2006)[3]).

As a consequence of the surface curvature effect on vapour pressure of a substance, the assumption in Section 2.1.2 that the saturation vapour pressure of water at the surface of the droplet is equal to the water activity in the droplet solution is not valid for droplets with radii <100 nm and $S_{w,a} \neq a_w$. Therefore a more general expression of Eq. 2.6 is that at an equilibrium state:

$$S_{w,a} = S_{w,\infty} \qquad 2.7$$

The Kelvin effect derives from the additional free energy that is associated to the surface curvature of a droplet if compared to a flat surface. The expression for the difference in the Gibbs free energy (ΔG) between a droplet and a vapour is given by Eq. 2.8[3]:

$$\Delta G = -\frac{4\pi a^3}{3V_{mol}} nRTlnS_{w,a} + 4\pi a^2\sigma \qquad 2.8$$

where the first term is the difference in the Gibbs free energy per molecule in the liquid and vapour states and n is the number of moles, R is the gas constant and V_{mol} is the volume of a molecule in the liquid phase. The second term is the free energy associated with a curved interface with curvature radius a and surface tension σ. The trend of ΔG as a function of the droplet radius and at three different saturation ratio of water in the gas phase is shown in Figure 2.4.

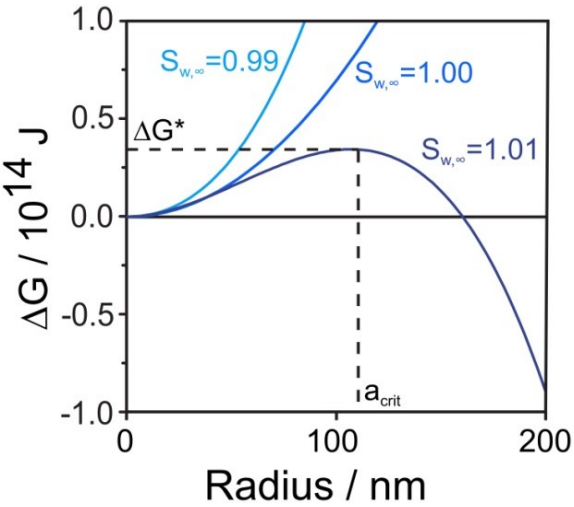

Figure 2.4: Difference in the Gibbs free energy (ΔG) between a droplet and a vapour as a function of the droplet radius for three water saturation values in the gas phase. a_{crit} and ΔG^* are the radius and ΔG values that need to be overcome for a droplet to grow.

When $S_{w,a} \leq 1$ (light blue lines), both terms in Eq. 2.8 are positive and a monotonic increase is observed for ΔG as a function of the radius. When $S_{w,a} > 1$ (dark blue line in Figure 2.4), the first term in Eq. 2.8 becomes negative and a different trend is observed: for small a values the surface term dominates and the trend is similar to the $S_{w,a} \leq 1$ case, whereas a maximum ΔG^* is reached in correspondence to a certain critical droplet size (a_{crit}). A droplet with $a > a_{crit}$ will continue to condensate water and grow since ΔG between the droplet and the vapour phases decreases. a_{crit} can be calculated according to:

$$a_{crit} = \frac{2\sigma V_{mol}}{nRTlnS_{w,\infty}} \quad 2.9$$

At the critical radius the $S_{w,a}$= $S_{w,\infty}$ and Eq. 2.9 can be rearranged to calculate the saturation of water per mole over the surface of the droplet by taking into account the surface curvature effect:

$$S_{w,a} = exp\left(\frac{2\sigma V_{mol}}{RTa}\right) \quad 2.10$$

The Kelvin effect in small for droplets with a>100 nm, because the $S_{w,a}$ tends to 1 and can be neglected. However, the Kelvin effect is important for smaller aerosol droplets and for their activation significant supersaturation values can be required.

2.1.4 Activation of Aerosol Droplets

Köhler theory[95] combines the solute effect (Section 2.1.2) and the Kelvin effect (Section 2.1.3) to predict the saturation ratio of water over a solution droplet:

$$S_{w,a} = a_w exp\left(\frac{2\sigma V_{mol}}{RTa}\right) \quad 2.11$$

Figure 2.5 shows the comparison of the functional forms of the solute and Kelvin effects and of the Köhler equation for two different particles with dry radius values of 20 nm (green curve) and 40 nm (pink curve). If the sole solute effect only is considered, a supersaturation of 0 is necessary for droplets to activate, and this is true for large particles (a>100 nm), for which the Kelvin effect is negligible. The combination of the solute and Kelvin effects results in a maximum in the Köhler curve and the supersaturation in correspondence to this maximum is referred to as critical supersaturation (S_{crit}). When the supersaturation ratio in the gas phase exceeds S_{crit} for the droplet, the activation of particles as cloud condensation nuclei (CCN) occurs and the droplet spontaneously starts to uptake water.

In Figure 2.5 a higher S_{crit} corresponds to the smaller droplet with a_{dry}=20 nm if compared to the droplet with a_{dry}=40 nm. The smaller the droplet and the higher the required saturation for the droplet activation. In addition, for aerosol droplets with the same size but with different chemical composition, a lower S_{crit} corresponds to droplets containing more hygroscopic chemical species[24]. Since atmospheric aerosols are composed of particles with both different dry size and chemical composition, larger and more

hygroscopic droplets will first, whereas the smaller droplets will activate only if the supersaturation of water in the gas phase increases sufficiently.

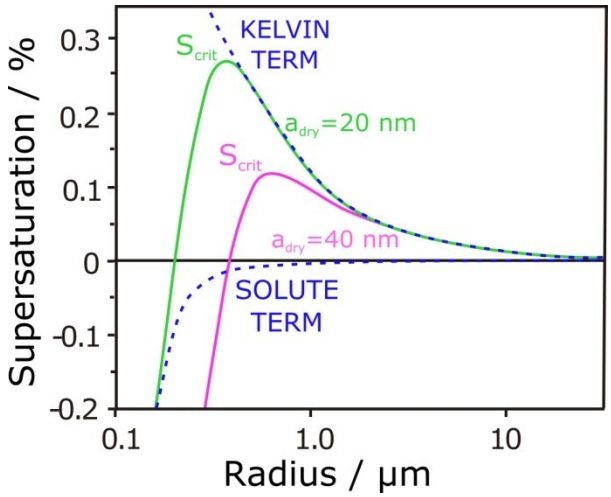

Figure 2.5: Köhler equation (Eq. 2.11) plots for two droplets with different dry size. The functional forms of the solute and Kelvin terms are represented, as well.

2.1.5 Representing the Hygroscopic Properties of a Compound

As a final remark, a description of the different parameters used in the literature and in this work to describe the equilibrium hygroscopic properties of atmospheric aerosols is presented. Usually, the hygroscopicity of aerosols is represented in diagrams similar to the one in Figure 2.1, where a parameter describing the water content of a particle (in Figure 2.1 the radial growth factor) is plotted against either the water activity in solution or the gas phase RH (note that for droplets with a>100 nm as in this work, they are equivalent for Eq. 2.6).

Radial growth factor (GF_r, Eq. 2.1, also referred to as size growth factor or diametric growth factor) is probably one of the most common parameters employed for the description of the hygroscopic properties[80,81,96-98] of aerosol particles, because both climate and health effects (Sections 1.2.1 and 1.2.2) depend on the size of particles and therefore it is useful expressing the water uptake by particles as a function of their increase in size. Similarly to GF_r, mass growth factor (GF_m) is also widely employed[21,45,93,99] and it is

defined as the ratio between the mass of the particle at a certain RH ($m(RH)$) and its dry mass:

$$GF_m = \frac{m(RH)}{m_{dry}} \quad 2.12$$

Mass fraction (mfs) or molality (b) as a function of the solution water activity can also be found to describe the water uptake by a solution droplet[97,100–102]. Note that both mfs and b tend to 0 for $a_w \rightarrow 1$, and that formally mfs is the reciprocal of GF_m.

$$mfs = \frac{m_{dry}}{m_{tot}} = \frac{1}{GF_m} \quad 2.13$$

$$b = \frac{n_{dry}}{m_{H_2O}} \quad 2.14$$

(Note that in the expression for molality the mass of water is expressed in kg).

When the hygroscopic properties need to be characterised on a molecular level[73,103,104], growth curves are represented in terms of absorbed moles of water per mole of solute in the solution:

$$n_{H_2O}/n_{solute} \quad 2.15$$

An alternative to the most common representation for hygroscopic proprieties discussed so far, stoichiometric osmotic coefficients (ϕ_{st}) vs. molality plots are also used for example fundamental studies that investigate the hygroscopic properties of a chemical species or of mixtures for parameterisation for thermodynamic models[73,105,106] (Section 2.2). Osmotic coefficients are related to the water activity in solution according to Eq. 2.16 and they indicate the deviation of the behaviour of the solvent from ideality.

$$\phi_{st} = \frac{-\ln(a_w)}{(m_{st} \cdot M_w/1000)} \quad 2.16$$

In the expression of osmotic coefficients, M_w is the molecular mass of water and m_{st} represents the stoichiometric molality, i.e. the sum of the molalities of all the ions in solution. An osmotic coefficient of 1 means ideal behaviour of the solvent and this values is approached for increasingly diluted solutions.

2.2 Modelling the Hygroscopic Properties of Aerosols

The understanding and modelling of the hygroscopic properties of aerosols is fundamental for predicting their water content and size distributions in a number of different applications: for the prediction of the activity of particles in clouds formation[24,107], for the modelling of their optical properties[108] and of their direct and indirect radiative forcing on the atmosphere[109–111] (Section 1.2.1), for the determination the partitioning of semi-volatile organic compounds (SVOCs) in the condensed aerosol phase[25,26] The capacity for aerosols to absorb water can also influence their deposition in the respiratory track on inhalation, potentially influencing the impact of aerosols on health[27] (Section 1.2.2). An accurate prediction of the phase transition RHs of particles composed of complex mixtures of chemical species is also desirable for the understanding and the prediction of the effects of aerosol particles deposited on surfaces of interest (i.e. electronics, cultural heritage artifacts, etc.)[51,112] (Section 1.2.3).

Different approaches have been developed in the literature for the modelling of aerosols hygroscopic properties. Rigorous thermodynamic models for calculating the hygroscopic response of mixed component aerosol have been developed based on bulk phase and aerosol phase measurements of the equilibrium response of binary solutions of a single solute and water. The Extended Aerosol Inorganics Model (E-AIM)[113,114] is one of the most widespread thermodynamic aerosol models and its thermodynamic treatments are widely applied in other models (e.g. ADDEM[115,116], ISORROPIA[117,118]). It allows the calculation of the partitioning equilibrium between a solid, two liquid (aqueous and hydrophobic) phases and a gas phase of systems containing H^+-NH_4^+-Na^+-SO_4^{2-}-NO_3^--Cl^--BR^--H_2O-organics at variable temperature ranges (depending on the considered system, overall T range: 200-330 K). The equilibrium state of the considered aerosol system is calculated by an iterative minimisation of its Gibbs free energy. In E-AIM Model, the activity coefficients of water and of the dissolved inorganic electrolytes are calculated using the Pitzer-Simonson-Clegg (PSC) equations, whereas a simplified treatment is applied for solutions containing both electrolytes and organics[119].

To represent the equilibrium properties of solutions containing the myriad of potential organic compounds found in the atmosphere, it is often necessary to resort to functional group activity models which require consideration of the interactions between electrolytes and organic species. In this respect, UNIFAC[120] (Universal Quasichemical Functional Group Activity Coefficient) is a commonly used semi-empirical group contribution method, which estimates the activity of non-electrolytic species by breaking down complex molecules into their fundamental constituent functional groups and smaller structural units. The advantage of the UNIFAC approach is clearly reducing the

complexity of multifunctional organic molecules for which direct parameterisations could not be available. On the other hand, this represents a simplified approach that has some intrinsic limitations, especially relating to calculations of systems containing multifunctional compounds and polar groups (e.g. -OH, -COOH)[121]. AIOMFAC model[122,123] (Aerosol Inorganic-Organic Mixtures Functional Group Activity Coefficients model) is another literature thermodynamic model that combines a modified UNIFAC approach for organic compounds and a Pitzer-like approach for electrolytes.

When rigorous thermodynamic approaches are combined with treatments of solution density and surface tension, accurate predictions of the variation in equilibrium particle size with relative humidity are possible. An example of this is given by ADDEM model[115,116], which couples E-AIM Model thermodynamic treatment and estimations of the Kelvin effect (Section 2.1.3) to account for the surface curvature of small droplets in the prediction of the equilibrium state of an aerosol system.

However, there is also a requirement to provide models of hygroscopic growth that are tractable in computational models of atmospheric chemistry, radiative transfer and climate models. To achieve this, models such as κ-Köhler theory have been developed to represent the hygroscopicity of aerosol particles using a single value of κ, which is related to the radial growth factor by Eq. 2.17:

$$GF_r = \left(1 + \kappa \frac{a_w}{1 - a_w}\right)^{1/3} \qquad 2.17$$

For organic compounds, κ value is between 0 (non-hygroscopic compounds) and 0.5 (very hygroscopic), whereas κ>0.5 for most hygroscopic inorganic species (e.g. $(NH_4)_2SO_4$, NaCl)[124,125]. Measurements of κ have been made for aerosols varying in complexity from binary component solution aerosol through to the complex multi-component mixtures found in the atmospheric aerosols[79,126,127]. A deviation of the κ parameter from a constant value is found when the RH is far from saturation[127], because the non-ideality of more concentrated solutions become more significant and the assumptions of the κ-Köhler theory are no longer valid. In addition, estimates of the critical supersaturation for CCN activation (Section 2.1.4) inferred from sub-saturated determinations of κ are often inconsistent with values determined directly from super-saturated measurements[74,75]. This highlights the need of measurements at values close to saturation to obtain κ values close to the infinite dilution limit that are not affected by such non-ideal behaviour. In addition, although the molecular complexity of secondary organic aerosol (SOA) precludes an accurate treatment of hygroscopic growth that explicitly accounts for each compound individually, simple empirical correlations that seek to exploit dependencies on average measures of composition (e.g. the variation of κ with O:C ratio) are often poorly defined and, at best, appropriate only for specific SOA precursors and environmental

conditions[79,126,127]. Hence, all this suggests that trying to reduce the complexity of hygroscopic properties by using single parameters relations, such as κ and O:C parameterisations, is not as straightforward as one would wish.

Besides the various approximations that underlie each aerosol model in the literature and the consequent uncertainties that arise from any simplified approach, there are also chemico-physical processes related to the nature of aerosol particles themselves that make the modelling of their hygroscopic properties even more complicated. For example, the slow deliquescence and low solubility of some organic components present challenges in interpreting measurements of hygroscopic growth[128]. Liquid-liquid phase separation into internal mixtures of hydrophobic and hydrophilic phases in mixed component aerosol remains a challenge in predicting equilibrium properties[22,129]. The extent of the depression of surface tension by surface active organic components and the interplay of surface and bulk partitioning in determining the critical supersaturation is often difficult to resolve[130,131]. Finally, the kinetics of water, VOC and SVOC condensation are often poorly determined with few quantitative measurements of the mass accommodation coefficients of organic species in particular[110,132,133].

In order to address the challenges in quantifying hygroscopicity for aerosols of complex composition, refinements in laboratory and field instrumentation, and improved frameworks for representing hygroscopicity, are required[21,98]. Hygroscopic growth measurements must be made up to water activities close to the dilute limit, ideally as high as 0.999. Such high a_w values are required for measurements to be directly relevant to CCN activation[134] and to place tighter constraints on the equilibrium solution compositions required to underpin the development of predictive models[135]. Single particle techniques represent a powerful tool for providing hygroscopicity measurements up to high a_w values. Specifically, the experimental technique proposed in Chapter 5 and applied in this work is very promising in this sense. On the other side, laboratory and field reliable measurements on atmospheric aerosols are needed, not only to characterise the hygroscopic behaviour of aerosols as they are actually found in the atmosphere, but also to provide data for the validation of the evolving thermodynamic models. The schematics in Figure 2.6 displays the process needed for the refinement of thermodynamic models just described.

The aerosol thermodynamic models discussed so far in this Section are able to provide prediction of the equilibrium hygroscopic properties of aerosols. For this reason, with respect to the phase transitions of aerosol particles, they are able to simulate deliquescence processes but not the crystallization of particles, since it is not an equilibrium process (Section 2.1.1).

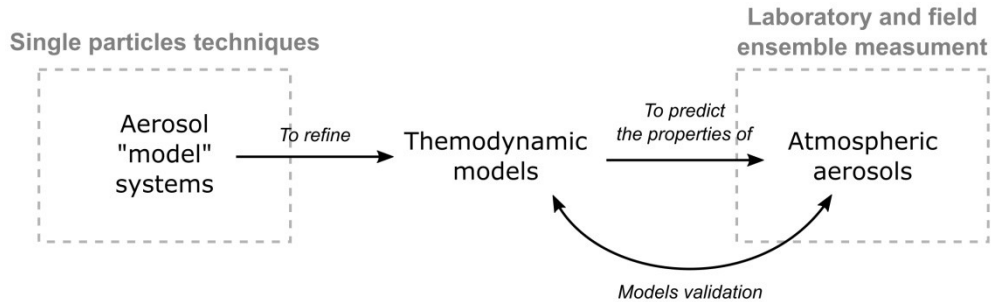

Figure 2.6: Processes for the development and refinement of current aerosol thermodynamic models.

In the literature, the only approach found for the modelling of CRH is a parametric model derived for a pure saline aerosol system of SO_4^{2-}-NO_3^--NH_4^+-H^+-H_2O by Martin et al. (2003)[136]. Since the parameterisation of this model are derived from the measurement of CRH for pure saline aerosol particles, it only considers homogeneous nucleation processes, without taking into account any effects of different kinds of inclusions embedded within an aerosol particle (i.e. silicates, organics, etc.) that can promote heterogeneous nucleation[87,137]. The implications of this are discussed further on in Section 4.2.2 and below just a brief description of the model is provided. The CRH parametric model by Martin et al. (2003)[136] is composed of two different empirical equations as a function of the ammonium over ammonium plus hydrogen fraction X and of the sulphate fraction Y, calculated over the sulphate+nitrate content:

$$X = n_{NH_4^+}/(n_{H^+} + n_{NH_4^+}) \tag{2.18}$$

$$Y = n_{SO_4^{2-}}/(n_{NO_3^-} + n_{SO_4^{2-}}) \tag{2.19}$$

The two expressions that compose this parametric model are reported in Eq. 2.18 and 2.21 and allow the calculation of the RH at which crystallization begins (CRH_{start}) and the RH at which the crystallization process ends (CRH_{end}), respectively. Both the equations for CRH_{start} and CRH_{end} refer to a temperature of 20 °C.

$$\begin{aligned} CRH_{start}(X,Y) = {} & -697.908 - 15.351X + 0.43X^2 - 22.11Y \\ & + 33.882XY - 1.818X^2Y + 0.772Y^2 - 1.636XY^2 \\ & + \frac{17707.6}{25 + (X - 0.7)(Y - 0.5)} \end{aligned} \tag{2.20}$$

$$\begin{aligned} CRH_{end}(X,Y) = {} & 3143.44 + 63.07X + 0.114X^2 + 87.97Y - 125.73XY \\ & + 0.586X^2Y + 0.95Y^2 - 1.384XY^2 \\ & - \frac{79692.5}{25 + (X - 0.7)(Y - 0.5)} \end{aligned} \tag{2.21}$$

2.3 Aerosol Evaporation and Condensation Kinetics

In Section 2.1.2, the equilibrium partitioning of water between the gas and the condensed phase of aerosol particles was described. In this Section, the response of an aerosol system to the perturbation of an equilibrium state is discussed and a literature theoretical framework for the modelling of dynamic mass transport to and from a droplet is presented.

In order to restore the equilibrium that has been perturbed by a variation of the external conditions experienced by an aerosol aqueous droplet (e.g. a variation in the gas phase RH that surrounds it), the response of the aerosol system is going to be either gas evaporation or condensation from or to the condensed phase. Note that for the following discussion, only the evaporation case is going to be addressed, but all the presented discussion is valid for condensation processes too. In fact, thanks to the principle of microscopic reversibility[138,139], condensation and evaporation can be considered equivalent but opposite processes and they can be described within the same theoretical framework. In addition, water is going to be considered the only evaporating species below, even though this treatment can be applied to any other volatile species.

Eq. 2.6 evidenced that, in an equilibrium state, the water activity within an aqueous solution droplet is equal to the gas phase RH. Figure 2.7 schematises a non-equilibrium situation and the dynamic response of a droplet with initial radius a that experiences a gas phase RH lower than its a_w (Panel A). The concentration of water in the gas phase decreases the further from the droplet surface and reaches a stable value in the 'bulk' of the gas phase, according to Fick's laws of diffusion[140]. In response to this perturbed situation ($a_w \neq$RH), water evaporates from the droplet, the water activity in solution decreases and the radius of the droplet decreases in time from a to a' (Panel B). The driving force of water evaporation is the spontaneous tendency of the system to re-establish the perturbed equilibrium, so that from a situation in which a_w>RH (Figure 2.7-A/B) tends to evolve towards a_w=RH (Figure 2.7-C). In Panel C, the water activity in solution has finally equilibrated with the gas phase RH, no further water evaporation is observed and the droplet has reached an equilibrated size (a_{eq}) such that a_w=RH.

The described mass transport of water from a droplet to the gas phase during evaporation is coupled to heat transfer, as well. The heat transport from the droplet to the gas phase is due to the removal of latent heat of vaporisation (L) associated with this phase change. For an accurate modelling of water evaporation kinetics, the mass and heat transport need to be coupled. The approach used in this and in other previous works[17,96,141–144] that employed the same experimental setup and a similar experimental

approach to the one used in this thesis (Chapters 6 and 7) for the coupling of mass and heat transport is that of Kulmala et al. (1993)[145].

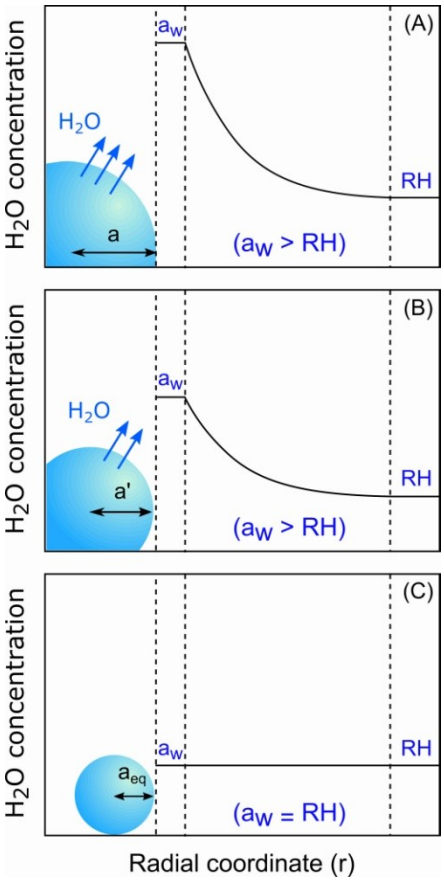

Figure 2.7: Water evaporation dynamics from a non-equilibrium state (Panel A) to an equilibrium state (Panel C).

The mass and heat transport equations from Kulmala and co-workers (1993)[145] allow the modelling of the evaporation and condensation kinetics of water or other volatile species from/to aerosol droplets. The mass flux (I) from a droplet with radius a is expressed as in Eq. 2.22:

$$I = -4\pi a(S_\infty - a_w)\left[\frac{RT_\infty}{M_W D_W \beta_M p_W^0(T_\infty)A} + \frac{a_w L_W^2 M_W}{KR\beta_T T_\infty^2}\right]^{-1} \qquad 2.22$$

S_∞ is the saturation ratio of water in the surrounding gas phase (also referred to as RH throughout this work), a_w is the water activity in the droplet solution, R is the ideal gas constant, T_∞ is the gas phase temperature, L_W is the latent heat of vaporisation of water,

M_W is the molar mass of water, D_W is the diffusion coefficient of water in the gas phase, $p_W^0(T_\infty)$ is the saturation vapour pressure of water at T_∞, K is the thermal conductivity of the gas phase and A is the Stefan flow correction, which accounts for convective transport generated at an interface by the removal of evaporating water molecules (Eq. 2.23).

$$A = 1 + p^0(T_\infty)\frac{S_\infty + a_w}{2p} \qquad 2.23$$

In Eq. 2.22, β_M and β_T are the mass and thermal transition correction factors respectively[146]. They take into account different mass and heat transport dynamics for droplets with variable sizes that can be described by means of the Knudsen number ($Kn=\lambda/a$), a dimensionless parameter that represents the ratio between the mean free path of molecule in the gas phase and the radius of the droplet. The kinetics evaporation of droplets with $Kn>>1$ ($a>1000$ nm) is governed by macroscopic gas diffusion laws, whereas droplets with $Kn<<1$ ($a<100$ nm) cannot be described with the same macroscopic laws since their evaporation is influenced by the random motion of molecules. The β_M and β_T transition correction factors are needed to reconcile the two different behaviour in the transition regime (100 nm$<a<$1000 nm, $Kn\sim1$) and take into account this free molecule behaviour in the area surrounding a droplet within one mean free path from its surface. The expression for β_M is reported in Eq. 2.24 and it is analogous to the one of β_T.

$$\beta_M = \frac{1 + Kn_M}{1 + \left(\frac{4}{3\alpha_M} + 0.337\right)Kn_M + \frac{4}{3\alpha_M}Kn_M^2} \qquad 2.24$$

The parameter α_M is termed mass accommodation coefficient and it represents the fraction of water molecules that are absorbed into the droplet bulk when they strike the surface. In this work, $\alpha_M=1$ is assumed, in agreement with previous studies which have reported the value of α_M for water accommodating/evaporation from a water surface[132,143,147]. Similarly to α_M, the thermal accommodation coefficient (α_T) indicates the efficiency with which a colliding water molecule is able to transfer energy to the droplet and is included in the expression for β_T, the heat transition correction factor. In this study, α_T was maintained constant at 1, in agreement with literature works on aqueous solution droplets[148,149].

Note that all the thermophysical parameters that appear in the mass flux treatment from Kulmala et al. (1993)[145] and their uncertainties have been thoroughly discussed in previous publications[17,96,141,143].

Having discussed the meaning of all the terms Eq. 2.22, its physical meaning can now be discussed. First of all, the mass flux (I) of water leaving an evaporating droplet represents the evaporation rate, since from the dimensional analysis of Eq. 2.22 I results expressed in terms of kg s^{-1}. Furthermore, from the relation in Eq. 2.22, the mass flux (i.e. the evaporation rate of water) is dependent on the concentration gradient of the evaporating species from the droplet surface to infinite distance, as schematically shown in Figure 2.7 (where a fast evaporation in Panel A is represented by three arrows and a slower evaporation is expressed with two arrows in Panel B). In fact, the higher the difference $S_\infty - a_w$ in Eq. 2.22 the higher the mass flux leaving the droplet. This means that faster evaporation rates are observed the more the studied aerosol system is far from the thermodynamic equilibrium.

The presented evaporation and condensation kinetics model by Kulmala et al. (1993)[145] is applied in Chapters 6 and 7 for the characterisation of the equilibrium hygroscopic properties of binary or ternary aerosol systems from the measurement of the water evaporation rate of single confined droplets.

2.4 Summary

In this Chapter, the thermodynamics that govern the partitioning of water between the vapour phase and the condensed phase of an aerosol were presented.

The phase transitions of simple saline systems were discussed at first, and the hysteresis that characterises deliquescence and crystallization processes was shown. The equilibrium water uptake following deliquescence was then described and it was pointed out that for large solution droplets in equilibrium with water vapour, the water activity within the solution is equal to the relative humidity in the gas phase. deviations from this

This represents the driving force for water evaporation or condensation from/to droplets that are not in equilibrium with the surrounding RH, because aerosol systems spontaneously tend to the equilibrium state. A literature modelling framework for the description of evaporation and condensation kinetics of water was presented and it is applied in Chapters 6 and 7 for the interpretation of evaporation profiles of single confined droplets.

Chapter 3 Electrical Conductance Measurements in the Aerosol Exposure Chamber

The experimental techniques for the determination of the hygroscopic properties of aerosols are numerous and diverse, as discussed in Section 1.3. Electrical conductance measurements for the determination of phase transitions of pure salts and of deposited atmospheric aerosols have been employed in a number of studies and they mainly differ on the considered substrates and on how particles are deposited on their surfaces. The aim of this Chapter is to give an overview of the different approaches that have been proposed in the literature for these conductance measurements, in order to give an overview of the background of the conductance experimental method used in this work. The Aerosol Exposure Chamber is then described and all the preliminary tests on the applied electrical conductance method are also discussed. Both $PM_{2.5}$ atmospheric aerosol and laboratory generated samples have been considered in this work. Therefore, a brief description of the atmospheric aerosol $PM_{2.5}$ sampling and chemical characterisation is given, together with the illustration of the techniques used for the generation of laboratory aerosol samples.

3.1 Determining DRH and CRH with Conductivity Measurements

The basic idea that underlies the application of electrical conductance measurements for the determination of phase transitions of hygroscopic compounds is relatively simple: when a saline substance deliquesces, it forms a saturated electrolytic solution that is electrically conductive. When the relative humidity in the surrounding atmosphere is increased beyond the DRH of the substance, more water is absorbed and the initially saturated solution gets increasingly more diluted; the conductance of the solution keeps rising because the number of free charge carriers increases as the solution gets more diluted. However, the solution can reach a certain critical concentration at which a

further decrease in the electrolytes concentration results in a decrease of conductance because the solution becomes more and more diluted[150,151]. If the RH of the gas phase is then decreased, during the dehumidification the opposite processes take place: water evaporates from the aerosol particles and the solution becomes more concentrated. As discussed in Section 2.1.1, when the DRH is exceeded during dehumidification no immediate crystallization occurs but the solution gets supersaturated and its conductance is still just slightly decreasing. In correspondence to the crystallization of the saline components (CRH) a stronger decrease in conductance is registered in a small RH range.

These chemical-physical properties of the hygroscopic species present in atmospheric aerosol particles were exploited in the literature to individuate the phase transitions of both single saline components and of more complex atmospheric aerosol. All the experimental approaches that carry out electrical conductance measurements for the determination of phase transitions of hygroscopic components can be defined '*indirect*', since no direct observation of deliquescence or crystallisation processes are involved. On the contrary, microscopy and optical techniques (see Section 1.3) can be defined '*direct*', because they involve the actual observation of water absorption (evaporation) during deliquescence (crystallisation). The different conductance techniques used the literature are reviewed in Section 3.1.1, the differences between them are highlighted and some solutions to overcome the setbacks of common literature approaches are proposed.

3.1.1 Conductivity Measurements on Aerosols in the Literature

The large majority of the literature works that apply electrical conductivity measurements for the determination of the phase transitions of aerosol particles are related to the study of the electrical failure of PCBs (printed circuit boards). The implications related to this aspect are discussed in detail in Sections 4.3.1 and 4.3.2. Anyway, for this reason, the preferred substrates for these literature studies are in many cases test boards[61,66,152–155]. If pure saline components are considered, small droplets of solution with known chemical composition can be either distributed on the substrate by means of a spin coating technique[154], simply deposited on the board[66,155], which is then dried before the RH cycle, or by atomizing a salt solution and subsequently drying the resulting droplets that are then deposited on the boards in a controlled environmental chamber[152,153]. If atmospheric aerosols are studied, particles are either collected from an environment of interest (e.g., a Data Center, see Section 4.3.1) and distributed on the board surface by means of a brush[61] (in agreement with the proposed method by the 2011 guidelines from ASHRAE[156], American Society of Heating, Refrigerating, and Air-

Conditioning Engineers), collected by washing a contaminated device with water and isopropyl alcohol and depositing on another test board the obtained solution[66] or by exposing the boards for long periods (weeks or months) in order to simulate a 'real' exposure to atmospheric aerosols[157]. When PCBs are directly contaminated with particles, typical experiments consist in measuring either the leakage current or the impedance degradation caused by deposited particles between two neighbouring plates during RH cycles.

A peculiar technique was employed by Schindelholz et al.[158], who measured the variation of the impedance of a microelectrode sensor (commonly used as RH and rainfall sensors) to study the hygroscopicity of deposited saline particles in RH cycles. A completely different kind of support was considered by Yang et al.[159], who soaked porous filtration paper sheets with saturated solutions of different salts and their mixtures and measured the variations of impedance during RH cycles.

All these techniques present benefices and disadvantages at the same time. Directly testing the effect of deposited particles on PCBs is desirable if their failure mechanisms are investigated. Testing pure salts solutions or their mixtures can be a good first approach not only to validate an analytical technique but also to evaluate the effects that these hygroscopic components have in electrical failure processes of PCBs, which is a relevant aspect since the saline components are the major responsible in the determination of the phase transitions of aerosol particles (Section 2.1.1). On the other side, in this way the role of other possible insoluble conductive species of atmospheric aerosols that can have some effects is neglected (see the evaluation of the role of conductive soot particles in Section 4.3.2). Besides, when the behaviour of deposited atmospheric aerosol particles is evaluated, the deposition methods described in the previously mentioned works[61,66,156] do not provide a reliable and reproducible procedure to make sure that the deposited particles are actually representative of those that can deposit on electronics in their operation environment, especially in terms of particles sizes and homogeneity of their surficial distributions.

Some work has been recently done to propose innovative techniques to overcome these disadvantages. The conductance measurements on $PM_{2.5}$ samples presented in this work and discussed by Ferrero et al. (2014)[112] and by D'Angelo et al. (2016)[160] go in this direction: the size distribution of the collected aerosol particles is controlled by the $PM_{2.5}$ sampling (Section 3.3) and a portion of the collected sample can be used to characterize the chemical composition of the sample (Section 3.5), so that the chemical-physical properties of the samples that undergo the electrical conductance measurements (Section 3.2) are known. A different sampling method was also proposed by D'Angelo (2016)[161] and Casati (2016)[162], which consists in a ROTating impactOR (ROTOR). Unlike usual cascade impactors, with which the collected particles are deposited along a rectangular

thin spot, in this device the sampling noozles are slowly rotated so that the sampling of circular homogeneous deposition spots can be carried out on non-filtering substrates virtually of any kind. A different approach was proposed by Casati et al. (2016)[162], who designed a deposition box for the controlled dry deposition of total suspended particles (TSP) on non-filtering substrates with standardised deposition rates. This sampling technique was specifically designed for the evaluation of particle-induced decay mechanisms on materials used cultural heritage artefacts (Section 4.3.3).

3.2 The Aerosol Exposure Chamber

The Aerosol Exposure Chamber (AEC, Figure 3.1) is a controlled environmental glass chamber with an internal volume of 1 m^3. It was developed at first for the electrical conductance measurements on deposited aerosol samples that are described in this work but it was designed to be versatile and to allow other kind of experiments that require controlled relative humidity and temperature conditions to be performed.

Figure 3.1: Frontal view of the Aerosol Exposure Chamber (AEC).

The AEC experimental setup is shown in Figure 3.2. Each of the three side walls of the chamber are equipped with six inert PTFE bypasses that give access to its inner

controlled environment in order to allow measurements and to vary the RH inside the AEC. A temperature and RH probe was used to monitor the conditions during the RH cycles (DMA572.1 probe with ELO008 M-Log Mini Data logger, LSI-Lastem; time resolution: 1 s; accuracy on RH: ±1% between 5 and 95% RH at 23°C; accuracy on T: ±0.1°C). The relative humidity in the chamber is decreased by phasing pure dry air (Aria Zero, Sapio) or increased with humidified pure air obtained by forcing an air flow through a sealed vessel saturated with water vapour (Milli-Q, Millipore, 18.2 MΩ cm @ 25°C). To make sure that the conditions inside the AEC are homogenous, a fan is operated during the RH cycles; in order not to direct an air flow straight to the samples, the fan is set at a 45° angle in respect to the back wall, on which it is placed, and slightly oriented to the ceiling of the chamber. A ventilation valve is also placed on one of the top corners of the back wall, so that the excess gas pressure that is formed in the sealed chamber because of the forced introduction of dry or wet pure air can be removed. The humidity cycles were performed with 1% RH steps in order to obtain good resolution in the measured conductivity curves, which results in a greater accuracy of the DRH and CRH estimated values than those reported in literature for similar methods but with lower RH resolution[61,159]. All the measurements in this work were performed at a constant temperature of 25°C.

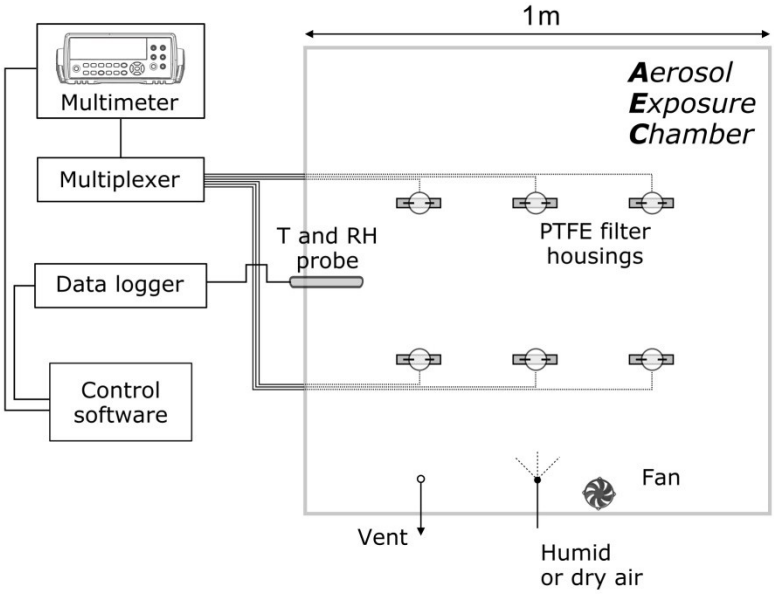

Figure 3.2: Scheme of the experimental setup, representing a top view of the AEC.

The front wall of the AEC can be opened and resealed allowing the placement of the aerosol samples on specifically designed filter housings. Up to six of these housings can be placed in the chamber to perform the conductance measurements on six aerosol samples

at a time during each RH cycle (Figure 3.2). The filter housings consist in a PTFE support and of a pair of electrodes set at a calibrated distance (either 5 or 2.5 mm) for the measurement of the variations in the conductance of the analyzed samples. Two different systems were used for the electrical conductance measurements: a HP 3421A module (electrical resistance detection limit: 30 MΩ) at first and then a system composed of a multimeter (Agilent 34411A; electrical resistance detection limit: 1 GΩ) coupled to a multiplexer (Agilent L4421A), that allows consecutive conductance measurements on different acquisition channels (six in this case, one for each of the six filter housings). A software interface (LabVIEW, National Instruments) was developed to control the measuring instrumentation. For each RH step, seven electrical conductance measurements are taken for each sample and averaged, with the highest and lowest of the measured values excluded from the calculation of the mean conductance from each acquisition channel.

3.2.1 Measurement of the Conductance of Deposited Aerosol Samples during RH Cycles

Before conductance measurements in the AEC, each sample is placed in a drier for 24 h in the darkness, so that their temperature can equilibrate with ambient temperature, which is necessary since they are kept in at -20 °C prior to the measurements. Once the samples are placed in the filter housings and connected to the electrodes for the electrical measurement, the chamber is sealed and the RH is kept at 30% for at least half an hour.

Figure 3.3 shows a typical electrical conductance measurement (G) on a $PM_{2.5}$ sample as a function of the relative humidity applied in the AEC during both humidification (blue circles) and dehumidification (red circles). Note that this and all the collected conductance curves were interpolated with a cubic spline every 1 % RH, in order to allow the comparison of conductivity curves from different samples that underwent separate RH cycles. DRH and CRH values together with the deliquescence and crystallization regions can be individuated as described in the work of Ferrero et al.[112].

The DRH and the CRH correspond to the maximum in the gradient (dG/dRH) of the humidification and dehumidification curves, respectively. The RH ranges in which the two opposite transitions take place are individuated where the gradient curve presents its greatest variations and significantly deviates from zero. The extremes of the deliquescence ranges are termed DRH_{start} and DRH_{end}, whereas the extremes of the crystallisation region are defined as CRH_{start} and CRH_{end}.

As a case study, a spring sample is shown ($PM_{2.5}$, 264.8 µg cm^{-2} on filter, collected on 14/03/2009, MI-TS site, 24 hours sampling). Within the humidification curve (blue circles), a 'dry' region can be individuated al low RH before the electrical activation point (black asterisk at RH=46%); this is then followed by the deliquescence region, which is characterised by a strong increase in electrical conductance, and by a following hygroscopic growth region. A similar behaviour is observed for the dehumidification curve (red circles), but the two branches registered during the humidity cycle show a well-rendered hysteretic behaviour, in agreement with literature studies[3,87,163]. In facts, on the basis of the maximum gradient method the DRH is individuated at 46% *RH* and the CRH at 57% *RH*. The deliquescence region lies between 50% and 62% *RH* and the corresponding increase in conductance ($\Delta G_{deliquescence}$) in this range is 17.23 µS. The crystallization region is located between 45% and 49% *RH* and it is characterized by a 9.91 µS conductance drop ($\Delta G_{crystallization}$).

Conductance trends as a function of the applied RH as similar to the curves reported in Figure 3.3 are in keeping with the shape of those reported by Yang et al.[159] and by Song et al.[61], who used similar conductance methods (Section 3.1.1). However, while Yang et al.[159] determined the DRH as the mid-point of the RH region where the largest change in conductivity was observed, Song et al.[61] did not identify the DRH but defined a critical transition range (a proxy of the DRH region) as the RH range between the start of impedance degradation (increase in conductivity) and a failure threshold level of 1MΩ (1 µS in terms of conductance).

Not all the analysed samples showed a strong increase (decrease) in conductance in correspondence to the deliquescence (crystallisation) of the soluble components. Ten atmospheric aerosol samples showed a gradual increase in conductance during humidification and a gradual decrease during dehumidification. An example of this kind of behaviour is shown in Figure 3.4 (sample: $PM_{2.5}$, 74.66 µg cm^{-2} on filter, collected on 30/07/2013, MI-TS site, 24 hours sampling). The reason behind similar behaviour is likely the presence of organic compounds (i.e. carboxylic acids, alcohols, SOA, humic like substances, levoglucosan) that alter the deliquescent behaviour of inorganic salts[23,90,92,94,99]. Carboxylic acids were quantified in this study (Section 3.5) but their content in samples that showed a gradual hygroscopic growth behaviour was on average similar to samples for which deliquescence and crystallisation were observed (see Section 4.1.1). The chemical composition of the organic fraction of the analysed samples was not characterised and therefore such non-deliquescent hygroscopic behaviour observed with conductance measurements could not be investigated any further.

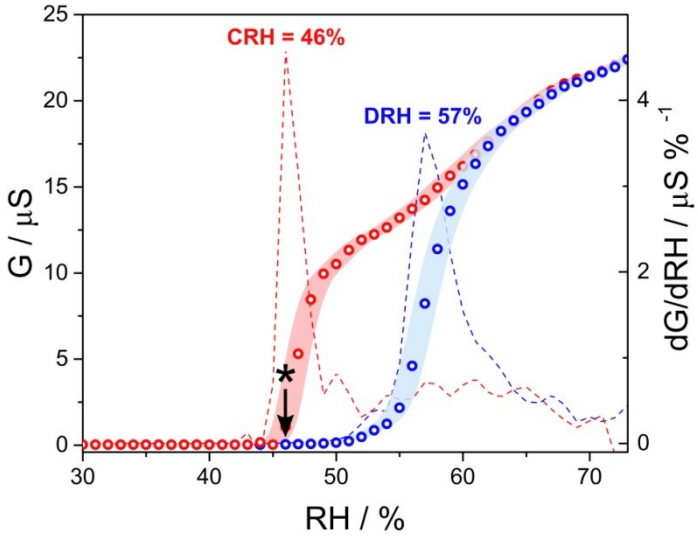

Figure 3.3: Typical electrical conductance (G) measurements during a humidity cycle (RH) in the AEC. Symbols: black asterisk – electrical activation point; circles – measured electrical conductance. Dashed lines – conductivity curves gradient, dG/dRH. Colours: blue – humidification; red – dehumidification. The shaded envelopes represent ±1% uncertainty on the measured RH.

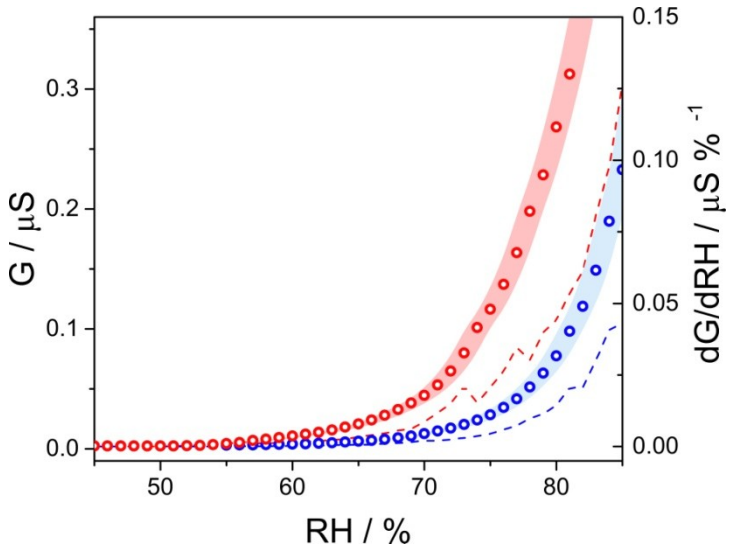

Figure 3.4: Measured conductance (G) vs. RH for a sample that did not show a deliquescent behaviour but a gradual increase in conductance with increasing RH. Symbols: circles – measured electrical conductance. Dashed lines – conductivity curves gradient, dG/dRH. Colours: blue – humidification; red – dehumidification. The shaded envelopes represent ±1% uncertainty on the measured RH.

3.3 Sampling of Atmospheric Aerosols

For the purposes of this work, $PM_{2.5}$ samples collected during the period 2006-2014 (in compliance with EN-14907), were analysed. The $PM_{2.5}$ was sampled using the FAI-Hydra dual channel Low-Volume-Sampler (LVS; 2.3 m^3 h^{-1}, 24 hours of sampling time, 47 mm PTFE filters with an sampling diameter of 39 mm). The $PM_{2.5}$ samples were collected in Milan at the Torre Sarca site (MI-TS; 45°31'19"N, 9°12'46"E), which is situated in the centre of the Po Valley, a European aerosol pollution hotspot[164–166]. The MI-TS sampling site has been active since 2005 within the campus of the University of Milan-Bicocca. A full description of the site and the related aerosol properties (chemistry, sources, vertical profiles and toxicity) is given in a series of previous studies[8,167–170]. In addition, samples collected at the rural site of 'Oasi Le Bine' (OB, 45° 8'17.24"N 10°26'10.99"E) we analysed. This second sampling site is still located within the Po Valley but it is defined as rural since it is situated in a natural reserve far from any major city[8,170].

After collecting the $PM_{2.5}$ samples, the filters were dried out and stored in darkness at -20°C at the Filter Bank of the University of Milano-Bicocca, that has been specially designed for the collection and storage of PM samples to be used later (after sampling) in order to investigate new aspects of aerosol science.

In order to both measure the DRH and CRH using the conductance method described in Section 3.2.1 and characterise their ionic fraction chemical composition (Section 3.5), the $PM_{2.5}$ samples were cut exactly into two halves. One half was analysed in the Aerosol Exposure Chamber, whereas the other half was used to determine the chemical composition of the ionic fraction. The uniformity of PM samples on filters has been examined in a previous work[171], and this allowed the use of different portions of the filter to investigate different chemico-physical aspects of the same collected aerosol sample.

3.4 Laboratory Generated Aerosol Samples

Beside atmospheric aerosol samples, different aerosol types (soot only, saline only, externally mixed saline and soot) were produced in the laboratory and analysed. Similarly to the atmospheric aerosol samples, the laboratory generated samples too were exposed to humidification and dehumidification cycles in the AEC and to ion chromatography analysis, in order to compare the obtained DRH of saline components with literature data and E-AIM Model calculations. The aim of this analysis (Section 3.6.4.1) was testing the validity of the proposed conductance method. In addition, these laboratory generated aerosol samples allowed the investigation of the role of different

chemical components in the determination of the electrical conductivity properties of aerosols (Section 4.3.2),

First of all, soot particles were generated from an acetylene non-premixed diffusion flame. Acetylene was produced from a controlled reaction between ultrapure water and calcium carbide. The generated acetylene was gurgled in ultrapure water in order to prevent any particle or solid contaminant to reach the flame. In addition, the gurgler avoids any possible backfire to the acetylene generation unit and represents an important safety component in this experimental setup. The flame was constantly kept at a height of 5 cm and the generated soot was sampled by means of a glass cone placed above the flame itself. In order to characterise the chemical-physical features of the generated soot, it was analyzed with a Thermal Optical Transmission method[172] (TOT, Sunset Laboratory inc.; NIOSH 5040 procedure) to quantify the elemental and organic carbon (EC and OC) content. The measured EC percentage on the total carbon content (TC) was determined on three soot samples and it was on average 95.2±2.5%. This average percentage indicates a low content of organic matter and is in agreement with what found in literature for acetylene flame soot[173–175]. In addition, the same samples were analyzed with gas chromatography according to the method described by Pietrogrande et al. (2010)[176] for the quantification of polycyclic aromatic hydrocarbons (PAHs) and n-alkanes (C_{20}-C_{32}), in order to verify the low content of organic species found with TOT measurements. On average, 104±62 pg of PAHs were quantified per gram of deposited PM mass while the content of n-alkanes was 305±184 pg μg^{-1}. If these amounts are compared with the average concentrations of PAHs and n-alkanes measured in atmospheric aerosols at the MI-TS site (PAHs from 100 to 600 pg μg^{-1}, n-alkanes in the 800-3000 pg μg^{-1} range, annual ranges[8]) the PAHs and n-alkanes content in the laboratory generated soot samples is either much lower or comparable with concentrations found in atmospheric aerosols at MI-TS.

Beside its chemical characterization, the number size distribution of the generated soot was determined by means of an SMPS 3936 (Scanning Mobility Particle Sizer, TSI Inc.) and it was found to be bimodal, with the two maximums at 60 nm and 270 nm, respectively. The generated soot conductance was also measured for eight soot samples (3 to 20 $\mu g\ cm^{-2}$ deposited on a PTFE filter) with the same experimental setup described in Section 3.2. The measured conductivities were in the 20-180 μS range at 30% RH, which is comparable to what measured for the soot from a gas turbine engine by Popovicheva et al. (2003)[177].

Pure saline aerosols were generated from aqueous solutions by means of the Aerosol Generator ATM 220 (Topas GmbH). The saline components considered used for the aerosol generation were $(NH_4)_2SO_4$, NH_4NO_3 and Na_2SO_4 because they are among the most abundant inorganic species found in atmospheric aerosols (Section 1.1.1). Mixtures

of ammonium sulphate and ammonium nitrate (WI-mix and SU-mix) were also considered and the relative abundances of the two salts reflect their Winter and Summer concentrations in the Po Valley[8] (WI-mix: 24% $(NH_4)_2SO_4$ + 76% NH_4NO_3; SU-mix: 86% $(NH_4)_2SO_4$ + 14% NH_4NO_3, on a mass basis). All the starting solutions were prepared at a concentration of ~$2.5 \cdot 10^4$ ppm, in order to achieve satisfactory particles concentrations according to the manufacturer specifications for the Aerosol Generator. The number size distribution of the generated aerosol was characterized with the SMPS, too (monomodal, maximum at 280 nm).

First of all, pure saline samples (three repetitions for each of the three considered salts) were generated and they were exposed to humidification and dehumidification cycles in the AEC (Section 3.2). At a later stage, mixed soot and saline aerosols were generated simultaneously and separately in two different Sampling Chambers (50 L volume each, PTFE), as shown in the schematic in Figure 3.5. All the generated aerosols were collected on PTFE filters (Ø=37 mm, PTFE, 2 µm porosity) by means of a pump (Leland Legacy, SKC, 15 L/min flow). In order to obtain well externally-mixed generated aerosol samples, the two flows from the two Sampling Chambers were conveyed through a three-ways glass connector, which couples the two flows before they get to the PTFE filtration membranes. In order to minimise contamination between two consecutive aerosol generation experiments, the two Sampling Chambers were cleaned with a pure air flow for at least three times their volume.

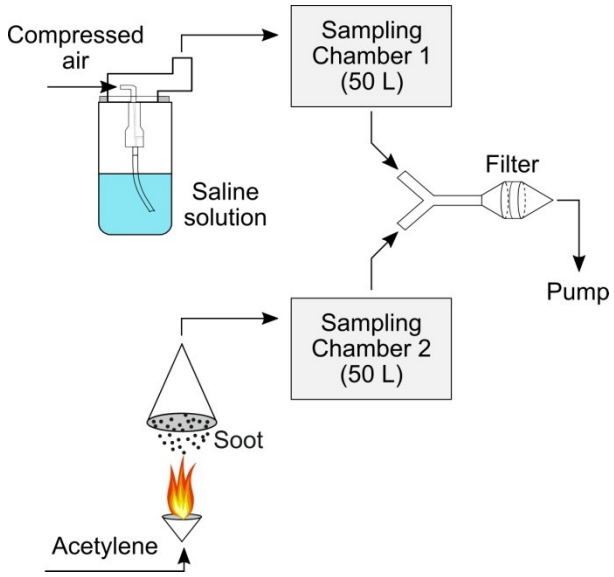

Figure 3.5: Generation of mixed saline and soot aerosol samples in the laboratory.

A total of 12 mixed saline and soot samples were generated. Their ionic content was quantified by ion chromatography (Section 3.5) and it resulted on average of 73.3 ± 5.5% on the overall deposited mass. The possible presence of other contaminant ionic species from the previous generation experiment was also assessed. This kind of impurities was quantified to be on average of 1.5±1.6 wt% of the overall sampled mass; the effect of such impurities is discussed in Section 3.6.4.1.

3.5 Ionic Fraction Characterisation with Ion Chromatography Analysis

The chemical composition of aerosol particles determine their hygroscopic properties and their deliquescence and crystallisation relative humidities[3,87,136,178]. Thus, the other half of the $PM_{2.5}$ samples that did not undergo RH cycles and conductance measurements in the AEC were used for ion chromatography (IC) analysis to determine the chemical composition of the ionic fraction of the samples.

The water-soluble fraction of the collected $PM_{2.5}$ aerosol samples was extracted in 3 mL of ultrapure water (Milli-Q®; 18.2 MΩ·cm @ 25 °C), measured by means of a calibrated pipette (DV5000, Discovery), for 20 minutes using an ultrasonic bath (SONICA, Soltec). The obtained solutions were then filtered (0.45 µm PTFE Syringe Filters, Phenomenex) in order to remove any possible solid particle in suspension that could contaminate the chromatographic columns and analysed within the following 24 h. Extraction efficiencies corresponding to this extraction experimental procedure have already been investigated in a previous work[179] and they were taken into account for the final quantification of the analysed chemical species.

Inoganic cations (Na^+, NH_4^+, K^+, Mg^{2+}, Ca^{2+}) and anions (F^-, Cl^-, NO_3^-, SO_4^{2-}), carboxylic acids (acetic, propionic, formic) and dicarboxylic acids (glutaric, malonic, succinic, oxalic) were analysed using two coupled chromatography systems (Dionex ICS-90 and ICS-2000) served by a shared auto-sampler (AS3000, Dionex). Cations were determined using a pre-column (IonPac CG12A-5 µm Guard 3x30 mm) and an analytical column (IonPac CS12A-5 Analytical 3x150 mm). An isocratic elution was performed with methanesulfonic acid (MSA, 20 Mm, Fluka) at a flow rate of 0.5 mL/min. The eluent signal was suppressed using a chemical suppressor (Dionex CMMS III 4 mm MicroMembrane Suppressor, regenerant: tetrabutylammonium hydroxide, TBA-OH, 0.1 M, Fluka). Anions were analysed using an Ion Pac AG11 4x50 mm Guard column and an AS11 4x250 mm Analytical column. A gradient elution was performed by means a solution of KOH with variable concentration (0.1-50 mM, Dionex), and the applied flow

rate was 1 mL/min. The eluent signal was suppressed by means of a, electrochemical suppressor (Dionex AMMS III 2 mm MicroMembrane Suppressor).

The quantification of the analysed compounds was achieved by means of the external standard method. Multi-component standard solutions were prepared separately for the analysed anions and cations from commercial starting solutions of each of the inorganic ions (1000 mg/L, Fluka) or from stock concentrated solutions prepared directly from the liquid carboxylic acids (acetic (98-100%), propionic (100%), formic (>99.5%), Sigma-Aldrich) and the solid dicarbolxylic acids (glutaric (>98%), malonic (>99.5%), succinic (>99%), oxalic (>99%), Sigma-Aldrich).

The uncertainties associated to the preparation procedure of samples and to the ion chromatography method used are here evaluated. The extraction procedure is affected by an uncertainty on the 3 mL extraction volume of ±0.6% (0.018 mL), according to the pipette manufacturer specifications. As already described, the efficiency of the extraction procedure of the water-soluble fraction prior to ion chromatography analysis was assessed in a previous work[179] and extraction efficiencies were taken into account for the quantification of the analysed components. A final source of uncertainty arises from the calibration procedure of the ion chromatography analysis carried out with the external standard method.

3.6 Development of the Conductivity Method in the AEC

A series of tests were performed in order to determine the optimal experimental setup for the conductance measurements on deposited aerosols and to validate the proposed method used in the AEC. These experiments focused on the evaluation of the response time needed for the electrical signal generated by aerosol samples to equilibrate after a change of the RH in the gas phase (Section 3.2), on the understanding and the lowering of the minimum aerosol loading necessary for conductance to be detected with the used experimental setup (Section 3.6.2) and on evaluating the effects on the measured electrical conductance that originate from the physical properties of the filtration membranes used for aerosol sampling (Section 3.6.3). In addition, the performance of the electrical method in reproducing pure salts DRH was evaluated (Section 3.6.4.1) and the DRH and CRH values obtained for a reduced dataset of 20 atmospheric aerosol samples were validated by comparing the measured conductance curves with GF_m curves obtained with a gravimetric method (Section 3.6.4).

3.6.1 Response Time of the Electrical Signal

Evaluating the response time of the electrical signal generated by samples housed in the electrodes housings in the AEC was essential in order to assess the reliability of the measured electrical conductance curves during RH cycles. For these equilibration tests, six $PM_{2.5}$ samples from the MI-TS site were housed in the AEC and the RH in the chamber was varied with ~1% RH steps between 50 and 70% RH; conditions were kept constant within the chamber for about 2000 s and after the equilibration of the RH conditions within the chamber (2 min) the conductance of the six samples was constantly monitored. Figure 3.6-A shows the variations of RH (black) and conductance of one of the six samples (red) during the whole duration of the test. The two trends are clearly well correlated and constant RH conditions are associated to constant measured electrical conductance (see in particular the enlarged graphs in Figure 3.6-B). With respect to the RH plot, it can be noticed that in correspondence to two steps (~56% and ~58%) the RH was not constant in the chamber (Figure 3.6-C). Anyway, in correspondence to these two equilibration steps, the conductance of the sample increases accordingly to the RH, showing that the electrical response of the sample as a consequence of an RH increase is immediate.

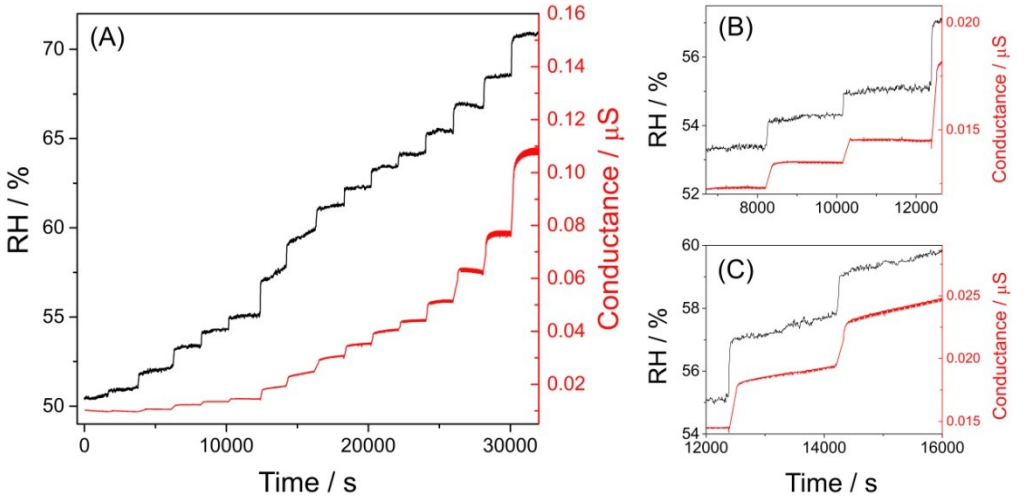

Figure 3.6: (A) Test of the electrical signal (red) response time during ~2000 s RH steps (black) in the AEC. (B) Enlargement of steps with stable RH. (C) Enlargement of steps with slightly increasing RH trends.

For a further evaluation of this aspect of the experimental procedure, for the same sample shown in Figure 3.6 four conductance curves as a function of RH are plotted in Figure 3.7. Each of these curves corresponds to conductance values measured at 0 s after the equilibration of RH (black), 180 s (brown), 1200 s (red) and 1800 s (pink). The first

three conductance curves (taken at 0, 180 and 1200 s) are virtually undistinguishable one from the other. Slight differences can be observed if these three curves are compared with the fourth curve of G measurements taken at 1800 s, but the general trends individuated by all four curves is very similar. Therefore, whether the conductance measurement is immediately taken after the RH equilibration in the chamber or after a longer period the final shape of the conductance vs. RH curve would be the same. In the light of the results of this time response test, during RH cycles the conductance measurements were taken after 2 minutes from the equilibration of the RH in the AEC.

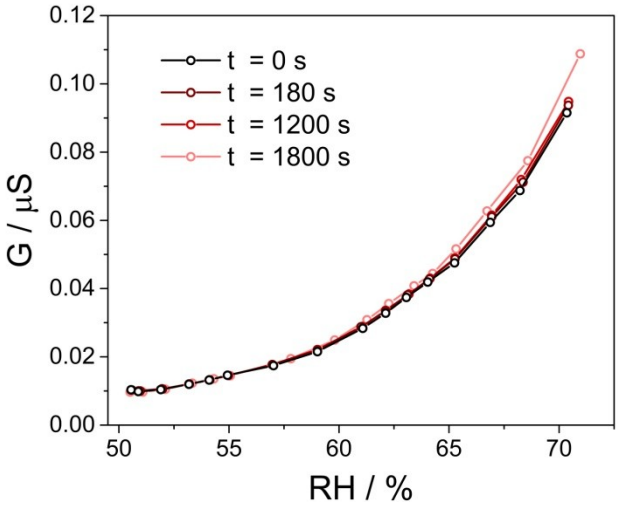

Figure 3.7: Conductance (G) curves measured at different times after the RH is varied within the AEC. Colours: black – 0 s; brown – 180 s; red – 1200 s; pink – 1800 s.

3.6.2 Lowering the Minimum Aerosol Loading on Filters

The existence of a minimum aerosol loading for the conductance measurements in this work was discussed by Ferrero et al.[112], with reference to this specific experimental approach ($PM_{2.5}$ sampling + AEC, HP 3421A module, Section 3.2).

The analysed dataset in the work by Ferrero et al.[112] consists in 55 $PM_{2.5}$ samples collected at the MI-TS sampling site and these aerosol samples span over a range of atmospheric concentrations of between 13.7 µg m^{-3} and 107.5 µg m^{-3}. These are typical values for the Po Valley, which is characterized by seasonally-modulated pollution levels[8,166,168]. These atmospheric concentrations turn into a similar broad range of aerosol loadings on the sampled $PM_{2.5}$ filters (24 h sampling time; flow 2.3 m^3 h^{-1}), from 63.2 µg

cm^{-2} (0.755 mg on filters) to 496.6 µg cm^{-2} (5.932 mg on filters). The average aerosol loading on the subset of the 45 $PM_{2.5}$ samples for which an electrical conductance response was detected was 221.9±13.5 µg cm^{-2} (2.651±0.161 mg on filters), which is slightly higher than the smallest surficial dose used by Song et al.[61] (150 µg cm^{-2}); conversely, the 10 $PM_{2.5}$ samples that did not show any electrical conductance, displayed a statistically lower (t Student at α=0.01) aerosol mass loading, with a value of 127.1±7.8 µg cm^{-2} (1.518±0.094 mg on filters). Due to the relevant role of the aerosol ionic fraction in the determination of the conduction of the electrical signal (Section 3.1), the average ion loading for both $PM_{2.5}$ samples subsets was also addressed: 85.7±9.2 µg cm^{-2} for those samples that showed any electrical conductance signal to RH changes and 53.1±6.5 µg cm^{-2} for those that did not. It is interesting that the ionic surficial loading for the 10 filters that did not show any signal is of the same order of magnitude of the threshold value (24.2 µg cm^{-2}) calculated by Weschler[180] for deposited 520 nm particles of pure NH_4HSO_4 on the basis of the percolation theory[181,182]; from this theory it results that the probability of forming an electrical bridge is 90% if 53% of the possible dust deposition sites are occupied by a particle[54]. However, Weschler[180] performed his calculation simply considering dry particles and, on the contrary, a critical surficial concentration of 15 µg cm^{-2} was calculated by Tencer[54], who took into account a bigger wet radius for NH_4HSO_4 particles in correspondence to its DRH (39% RH).

It is important underlying that it is not possible to discriminate whether these samples did not actually electrically activate or their electrical signal was too low to be detected with the employed experimental setup (upper detection limit for electrical resistance of 30 MΩ for the HP 3421A module, 0.5 mm distance between the electrodes).

However, this minimum aerosol loading limit was partially overcome in the following part of this study by simply modifying and improving the experimental approach in different ways. First of all, the experimental setup was modified by the introduction of a new multimeter with a higher resistance detection limit (Agilent 34411A, maximum detected resistance: 1 GΩ) and by reducing the distance between the electrodes in the filter housings from 5.0 mm to 2.5 mm. In addition, the sampling method was modified by reducing the sampling spot over which samples are collected from 39 mm (for a 47 mm PTFE filter) to 30 mm. Thanks to this adjustment, the surficial mass concentration of particles collected on a filter is increased by ~70%, even if the overall sampled mass is the same, because the sampling flow is kept constant (2.3 m^3 h^{-1}, Section 3.3). An example of the effect of this procedure on the measured conductance curve is shown in Figure 3.8: two samples were collected simultaneously at MI-TS (Sample 1 - green: 1.292 mg on filter, surficial loading of 182.8 µg m^{-3}; Sample 2 - blue: 1.231 mg on filter, surficial loading of 103.1 µg m^{-3}) and their conductance as a function of the gas phase RH was measured during humidification. Being collected at the same time, the two samples are characterised by the same chemical composition and therefore by the same DRH. The

measured conductance of Sample 1 is about four times higher than that of Sample 2, simply because its surficial distribution of particles is higher. The two curves are very well comparable and the obtained DRH values in correspondence to the maximum gradient are in agreement within the experimental uncertainty on the measured RH (71% for Sample 1 and 72% RH for sample 2). Note that in Figure 3.8 the gradient curves (dashed lines) are multiplied by 10 for clarity in the graph. Following to these modifications and improvements in the experimental setup and procedures, the percentage of non-detected samples was significantly decreased and the issue of a minimum aerosol loading needed on filters for conductance measurements was mostly overcome.

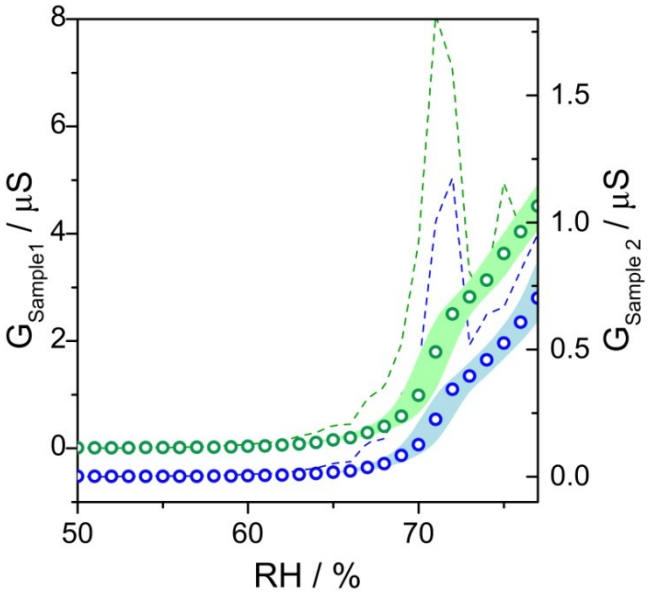

Figure 3.8: Comparison of the humidification curves of two samples collected simultaneously (i.e. with same chemical composition) but with different surficial mass distribution.

3.6.3 The Effect of the Filtration Membrane on Conductivity Measurements

The filtration membranes employed for the collection of atmospheric aerosol particles are various and diverse with respect to their physical properties and chemical composition. Among the most commonly used substrates, PTFE (polytetrafluoroethylene) membranes are preferred in many field of application because of several reasons: low contamination levels, hydrophobic and chemically inert material, low tare mass value suitable for

gravimetric analysis, semi-surface filtration membranes. Quartz or glass fibre membranes are also widespread, in particular for the analysis of organic components. They are depth filters and they need to be baked before sampling in order to remove possible organic compounds adsorbed to their fibrous matrix[183].

Because of the different chemico-physical properties of different filtration membranes, at a first stage conductance measurements during RH cycles in the AEC were performed on samples collected simultaneously at MI-TS on PTFE and quartz fibre filters. The most relevant physical difference between the two substrates is their affinity with water. Awakuni and Calderwood (1971)[184] reported a contact angle of a water droplet over a PTFE surface of 104°, which classifies the material as 'non-hydrophilic'; in addition, they measured the adsorption of water vapours by PTFE and quartz fibre surfaces and close to saturation conditions they quantified three adsorbed layer for PTFE and 7 for quartz.

With respect to the conductance measurements in the AEC for the determination of the phase transitions of deposited particles, evaluating the effect of filtration substrates with different physical nature and with different affinity to water vapour is therefore essential. Eom et al. (2014)[185] demonstrated that hydrophobic supports (in their case parafilm-M and TEM grids) are the most suitable for hygroscopicity measurements on deposited saline particles with optical microscopy methods. An analogous evaluation was performed in this work by measuring the electrical conductance variation of 18 pairs of aerosol samples collected simultaneously at MI-TS on PTFE and quartz fibre filtration membranes. Similarly to the pair of samples in Figure 3.8, the two samples within a pair are characterized by the same chemical composition, because they were collected at the same time. Therefore, any observed difference in their electrical behaviour can be reasonably attributed to the different nature of the substrate.

In order to compare the obtained curves, the measured conductance as a function of RH was normalized over the maximum measured value in each curve and all the normalized curves were averaged to obtain collective trends for samples deposited on PTFE and quartz fibre. The two averaged curves obtained during humidification (blue) and dehumidification (red) are shown in Figure 3.9, where the shaded envelopes represent the standard deviation. With respect to the PTFE case (Panel A), a well-rendered hysteretic behaviour can be observed between the increasing-RH and the decreasing-RH branches and two broad deliquescence and crystallization regions can be individuated (~70-75% and ~68-64% RH, respectively) even if the curves are averaged. In the case of samples deposited on a quartz fibre membrane (Figure 3.9-B), essentially no hysteresis is observed and the average electrical signal gradually increases with increasing RH with no steep increase or decrease that could be associated to any deliquescence or crystallization phenomenon. In addition, the narrow standard deviation of the averaged curve obtained for the quartz fibre samples suggests that the original measured curves do not

significantly differ one from the other. This smaller variability found for samples deposited on quartz fibre filters implies that this electrical behaviour is mainly due to the physical properties of the filtration membrane rather than to the hygroscopic properties of the deposited aerosol particles. Such electrical response is likely due to the hydrophilic nature of quartz fibre, that may adsorb water itself thus disguising any possible electrical signal generated by phase changes of the aerosol particles.

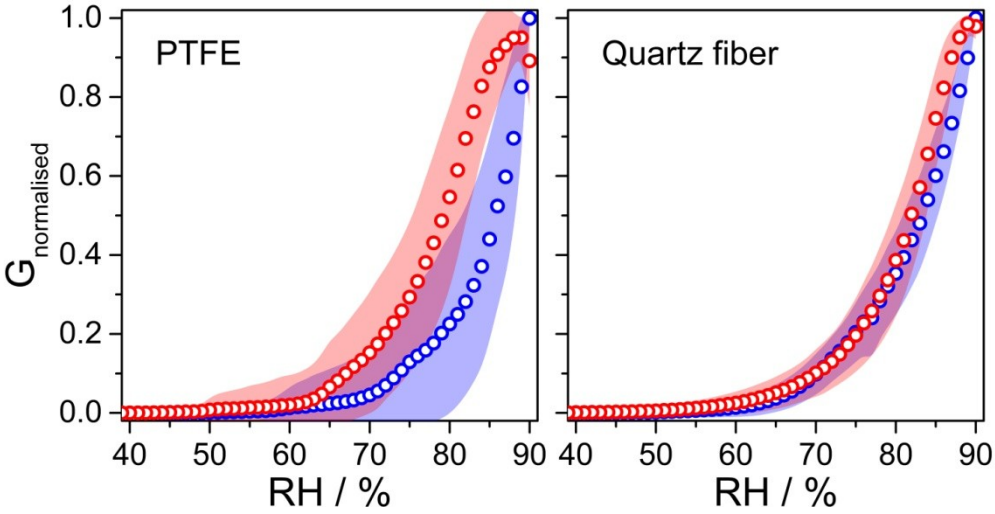

Figure 3.9: Average normalised conductance curves for 18 pairs of MI-TS aerosol samples collected on PTFE (Panel A) and on quartz fibre (Panel B) filtration membranes.

For these reasons, PTFE was then preferred for the investigation of DRH and CRH of atmospheric aerosol samples. Besides, its hydrophobicity makes it similar to epoxy-based composites that constitute printed circuits boards and circuit components encapsulates[186]; this aspect is important for the application of these measurements to Free-Cooled Data Centers that is discussed in Section 4.3.1.

3.6.4 Comparison of the Electrical Conductance Method with a Gravimetric Method

In order to evaluate the validity of the proposed conductance method to determine the phase transition RHs of atmospheric aerosol samples, DRH and CRH were also identified by means of a gravimetric method[160] for a sub-dataset of 20 MI-TS samples and for mixed saline and soot laboratory generated samples. The gravimetric method consists in placing a precision weighting analytical balance (Sartorius SE-2F; precision: ±0.1 µg) in

the AEC and measuring the variations in the mass of a sample at each RH step during RH cycles in the chamber. The mass increase (during humidification) or decrease (during dehumidification) is entirely attributed to water absorption by the deposited particles and a mass growth factor (GF_m) can be calculated from the measured mass variation according to Eq. 2.12. DRH and CRH were obtained with the same gradient method used for conductance vs. RH curves described in Section 3.2.1. This evaluation is important because it compares the direct measurement of water absorption during RH cycles and an indirect determination of the phase transitions of deposited aerosol, which is provided by the conductance method. As an example, the comparison of the conductance curves obtained with the electrical method and the GF_m curves measured with the gravimetric method for a MI-TS sample ($PM_{2.5}$, 266.4 µg cm^{-2} on filter, collected on 20/03/2014, 24 hours sampling) is shown in Figure 3.10, both for data registered during humidification (Panel A) and during dehumidification (Panel B). The steep increase/decrease in electrical conductance detected with the electrical method (open circles) in correspondence to the deliquescence and crystallisation processes (Section 3.2.1) matches with a substantial water condensation/evaporation measured with the gravimetric method (solid squares). These correlated trends individuated by means of the two independent methods confirm the validity of the proposed approach for the determination of DRH and CRH by means of electrical conductance measurements.

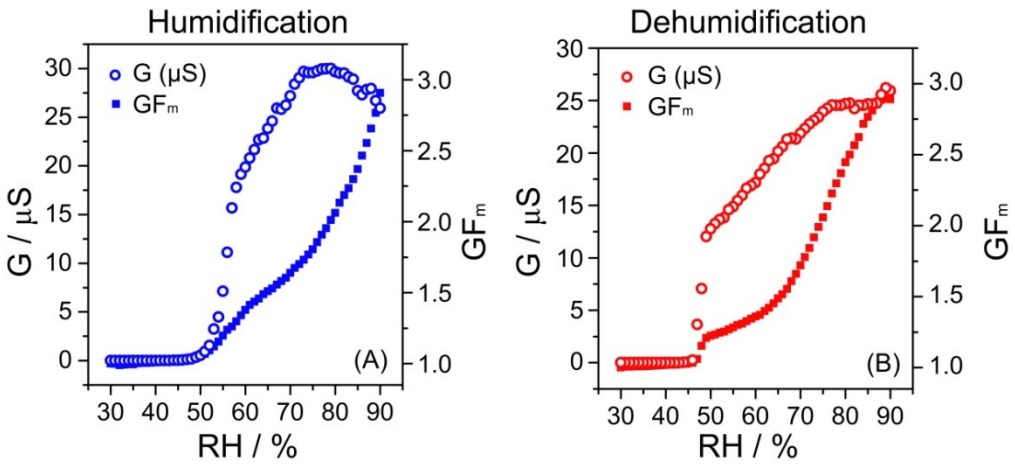

Figure 3.10: Comparison of conductance (G, open circles) and GF_m (solid squares) as a function of RH measured with the electrical conductance and with the gravimetric methods, during humidification (Panel A) and dehumidification (Panel B).

On a side note, a consideration on the shape of the electrical conductance curve shown in Figure 3.10-A is necessary. At RH~70%, the measured electrical conductance reaches a maximum value, is then relatively constant up to RH~80% and then decreases in the

very last part of the humidification diagram. On the contrary, the corresponding GF_m curve is characterised by a monotonic increasing trend, typical of aerosol growth curves (as the one shown in Figure 2.1). Such electrical behaviour after deliquescence at high relative humidity was sometimes observed and it was attributed to a considerable dilution[150,151] of the electrolytic solution that is formed after deliquescence, as anticipated in Section 3.1. This interpretation is also supported by the measurement of the mass increase measured with the gravimetric method as a function of the RH. In fact, at RH=90% the measured mass growth factor is 2.9, meaning that the aerosol particles on filter have absorbed an amount of water equal to almost three times their original mass.

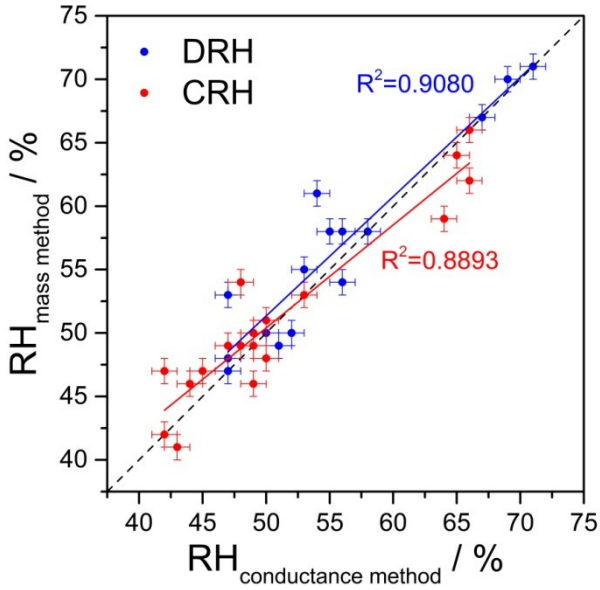

Figure 3.11: Correlation plot of DRH (blue) and CRH (red) values obtained with the conductance method (x axis) and the gravimetric method (y axis). The dashed line represents 1:1 correlation, whereas the blue and red lines are fitted through the DRH and CRH data points, respectively.

The DRH and CRH values obtained both with the conductance and the gravimetric methods were compared for the 20 MI-TS atmospheric aerosol samples that were characterised by means of both approaches. Figure 3.11 shows the correlation plot between DRH (blue) and CRH (red) values corresponding respectively to the maximum gradient of the conductance vs. RH and mass vs. RH curves during humidification and dehumification in RH cycles. The error bars take into account the 1% experimental uncertainty on the measured RH and the dashed line indicates the 1:1 correlation line, which is plotted for comparison. The agreement between the values determined independently with the two methods is satisfactory (R^2 of 0.908 and 0.889 for DRH and

CRH, respectively). No general trend of overestimation or underestimation was found and this indicates that the determination of DRH and CRH by means of electrical conductance measurements is not affected by any systematic error.

3.6.4.1 Laboratory Generated Aerosol Samples DRH Comparison

As a further evaluation of the performance of the conductance method, pure saline aerosol samples were generated according to Section 3.4. Unfortunately, it was not possible to perform conductance measurements on these samples; the reasons for this are detailed further on in Section 4.3.2.4 and are not discussed here. However, conductance measurements were successful for mixed saline and soot aerosol generated samples. Figure 3.12 shows the DRH values obtained for $(NH_4)_2SO_4$, NH_4NO_3, Na_2SO_4, WI-mix and SU-mix by means of the conductance (dark grey) and the gravimetric (light grey) methods. The bars corresponding to each of these values represent the deliquescence range, individuated according to Section 3.2.1. The agreement between results from the two different measurement techniques is good within the experimental uncertainty on RH, both for the DRH and for the deliquescence range.

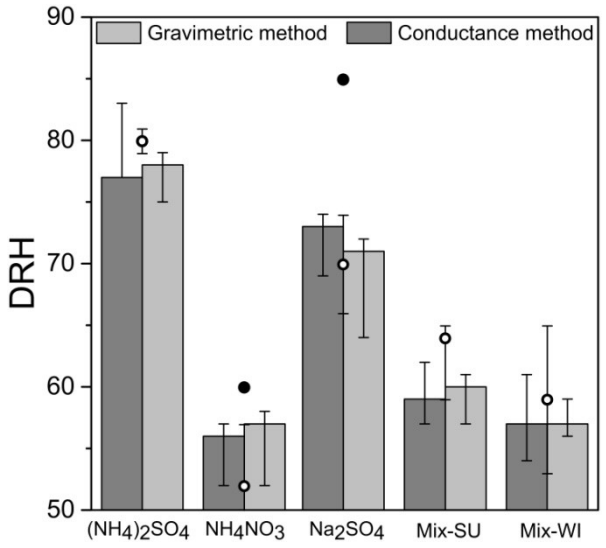

Figure 3.12: Comparison of DRH values for pure salts ($(NH_4)_2SO_4$, NH_4NO_3, Na_2SO_4) and $(NH_4)_2SO_4/NH_4NO_3$ mixtures (Mix-SU, Mix-WI) mixed with soot particles. Data were experimentally obtained with the conductance (dark grey) and gravimetric (light grey) methods, taken from literature[3] (black circles) and from calculations with E-AIM Model (open circles), which takes into account the impurities quantified by means of ion chromatography. The bars indicate the deliquescence range as defined in Section 3.2.1.

The experimentally determined values are also compared with the corresponding pure component DRH literature values[3] (black datapoints in Figure 3.12) and calculations from E-AIM Model (open circles), which were performed by taking into account the measured contamination of other ions from ion chromatography analysis (note that the literature DRH for $(NH_4)_2SO_4$ is hidden by the open circle). It is evident that even the presence of a small amount of contamination from previous generation experiments (<3 wt% on the total ionic content, Section 3.4) significantly affects the DRH of the three considered pure saline components. The agreement of the experimental values with the DRH is evidently better with this calculation for NH_4NO_3 and Na_2SO_4 rather than the pure component literature value. The agreement between the calculated values and the DRH obtained from both the conductance and the gravimetric methods is satisfactory, even though not perfect. In addition, no overall trend of constant overestimation or underestimation was found and therefore no constant bias can be attributed to any of the two experimental methods used for this validation. These discrepancies are possibly due to the presence of other contaminant species from the generation procedures of these synthetic samples that were not quantified. Moreover, ion chromatography analysis are subjected to some experimental errors as discussed in Section 3.5 and this could reflect in some uncertainty on the DRH values calculated from E-AIM Model.

Overall, the good agreement between the conductance and the gravimetric method within the experimental uncertainties that was found for both laboratory generated samples and for atmospheric aerosol $PM_{2.5}$ samples indicates that the individuation of DRH and CRH with electrical conductivity measurements in the AEC and applying the gradient method (Section 3.2.1) represents a valid and reliable approach.

3.7 Summary

In this Chapter, the electrical conductance method for the determination of deliquescence and crystallisation relative humidities in an Aerosol Exposure Chamber were presented. At first, a general overview of the physical concept behind this experimental approach was given and the literature studies that have previously used similar electrical conductance techniques were briefly summarised. All the specific features of the AEC experimental setup have been described and the determination of DRH and CRH from conductance vs. RH curves was discussed. In addition, the samples analysed in this work were described: $PM_{2.5}$ atmospheric aerosol samples from an urban (MI-TS) and a rural (OB) sampling site and laboratory generated saline and soot aerosol samples. The sampling and generation techniques were fully describes as well, together with the ion

chromatography analysis performed to characterise the ionic fraction of the collected aerosol particles.

In the last Section of this Chapter, the preliminary tests that were carried out to assure the reliability of the electrical conductance method and to reach the best experimental setup were discussed. The comparison of the conductance behaviour of particles deposited on two different substrates (PTFE and quartz fibre) allowed the determination of the most suitable filtration membrane for this work, which was PTFE. The existence of a minimum aerosol loading for the first version of the AEC experimental setup was discussed and all the variations and improvements adopted to overcome the minimum aerosol loading issue were described. The evaluation of the electrical signal response time and the comparison of the DRH and CRH values obtained with the electrical conductance method and with a 'direct' gravimetric method demonstrated the validity of the proposed experimental approach.

The electrical conductance technique in the Aerosol Exposure Chamber that has been fully described in this Chapter was applied for the investigation of the phase transitions of atmospheric aerosols in Chapter 4.

Chapter 4 Measurements of DRH and CRH of Atmospheric Aerosol Smples

Electrical conductance measurements during humidification and dehumidification cycles in the AEC were performed on $PM_{2.5}$ samples, collected both at the urban MI-TS site and at the rural OB site, and results are presented in the following Chapter. The ionic fraction of these samples was characterised as well and a particular accent is put below on the relation between seasonal DRH/CRH trends and the seasonally modulated chemical composition of atmospheric aerosol particles in the Po Valley. A comparison between experimental and modelled values is also offered and the ability of the employed models to predict the phase transitions relative humidity of complex atmospheric aerosol samples by considering the sole ionic fraction is evaluated (Section 4.2). At the end of this Chapter, the implications of the presented results are discussed in relation to different fields of applications: reliable use of the Direct Free-Cooling in Data Centers[112,187] (Section 4.3.1), potential damage on cultural heritage stone porous surfaces[51] (Section 4.3.3) and application of remote sensing techniques for the quantification of ground-level atmospheric particles concentrations[160] (Section 4.3.4). In addition, the role of the carbonaceous fraction in the determination of the conductive properties of samples is also considered and discussed (Section 4.3.2). While this aspect is not directly related to the hygroscopic properties of aerosols, its investigation is useful for a better understanding of what governs the detection of any electrical signal in conductance measurements in the AEC. It also has some implications for Data Centres and more generally speaking for any situation where aerosol particles are deposited on electronics, since it gives information about the possible factors that would determine the formation of electrical bridges on hydrophobic substrates induced by the presence of deposited particles.

As pointed discussed in Section 3.6, the experimental setup ad technique used in AEC experiments have been improved and developed with time; in addition, the investigation of the phase transitions of atmospheric aerosols was both carried out on samples from the Filter Bank of the University of Milano-Bicocca, but ad-hoc samplings were performed during the period 2013-2014 (Section 3.3), as well. Therefore, different aspects were

investigated on different portion of the overall samples dataset and were subject to publications[51,112,160,187] that covered partial aspects of this final comprehensive work. For this reason, in each of the following Sections, the number and the nature of samples is explicitly described and the results presented in Sections 4.1, 4.2 and 4.3 refer to specified portions of the overall dataset, which is composed by 147 samples collected on PTFE filters in the four seasons (Spring: 16, Summer: 52, Autumn: 23, Winter: 56) at the two sampling sites (MI-TS: 135, OB: 12). Winter samples are predominant on a number basis followed by Summer samples, while aerosol samples collected in the two intermediate season are less represented in the overall dataset. This is because samples collected in the cold and warm seasons are characterised by the most significant differences in chemical composition (Section 4.1.1) that result in the most significant differences in deliquescence and crystallisation RH values (Section 4.1). In this Chpater, All mean values data are reported here as average±standard deviations of the average.

4.1 DRH and CRH Seasonal Variations

With respect to samples collected at the urban site in Milan (MI-TS), among the overall set of 135 $PM_{2.5}$ samples DRH and CRH values were determined for 80 of them by means of the electrical conductance method described in Section 3.2 (Spring: 6, Summer: 22, Autumn: 8, Winter: 44). The other 55 samples either presented an gradually increasing electrical signal with increasing RH with no evident deliquescence or crystallisation (Section 3.2.1), or did not show any electrical activation (see discussion of the minimum aerosol loading, Section 3.6.2, and more considerations on this in Section 4.3.2). The frequency distribution for measured DRH and CRH are shown in Figure 4.1. The obtained values were organised in 5% RH bins and the bars in the histogram are colour-coded in order to distinguish the contribute of samples corresponding to each season in every RH range.

First of all, both plots are characterised by a 'bimodal' distribution. With respect to the DRH frequency distribution (Figure 4.1-A), for most of the samples the deliquescence was detected in the RH range 55-60% and a second peak is present at 70-75% RH. A similar trend is observed for the CRH distribution plot (Figure 4.1-B), but in this case the two modes are observed at lower RH ranges of 45-50% and 65-70%, respectively. This two analogous but shifted frequency distributions for the two phase transitions relative humidity reflect the hysteresis of the hydration state of aerosol particles discussed in Section 2.1.1 and shown in the exemplifying conductance curve in Section 3.2.1.

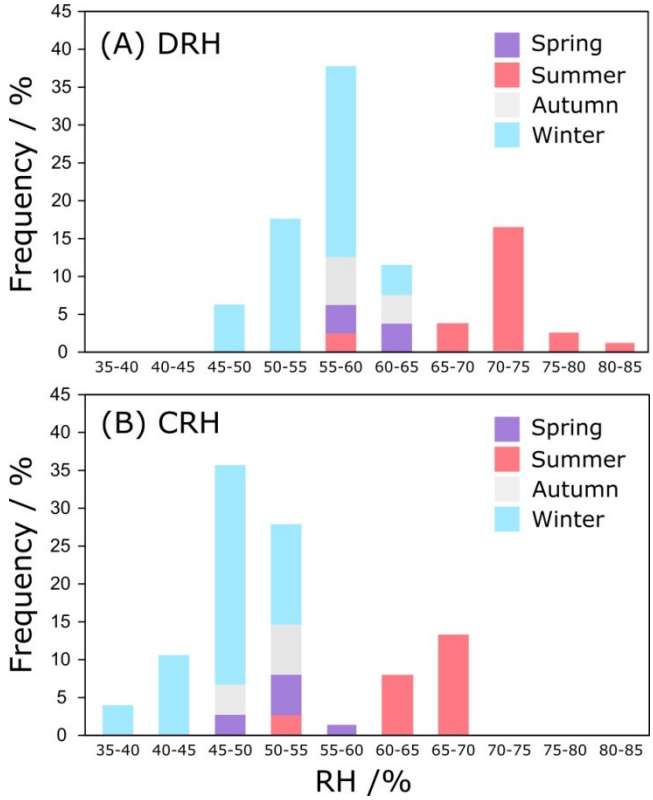

Figure 4.1: Frequency distributions of the DRH (Panel A) and CRH (Panel B) values for MI-TS $PM_{2.5}$ samples obtained with the electrical conductance method. Colours: Violet – Spring; red – Summer; light grey – Autumn; light blue: Winter.

Season	DRH	CRH	Inorganic ionic fraction (wt%)
Spring	59.8% ± *0.7%*	50.0% ± *0.6%*	44.4% ± *3.8%*
Summer	71.0% ± *1.1%*	63.2% ± *1.1%*	28.2% ± *1.5%*
Autumn	59.0% ± *0.9%*	50.0% ± *0.5%*	35.5% ± *3.4%*
Winter	54.8% ± *0.7%*	47.0% ± *0.6%*	37.0% ± *2.2%*

Table 4.1: Average measured DRH and CRH values and overall ionic content for samples collected in the different seasons.

The different distribution in these frequency plots of samples collected in different seasons is evident and average seasonal DRH and CRH values are also reported in Table 4.1. Winter atmospheric aerosol samples are characterised by the lowest mean DRH and CRH (54.8±0.7% and 47.0±0.6%, respectively), while Summer samples contribute mainly to the second mode in the frequency distributions and are characterised by an average

DRH of 71.0±1.1% and by an average CRH of 63.2±1.1%. Aerosol samples collected in Spring and in Autumn showed an intermediate behaviour between the two extreme seasons but they can be more assimilated to Winter samples. The obtained frequency distributions and these kind of seasonal trends can be rationalized by considering the chemical compositions of samples collected in different seasons.

4.1.1 The Dependency of Seasonal Trends on Seasonally-Modulated Chemical Composition of Samples

In Section 1.1.1, the spatial and time variability of the chemical composition of atmospheric aerosols has been individuated as a further factor that contributes to make even more complex such heterogeneous chemical systems. Furthermore, since the chemical composition of particles plays a fundamental role in the physico-chemical processes they are involved in, seasonal and spatial trends in chemical composition can also reflect in seasonally-modulated variability of other properties of aerosols. Therefore, below the correlation between the chemical composition of the analysed samples and the seasonal DRH and CRH trends shown in the previous Section is investigated.

First of all, a consideration on the overall inorganic ionic content is necessary. As reported in Table 4.1, it spans from an average of 28.2±1.5% in Summer to an average of 44.4±3.8% for Spring $PM_{2.5}$ samples, values in keeping with previous studies conducted in the Po Valley[8,166,170,179,188]. As of now, it is important to underline that this chemical components account on average for less than half of the overall mass of the analysed samples. It is true that inorganic electrolytes are the major responsible for the water uptake by atmospheric aerosols, but at the same time the presence of other hygroscopic organic components can have a relevant role in the phase transitions of particles[23,90,92,94,189]. Therefore, it should be kept in mind that the following rationalisation of the found seasonal trends does not take explicitly into account the contribution of organic components other than carboxylic acids.

Table 4.2 displays the average content of all the quantified chemical components in all the four seasons, determined by means of ion chromatography (Section 3.5) and shown on a mass percentage basis. The major differences are registered between the chemical composition of Summer and Winter $PM_{2.5}$ aerosols. Figure 4.2 shows the average relative content in Summer and Winter samples of the three main ionic components of typical Po Valley aerosol samples (ammonium, nitrates and sulphates), the other inorganic ions (F^-, Cl^-, PO_4^{3-}, Na^+, K^+, Ca^{2+}, Mg^{2+}) and the carboxylic acids (acetic, propionic, formic, glutaric, succinic, maleic, ossalic acids). These percentages are calculated on the

quantified ionic content reported in Table 4.1 and not on the overall $PM_{2.5}$ collected mass. The first evident feature that emerges from these plots is that the ionic content is dominated by nitrates for Winter samples and by sulphates for Summer samples. This is the result of the different atmospheric conditions in the two seasons and of the seasonal variability of emission sources of the two components. Nitrates mainly derive from NO_x produced in combustion processes (motor vehicles, industrial combustions, domestic heating, etc.), while sulphates are secondary compounds that are mainly the products of photochemical reactivity of gaseous SO_2[3]. A first reason for the observed season trend of nitrates is that the warmer Summer temperatures partially promote the partitioning of ammonium nitrate to the gas phase, thus reducing its amount in the condensed particle phase. In addition, in Winter domestic heating is a further source of nitrates that is not present during Summertime. Finally, photochemistry is stronger in Summer because the incoming solar radiation is more intense and this results in a, enhanced production of sulphates[164]. With respect to the other quantified chemical species, the other inorganic ions do not present significant seasonal trends in their contribution to the overall mass of $PM_{2.5}$, while carboxylic acids are slightly more present in Summer samples; in particular, this is due to an increment of dicarboxylic acids, most of all oxalic acid, which accounted on average for 2.6±0.2% and for 0.48±0.04% of the overall $PM_{2.5}$ mass of Summer and Winter samples, respectively. These compounds can both be primarily emitted (antropogenic and biogenic sources) or originate from photochemical reactions[190]; this observed seasonal trend, which was also evidenced in previous works[8,191], suggests that this second pathway might be the most relevant at the urban site of MI-TS.

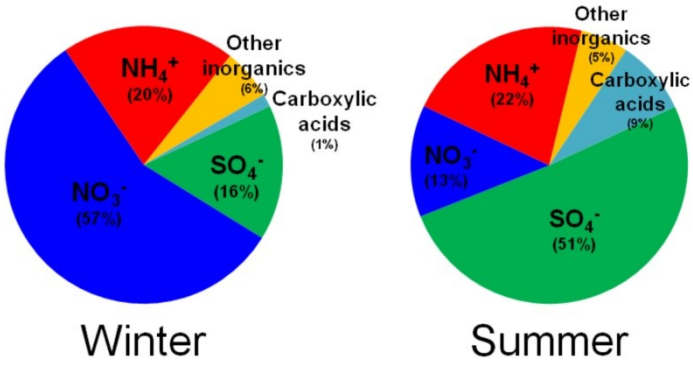

Figure 4.2: Relative mass content in the ionic fraction of the main inorganic ions (NH_4^+, SO_4^{2-}, NO_3^-), other inorganic ions (F^-, Cl^-, PO_4^{3-}, Na^+, K^+, Ca^{2+}, Mg^{2+}) and carboxylic acids (acetic, propionic, formic, glutaric, succinic, maleic and ossalic).

A first comparison of the seasonal average DRH values with the single-component DRH of the two most abundant ionic compounds can be useful. Different literature values were measured in different literature works and are recapped in the review by Martin (2000)[87];

DRH is reported to be on average of 80% for $(NH_4)_2SO_4$ and of 60% for NH_4NO_3. By simply considering these DRH values for pure ammonium sulphate and nitrate, it is clear that the seasonal DRH trends in Figure 4.1-A are governed by the relative abundance of this compounds: ammonium sulphate DRH is higher than that of ammonium nitrate and similarly Summer samples that are sulphate-rich are characterised by higher DRH values than the Winter samples, which are nitrate-rich instead. Summer and Winter average DRH (54.8±0.7% and 71.0±1.1%, Table 4.1) are respectively lower than the values of pure $(NH_4)_2SO_4$ and NH_4NO_3; this is due to the presence of other deliquescent chemical species and to the fact that the MDRH for a mixture is always lower than those of the single separate components[3], as discussed in Section 2.1.1. In addition, note that the chemical composition of Spring and Autumn samples can be assimilated to that of Winter samples, with a predominance of nitrates over sulphates (Table 4.2). This explains why they appear within the lowest RH mode in the frequency distributions in Figure 4.1, with respect to both DRH and CRH.

Season	**NH_4^+ (wt%)**	**SO_4^{2-} (wt%)**	**NO_3^- (wt%)**	**Other inorganic (wt%)**	**Carboxylic acids (wt%)**
Spring	10.8±0.8%	9.8±1.2%	22.7±2.3%	1.2±0.1%	\
Summer	6.6±0.4%	16.2±1.0%	3.9±0.6%	1.5±0.2%	3.2±0.2%
Autumn	8.9±0.7%	10.2±1.6%	17.4±2.2%	1.2±0.1%	\
Winter	7.6±0.5%	5.5±0.6%	21.8±1.9%	2.0±0.2%	0.76±0.1%

Table 4.2: Seasonal percentage mass calculated on the overall $PM_{2.5}$ mass of the main inorganic ions (NH_4^+, SO_4^{2-}, NO_3^-), other inorganic ions (F^-, Cl^-, PO_4^{3-}, Na^+, K^+, Ca^{2+}, Mg^{2+}) and carboxylic acids (acetic, propionic, formic, glutaric, succinic, maleic and ossalic), with respect to samples collected at MI-TS.

If the measured CRH values are considered, a similar comparison is not as straightforward as that for DRH, since the presence of solid inclusions in atmospheric aerosol samples strongly influences the relative humidity of crystallization by providing heterogeneous surfaces that promote the crystallisation of saline components in solution[87,136,192,193]. CRH for pure ammonium sulphate has been observed in the 33-48% RH range, while no crystallization is observed for pure ammonium nitrate[87]. These values are clearly far from representing a first simple estimate of the average CRH values measured for Summer (63.2±1.1%) and Winter (47.0±0.6%) samples in this work, even if in case too Summer CRH values are higher than those determined for Winter samples.

From the graphs in Figure 4.2, it is observed that the mass percentage associated to ammonium is relatively constant in the two compared seasons. Anyway, this doesn't give any specific information on the degree of neutralization of the analyzed MI-TS samples, which is interesting to investigate in order to evaluate its potential influence hygroscopic

behaviour of particles. In fact, the presence of an acid excess in aerosol systems would result in a lowering of DRH values[178]. In order to assess the degree of neutralization of the studied aerosols, the ionic contents reported in Table 4.2 were converted to moles and plotted in Figure 4.3, where $\Sigma(n^+)$ refers to NH_4^+ positive charges only, while $\Sigma(n^-)$ is the sum of the charges resulting from SO_4^{2-}, NO_3^- and carboxylic acids. In general, the neutralisation degree of the samples is almost complete, as most of the data points in Figure 4.3 lie close to the 1:1 correlation line (dashed) and the equation of the linear fitted line is characterised by a slope close to 1 (0.95) and by a good R^2 of 0.9666. Anyway, some of the analysed samples lie a bit further away from the 1:1 line and in particular below it, meaning that an excess of negative charges is not neutralised by ammonia. These points represent most of all samples collected in the Winter season (light blue data points). It is not possible to discriminate whether this plot is able to give a perfectly exact representation of the actual degree of neutralisation of these samples, since other acid or basic species could be present in minor amounts and slightly alter it. For example, short-chained alkylamines were quantified at the MI-TS sampling site[191] and dimethylamine and triethylamine concentrations were in the order of tens of ng m^{-3} (0.1% wt% on the overall total suspended particles mass). However, NH_4^+, SO_4^{2-}, NO_3^- and carboxylic acids are surely the most abundant components that would determine this degree of neutralisation and for this reason the generally neutral nature of the samples individuated in this way can be considered accurate.

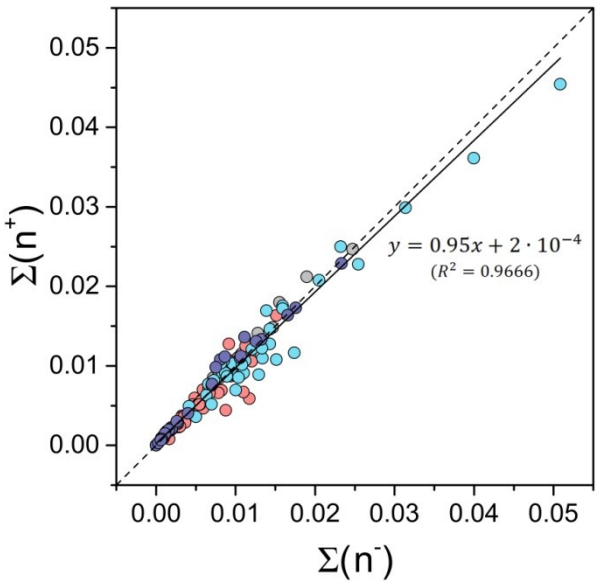

Figure 4.3: Correlation plot between the quantified charge equivalents of $\Sigma(n^+)$ (NH_4^+ only) and $\Sigma(n^-)$ (SO_4^{2-}, NO_3^- and carboxylic acids). Colours: Violet – Spring; red – Summer; light grey – Autumn; light blue: Winter.

In order to get a further insight of the relation between the variation in chemical composition and the seasonal trends individuated for DRH, the mole fraction of sulphate over the total sulphates+nitrates content (Y) and the ammonium mole fraction over the sum of ammonium and H^+ moles (X) were considered. Expressions for X and Y were reported in Section 2.2 calculated according to Potokuchi and Wexler (1995)[178], and are reported here again for clarity:

$$Y = n_{SO_4^{2-}}/(n_{NO_3^-} + n_{SO_4^{2-}}) \quad 4.1$$

$$X = n_{NH_4^+}/(n_{H^+} + n_{NH_4^+}) \quad 4.2$$

n_{H^+} were estimated as the difference between the negative charges carried by sulphates and nitrates and the positive charges of NH_4^+, in order to neutralize any possible excess of negative charges. In case the moles of NH_4^+ exceeded those necessary for the neutralization of SO_4^{2-} and NO_3^-, the X ratio was automatically set at 1.

The same frequency distributions shown in Figure 4.1, were reworked in order to show the variability in chemical composition of samples belonging to different DRH classes according to Eq. 2.19 and 2.18; the obtained frequency plots are shown in Figure 4.4. Panel A displays the variability in the quantified Y ratio: blue corresponds to Y=0 (nitrates only) and red to Y=1 (sulphates only). The differences in chemical composition of samples contributing to the two modes in the frequency distributions are evident: sulphate-rich samples mostly contribute to the higher mode (maximum in the RH range 70-75%), while the lower mode (maximum in correspondence to the 55-60% RH bin) is mainly composed by samples characterised by a nitrates-dominated ionic fraction. Obviously, the separation of nitrate-rich and sulphate-rich atmospheric aerosol samples is not completely sharp and samples characterised by Y~0.5 (violet to dark red colours) correspond to DRH values spanning from 50% to 75% RH. Once again, this is likely due to the presence of other deliquescent chemical species in aerosol; however, it is remarkable that most of this bimodal trend in the DRH frequency distribution plot can be rationalised by simply considering the relative amounts of ammonium nitrate and ammonium sulphate, which account only for up to ~40% of the total aerosol mass (Table 4.2).

Similarly, Figure 4.4-B shows the DRH frequency distribution with the representation of the estimated H^+ content in the samples attributed to each RH range in the plot, in order to evaluate where the more acidic samples are located within this frequency distribution. Light green indicates X=1, i.e. samples that are fully neutralized by NH_4^+, while dark green indicates X=0.5, i.e. half of the negative charges are neutralized by NH_4^+ and the other half by H^+. First of all, samples with X<0.8 are less than 10% of the total amount of the samples for which DRH was individuated by means of electrical

conductance measurements in the AEC. In fact, most of the bars in Figure 4.4-B appear coloured in light green meaning that the analysed samples are mainly neutral, as indicated by the good correlation between positive and negative charges in Figure 4.3.

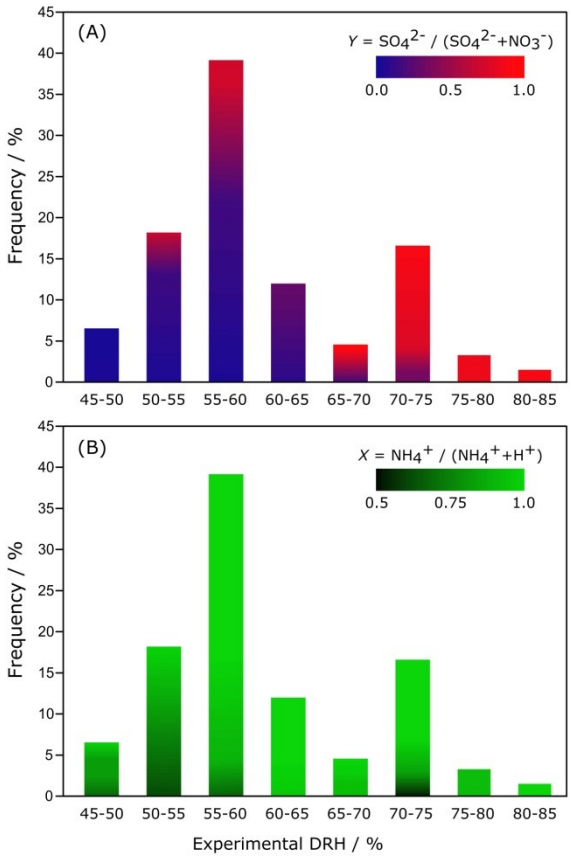

Figure 4.4: DRH frequency distribution represented with different colour scales to highlight the chemical composition of samples in different RH ranges. Panel A: X (Eq. 2.19) values from 0 (nitrates only, blue) to 1 (sulphates only, red). Panel B: Y (Eq. 2.18) values from 0.5 (equal amount of H^+ and NH_4^+) to 1 (NH_4^+ only).

Most of the samples associated to lower Y values are concentrated in the 45-60% RH range and only one sample with X=0.54 lies in the 70-75% RH bin. This reflects the trends evidenced by Potukuchi and Wexler (1995)[178]. They estimated the deliquescence relative humidity of aerosol systems characterised by variable sulphates/nitrate ratios (Y, Eq. 2.19) and by variable acidity (X, Eq. 2.18); generally speaking, their model indicates that more acidic systems present lower DRH than analogous systems characterised by the same Y ratio but with smaller H^+ content (higher X values). With respect to the analysed $PM_{2.5}$ atmospheric aerosol samples, it is not possible to determine to what extent this estimated acidity is actual or simply derives from the fact that the

complex overall chemical composition of the collected particles was just partially analysed by means of ion chromatography. However, it seems likely that samples characterised by low X estimated values are actually more acid because of their significant contribution to the 45-50% and 50-55% classes in the DRH frequency distribution plot.

4.2 Comparison with Model Predictions of DRH and CRH

In the previous Section, the individuated seasonal trends for the values of DRH and CRH determined by means of electrical conductance measurements on $PM_{2.5}$ samples collected at MI-TS were shown and explained by considering the seasonal variability of their chemical composition. It is noteworthy that it was possible to rationalise such complex behaviour by simply referring to the quantified inorganic ionic fraction.

In this Section, further analysis of the measured phase transition relative humidities is proposed by comparing the experimental results to calculations from two literature aerosol models. The aim is to investigate the ability of these models to quantitatively predict the deliquescence and crystallization processes of chemically-complex atmospheric aerosol systems by considering just a portion of their overall chemical composition. This would be particularly relevant for the estimation of the phase transition RHs of aerosols with known chemical composition in applications such those discussed further on in Section 4.3.

4.2.1 DRH

Among the aerosol models described in Section 2.2, E-AIM Model[100,194] is one of the most commonly used within the aerosol scientific community and it was used for the simulation of DRH in this Section. Simulations were performed by means of Model II with the inclusion of the seven quantified carboxylic acids (Section 3.5) at 298.15 K. DRH values were estimated from water mole vs. RH% curves with the same procedure described in Section 3.2.1 for the conductance curves, i.e. in correspondence to its maximum gradient point. DRH_{start} is at the lowest RH point where an aqueous phase is present in the system and DRH_{end} at the lowest RH where all the solid components have completely dissolved. The input for these simulations consisted of the molar amounts of NH_4^+, SO_4^{2-}, NO_3^- and carboxylic acids quantified by means of ion chromatography analysis. In addition, the model requires charges neutrality in order to perform any simulation and for this reason, H^+ was added when ammonium was not enough to

balance all the negative charges, whereas NH_4^+ was partially removed if it was in excess with respect to the negative charges, as it was described in Section 4.1.1.

As a first comparison, a frequency distribution plot of DRH values calculated from E-AIM Model was calculated similarly to those for experimentally determined values in Figure 4.1-A. The comparison of the experimental and modelled DRH frequency distributions is shown in Figure 4.5, where the light blue bars represent the same experimental distribution as in Figure 4.1-A, whereas the orange bars refer to the E-AIM Model simulated distribution. Firstly, it is possible to observe that the frequency distribution of E-AIM Model is bimodal, similarly to that resulting from electrical conductance measurements. In this case though, the most populated DRH ranges 60-65% and 75-80% for the two modes respectively; this means that a positive shift of 5% was found with respect to the peaks individuated in Section 4.1 for the experimental data (55-60%, 70-75%). Accordingly, the overall bimodal shapes of the two frequency distributions are well comparable, even if on average the E-AIM Model simulations are effected by some overestimation of DRH values.

Moreover, the overall RH range covered by the calculated DRH is wider than that covered by the experimental DRH values, since in this case some samples are also

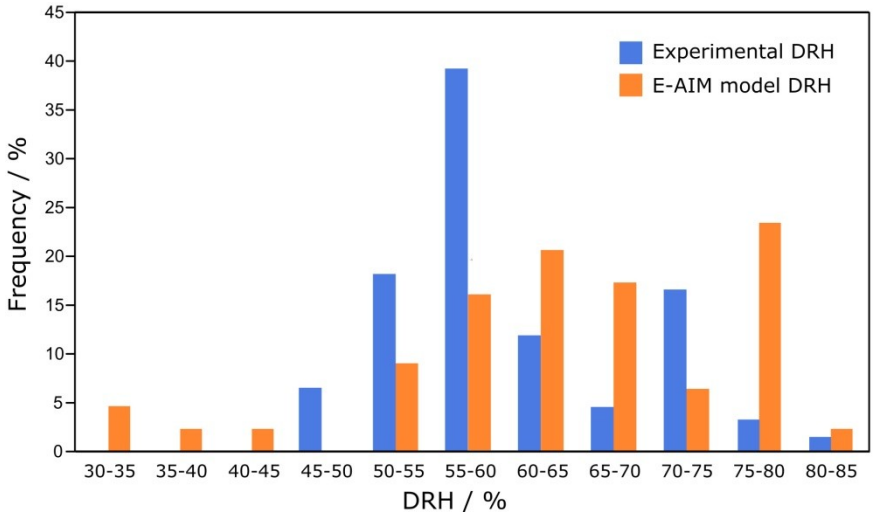

Figure 4.5: Comparison of the DRH frequency distribution obtained with the electrical conductance experimental method (light blue) and with calculations from E-AIM Model (orange).

attributed to classes within 30% and 45% RH. On the contrary, no DRH values were registered below 45% RH by means of the conductance method for the $PM_{2.5}$ atmospheric aerosol samples collected at MI-TS. These low calculated DRH are due to the high sensitivity of the E-AIM Model to H^+ concentration in the prediction of DRH: in fact,

these samples are precisely those with a low X value individuated during the discussion of Figure 4.4-B.

In order to provide a further evaluation of the point-to-point ability of the E-AIM Model in the prediction of DRH for each single sample separately, correlation plots were considered for DRH, DRH_{start} and DRH_{end}. They are shown in Figure 4.6, where the experimental values determined with the conductance method are plotted on the y axis and the calculated DRH from E-AIM Model on the x axis. The simulation of the initial point of the deliquescence region (DRH_{start}, Panel A) is clearly the most critical, since no correlation was found at all between the modelled and the experimental values. Experimental conductance measurements never evidenced the start of the deliquescence process below 45% RH for any of the analysed samples, whereas $DRH_{start}<45\%$ is predicted by E-AIM Model for 35% of the samples. Again, this is likely due to the fact that DRH_{start} is significantly affected by the acidity of the chemical system given as an input to the E-AIM Model, and even a small amount of H^+ in the system leads to the prediction of the presence of a liquid phase even in correspondence to very low RH values. On the other hand, if DRH and DRH_{end} are considered (Panels B and C), the two datasets appear to be a little more correlated, even if the agreement of the DRH and DRH_{end} from EAC conductance measurements and from E-AIM Model simulations is still far for most of the data points (R^2 of 0.359 and 0.543, for the linear fits in Panels B and C, respectively). Anyway, the data points in these two correlation plots display following a certain increasing correlated trend, which confirms that E-AIM Model is able to reproduce on average the experimental DRH trends individuated in the frequency distribution in Figure 4.5. In addition, the majority of data points in Panels B and C lie below the 1:1 correlation line, meaning again that the Model tends to overestimate the experimentally measured DRH.

In conclusion, despite the poor point-to-point agreement that was found, generally speaking it is relevant that E-AIM Model is able to reproduce the shape of the frequency distribution of the experimental $PM_{2.5}$ DRH values, as shown in Figure 4.5. This means that the driving force of the deliquescence of atmospheric aerosol particles is actually the inorganic ionic fraction together with the carboxylic acids, since the experimental data are partially reproduced by E-AIM Model considering just these two components of aerosols. However, the 5% overestimation in the frequency correlation plot and the lack of agreement when experimental and simulated data are compared separately for each sample (Figure 4.6) imply that the presence of other unaccounted chemical species play an important role in the determination of the overall hygroscopic properties of atmospheric aerosols. As anticipated in Section 2.2 when an overview of the state-of-the-art in atmospheric aerosols modelling was given, some effort is needed for the improvement of aerosols models (E-AIM Model, in this case) since it was shown that considering the main chemical species is a good starting point for the evaluation of the

hygroscopic properties of aerosols but to make such simulations more and more accurate other organic trace components need to be included.

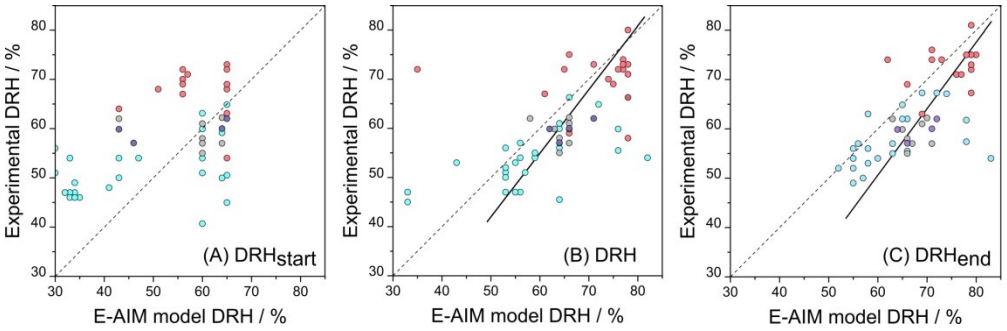

Figure 4.6: Correlation of DRH_{start}, DRH and DRH_{end} from electrical conductance measurements (y axis) and E-AIM Model calculations (x axis). Lines: dashed – 1:1 correlation line; solid – linear fit of the datapoints. Colours: Violet – Spring; red – Summer; light grey – Autumn; light blue: Winter.

So far, both the discussion of seasonal trends (Section 4.1) and the comparison with E-AIM Model have focused on the phase transition relative humidities that characterise atmospheric aerosols. As anticipated in the previous Chapter, the reason for this lies in the fact that AEC conductance measurements provide an *indirect* estimate of DRH and CRH by taking advantage of the conductivity of the electrolytic solutions formed by deliquescent (or crystallising) components in atmospheric aerosol particles. As a matter of fact, with this experimental technique the evaluation of the hygroscopic growth properties of aerosols is not possible. On the contrary, the gravimetric measurements that were performed on a subset of 20 $PM_{2.5}$ samples from MI-TS (Section 3.3) provide some *direct* information of the amount of water absorbed by deposited particles as a function of the applied RH in the chamber. It is true that the aim of those gravimetric measurements was the evaluation of the conductance method to determine the DRH and CRH values of atmospheric aerosol samples. However, this direct gravimetric method provides an significant (even if limited) dataset for the evaluation of the performance of E-AIM Model in predicting not only the deliquescence RH, but also the hygroscopic growth of a complex chemical mixture by simply considering its inorganic fraction and mono and di-carboxylic acids.

In this respect, Figure 4.7 shows the correlation between the mass of water that was measured as a function of the RH in the AEC with the gravimetric method (Section 3.6.4) on the y axis and the estimated mass of H_2O from E-AIM Model on the x axis; data refer to a subset of 20 $PM_{2.5}$ samples collected at MI-TS. The dashed line indicates perfect 1:1 correlation whereas the solid line is fitted through the data points (R^2=0.944). Colours from black to light blue indicate increasing RH from 60% to 90%; note that for

clarity not all the measured water mass values were plotted, but just a subset of five RH values is displayed. A satisfactory overall agreement is found for experimental and E-AIM Model data for low absorbed water mass values (below 1 mg), especially in correspondence to 60% and 70% RH data. When the RH is increased and the amount of absorbed water is greater as well, the discrepancy between measured and modelled data becomes increasingly significant and in particular E-AIM Model simulations tend on average to underestimate the content of water absorbed by the aerosol systems. The hydrophobic nature of PTFE membranes (Section 3.6.3) assures that the registered increase in mass is only due to water absorption by the deposited particles with increasing/decreasing RH in the gas phase; in addition, these gravimetric measurements were performed only up to 90% RH and, being far from saturation, water adsorption by PTFE can be excluded. A similar underestimation of the absorbed water from E-AIM Model was also found by Khlystov et al. (2005)[85] for ambient aerosol particles analysed online by means of two coupled mass spectrometers that analyse simultaneously dry and wet particles (DAASS, see Section 1.3).

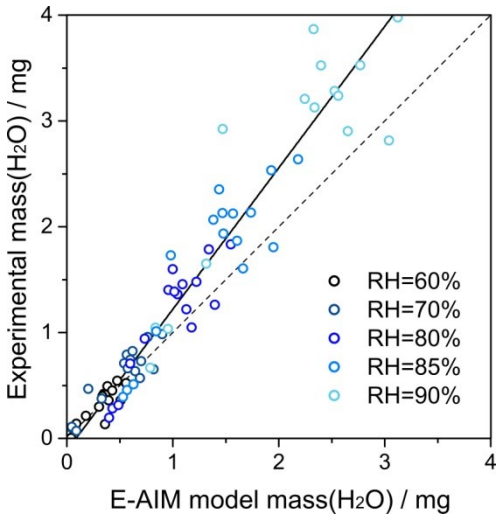

Figure 4.7: Correlation of the measured (y axis) and estimated with E-AIM Model (x axis) mass of absorbed H_2O for a subset of 20 MI-TS samples. of Lines: dashed – 1:1 correlation line; grey envelope – estimated error on the mass of water considering 1% uncertainty on RH. Colours: black to light blue indicate increasing RH. From 60% to 90%.

It is clear that this trend of underestimation was individuated from the analysis of a small number of samples and that further measurements should be carried out in order to better characterise it; however, this represent an interesting result since it indicates that neglecting the presence of organic compounds other than carboxylic acids leads to an underestimation of the water content of aerosols. This result underlines once again the

need of taking into account the organic fraction for an accurate description of the hygroscopic properties of aerosols and, as a consequence, the need of improved representations of these chemical species in current aerosol models.

4.2.2 CRH

The experimental CRH values obtained for $PM_{2.5}$ samples collected at MI-TS by means of electrical conductance measurements in the AEC were compared with calculations from the parametric model proposed by Martin et al. (2003)[136] and described in Section 2.2. The X and Y parameters that feature in the equations for the calculation of CRH_{start} and CRH_{end} are those in Eq. 2.19 and 2.18. The domain of applicability of this parametric model is such that CRH(X,Y)≥1%; this corresponds to X>0.5 (if Y is set constant at 1) and Y>0.25 (if X is set constant at 1). Within the studied dataset, the condition on X is always satisfied, whereas that on Y is satisfied for all the Summer samples, which are sulphates-rich, but for 10% of Winter, Autumn and Spring samples because they are nitrates rich and are characterised by Y values close to 0. Overall, the CRH parametric model by Martin et al. (2003)[136] was applicable to 40% of all the collected MI-TS $PM_{2.5}$ samples. Because of the very low statistic about Spring and Autumn samples, the following comparison (summarised in Table 4.3) was only carried out for MI-TS $PM_{2.5}$ samples collected in Summer and Winter.

	Experimental	***Martin et al. (2003)***[136]	
	CRH	**CRH_{start}**	**CRH_{end}**
Summer	63.2±1.1%	28.1%±2.4%	27.1±2.2%
Winter	47.0±0.6%	25.4±4.5%	24.0±4.7%

Table 4.3: Comparison of experimental CRH (maximum gradient of electrical conductance curves) and CRH values calculated with the parameterisation from Martin et al. (2003)[136].

The average modelled CRH_{start} and CRH_{end} differ by ~35% RH from the experimental CRH for Summer samples and by ~22% for Winter samples (data in Table 4.3). The reason of these wide discrepancies lies in the presence of solid surfaces in atmospheric aerosols that can lead to heterogeneous nucleation, whereas the parametric model by Martin et al. (2003)[136] was derived for pure H^+-NO_3^-- SO_4^{2-}-NH_4^+ aerosol systems. For example, the presence of metal oxides (i.e. Fe_2O_3, TiO_2…) in ammonium sulphate aerosol

particles was found to lead to an increase of 32% in CRH if compared to pure $(NH_4)_2SO_4$; the reason of this is that such insoluble chemical species can act as crystallization nuclei driving heterogeneous nucleation, which results in crystallization at higher RH values[87,137]. Furthermore, the presence of organic material, such as glycerol or carboxylic acids, was also found responsible of increasing the CRH of saline aerosols[91]. Previous studies on $PM_{2.5}$ in Milan[164] individuated up to ~2 wt% of mineral dust (AL, Si, K, Ca, Ti, Fe, Na and Mg oxides) and ~1 wt% of heavy metal oxides (Cu, Zn and Pb oxides) on the overall $PM_{2.5}$ mass. Carboxylic acids were indicated to account for up to ~3% wt% of the total $PM_{2.5}$ mass for aerosol particles collected at MI-TS in this work and at the same sampling site the entire organic fraction was found to account for ~30% to ~50% of $PM_{2.5}$ particles mass[8].

Therefore, it is likely that insoluble inclusions and organic matter cause these discrepancies between experimental CRH values and data obtained from the parametric model by Martin and co-workers (2003)[136] for an homogeneous system composed of H^+-NO_3^-- SO_4^{2-}-NH_4^+, which is thus not suitable for the simulation of the CRH of the complex atmospheric aerosol. This is in contrast to what found for DRH values simulated with E-AIM Model: deliquescence, which is an equilibrium process (Section 2.1.1) driven by hygroscopic species, can be estimated (even if with some bias) by means of a thermodynamic model by just partially taking into account the chemical composition of aerosol particles; on the other hand, crystallisation is a kinetic process and the presence of insoluble inclusions and other chemical species that can promote heterogeneous nucleation necessarily need to be taken into account for a more realistic estimation of CRH values. This makes the CRH measurements in this work particularly valuable, since there is no way of estimating the RH of crystallisation for complex atmospheric aerosol system, as for DRH instead (even if, again, the estimated DRH values are affected by some uncertainties).

4.3 Effect of the Physical State of Atmospheric Aerosols in Various Fields of Application

In this Section, implications of the previously presented phase transition relative humidities of atmospheric aerosols and of their hydration state for three different fields of application are discussed. The importance of evaluating DRH and CRH of atmosperic aerosols for energy saving strategies in Free-Cooled Data Centers[112,187] is discussed in Section 4.3.1, the impact of deposited aerosol particles as a function of their physical state on cultural heritage stone artifacts[51] is presented in Section 4.3.3 and the

importance of considering the hysteresis of the aerosol hydration state for remote sensing techniques[160] is evaluated in Section 4.3.4.

4.3.1 Implications for DFC Data Centers

In a Data Center (DC), a high density of computers (Information Technology, IT: data storage, computational power, global networks, etc.) results in a power density demand that can reach 1 kW/m^2, which is coupled as well to a substantial rise of the temperature inside the DC[58,195,196]. As a result, the cooling systems in a DC may use up to 35-50% of the entire installed power[195–197], which is considerable given that DCs alone are estimated to be responsible for 1-2% of the overall electricity consumption worldwide[58,198,199]. Traditional cooling apparatuses are based on industrial air conditioning units, whose operational and environmental costs could be reduced by using Direct Free Cooling (DFC) systems, in which outside air is used to directly cool the IT under favourable weather conditions.

However, this approach implies the introduction in the DC of outdoor aerosol particles that can deposit on electronic circuitry and represent a potential danger for the installed electronic components, especially when hydrated[58–61], because of the electrical an electrochemical processes they can trigger that were discussed in Section 1.2.3. Besides, the effects of deposited aerosol particles on printed circuit boards (PCBs) depend on the density of particles on the PCB surface. In fact, according to the percolation theory[181], the aerosol loading has to exceed a critical surficial concentration value in order to create a continuous conductive path. A further factor that affects electrical bridging caused by deposited particles is that the conductance of aerosols can be different as a function of their physical state. If the aerosol particles are hydrated (i.e. over the DRH with increasing RH or over the CRH if RH is decreasing from above the DRH) the ionic components spontaneously dissolve, creating a conductive electrolytic solution. Therefore, hygroscopic particles can potentially originate conductive paths and cause electrical leakage[200].

For these reasons, the American Society of Heating, Refrigerating and Air-Conditioning Engineers (ASHRAE) has published guidelines on the gaseous and particulate contaminants concentrations (ISO-8 class threshold, ISO14644-1, maximum particles concentrations summarised in Table 4.4) and thermodynamic conditions permitted in DCs ("allowable": 15 °C to 32 °C, 29—54% RH at 25°C; "recommended": 18 °C to 27 °C, 20-61% RH at 25°C)[156,201,202]. Nevertheless, these are general guidelines and do not take into account the site-specific and seasonal chemical composition of atmospheric particles that determine their DRH and CRH in a given location.

A method for the optimization of the operating conditions of a DC to achieve simultaneous energy saving and aerosol corrosion prevention by complying with these guidelines from ASHRAE[156,201,202] at the same time was proposed in the work by Ferrero et al. (2013)[187]. The presented case study was conducted at Sannazzaro dè Burgondi (Po Valley, Italy) and was aimed at the optimization of the operating conditions of a DC designed for the Italian Oil and Gas Company (ENI) (5200 m^2 of IT installed, 30 MW, opened in December 2013). The proposed approach was based on a DFC system and on the chemical characterisation of the atmospheric aerosols on-site.

The study consisted in the characterisation of chemical-physical properties of atmospheric aerosols at the DC site. Particle number size distribution measurements (two OPCs (Optical Particles Counter) Grimm 1.107, 'wet' and 'dry') were carried out and in order to simulate the conditions inside the DC before its construction was finished and a literature approach was applied for the estimation of indoor aerosol concentrations[58,59,203]. An overview of the measured outdoor and of the indoor simulated concentrations for three dimensional classes (d>0.5 µm, d>1.0 µm, d>5.0

		Average concentration (particles m^{-3})		
		Outdoor	**Simulated indoor**	**ASHRAE limits**
24/03 – 19/03	$d > 0.5\,\mu m$	$1.1 \cdot 10^7$	$2.2 \cdot 10^6$	$3.52 \cdot 10^6$
	$d > 1.0\,\mu m$	$6.2 \cdot 10^5$	$2.7 \cdot 10^4$	$8.32 \cdot 10^5$
	$d > 5.0\,\mu m$	$4.0 \cdot 10^4$	0.0	$2.93 \cdot 10^4$
10/06 – 10/07	$d > 0.5\,\mu m$	$5.3 \cdot 10^6$	$4.3 \cdot 10^5$	$3.52 \cdot 10^6$
	$d > 1.0\,\mu m$	$5.9 \cdot 10^5$	$2.4 \cdot 10^4$	$8.32 \cdot 10^5$
	$d > 5.0\,\mu m$	$2.5 \cdot 10^4$	0.0	$2.93 \cdot 10^4$

Table 4.4: Measured outdoor and simulated indoor particles concentrations compared with recommended limits from ASHRAE.

µm) are shown in Table 4.5. These results imply that the DC can be subjected to aerosol concentrations that can be both above and below the ISO-8 guidelines and therefore revealed the need of an air filtration system so that these limit number concentrations could be satisfied[156,201], also considering that high pollution events in the Po Valley are common. Consequently, 456 MERV13 filters were installed in the DC but, since their overall filtering efficiency is known to be lower than 100% and it is dependent on the particles' size and on the filter's load[203], there was still the need to chemically characterise the smaller particles that are able to enter the DC despite the filtrations systems. Therefore, PM_1 and $PM_{2.5}$ outdoor sampling and their ion fraction chemical characterisation (Section 3.5) were performed; their average concentrations during the two sampling campaigns are shown in Table 4.5.

The DRH was estimated with the E-AIM Model from the ionic composition of the outdoor samples: all the mean DRHs (Table 4.5) were found to be higher than 60%. Moreover, the values for PM_1 were above 60% for 55% of the time (sampling campaign: 24/03 – 19/03) and for 66% of the time (sampling campaign: 10/06 – 10/07), while for $PM_{2.5}$ the same was observed for 69% and 64% of the time, respectively. Thus, 60% RH was chosen as the upper limit for the DFC operating cycle, as a rule to prevent the corrosive effects of the potential deposited aerosols. In addition, the chemical composition of indoor particles was also simulated by applying a volatilisation correction parameter[204] for NH_4NO_3 to the measured outdoor chemical compositions, since phase changes can occur when outdoor aerosols are introduced in the DC[58], which is always operated at a fixed temperature of 25° C. This means that inside the DC, the ammonium nitrate in atmospheric particles can partially volatilize and if the DRH is estimated considering this volatilisation correction it increases on average of 7.5±0.7% for PM_1 and of 4.3±0.6% for $PM_{2.5}$ with respect to the values reported in Table 4.5 when particles enter the DC, because they are poorer in nitrates. This confirmed that the precautionary 60% RH threshold represents the most restrictive operation scenario and that slightly higher RH conditions could be safely adopted, following a chemical characterisation of aerosol particles actually entering the DC.

		Outdoor		**Simulated indoor**	
		Concentration ($\mu g\ m^{-3}$)	*DRH*	*Concentration* ($\mu g\ m^{-3}$)	*DRH*
24/03 –	PM_1	11.9±0.4	61.2±1.1%	2.7±0.1	69.2±1.1%
19/03	$PM_{2.5}$	20.6±0.6	68.4±1.4%	3.0±0.1	75.5±0.8%
10/06 –	PM_1	13.1±0.4	60.8±1.4%	1.9±0.1	64.5±1.0%
10/07	$PM_{2.5}$	17.0±0.4	62.4±0.9%	2.1±0.1	67.3±0.9%

Table 4.5: Outdoor and simulated indoor concentrations of the PM1 and PM2.5 fractions from two sampling campaigns, together with average DRH values obtained with E-AIM Model simulations.

Figure 4.8 shows a psycrometric chart with the "allowable" (blue area) and the "recommended" (red area) thermodynamic ranges indicated by ASHRAE[156,201,202]. The area delimited with black lines indicates the conditions when the DFC is operated in the ENI Data Center. This region was individuated combining the lower limits for T and RH of the "allowable" and the evaluation of the chemical-physical properties of aerosols entering the DC.

Thanks to the analysis of meteorological data at the DC site (Environmental Protection Agency, ARPA Lombardia), it was possible to estimate how often during a year the environmental conditions match those that were individuated by Ferrero et al. (2013)[187]

and the DC can be geared with Direct Free Cooling. As a result, it was found that the DFC system can be operated for 78% of the time, which reflects in a potential energy saving of 7.4 MWh and 2.7 fewer tons of emitted CO_2 (calculated with an emission factor of 362 g(CO_2) kWh^{-1}, European Environmental Agency) per year for each kW of installed IT. The associated overall economic saving is considerable too and was estimated to be of € 33 million (considering a cost of energy of 0.15 € kWh^{-1}). It is important to underline that even thought the obtained results are site-specific, the proposed methodology is of general application.

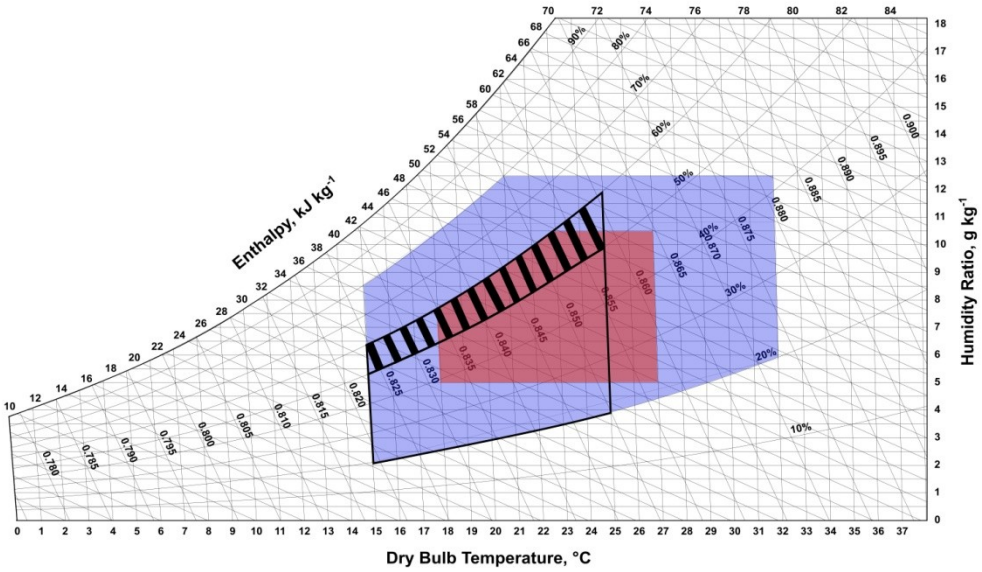

Figure 4.8: Psycrometric chart representing the "allowable" (blue area) and the "recommended" (red area) from ASHRAE[156,201,202], together with the operating conditions of ENI DC (black box) individuated by Ferrero et al. (2013)[187]. The striped area represents the hysteresis region between DRH and CRH[112].

This work by Ferrero et al. (2013)[187] proposed the first experimental approach to achieve the determination of safe conditions of operation of DFC thanks to the knowledge of the on-site aerosol properties. Some other recent studies used conductivity measurements in order to investigate these aspects (see also Section 3.1.1), but they either considered simple salts solutions[159] or they[61] followed the vague ASHRAE guidelines[156], which suggest to "brush off" some dust from a server surface and sprinkle it on the surface of a test circuit board, with a procedure that lacks of any standardisation. In addition, these guidelines only indicate the need to estimate the DRH of deposited aerosol and none of the cited studies takes into account any CRH estimation.

Hence, a following study by Ferrero et al. (2015)[112] fills these gaps by directly measuring the DRH and CRH of atmospheric aerosols with a conductance method (Section 3.2) and comparing the experimental results with calculations from E-AIM II[119,194] and a parametric model[136] (also applied in Section 4.2.1 and 4.2.2, respectively), in order to lay the foundations for the real-time estimation of the aerosol hydration state within a DC, knowing its chemical composition. Furthermore, a way of overcoming this lack of methodology standardisation was proposed and it involved the sampling of atmospheric aerosol using those standard methods adopted for atmospheric PM gravimetric determination both in Europe and in the USA. In addition, the collection efficiency of $PM_{2.5}$ aerosol sampling decreases with increasing particle size (50% at 2.5 µm) and drops to zero above 3 µm. This approach makes possible to collect particles smaller than those characterised by 100% filtration efficiency of the MERV13 filters usually installed in a DC.

The direct measure of CRH allowed the individuation of the striped region in the psychometric chart in Figure 4.8, which indicates the area between DRH and CRH, where the application of DFC depends on the RH previous history. This would not have been possible without direct measurements of the CRH because, as it was shown in Section 4.2.2, the only literature parametric model for CRH[136] is not applicable for the estimation of the CRH of complex atmospheric aerosols.

4.3.2 Effect of the Carbonaceous Components on the Conductance Properties of Deposited Aerosols

All the previous studies focused on the potential risk deriving from particles deposited on electronics, both presented in this work[112,187] and from literature[61,66,152–155,157–159], mainly took into account either pure salts or the sole inorganic hygroscopic fraction. However, it is also well-known that other components in aerosols are hygroscopic, such as carboxylic acids, aminium salts and other organic compounds classes[79,81,97,104,189,205], and they could consequently be involved in this kind of phenomena[155,206]. In addition, Anderson et al. (1988)[207] experimentally demonstrated that even non-electrolyte substances (sucrose in his study) can provoke deterioration of PCB components. Nevertheless, to the authors' knowledge, the synergy between ionic components and other common atmospheric aerosol conductive species, such as soot, in the formation of this kind of electrical bridges was never investigated. The term "soot" indicates carbonaceous particles deriving from combustion processes and composed of graphene layers with small contents of heteroatoms, especially oxygen and hydrogen[208]. Laboratory flame soot was proven to be electrical conductive[177], even if the measured conductivity values (between 10^{-6} and 10^{-2}

$\Omega^{-1}cm^{-1}$, depending on the sample density and on the fuel used for soot production) could be some orders of magnitude less than pure graphite (between 10^{-3} and 10^{-1} $\Omega^{-1}cm^{-1}$, depending on the sample density). This is caused by the mainly disordered and amorphous structure of soot: in fact, unlike pure graphite that has just hybrid sp^2 C atoms and valence electrons in the remaining π-orbital, flame soot contains also sp^3 bonds[209,210]. Accordingly, supposing that soot could play a role in electrical bridging processes caused by aerosols deposited on electronics seems reasonable.

In this Section, the role of the inorganic ionic and carbonaceous fractions in the measurement of the conductance of deposited aerosols is investigated, with particular reference to the synergy between these different chemical species. A data set of 56 $PM_{2.5}$ aerosol samples collected at MI-TS (urban site, 44) and at OB (rural site, 12) (Section 3.3) was examined. Each sample was measured in the AEC by means of the conductance method (with the first experimental setup described in Section 3.6.2) and their ionic fractions were characterized by means of ion chromatography (Section 3.5). In addition, pure saline and externally mixed soot and saline aerosols were generated and collected on PTFE filters (Section 3.4); their conductance during humidity cycles was measured as well. In the following Sections, the ionic and carbonaceous contents are presented separately for samples with detected or not-detected conductance for the two different sampling sites. The results of the performed conductance measurements are discussed in relation to the quantified ionic content and the possible influence of the carbonaceous fraction on these measurements is discussed for atmospheric aerosol, pure saline and mixed saline-soot samples.

4.3.2.1 Measured $\Delta G_{deliquescence}$ and $\Delta G_{crystallization}$

Average, highest and lowest measured $\Delta G_{deliquescence}$, $\Delta G_{crystallization}$ (which are the variations in conductance, G, associated to deliquescence and crystallization, see Section 3.2.1) and maximum conductance for the subset of samples with measured DRH and CRH (31 samples) are reported in Table 4.6. $\Delta G_{deliquescence}$ is always higher than $\Delta G_{crystallization}$ (average values of 11.2±2.7 and 2.55±0.49 μS, respectively), simply because the crystallization occurs at supersaturated conditions: during the dehumidification, between the DRH and the CRH the measured conductance gradually decreases as water evaporates until the actual crystallization occurs, and therefore $\Delta G_{deliquescence} > \Delta G_{crystallization}$.

	$\Delta G_{deliquescence}$ (µS)	$\Delta G_{crystallization}$ (µS)	G_{max} (µS)
Minimum	0.348	0.0381	0.572
Maximum	64.4	10.01	130.2
Average	11.2	2.55	52.3
s_{mean}	*2.7*	*0.49*	*6.5*

Table 4.6: $\Delta G_{deliquescence}$, $\Delta G_{crystallization}$ and maximum conductance (µS) for the subset of samples (31) with measured DRH and CRH.

The comparison between measured $\Delta G_{deliquescence}$ and of G_{max} values with the 10^6 Ohms failure threshold (corresponding to a conductance of 1 µS) usually set for PCBs[61,154] can show if the deliquescence and the water absorption promoted by atmospheric aerosols deposited on PCBs can represent an actual danger for them. This failure threshold indicates the minimum resistance (maximum conductance) beyond which electrical bridging between two neighboring plates can cause failure. On average, the increase in conductance associated with the deliquescence of the water soluble components in the samples is 11.2±2.7 µS, which is one order of magnitude higher than this threshold value. In addition, $\Delta G_{deliquescence} < 1$ µS was measured for just the 16% of the samples and for just one sample over the entire dataset the measured G_{max} was below this threshold level. This means that for the large majority of the samples the 1 µS threshold is exceeded either during the deliquescence process or because of the subsequent water absorption by the deposited aerosol particles. It is true that the measured conductance values depend on the setup of the experimental apparatus, but the orders of magnitude of $\Delta G_{deliquescence}$ and of G_{max} measured in this work indicate anyway that these processes can be potentially dangerous for PCBs contaminated with deposited hygroscopic aerosol.

Beside the electrical conductance increase caused by deliquescence, it is also worth noting that during the humidification phase the electrical conductance of the samples is always activated before the deliquescence range (see the case study sample in Figure 3.3). For 55% of the samples the measured conductance was already higher than 1 µS at the initial point of the deliquescence region. These results indicate that the hygroscopic components are not the only potentially dangerous components in aerosol, but other conductive species could be involved in the formation of electrical bridging phenomena too, also at RH values below the DRH of the water-soluble components. Understanding what causes the activation in these conductance measurements is therefore crucial to better comprehend all the factors involved in the determination of the electrical conductance properties of aerosols.

In this respect, an important aspect is that no electrical signal was detected for 20 out of the 56 considered samples. The existence of a minimum aerosol loading for the conductance to be detected with this experimental setup was discussed in Section 3.6.2.

Thus, there is the need to investigate what gives rise to it in order to understand what determines the electrical conductance properties of aerosol samples. Therefore, in Section 4.3.2.2 the 'quantity' (surficial loading) and the 'quality' (chemical composition) of the considered aerosol samples is investigated.

4.3.2.2 Chemical Composition Differences for Detected and Not-Detected $PM_{2.5}$ Samples in AEC Conductance Measurements

In Table 4.7 a comparison between detected (36) and not-detected samples (20) is shown and it refers to the whole dataset, i.e. to samples from both sampling sites (MI-TS and OB). (Note that in this Section and in the following, for every t-student test presented a significativity value of α=0.02 was considered).

First of all, the average $PM_{2.5}$ mass concentrations on filter are on average higher for detected samples (199.3±8.6 µg cm^{-2}) than for not-detected ones (128.4±5.8 µg cm^{-2}) and the t-student test confirms that for the two sets of samples these means are statistically different. In order to understand if it is just the overall amount of deposited aerosol that determines its electrical conductance or also its chemical composition, the same comparison was carried out for the different chemical species considered.

The inorganic ionic fraction average masses need to be considered, because when charged species pass in solution they form a conductive medium (Section 3.1). The data reported in Table 4.7 show that they do not statistically differ for detected and not-detected samples and they turn out to be 70.8±5.4 µg cm^{-2} and 57.6±5.2 µg cm^{-2}, respectively. In addition, a quite surprising result can be obtained comparing mass/mass percentages (wt%) for the ionic inorganic fractions, since they even result statistically higher for not-detected samples (43.7±2.6%) than for samples with detected conductance (35.3±2.1%). If the samples with the highest ionic surficial content are those that are not conductive, it can be supposed that the presence of saline hygroscopic compounds is not the only necessary condition to create a continuous conductive path between particles deposited on a hydrophobic substrate such as PTFE, and therefore to provoke electrical bridging phenomena in contaminated PCBs. For this reason, the hypothesis that conductive soot plays a role in this process was investigated.

The elemental carbon (EC) and organic carbon (OC) content in the 56 samples in the dataset was estimated from simultaneous sampling campaigns of $PM_{2.5}$ on quartz fibre carried out at MI-TS and OB. The results of these sampling campaigns and of the quantification of EC and OC by means of a Thermal Optical Transmission method[172]

were presented in a previous study[8]. The overall seasonal EC and OC mass percentages are reported in Table 4.8 for both sampling sites.

			Mass concentration / μg cm^{-2}					wt%	
	n		$PM_{2.5}$	Ionic fraction	Unaccounted	EC	OC	Ionic fraction	Unaccounted
Detected samples	**36**	**Mean**	**199.3**	**70.8**	**128.5**	**24.9**	**48.7**	**35.3%**	**64.7%**
		s_{mean}	*8.6*	*5.4*	*6.7*	*1.5*	*3.0*	*2.1%*	*2.1%*
Not detected samples	**20**	**Mean**	**128.4**	**57.6**	**70.8**	**12.0**	**25.8**	**43.7%**	**56.3%**
		s_{mean}	*5.8*	*5.2*	*3.6*	*1.4*	*1.3*	*2.6%*	*2.6%*
		t	6.834	1.767	7.572	6.230	6.967	2.531	2.531
		t_{crit}	2.399	2.403	2.403	2.403	2.410	2.421	2.421
t-student test		**Result**	$t > t_{crit}$ different means	$t < t_{crit}$ equal means	$t > t_{crit}$ different means	$t > t_{crit}$ different means	$t > t_{crit}$ different means	$t > t_{crit}$ different means	$t > t_{crit}$ different means

Table 4.7: The mean mass surficial concentrations for the overall $PM_{2.5}$ content, the inorganic ionic fraction (calculated as the sum of F^-, Cl^-, NO_3^-, SO_4^{2-}, Na^+, NH_4^+, K^+, Ca^{2+}, Mg^{2+}), the unaccounted fraction (calculated as a difference between the previous two quantities), the EC and OC content are presented. Weight percentages (wt%) for the inorganic ionic and the unaccounted fractions are reported, as well. Average values are reported alongside the corresponding standard deviation of the mean (s_{mean}) and the whole data set is split into detected and not-detected samples, in relation to the conductivity measurements in the AEC. *n* indicates the number of samples in each subset. t-student test results are also shown (t is calculated value for the samples, t_{crit} (0.02 significativity) is the calculated critical value for the case of the comparison between two averages that come from different populations).

		EC %	OC %
MI-TS site	*Spring*	12.0	21.6
	Summer	15.1	19.1
	Autumn	13.0	21.6
	Winter	10.9	24.0
OB site	*Spring*	4.0	16.9
	Summer	4.9	16.8
	Autumn	4.0	16.9
	Winter	3.1	16.9

Table 4.8: Elemental carbon (EC) and organic carbon (OC) mass percentages for the two sampling sites (MI-TS and OB) in the four seasons, from the data in Perrone et al. (2013)[8].

In Table 4.7 the average surficial masses for EC and OC are presented. The most relevant result is the one relating to elemental carbon: as envisaged, the mean surficial distribution for detected samples is statistically higher for detected samples (24.9±1.5 µg cm^{-2}) and it is more than double than for not-detected ones (12.0±1.4 µg cm^{-2}). The mean OC masses are another relevant factor, since many organic compounds have a well-known hygroscopic behavior (Section 4.3.2) and can therefore have a role in the formation of a potentially dangerous conductive solution on PCB surfaces. In a similar way to what has been pointed out for EC, detected samples result richer in OC than those that did not show any electrical conductance response, and their average OC contents are 48.7±3.0 µg cm^{-2} and 25.8±1.3 µg cm^{-2}, respectively. This broad discrepancy observed for the carbonaceous fractions together with the fact that the average ionic content is not statistically different for detected and not-detected samples represents a first important indication that a synergy between these different chemical components is necessary to determine the electrical conductance of aerosols.

4.3.2.3 Comparing Samples from an Urban and a Rural Site

Furthermore, if the entire dataset is split between samples collected at the urban site (MI-TS) and at the rural site (OB) (Section 3.3), other proof of a synergy between the ionic fraction and elemental carbon can be found.

The statistically higher $PM_{2.5}$ surficial mass for detected samples that was found for the entire dataset is reproduced once samples from the two different sampling sites are separated. The OB samples present a mean $PM_{2.5}$ loading of 201.6±9.2 µg cm^{-2} for detected ones and 126.7±8.6 µg cm^{-2} for not-detected ones; for MI-TS samples, the mean $PM_{2.5}$ loading is 174.2±8.9 µg cm^{-2} for detected ones and 130.5±8.2 µg cm^{-2} for not-detected ones.

In this case, though, it is worth highlighting that only 25% of OB samples showed an electrical conductance response (3 out of 12), while this percentage was 75% for MI-TS samples (33 out of 44), even if the two samples subsets have similar total $PM_{2.5}$ average masses deposited on filter (MI-TS samples: 74.8-315.8 µg cm^{-2}; OB samples: 100.0-184.4 µg cm^{-2}). To better understand this different behavior of the samples from the two different sampling sites, the chemical composition of the two subsets has to be considered (Figure 4.9).

First of all, the average ionic contents of the samples from both the rural and the urban site are comparable and do not statistically differ for detected and not-detected samples (t-student test, α=0.02). Therefore, if the sole ions determined the electrical

conductance properties of these two different types of aerosols, the discrepancies in the percentages of detected and not-detected samples observed for the two different sampling sites could not be explained. Secondly, when the EC average contents are compared, they are statistically higher for the MI-TS site (26.5±1.3 µg cm^{-2} for detected samples, 17.0±1.1 µg cm^{-2} for not-detected samples). The poor EC content for rural samples is therefore responsible for the fact that the majority of OB samples didn't show any electrical response and they are respectively 7.3±1.3 µg cm^{-2} for detected samples and 5.9± 0.5 µg cm^{-2} for not-detected ones.

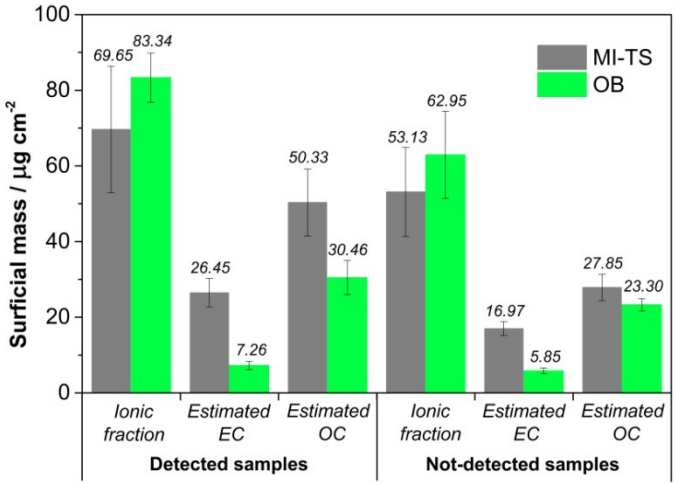

Figure 4.9: Average surficial mass distributions (µg cm^{-2}) are compared for MI-TS (grey) and OB (green) samples. Data for the quantified inorganic ionic fraction, the estimated EC and OC content are shown and data are reported separately for detected and not-detected samples. Error bars indicate the standard deviation.

Accordingly, the two different subsets of samples collected in the two different sampling sites and with distinct chemical composition present a different electrical response. This result highlights once again the aforementioned synergy between the inorganic ionic components and the conductive elemental carbon fraction in the determination of aerosol conductance properties.

4.3.2.4 Laboratory Generated Aerosol Samples

In order to prove the role of this synergy in the determination of the electrical conductance of deposited aerosols, conductance measurements on laboratory generated aerosol samples (Section 3.4) were performed.

First of all, pure saline aerosol samples collected on PTFE filters were exposed to humidification and dehumidification cycles in the AEC. None of the 9 samples showed any electrical signal when humidity was varied inside the chamber, even if their mass loadings were considerable (from 116.584 to 857.716 µg cm^{-2}) and at least comparable or even significantly higher than the surficial mass distributions of the atmospheric samples presented in Sections 4.3.2.2 and 4.3.2.3. The formation of little droplets of saline solution over the surface of the PTFE filter was visible to the naked eye at high RH values. This kind of behavior was attributed to the hydrophobic nature of the filtering substrate and it results in the formation a discontinuous medium and in the lack of any conductance signal between the electrodes. Electrical conductance measurements were conducted on pure laboratory generated soot, as well. The measured electrical conductance at 30% RH for the eight considered samples was in the 20-180 µS range despite they had a surficial mass distribution of 3 to 20 µg cm^{-2}, at least of one order of magnitude lower than the mass loading for pure saline aerosol samples.

At a later stage, 12 mixed saline and soot samples were exposed to the same humidity cycles in the AEC as the atmospheric aerosol samples. Contrary to the pure saline samples, an electrical conductance signal was measured for all the mixed saline and soot samples. Therefore, the presence of soot is essential for the creation of a conductive medium in these laboratory generated samples. The reason for this is schematized in Figure 4.10, which represents the portion of aerosol deposited on PTFE filters between a pair of electrodes in the AEC filter housings. When a pure saline aerosol is deposited on a hydrophobic surface like PTFE and the deliquescence of its components occurs, tiny isolated droplets of an electrolytic solution are formed, thus preventing the creation of a continuous conductive path on the surface of the sample (Figure 4.10-A), even with a very high surficial mass distribution on filter. When soot is added to the saline components, it helps the formation of an electrical bridge thanks to its conductive nature (Figure 4.10-B); in this case, an electrical signal is measured between the two electrodes because a conductive continuum is formed between them.

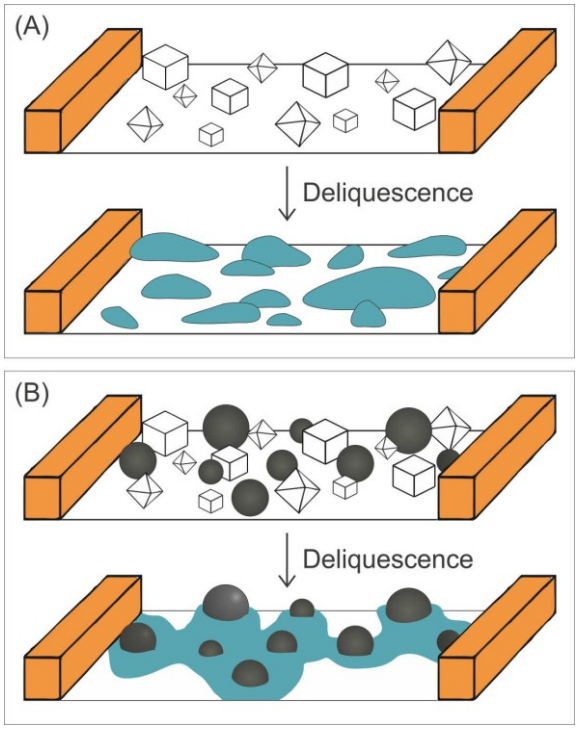

Figure 4.10: Interpretation of the results of the conductance measurements on pure saline samples (Panel A) and for mixed saline and soot samples (Panel B). The area between a pair of electrodes in the AEC is represented with an exemplification of the laboratory generated aerosol samples deposited on a PTFE filter, before and after the deliquescence of the saline components.

Some pictures were taken with a stereomicroscope (Leica Wild M420, 64x enlargement) for mixed saline and soot samples, before and after the AEC humidity cycles, in order to qualitatively investigate any possible visible change in the morphology of the samples due to the deliquescence and recrystallization of the saline components that could support this interpretation of the obtained results. In Figure 4.11 a mixed ammonium sulphate and soot sample is shown before (Panel A) and after (Panel B) the RH cycle in the AEC. The two images represent different portions of the same sample. In the image in Panel A, the surficial distribution of the sample is essentially uniform: the soot particles are visible and they appear mostly uniform in size, even if just a few coarse agglomerates are present. In Figure 4.11-B, which was taken after the humidity cycle, the effect of the deliquescence and crystallization of $(NH_4)_2SO_4$ on the morphology of the sample is clearly visible. The distribution of the particles is uneven on the filter and some white crevices have formed in the previously uniform texture of the sample. A possible explanation for this is that when the saline component deliquesces on the hydrophobic surface of the PTFE filter the formed solution tends to form structures like

that showed in the scheme in Figure 4.10-B; afterwards, when crystallization occurs, the creation of crystals in certain localized areas results in the formation of these structured fissures.

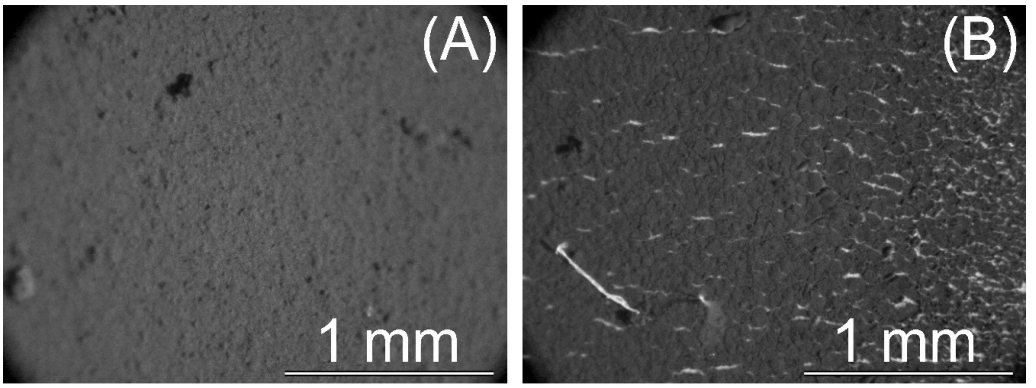

Figure 4.11: 64x enlargement of a mixed $(NH_4)_2SO_4$ and soot laboratory generated sample, before (Panel A) and after (Panel B) a RH cycle in the AEC.

In conclusion, with the results presented in this Section, it was shown that other aerosol conductive species, such as soot, and their interaction with the hygroscopic components have a role in the formation of electrical bridging phenomena that can be potentially dangerous for PCBs, if aerosol is deposited on them with a certain surficial mass. This is particularly relevant for studies that focus on this area of research, because so far all the effort has been to put in the understanding of the effects of saline hygroscopic components only. The present study included measurements on laboratory generated samples and simple considerations on the EC and OC contents in $PM_{2.5}$ aerosol samples from the two sampling sites. A further step ahead in this field of investigation could be achieved by means of direct measurements of the carbonaceous fractions to confirm what found with these estimations in Section 4.3.2.2 and 4.3.2.3. A further step ahead could be evaluating the effect of atmospheric aerosols directly on test boards; with this respect, a standardised deposition method on aerosol particle is fundamental and a good option is represented by the Rotating Impactor described in Section 3.1.1 and more in detail in the works by D'Angelo (2016)[161] and Casati (2016)[162].

4.3.3 Implications in Heritage Climatology

In the work of Casati et al. (2015)[51] the electrical conductivity measurements for the determination of DRH and CRH on Milan $PM_{2.5}$ samples were coupled to meteorological data to give an indication of the possible hazards for cultural heritage stone artefacts

that can be originated by deposited aerosol particles, within a so-called 'Heritage Climatology approach'[53]. In a recent publication, Brimblecombe (2013)[211] says that, even if this approach is still not well-defined, it needs to "characterise climate elements particularly relevant to heritage and recognise the importance of a number of critical meteorological parameters relevant to material heritage". He also pointed out that the damage associated to particular combinations of these parameters or to the persistence of certain conditions can result enhanced, and this would need to be considered.

The decay of outdoor-exposed stone materials strongly depends on factors related to climate and pollution[47,52,70,212] of their surrounding environment. In particular, deposited aerosol particles can damage stone surfaces[67,213,214] and their hygroscopic properties are considered among the most relevant factors influencing this kind of processes[67,215,216].

As discussed in Section 1.2.3, different chemical-physical mechanisms are associated to different types of stone-decay hazards. First, the presence of liquid water adsorbed on a stone surface can trigger a wide number of different decay processes (such as solid-liquid reactions, acid attack, penetration of salts solutions in the porosity of materials and biofilms formation) and the Time Of Wetness (TOW) was therefore indicated to be a good indicator for the hazard associated to "chemical" decay-mechanisms[46,67–70]. TOW represents the time fraction in which liquid water could be present on a stone surface. Besides, "mechanical" decay-mechanisms can be induced by the physical stress associated to the crystallization of dissolved saline components, due to variations in the ambient RH. The number of crystallization-dissolution cycles (Ncy) that deposited aerosols can undergo was indicated in literature as a possible indicator of this kind of decay hazard[71]. So far, these promising indicators have been calculated with simplified approaches. For example, TOW is usually estimated by fixing a threshold (80% RH, 0° C) above which a surface is considered wet[69,70]; in addition, the calculation of Ncy in most literature studies is based on the sole DRH[46,213,217]. In this way, the presence of particulate contaminants that can deliquesce at lower RH values, the seasonal variability of their deliquescence and crystallization points and the presence of an hysteresis cycle in the hydration state of the deposited particles are not taken into account. If the DRH and CRH are characterised over the different seasons, a more accurate site-specific assessment of the hazards for stone substrates can be performed considering the synergy between the properties of the deposited aerosols and regional climatic conditions.

Therefore, a new method that considers all these aspects was proposed and it is based on the measurements of seasonal DRH and CRH of $PM_{2.5}$ samples collected in Milan (TS sampling site, Section 3.3) for the computation of TOW and Ncy in combination with T and RH data over the decade 2003-2013 (hour averages from the five monitoring stations of the local Environmental Protection Agency ARPA Lombardia). The obtained results are summarised in Figure 4.12, which allows the site-specific individuation of the

different decay mechanisms that can be potentially active in different seasons, as a result of the synergic effects of the climatic conditions and the chemical composition of deposited particles. The variability within each month shown in Figure 4.12 is expressed in terms of standard deviation and derives from the different climatic conditions that have characterized each month in the considered decade. On average, winters in Milan are characterized by high time of wetness (89±11%) and low number of cycles (3±3 cycles/month). Conversely, summers are characterized by low time of wetness (20±13%) and high number of cycles (11±5 cycles/month). Interestingly, spring and fall resulted the most dangerous seasons for outdoor-exposed stones, since they presented both high *TOW* (61±16% and 83±15%, respectively) and *Ncy* (14±5 and 8±6 cycles/month, respectively).

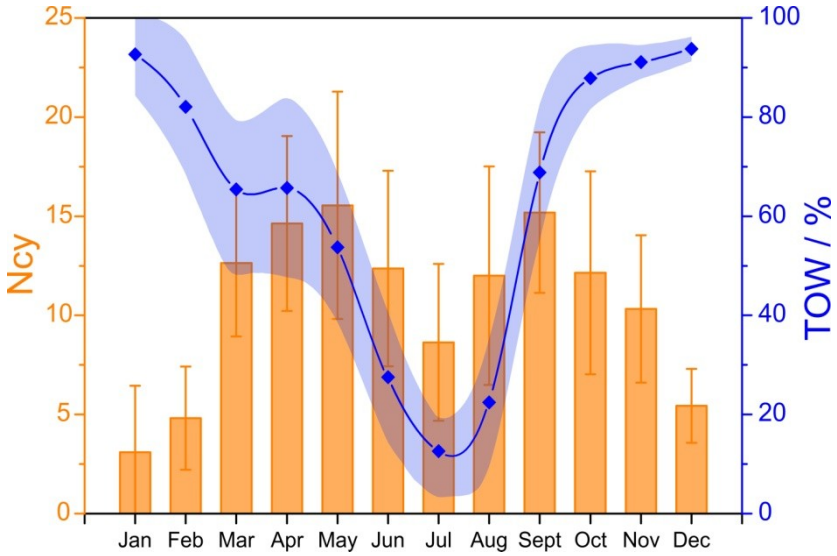

Figure 4.12: Ncy and TOW monthly values calculated according to the work of Casati et al.[51].

A comparison with the simplified approaches reported in literature and previously discussed was also performed and it allowed the estimation of the bias that the absence of an accurate knowledge of the hysteresis loop introduces in the calculation of these hazard indicators. The annual trend found over the same dataset for *TOW* is very similar if it is computed either with the method proposed in this work[51] or with a commonly used fixed threshold at 80% RH[69,70]; however, with this simplified algorithm the absolute percentage values result underestimated all year long of at least 9% (July) to a maximum of 49% (February). With respect to *Ncy*, it was computed by considering just the DRH[46,213,217] or both DRH and CRH. Similarly to what found for the time of wetness, the annual trend individuated by the two

different methods is similar, but the monthly number of cycles is overestimated for most months (except July and November) and on average about 64% more cycles per year are calculated when the existence of the hysteresis loop is neglected.

Therefore, the seasonal differences in the chemical compositions of particles, DRH and CRH values, coupled to variations in the climatic conditions, were demonstrated to determine different seasonal trends in the calculated time of wetness and number of dissolution and crystallization cycles and different types of related stone-decay hazards. Accordingly, even if presented results are site-specific for the city of Milan, the proposed method provides a tool to make nowadays hazard-assessment that is also potentially exploitable for the evaluation of future hazardous situations.

4.3.4 Implications for Remote Sensing Techniques

Remote sensing techniques are commonly used to investigate properties on the earth's surface with data acquired from satellites and aircrafts[218]. Satellite remote sensing has been employed to detect atmospheric aerosols since the 1970s[219]. With respect to ground-level experimental approaches, satellite measurements allow the characterisation of the concentrations and the properties of atmospheric aerosols on a global scale. The importance of studying aerosols on a global scale has been increasingly recognised in the last decades, in particular because of the increasing effect attributed to atmospheric aerosols on radiative forcing and climate change (Section 1.2.1). The information that can be retrieved using remote sensing techniques are related to particles concentrations and optical properties, aerosol direct and indirect radiative forcing, emission sources and the seasonal and inter-annual variation of these properties[219].

In the last years, several authors focused on the behaviour of aerosol hygroscopic growth in terms of size, mass and optical properties above a critical RH value[55,85,163,220], and a growing number of works investigated the effects of the hysteresis properties of the hydration state of aerosols on their light-scattering and radiative forcing. For example, Boucher and Anderson[221] estimated an uncertainty of $\pm 20\%$ on the direct climate forcing (Section 1.2.1) of sulphate aerosols due to the physical state of particles within the hysteresis loop. Similarly, Martin et al.[222] considered a simple sulfate-nitrate-ammonium aerosol system and found a difference of 21-32% in forcing of particles when they are considered either in the upper or in the lower branch of the hysteresis loop. The most common remotely sensed parameter used for the retrieval of ground-level aerosol concentrations ([PM]) is the aerosol optical depth (AOD or τ, also addressed to as aerosol optical thickness)[223,224], which represents a measure of the extinction of the solar

radiation due to atmospheric aerosol particles along a vertical profile. Inferring PM concentrations from τ satellite measurements is not a straightforward operation, since they are very different physical quantities, τ being related to the instantaneous optical properties of particles on a vertical column and [PM] representing ground-level and time-averaged measurements[225]. This is why a linear relation between PM concentrations and τ can be found only when the majority of the particles are concentrated near the earth's surface[224] but such linear relations can vary because of changes in the chemical composition of aerosols and of humidity (i.e. changes in the phase state and water content of the particles). As highlighted by Barnaba et al.[226], the hygroscopicity of atmospheric aerosols strongly affects data comparison of aerosol optical thickness obtained by remote sensing measurements and in situ PM concentrations. They also stressed that another factor that complicates the comparison of τ and PM concentrations is that the ground concentrations are normally measured by gravimetric analysis at 50% RH (according to EN-14907), while remote sensing measurements are carried out at ambient RH.

Levy et al.[225] proposed a more physical, but relatively simple, algorithm for the quantification of $PM_{2.5}$ concentrations from measured τ:

$$[PM_{2.5}] = \frac{\rho_0}{\Delta Z_{\mathrm{PBL}}\mathrm{GF}}\tau M'_c \qquad 4.3$$

where: ρ_0 is the aerosol dry density, τ is the measured aerosol optical depth, M'_c is a mass conversion coefficient, ΔZ_{PBL} indicates the thickness of the boundary layer and GF is the hygroscopic growth factor. Within the hysteresis loop, this last parameter cannot be univocally defined because it depends on the RH history (Section 2.1.1) the particles have been exposed to and errors could also be committed if the hysteresis of the deliquescence and crystallization processes are not taken into account.

For this reason, in order to demonstrate the importance of knowing both DRH and CRH in combination with the hygroscopic growth factor, the algorithm by Levy et al.[225] was tested in the work of D'Angelo et al.(2016)[160]. The average GF_m values in the upper (GF_{mU}) and lower branch (GF_{mL}) of the hysteresis loop measured with the gravimetric technique described in Section 3.6.4 were compared for 20 samples (MI-TS sampling site). The uncertainty associated to the determination of [PM2.5] by including either GF_{mU} and GF_{mL} in 4.3 was evaluated as a percentage overestimation (Δ[PM2.5]%, 4.4), so that no assumption on ρ_0, τ, ΔZ_{PBL} and M'_c was needed.

$$\Delta[PM_{2.5}]\% = \left(\frac{[PM_{2.5}]_U - [PM_{2.5}]_L}{[PM_{2.5}]_U}\right)\% = \left(\frac{GF_{m_U} - GF_{m_L}}{GF_{m_U}}\right)\% \qquad 4.4$$

To calculate the most accurate potential error in the retrieval of PM concentrations from satellite data with the algorithm by Levy et al.[225], it is also relevant that during humidification an early water uptake was detected even before the DRH. Even though small, this phenomenon results in GF_m values only slightly higher than 1 before the DRH. For Winter samples this region of the mass growth curves occurred on average in the 44.3-51.6% RH range, where GF_m was on average 1.02±0.03, while the upper branch of the hysteresis region was identified on average between 48.1% and 58.5% RH. Since the average estimated GF_m was 1.25±0.02 in the upper branch of the GF_m growth curves, not considering the history of the RH can produce an underestimation of GF_m up to 23.2±0.8%. Similarly, for Summer aerosols, the average GF_m for the upper branch of the hysteresis loop (63.0-72.8% RH) was 1.43 while, for the lower branch (59.3-68.3% RH), was 1.15±0.06, with a potential mean error of 24.1±2.0%. In the light of these GF_m values measured within the hysteresis loop in correspondence to the upper and lower branches, $\triangle$[PM2.5]% resulted 18.9±0.7% for Winter samples and 19.4±1.6% for Summer samples when aerosols are in the upper branch (metastable state) of the hysteresis loop rather than in the lower branch.

Therefore, for the retrieval of PM concentrations from remote sensing data, it becomes fundamental to correctly understand whether the aerosol particles are in the upper or lower branch of the hysteresis loop. Thus, in order to estimate the frequency of wrong assignments of GF_m within the hysteresis loop, experimental DRH and CRH values were used to evaluate the hydration time of aerosols for both seasons as a function of the RH history. Data on the ambient RH from 2006 to 2014 (Environmental Protection Agency, ARPA Lombardia) and its variation over time was compared with DRH and CRH using the same algorithm described in Secition 4.3.3 for the calculation of TOW.

In the wintertime (66±2% RH, 280±1 K, on average), these calculations suggested that aerosols were in prevalence hydrated since the RH was above the DRH for 62.4±4.6% of the considered time and the situation in which aerosols were in the upper branch of the hysteresis loop accounted for 11.9±1.7% of the time. During Summer, the low RH conditions (44.3±1%, 300±0 K, on average) result in a prevalence of aerosols in their dry state: the RH≤CRH case accounted for 92.5±0.8% of the total time; even if the hydration time was estimated to be only 6.9±0.7%, the upper branch case occurred for 2.4±0.3% of the time, which suggested that when the RH is between CRH and DRH this situation is less frequent but still present in Summer, too.

4.4 Summary and Conclusions

In this Chapter, the results of DRH and CRH measurements by means of the electrical conductance method in the AEC (Section 3.2) on $PM_{2.5}$ atmospheric aerosol samples collected at the sampling site of MI-TS were presented and discussed. The frequency distribution of the phase transition relative humidities showed a bimodal behaviour, in which Winter samples accounted most of all for the lower RH modes (peak in the 55-60% range for DRH and in the 45-50% range for CRH), whereas Summer samples were mainly represented in the higher RH modes (peak in the 70-75% range for DRH and in the 65-70% range for CRH). The identified seasonal trends were at first explained by considering the chemical composition of the inorganic ionic fraction of the samples analysed using ion chromatography (Section 3.5). Winter samples resulted nitrates-rich whereas the ionic fraction of Summer samples is dominated by sulphates. This seasonally modulated chemical composition explains the seasonal trends individuated for DRH and CRH average values. It was also shown that more acidic samples tend to deliquesce and crystallise at lower RH values.

In order to evaluate the possibility of using aerosol models for the prediction of DRH and CRH of complex atmospheric aerosols by simply taking into account the main ionic inorganic and organic components, a comparison of the experimental results presented in Section 4.1 and of modelled simulations was performed. In particular, E-AIM Model[100,194] was used for the simulation of DRH: results showed E-AIM Model was able to reproduce the bimodal trend found for the experimental DRH frequency distribution, even though with a 5% overestimation bias, but the point-to-point agreement for each sample considered separately was shown to be poor. These results indicated that the driving force of the deliquescence process is the hygroscopicity of the most abundant inorganic ions and carboxylic acids and for this reason E-AIM Model is able to partially represent the overall seasonal trends individuated from conductance measurements. However, in order to achieve a more accurate DRH estimation for each single sample, taking into account the entire organic fraction is necessary. As a consequence, this indirectly implies the need of on accurate representation of the hygroscopic properties of an increasing number of organic components characterised by an increasing degree of chemical complexity in aerosol models, as well as the necessity of correctly accounting for the interactions of inorganic and organic species in aqueous solutions. Simulations of CRH performed using the parametric model by Martin et al. (2003)[136] demonstrated that this model is completely not applicable for complex aerosol systems, since the effect of insoluble inclusions that promote heterogeneous crystallisation is not accounted for.

Section 4.3 was devoted to show the importance of taking into account deliquescence and crystallization relative humidities of atmospheric aerosol particles in three different fields

of application. First, the development of a standardised methodology for the safe application of Direct Free Cooling in Data Centers by considering the chemical composition and the hygroscopic properties of aerosol particles was presented. This approach consisted at first in the estimation of DRH values from the analysis of ion fraction composition of aerosol samples[187], followed by direct measurements of DRH and CRH of $PM_{2.5}$ aerosol samples by means of the AEC conductance method[112]. In this way, it was possible to determine safe T and RH working conditions within the Data Center such that aerosol particles that enter the DC and deposit on electronics are not hydrated, thus preventing electrical failures promoted by deposited hygroscopic species. As a further contribute to this field of application, it was also shown that the synergy of hygroscopic and non-hygroscopic but conductive species in aerosol particles (i.e. elemental carbon) can potentially promote failure of PCBs by originating electrical bridging phenomena between circuitry components that would normally be insulated.

The second considered application of the DRH and CRH measurements was related to the effects of deposited particles on porous surfaces of cultural heritage artefacts[51]. Two hazard indicators for stone materials were suggested to describe both a "chemical" (time of wetness, TOW) and a "mechanical" hazard (number of deliquescence and crystallisation cycles, Ncy). By coupling meteorological data and average seasonal values of DRH and CRH measured using the electrical conductance method in the AEC, these indicators were computed and a site-specific hazard assessment for the site of Milan was performed. The proposed approach is not only an improvement of previous simplified literature approaches, but is also applicable to any site of interest and potentially for the evaluation of future hazardous situations.

Finally, the hysteresis of the hydration state of aerosol particles was considered in order to estimate the potential bias it can cause in the estimation of ground-level aerosol concentrations with remote sensing techniques[160]. The measurement of mass growth curves of $PM_{2.5}$ samples collected at MI-TS were performed using a gravimetric method in the AEC and average mass growth factor values for the upper and lower branches within the hysteresis loop were calculated. A simple remote sensing literature algorithm[225] for the calculation of $PM_{2.5}$ ground concentrations was considered and the bias in the estimation of $PM_{2.5}$ concentrations deriving from the different size of droplets in the upper or lower branch within the hysteresis loop was calculated. The bias resulting from neglecting the hysteresis of deliquescence and crystallisation processes was $18.9 \pm 0.7\%$ for Winter samples and $19.4 \pm 1.6\%$ for Summer samples, when the atmospheric conditions experienced by aerosol particles are such that $CRH<RH<DRH$. Therefore, these results evidenced the need of taking into account the hysteresis cycle of aerosol hydration state and the history of ambient RH for an accurate estimation of ground-level aerosol concentrations using remote sensing techniques.

Chapter 5 The Cylindrical Electrodynamic Balance

Ensemble measurements on atmospheric aerosol samples are important because they allow observation of the overall behaviour and interactions of aerosol particles as they exist in the environment. However, the chemical heterogeneity of atmospheric aerosols (Section 1.1.1) can make the interpretation of ensemble measurements quite challenging, because thorough chemical characterisation of atmospheric aerosol samples is not always easily achievable. In addition, particle-particle interactions can add a further complication which needs to be avoided in case more fundamental chemico-physical properties of aerosols are investigated. Therefore, even though studying the behaviour of 'real' atmospheric aerosol ensembles is essential for many fields of study, such as those discussed in Section 4.3, considering simplified but atmospherically-relevant aerosol systems and single isolated particles is a necessary approach to improve the understanding and modelling of the basic properties that characterise multi-component atmospheric aerosols (Section 2.2).

Electrodynamic trapping is an experimental technique that was developed to levitate single droplets in a controlled environment. Electrodynamic trapping has proven to be effective for the study of aerosol properties and processes, such as optical properties[227], vapour pressures of low volatility compounds[93], hygroscopic properties of atmospherically-relevant aqueous solutions[91,121,127,228] and of pharmaceutical aerosols[45,229], evaporation dynamics of aqueous droplets[18,20,230], oxidation chemistry in the aerosol phase[231,232], exchange reactions between gaseous components and chemical species in the condensed droplet phase[233].

Several different electrodynamic balance (EDB) setups have been proposed in the literature and their historical development is described in the first part of this Chapter (Section 5.1). The cylindrical electrodynamic balance (C-EDB) experimental setup used for the acquisition of data in this study is fully described in Section 5.2, together with all the operations for the generation, trapping and sizing of single droplets in the C-EDB.

The features of the C-EDB used in this work were also subject of previous publications[17,96,142–144,234].

5.1 Hystorical Development of EDBs

Electrodynamic trapping was hystorically developed with the aim of accurately determining the fundamental charge of the electron. With this aim, Wilson (1903)[235] was the first to developed a method to observe the forces on a cloud of charged droplets between two parallel plate electrodes. A few years later, Millikan (1910)[236] modified the Wilson's experiment in order to levitate single droplets within the electrical field generated by the two plate electrodes. Thanks to his experimental setup he performed his famous oil drop experiment, with which he was able to measure a very accurate estimate of the elementary charge that earned him the Nobel prize in Physics in 1923.

Some issues with the lateral stability of the plate electrodes experimental setup were solved in the following years by Straubel (1956)[237], thanks to the addition of a electrode disc in the middle of the two plates, and by Wuerker et al. (1959)[238], who developed the so-called standard hyperboloidal levitator. In the latter experimental setup, the stability of trapped droplet was substantially increased, but the electrodes geometry limited the access to the centre of the trap, that was necessary to apply optical methods for the characterization of levitated droplets. In order to overcome this issue, a pair of ring electrodes were successfully used by Ray et al. (1989)[239] to generate the electrodynamic field in their trap and since then the double-ring setup has been widely used[31]. The term electrodynamic balance was introduced to indicate that the mass of a single levitated droplet can be inferred by the variable strength of the DC voltage the electrodynamic field to balance the force of gravity acting on the droplet.

The experimental setup used in this work is the concentric cylindrical electrodynamic balance (C-EDB) that was first proposed by Heinisch et al. (2009)[230]. The electric field generated by the cylindrical electrodes is substantially stronger and more stable than that resulting from the double-ring geometry. The importance of this feature of the concentric cylindrical electrodes setup is discussed in Section 5.2, which is focused on the description of the C-EDB experimental setup used in this work.

5.2 Cylindrical EDB Experimental Setup and Operations

The schematic presented in Figure 5.1 (Panel A) shows a top view of the main components in the C-EDB experimental setup. The core of the C-EDB setup is an octagonal aluminum chamber in which two sets of concentric cylindrical copper electrodes (Figure 5.1, Panels B-C) are housed and used to generate the electrodynamic field in which single droplets are confined (Section 5.2.1). A circular window is placed on each wall of the octagonal chamber, giving access to the core of the C-EDB. Microdispensers are used to generate and deliver single droplets to the trapping region within the C-EDB (Section 5.2.1). The two windows through which the droplet microdispensers inject particles into the C-EDB are left open and are equipped with an induction electrode that charges the droplets before entering the trapping chamber. A sizing camera is placed at a 45° angle with respect to the direction of propagation of the forward scattered 532 nm laser light. The camera collects the scattered light pattern that originates from refraction and reflection of the incident light by the droplet. The scattered light pattern is used to infer the size of the confined droplet in time (Section 5.2.2). A positioning camera is placed perpendicularly to the laser beam and it is useful for visualizing the trapped droplets and keeping track of their position during the experiments. The temperature in the trapping chamber is regulated by means of the recirculation of liquid from a thermostatic bath through the lid (Section 5.2.4). All the operations in the C-EDB are controlled through a software interface (LabVIEW, National Instruments).

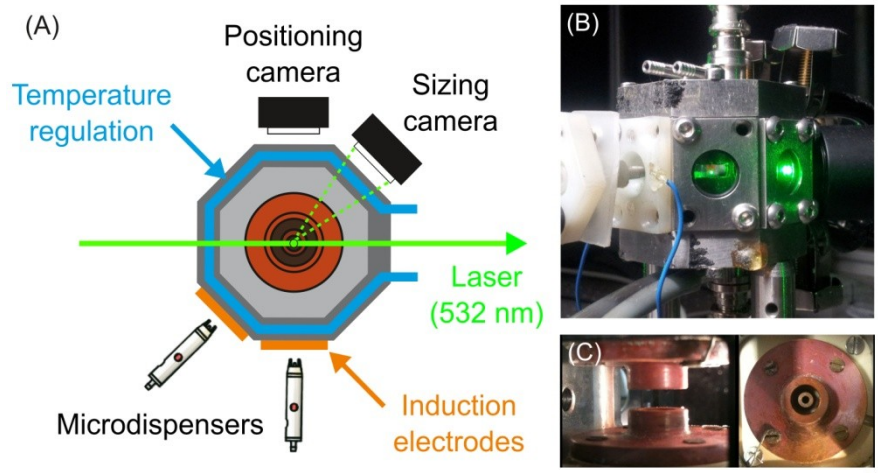

Figure 5.1: (A) Schematic showing the main components of the C-EDB setup from the top. (B) The C-EDB trapping chamber with a single levitated droplet illuminated by green laser light. (C) Side (left) and top (right) views of the concentric cylindrical electrodes.

5.2.1 Generating and Trapping Droplets in the C-EDB

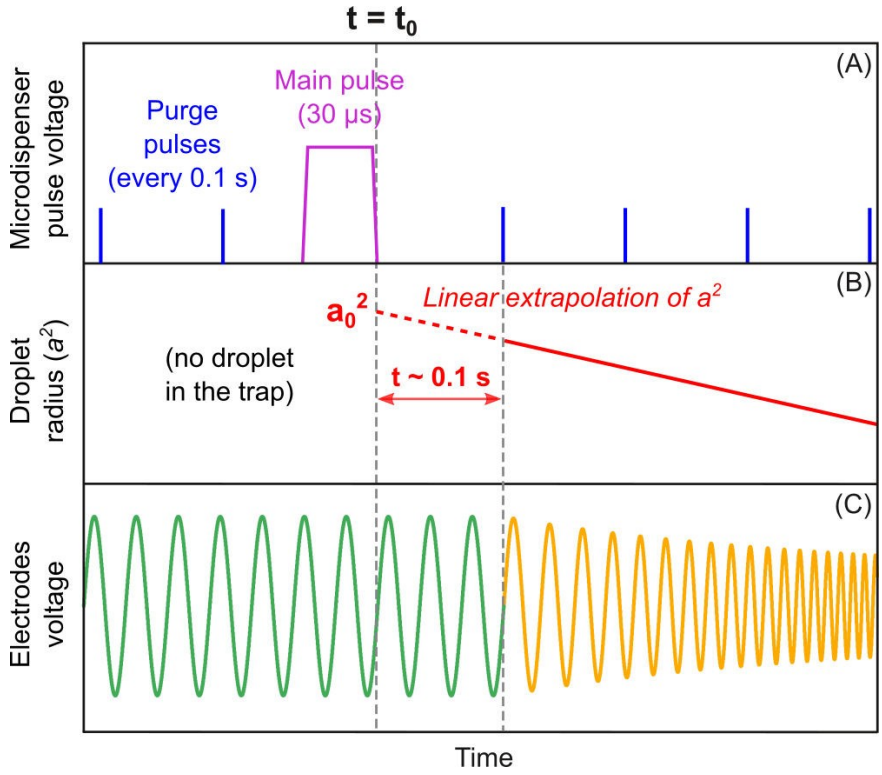

Figure 5.2: Operations of the C-EDB for the generation and trapping of single droplets. (A) Pulse voltage applied to the microdispensed for the generation of droplet (main pulse) and for the purge of the microdispenser tip. (B) Variation of the squared radius of an evaporating trapped droplet. (C) Adjustment of the electrodynamic field within the trapping chamber to respond to the size variation of the trapped droplet. (Note: timescales are arbitrary).

Single droplets can be generated on demand to be delivered to the EDB trapping chamber using a voltage-activated droplet microdispenser (MJ-ABP-01, Microfab). The dispenser reservoir (<10 µL internal volume) can be filled with a solution of known composition and concentration. Once the microdispenser is loaded, a pulse voltage is applied to it. The pulse voltage generates a pressure wave inside the solution that forces a small volume of liquid through the dispenser's orifice (30 µm diameter), thus producing a droplet. The amplitude and the width of the pulse voltage can be controlled in order to alter the trajectory of the droplet inside the trapping chamber, so that each droplet can be delivered to the centre of the trap and effectively confined. Typically, to obtain suitable trajectories, the amplitude of the applied pulse voltage is ~40 V, while its amplitude is varied from 25 µs to 40 µs. In addition, between two consecutive voltage

pulses a series of smaller purge pulses are also applied, typically every 0.1 s and with an amplitude of about half of that of the main pulses (Figure 5.2, Panel A). These purge pulses ensure that the solution is continuously refreshed at the tip of the microdispenser, in order to prevent any possible solvent evaporative loss and avoid any subsequent artefacts due to a higher solution concentration. The initial time (t_0) corresponds to the time at which the main pulse voltage is applied and is necessary for the estimation of the initial squared-radius of the droplet (a_0^2, Figure 5.2, Panel B, see also Section 6.1.2). Since the measured squared-radius vs. time is linear at the beginning of the evaporation of water, a_0^2 can be linearly extrapolated to time t_0. In this work, the linear extrapolation was performed over the first 150 measured points (corresponding to the first 1.5 s after droplet generation).

One key feature of the C-EDB experimental setup is the presence of two microdispensers that can be operated sequentially, thus allowing the generation of aerosol droplets with different chemical compositions in rapid succession. This double dispenser setup allows comparative kinetics measurements to be performed. As will be thoroughly discussed in Chapter 6, comparative kinetic measurements consist in alternatively levitating a probe droplet (water or a well-characterised salt solution, such as NaCl) and a sample droplet and in comparing the evaporation kinetics of the well-characterised probe droplets for the interpretation of the unknown sample droplets.

In order to trap the dispensed droplets within an electrical field, a charge needs to be conferred to them. The microdispensers are placed at about 1-5 mm from two of the windows of the octagonal trapping chamber, each of them equipped with a copper plate induction electrode. A positive potential of 500-600 V is applied to the induction electrode, which causes a separation of the charges in the liquid jet leaving the dispenser's orifice. When the liquid jet breaks into a single droplet because of the pressure wave generated by the applied pulse voltage, an excess of negative charge is present on it allowing the droplet to be confined in the electrical field inside the trapping chamber. The charge on the droplets generated with this experimental setup is not well known, but it has been determined to be ~5-50 fC for similar methods used in literature[234,240,241]. In addition, Davies (2014)[144] performed simulations on the evaporation of pure water droplets with variable charge on their surface (using Eq. 6.2) determining that the amount of charge conferred to droplets using this experimental setup does not affect the evaporation rate of water from the droplets. Variability in the rate of evaporation of water from the droplets could happen if during evaporation the surficial charge distribution exceeds a certain threshold, since droplets decrease in size during evaporation and their initial surficial charge density consequently increases with time. With these simulations, Davies (2014)[144] predicted that a deviation from linearity in squared radius vs. time evaporation profiles for pure water is expected when the charge conferred to droplets exceeds 10 fC. The author then compared these evaporation

simulations with experimental evaporation profiles of water droplets charged by an increasing voltage applied to the induction electrode (from 250 V to 850 V). No deviation from linearity was observed for these experimental evaporation profiles, suggesting that the charge on trapped droplets in the C-EDB does not exceed 10 fC and that the charge density on the droplet surface does not affect the evaporation rate in this experimental system.

The electrodynamic field used to confine droplets in the trapping chamber is generated by a set of four cylindrical electrodes. The four electrodes comprise an upper and a lower pair of two concentric cylindrical electrodes that are insulated from each other. The outer electrodes are kept at 0 V, while an AC voltage of up to 1000 V, with a frequency usually around 95 HZ, is applied to the inner electrodes. In addition, a DC voltage is applied to one of the inner electrodes to balance the permanent forces that act on the trapped droplet, i.e. the gravitational and drag forces. The initial AC voltage and amplitude and the DC voltage of the trapping electrodes can be adjusted by means of the C-EDB control software in order to successfully trap droplets with variable initial radii. Once a droplet is trapped, the AC voltage amplitude, *V(a)*, and frequency, *f(a)*, of the cylindrical electrodes are automatically varied as a function of the measured droplet radius (a), according to Eq. 5.1 and 5.2:

$$V(a) = V_0 - dV/(1 - a/a_0) \quad 5.1$$

$$f(a) = f_0 - df/(1 - a/a_0) \quad 5.2$$

where V_0 and f_0 are the initial voltage and frequency, and dV and df are adjustable parameters that modify V_0 and f_0 as a function of the ratio between the measured droplet radius and its initial radius, a_0.

This dynamic variation of *V(a)* and *f(a)* is needed because, as the trapped droplet is evaporating and its radius decreases, the charge distribution on its surface increases. Therefore, in order to compensate this surficial charge density variation on the droplet, the strength of the electrodynamic field is accordingly varied in order to keep the droplet in the trap. In the exemplification shown in Figure 5.2-C, the voltage amplitude is lowered with decreasing measured a (Panel B), whereas the voltage frequency is increased.

The concentric cylindrical electrodes setup results in a strong electrodynamic field, which is characterised by a steep gradient in correspondence to the trapping region. A simulation from the data by Heinisch et al.[230] of the electrical field strength when a 1000 V potential is applied is shown in Figure 5.3 (Panel A). Figure 5.3 also compares the electric field strength of the ring electrodes geometry (Panel B). The greater strength of

the electric field is an important benefit of the C-EDB experimental technique for several reasons. First of all, the strength of the electric field allows droplets to be tightly confined within 100 ms from their generation, which is important in order to accurately retrieve the initial radius of the droplet in the measurement of fast evaporation processes. In addition, the strong electric field and accompanying tight confinement limit the movement of a droplet once it is trapped, allowing a gas flow to be introduced in the trapping chamber (Section 5.2.4) and optical measurements (Section 5.2.2) to be performed without the need to take into account variation in the droplet position during time.

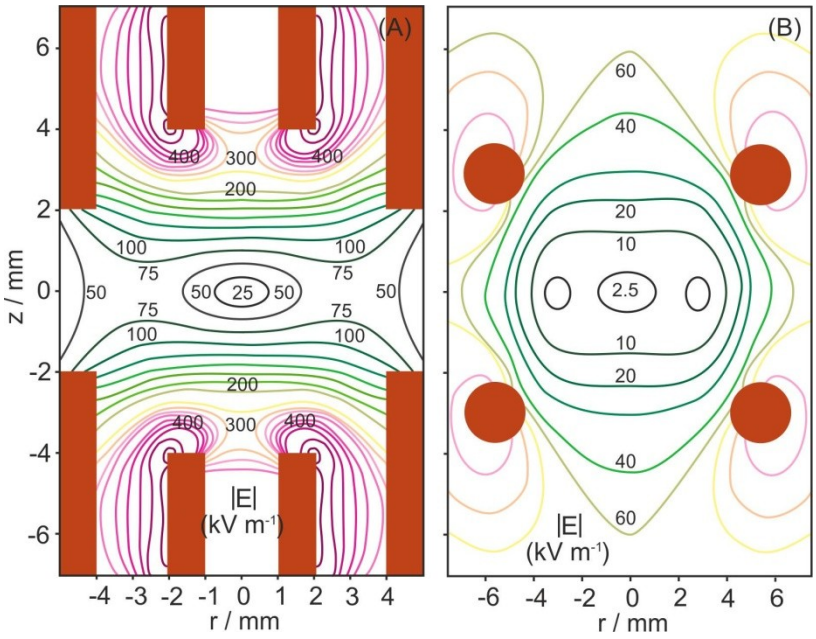

Figure 5.3: Electrical field strength (|E|, kV m^{-1}) for cylindrical (Panel A) and for ring electrodes (Panel B) EDB setups from simulations by Heinisch et al.[230]. On the x axis r indicates the radial distance from the centre of the electrodynamic field, whereas z refers to the vertical distance from the centre.

5.2.2 Sizing Trapped Droplets

Once a single droplet is trapped, accurately keeping track of how its radius varies in time due to water evaporation is essential to determine the evaporation rate of water from the droplet, the use of which is detailed in Sections 6.1.1 and 6.1.2. For this purpose, the optical properties of aerosol particles described in Section 1.1.3 are exploited as described in this Section. Each confined droplet is illuminated by monochromatic planewave light

from a green laser (Ventus, Laser Quantum, λ=532 nm, operated at 25-50 mW). The light is reflected and refracted by the droplet and the resulting interference elastic scattering pattern is collected every 10 ms over a range of solid angles centred at 45° with respect to the direction of propagation of the forward scattered light by means of a CCD camera (Thorlabs DCC1545M, operated with a resolution of 1280 x 100 pixels). Figure 5.4 schematically shows the scattered light collection in the C-EDB. The collected scattering pattern appears as a series of bright and dark fringes that results from the interference of light reflected and refracted by the droplet surface (see also the simulations in Figure 1.3). The scattered light intensity is converted to a one-dimensional plot and the resulting phase function (angular distribution of the scattered light intensity) is registered.

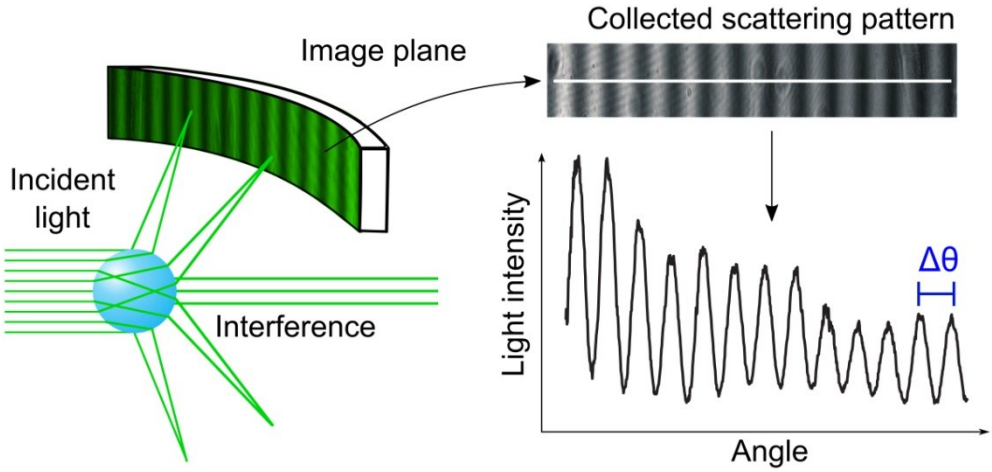

Figure 5.4: Interference pattern of the light refracted and reflected by a spherical droplet when illuminated by plane-wave light. The experimental angularly resolved scattering pattern is collected and the average angular separation of the fringes (**Δθ**) is used to calculate the droplet radius with Eq. 5.3.

As discussed in Section 1.1.3, Mie theory[29] provides an exact solution of the Maxwell equations for spherical and homogeneous droplets illuminated by monochromatic plane wave light. Mie theory can be used to determine the radius of a droplet from its experimental angularly-resolved light scattering pattern, which is dependent on the size of the droplet, on its refractive index and on the incident wavelength. This procedure is computationally demanding and therefore it cannot be used to determine the radius of a levitated droplet in real-time. Instead, the simplified geometrical optics approach proposed by Glantschnig and Chen[242] can be applied to infer the radius of a confined droplet in real-time with very good accuracy. The uncertainties in the radius

determination associated with each procedure will be discussed in the following sections (5.2.2.1 and 5.2.2.2) and were taken into account in the calculation of the errors associated with each measurement (as discussed in Section 6.1.3). In this work, the geometrical optics approximation was routinely used for all the comparative kinetics measurements in Chapters 6 and 7, while the full Mie theory approach was only applied in the case of long trapping measurements for the determination of vapour pressures of aminium sulphates (Section 7.1.6).

5.2.2.1 Determining the Radius of Droplets with the Geometrical Optics Approximation

Generally speaking, geometrical optics describes the propagation of light in terms of 'rays', and assumes that each ray propagates linearly in a homogeneous medium, whereas it splits into two separate rays at the interface between two separate and different media. From a physical point of view, these assumptions are only applicable when light interacts with objects that are much bigger than its wavelength. When the geometric optics approach is applied to levitated droplets, the interface that causes the reflection and refraction of light is that between the gas phase and the condensed particle phase. Glantschnig and Chen[242] proposed a simplified but accurate approach for the description of the intensity of light scattered by a spherical homogeneous particle as a function of the scattering angle. The considerations that underlie their approach are simple: light is scattered mostly in the forward direction and the intensity of the scattered rays that refract through more than two surfaces is negligible. For these reasons, their simplified geometrical optics approach only considers rays that hit a first gas phase/particle interface, are then scattered through the particle bulk and finally leave the droplet after being refracted by a second particle/gas phase surface. Using these considerations, they were able to derive a useful relation of the average separation between the fringes in the generated scattering pattern ($\Delta\theta$, as illustrated in Figure 5.4) and the radius of a droplet:

$$a = \frac{\lambda}{\Delta\theta}\left(\cos(\theta/2) + \frac{m\ sin\ (\theta/2)}{\sqrt{1 + m^2 - 2m\ cos\ (\theta/2)}}\right) \qquad 5.3$$

where λ is the incident wavelength (in the case of the experiments conducted in this work, 532 nm), θ is the central viewing angle and m is the refractive index of the droplet.

As a result of the assumptions made for the derivation of Eq. 5.3, the application of the Glantschnig & Chen approach is limited to the analysis of light scattered in the forward direction and when the scattering angles are close to the direction of light propagation

(no more than 60°). In the case of the C-EDB experimental setup, the central viewing angle in 45° and the angular width of the images collected by the camera is ~24°. As such, the maximum scattering angle observed is ~57° and thus the geometrical optics relation derived by Glantschnig and Chen[242] can be reliably applied.

When the geometrical optics approximation is applied for the real-time determination of the radius of an evaporating droplet, the accuracy in a depends both on factors relating to the experimental setup (the angular pixel resolution of the camera (0.025°) and the uncertainty in the calibrated angular width) and on intrinsic limitations of the geometrical optics approach. Davies (2014)[144] estimated an overall uncertainty of ±100 nm associated with the radius determined with this method.

5.2.2.2 Determining the Radius of Droplets with Mie Theory Simulations

The determination of the radius of a trapped droplet can also be performed by collecting full phase functions (scattered light intensity vs. scattering angle plots, as in Figure 5.4) during the whole duration of an evaporation experiment and comparing them with a library of Mie theory simulations[243,244]. As reminded at the beginning of Section 5.2.2, the scattering pattern originated by a droplet is defined by the droplet radius and refractive index and by the incident wavelength. Therefore, Mie theory can be used to generate a series of phase functions for a set of a and m values, which are then compared to the experimental registered scattering pattern to individuate the Mie simulated phase function that best fits the experimental one.

Mie theory simulated scattering pattern are generated for a defined range of radii and with a constraint on the droplet refractive index (m), according to Eq. 5.4[243,244]:

$$m = m_0 + \frac{m_1}{a^3} + \frac{m_2}{a^6} + \cdots + \frac{m_k}{a^{3k}} \qquad \textbf{5.4}$$

where m_0 represents the refractive index of pure water (1.335 at a wavelength of 532 nm), while m_1, m_2, ..., m_k are parameters that determine the dependence of refractive index on the droplet radius. The Pearson correlation coefficient is calculated for each simulated and measured phase function pair and a first radius value is attributed to each measured phase function, which corresponds to the one with the lowest C value. In the following step, the refractive index is varied according to Eq. 5.4 and the same comparison is performed again with the new library of simulated phase functions. Average C values are calculated for each set of m_1, m_2, ..., m_k parameters over all the

analysed phase functions, and the one that shows the highest average Pearson correlation coefficient is selected for the determination of the final a values.

The Mie theory approach is more computationally demanding than the geometric optics approximation and needs to be applied as an off-line data analysis step. For this reason, Mie theory analysis was only conducted for the long trapping measurements presented in Section 7.1.6, because in this case the variations in droplet radius that are observed are very small (of the order of a few hundred nanometres) and thus the highest possible accuracy is required. Davies (2014)[144] estimated an uncertainty within ±30 nm for radii determined by fitting full phase functions with Mie theory simulations, taking into account the resolution of the camera, the minimum detectable light intensity change and the uncertainty in the angular width.

5.2.3 Accounting for Variable Refractive Index in Evaporating Droplets

The refractive index of solution droplets evaporating in the C-EDB is not constant because the solute concentration increases as water evaporates. The variation of the refractive index with time is taken into account to accurately determine droplet radii in Eq. 5.3. At first, during the data acquisition, m is set constant at 1.335, the value for pure water at 532 nm. In a post-acquisition analysis step, the radii data are corrected by taking into account the variation of the refractive index with mass fraction of solute (mfs).

The variation of m for a multicomponent mixture as a function of the contribute to the mixture of its different components can be estimated by combining the single component refractive indices and weighing them using a mixing rule (either on a volume, mass or molar basis). In this work, the parameterisation of the refractive indices of the analysed solutions against the solution mfs was performed by applying the molar refraction mixing rule[245]. Among the different mixing rules that can be found in the literature, the one based on molar refraction is the only that has an actual physical basis, since it is the only one to be consistent with the fundamental Lorentz-Lorenz relation, which associates the refractive index of a substance with the polarisability of its molecules[245]. The molar refraction mixing rule was demonstrated to be the most representative mixing rule to describe a number of inorganic systems[244].

The molar refraction (R) of a species is defined by:

$$R = \frac{(m^2 - 1)M}{(m^2 + 2)\rho} \qquad 5.5$$

where M is the compound's molecular mass and ρ is its pure melt density. The molar refraction for a mixture of different components is defined as the sum of the molar refractions of each compound weighted by their mole fractions (x):

$$R = \sum_i x_i R_i \qquad 5.6$$

In this study, the relationship between solution densities and mass fraction of solute and the pure solute melt densities for the inorganic compounds shown in Chapter 6 were taken from the work of Clegg and Wexler[103]. For ease of data processing, the density data were plotted as a function of the square root of the mass fraction of solute ($mfs^{0.5}$) and fitted with a polynomial curve (orders ranging from 4th to 7th) so that the residual from the fit was <0.005 g.cm^{-3} across the whole $mfs^{0.5}$ range. The density parameterisations were then used in conjunction with tabulated data of solution refractive indices (at λ = 589 nm) as a function of mfs taken from the CRC Handbook[246], and a least squares fit with respect to m based on the molar refraction mixing rule was perfomed in order to calculate the pure component refractive index of the molten salt (m_{melt}). An example of the densities and refractive indices parameterisations obtained for ammonium sulphate and sodium chloride are shown in Figure 5.5.

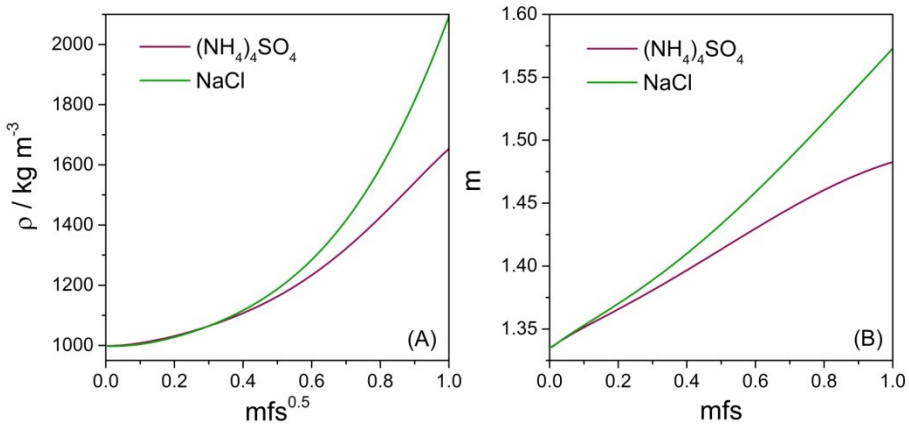

Figure 5.5: Density (ρ vs. $mfs^{0.5}$) and refractive index (m vs. mfs) parameterisations obtained for $(NH_4)_2SO_4$ (purple) and NaCl (green), according to the description in the text.

In order to perform the refractive index correction for the aminium sulphate evaporating droplets (Chapter 7), the density and refractive indeces for at least 10 solutions with

variable solute concentrations were measured a refractometer (Palm Abbe II, Misco) and with a density meter (Densito 30PX, Mettler Toledo), respectively, since no literature data was available for such compounds. ρ vs. $mfs^{0.5}$ data were fitted with a 3rd order polynomial and the molar refraction mixing rule was applied in this case, as well.

The procedure used to take into account the variation in refractive index during the evaporation is discussed below. The initial size of the droplet is estimated with a linear extrapolation of the a^2 vs. time plot to t_0=0 s (as described Section 5.2.1), and the initial solute mass fraction and density of solution at t_0 are known from the prepared solution. The elastic light scattering data are first analysed with m=1.335 to yield an initial estimate of the variation in radius with time, also providing a first estimate of the variation of the solute concentration and of the solution density during the evaporation. A set of corrected refractive indices for the droplet solution is then calculated at every time-step based on the change in size using the molar refraction mixing rule (Eq. 5.5 and 5.6). These corrected refractive indices at each time point are then used to fit a new set of corrected radii with Eq. 5.3. This procedure is then repeated for the new set of corrected radii until the refractive indices and radii values converge, typically after 2-3 iterations.

The result of such refractive index corrections are shown in Figure 5.6 for radius data as a function of time collected for two NaCl solution droplets (with an initial *mfs* of 0.05 and initial radius of ~25 μm) evaporating into different gas phase RHs.

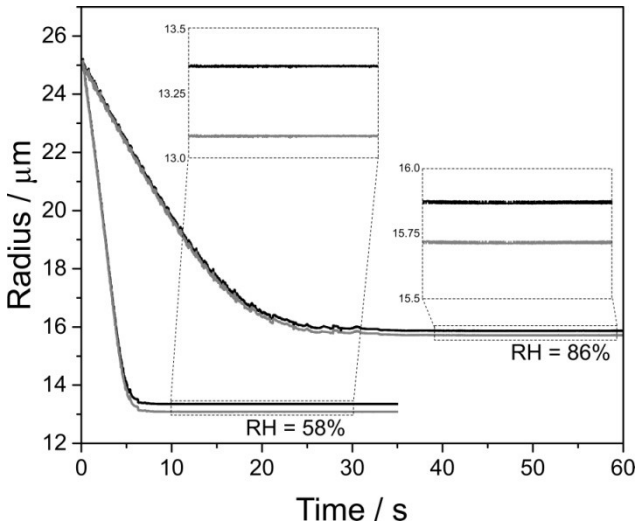

Figure 5.6: Effect of the variable refractive index corrections on the evaporation plots (radius vs. time) of two NaCl droplets evaporating into different RHs.

The difference between the evaporation curves collected at first with a fixed m of 1.335 (grey) and those obtained after this variable refractive index correction (black) is evident in Figure 5.6. In particular, the correction becomes more significant in the final parts of the evaporation curves, since in that region the solute concentration is higher as a result of water evaporation, and therefore the refractive index of the solution is higher as well. For this same reason, the m correction is also more significant for the NaCl droplet that evaporates into an RH of 58% than the droplet that evaporates into the higher RH (86%). In fact, their final equilibrated radii are observed to have been corrected by ~300 nm and ~150 nm, respectively (inset in Figure 5.6).

5.2.4 Temperature and RH Control in the C-EDB

Since the confined droplets are very tightly trapped within the C-EDB electrodynamic field, a gas flow can be introduced into the trapping cell and it can be used to regulate the RH and temperature conditions experienced by the evaporating droplets.

A single droplet is confined in a nitrogen gas flow (BOC, oxygen free), which results from the mixing of wet and dry N_2 flows. The wet flow is generated by forcing a dry N_2 flow through a humidifier composed of a sealed vessel containing distilled water, resulting in a gas flow that is saturated with respect to water vapour (wet flow). In this way, a nitrogen flow with RH close to saturation leaves the humidifying vessel and it is then mixed at a desired ratio with the other dry N_2 flow. The mixing ratio of the wet and dry flows are varied using two mass flow controllers (MKS 1179A, operated by means of a MKS 247D power supply), allowing control of the gas phase relative humidity within the trapping cell.

In the C-EDB experimental setup, the gas flow can be introduced in the trapping chamber either as a sheath flow, which passes through the inner and outer electrodes, or as a jet flow, which goes through the inner electrode. All the measurements taken in this work were performed using a sheath flow from the bottom electrodes and operated at a flow rate of 50 or 200 sccm (corresponding to gas velocities of 1 and 3 cm s^{-1}, respectively). The reason behind the preferable use of the sheath flow is that it results in more rigorously defined RH conditions within the chamber than the jet flow, because it requires a higher flow rate to produce a flow with the same gas velocity.

The RH in the C-EDB trapping chamber is measured by observing the evaporation kinetics of probe droplets (either pure H_2O or NaCl solution droplets). The RH determination procedure and the experimental uncertainties associated to it are fully described in Section 6.1.1. If compared to commercial RH probes, this comparative

approach results in smaller associated uncertainties, which is extremely important for the determination of growth curves (Section 6.1.3) for values close to saturation. In fact, the uncertainty in RH for commercial RH probes is typically between ±1% and ±5% in the RH range 10-90%, increasing for RH values above 90%.

In addition, the temperature of the gas phase within the trapping chamber is controlled by recirculating a mixture of water and ethylene glycol (50% v/v) from a thermostatic refrigerated/heating circulator (Julabo, F32-HE) through the lid and the bottom of the octagonal chamber. The accessible temperature range of the circulator goes from -25 to 50 °C, but in this study all the measurements were performed at 20 °C.

5.3 Summary

In this chapter, the Cylindrical Electrodynamic Balance setup used in this word has been described together with all the operations needed for the generation, the trapping and the accurate optical sizing of droplets. The most relevant benefit deriving from the concentric cylindrical geometry of the electrodes is that the generated electrical field within the trapping chamber is strong and is characterised by a steep gradient in correspondence to its centre. This allows single droplets to be trapped steadily in a controlled nitrogen flow right after their generation and it represents an essential feature of the C-EDB experimental setup because, together with the double dispensers setup, it makes the comparative kinetics measurements described in Chapter 6 possible. The two sizing procedures that are used to keep track of the radius variation of a trapped droplet were described. The simplified geometrical optics approach was routinely used for the real-time sizing of trapped droplets, whereas the fitting of full phase functions was used just for the long trapping measurements presented in Section 7.1.6. The post-acquisition procedure used to take into in account the variation of the refractive index of evaporating droplets for an accurate determination of their radius with the geometric optics approximation was described.

In Chapter 6, the comparative evaporation kinetics technique for the quantification of the equilibrium hygroscopic properties of aerosol droplets using the C-EDB setup described here is presented. The comparative kinetics approach will also be validated with measurements on well-characterised binary and ternary mixtures of atmospherically –relevant inorganic compounds.

Chapter 6 Measuring Aerosol Hygroscopic Properties over a Wide Range of RH with Comparative Kinetics Experiments

In Section 2.2, it was discussed how current aerosol thermodynamic models could benefit from improved representations of the hygroscopic properties of aerosol systems containing organic components and their mixtures with inorganic electrolytes, in order to better simulate the water uptake by atmospheric aerosol particles. Single particle techniques are a powerful tool for the investigation of fundamental chemico-physical properties of aerosols (such as vapour pressures, hygroscopic growth, phase transitions and phase separations, etc.[21]) and can provide laboratory data for the parameterisation of these properties in aerosol thermosynamics models.

In this Chapter, the determination of equilibrium hygroscopic properties of aerosols, collected from comparative evaporation kinetics experiments in a Cylindrical Electrodynamic Balance, is fully described. This approach is defined 'comparative' since the evaporation rates of probe aerosol droplets containing reference compounds are compared to those measured for sample aerosol systems of which the hygroscopic properties need to be determined.

The proposed experimental technique employs the literature kinetic model by Kulmala et al. (1993)[145] (Section 2.3) and it lays its foundations in the work of Davies et al.[96,144]. A previously developed method was expanded in order to cover a wider water activity (a_w) range, from 0.5 to >0.99[96]. The proposed approach is discussed with respect to the limitations of the applied kinetics model in the representation of the vapour pressure of water as a function of the evaporating droplet temperature and their implications on the determination of the hygroscopicity of aerosol systems are shown. This experimental technique involves the combination of multiple datasets from different comparative kinetics experiments performed at different RHs for the determination of hygroscopic

properties over the investigated water activity range. The calculations needed for the retrieval of hygroscopic growth curves from the radial evaporation profiles of single droplets are described in detail, as well. Finally, the proposed methodology is validated by the comparison of the experimentally determined hygroscopic properties of binary and ternary mixtures of well characterised inorganic compounds and simulations from the Extended Aerosol Inorganics thermodynamic model(E-AIM)[100,194].

6.1 Comparative Kinetics Measurements

The mass and heat transport model presented in Section 2.3 is used to compare the evaporation kinetics of probe and sample droplets and estimate aerosol hygroscopic growth curves as follows.

The raw output of a typical comparative kinetics experiment is shown in Figure 6.1. It consists of a sequence of the alternating evaporation profiles (radius vs. time plots) of probe (black) and sample (red) droplets. As mentioned in the previous Chapter, probe droplets are well-characterised aerosol systems that can be used as a reference for the determination of the relative humidity of the gas phase within the EDB trapping chamber. The probe droplet can be either pure water or a NaCl solution with known concentration (in Figure 6.1, pure water is used as a probe). Davies et al.[96] demonstrated the validity of both methods for the determination of the RH in this kind of comparative kinetics measurements and also estimated the errors on the RH retrieved in both cases (Section 6.1.1).

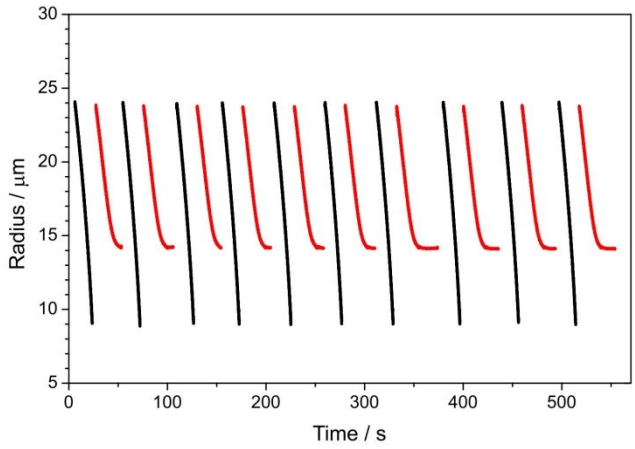

Figure 6.1: Example of a sequence of probe (black, water) and sample (red) droplets in a comparative kinetics experiment.

In a first post-acquisition step, the measured radii data need to be corrected in order to account for the varying refractive index of the evaporating droplets, as described in Section 5.2.3. Subsequently, for each pair of probe and sample droplets, the probe droplet evaporation profile is analysed using the kinetics model by Kulmala et al. (1993)[145] to determine the gas phase RH.

In order to do this, the kinetics model by Kulmala et al. (1993)[145] needs to be modified to account for the experimental conditions that characterise the evaporation experiments in the C-EDB, according to Davies (2014)[144]. The applied corrections take into account the presence of charges on the evaporating droplet[247] and the Kelvin effect (Section 2.1.3). The latter correction is applied even though the Kelvin effect for the droplets considered in this work (a>5 µm) is negligible, as discussed in Section 2.1.3. Both the Kelvin effect and the charge on the droplet modify the effective vapour pressure at the surface of the droplet and to take this effect into account, the expression in Eq. 6.1 for the effective vapour pressure of water ($S_{w,a}{}'$) is introduced in the model by Kulmala et al. (1993)[145].

$$S_{w,a}{}' = S_{w,a} exp\left(\frac{2\sigma V_{mol}}{RTa} - \frac{q|p|}{4\pi a^2 \epsilon_0 k_B T}\right) \qquad 6.1$$

In Eq. 6.1, the first term is essentially the Kelvin equation (Eq. 2.10) and the second term[247] takes into account the reduction of the effective vapour pressure caused by the presence of charge (q) on the droplet. $|p|$ is the dipole moment of the evaporating molecule, ϵ_0 is the vacuum permittivity and k_b is the Boltzmann constant.

A further correction is necessary because the single levitated droplets in the C-EDB sit in a nitrogen gas flow. The mass transfer enhancement resulting from the flowing gas surrounding the droplet is accounted for by the inclusion of a Sherwood number (Sh) scaling of the mass flux[142,248]. The resulting expression for Kulmala et al. (1993)[145] kinetics model modified as just described is shown in Eq. 6.2.

$$I = -2Sh\pi a\left(S_{w,\infty} - S_{w,a}{}'\right)\left[\frac{RT_\infty}{M_w D_w \beta_M p_w^0(T_\infty) A} + \frac{S_{w,a}{}' L_w^2 M_w}{KR\beta_T T_\infty^2}\right]^{-1} \qquad 6.2$$

Eq. 6.2 can be rearranged and solved for $S_{w,a}{}'$ in order to calculate the water activity in the droplet at each point in time during evaporation, remembering that the saturation vapour pressure of water is equal to the water activity in the droplet solution (Section 2.1.2):

$$a_w = \left[S_{w,\infty} - \frac{IRT_\infty}{2Sh\pi a M_w D_w \beta_M p_w^0(T_\infty) A}\right]\left[\frac{IL_w^2 M_w}{2Sh\pi aKR\beta_T T_\infty^2} + 1\right]^{-1} \qquad 6.3$$

The solution of this equation is possible because the particle radius is measured, $S_{w,\infty}$ is determined from the probe droplet and the mass flux I can be calculated from the collected radius versus time plot (as described in the following paragraph), while all the other quantities are known.

In Section 6.1.1 and 6.1.2 the application of the modified evaporation kinetics model (Eq. 6.2 and 6.3) for the calculation of the gas phase RH from probe droplets and for the retrieval of the equilibrium hygroscopic properties from samples droplets are described.

6.1.1 Retrieving the RH from Probe Droplets

Figure 6.2, presents simulated evaporation profiles for pure water (Panel A, both in terms of a^2 vs. time and a vs. time in the inset) and NaCl solution droplets (Panel B) corresponding to variable relative humidity in the gas phase and calculated by means of Eq. 6.2. With respect to pure water (Panel A), the radius-squared profiles are linear plots with a decreasing slope as the gas phase RH decreases; if the NaCl curves (Panel B) are considered, the evaporation of water is faster the lower the surrounding RH, as in the case of pure water droplets, and the equilibrated droplet radius depends on the RH, as well.

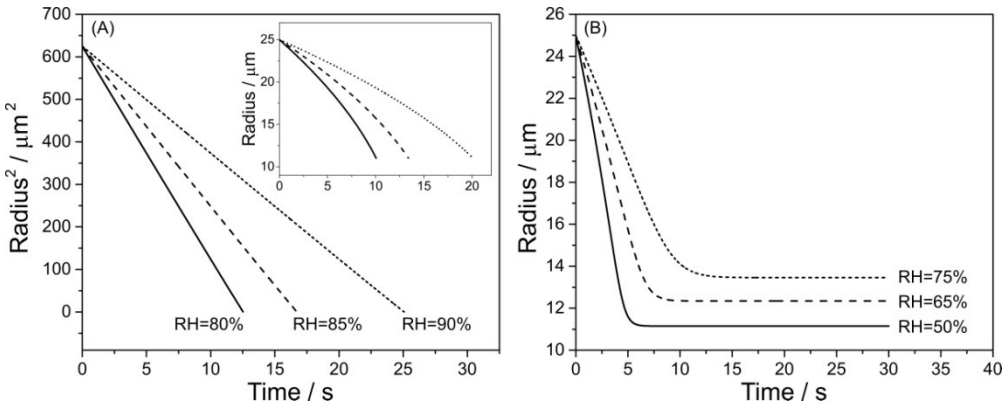

Figure 6.2: Modelled evaporation profiles for pure water and for NaCl solution droplets at variable surrounding RH.

When a pure water droplet is used as a probe, its experimental radius-squared versus time evaporation profile is compared to simulated evaporation curves at different RH, calculated using Eq. 6.2. The mean squared difference (MSD) between the experimental profile and each calculated curve is estimated and the RH corresponding to the curve

with the lowest MSD is selected. In this case, the lower and upper values of the RH come from uncertainties in the thermophysical parameters D (±6%) and K (±2%)[143] in Eq. 6.2 and are given by:

$$RH = RH_w{}^{+(0.169RH_w{}^2-0.364RH_w+0.194)}_{-(-0.020RH_w+0.021)} \quad 6.4$$

When a NaCl solution with known initial concentration is used as a probe, the equilibrated size of the droplet after water evaporation may be used to determine the water activity in the solution, and therefore the RH in the gas phase (according to Section 2.1.2). In order to do this, the thermodynamic Extended Aerosol Inorganics Model (E-AIM, Section 2.2)[100,194] is used to calculate how water activity and density change with the solution composition during evaporation and to predict the equilibrated radius of the droplet after water evaporation has ended at a given RH. The lowest RH value that can be determined with this method is limited by the crystallisation RH of NaCl, which is reported in the RH range 43-50%[87]. In theory, if a different reference compound that crystallises at a lower RH and for which a_w and density variations as a function of solute concentrations are well characterised was used as a probe, this comparative technique could be potentially pushed to the measurement of hygrocopity in the lower water activity region.

If this equilibrated size method is used, the uncertainties in RH arise from the accuracy with which the equilibrated radius is known (±100 nm) and the uncertainty in the determination of the initial droplet size at t=0 s ($^{+150}_{-100}$ nm), which corresponds to an uncertainty of less than 0.8% on the dry radius for the droplet sizes considered in this work. In this case, the lower and upper values of the RH are expressed as:

$$RH = RH_{eq}{}^{+(-0.0175RH_{eq}{}^2-0.0005RH_{eq}+0.017)}_{-(-0.0266RH_{eq}{}^2+0.0086RH_{eq}+0.017)} \quad 6.5$$

Figure 6.3 shows the absolute uncertainties on the solution a_w deriving from using both pure water (blue) and an NaCl solution droplet as a probe (orange) calculated from Eq. 6.4 and 6.5 as a function of the gas phase RH. Using a pure water droplet as a probe of RH is preferable as the equilibrated size method includes a further uncertainty from the initial NaCl solution concentration. Nevertheless, NaCl was used as a probe for measurements at RH<80% since the associated uncertainties on the RH determined with water in this range as a probe droplet would be too significant, as shown in Figure 6.3. In fact, uncertainties on the simulation of pure water evaporation become increasingly large below this RH value due to uncertainties in the thermophysical parameters D and K[143] and because of the approximation in the expression of the vapour pressure of water at the droplet surface (discussed further in Section 6.2).

According to Eq. 6.4, the RH can be determined with an uncertainty smaller than $^{+0.33\%}_{-0.3\%}$ for RH values above 90% when pure water is used as a probe. At 50% RH, the error associated with the determination of RH with the equilibrated size method is $^{+1.2\%}_{-1.5\%}$, according to Eq. 6.5. Knowing the RH with such a high accuracy is crucial for an accurate application of the kinetics model presented in Section 2.3. The uncertainty of commercial RH probes is typically between ±1% and ±5% in the RH range 10-90% and it usually dramatically increases for RH values above 90%. Both the methods used in this work to retrieve the gas phase RH are associated with smaller uncertainties in the RH determination, especially for measurements at high RH. The RH of the gas phase in the EDB trapping chamber is kept constant during the evaporation measurements, but slight fluctuations in RH can sometimes be observed. However, the RH is monitored with probe droplets during the entire duration of the experiments (5-15 minutes for ten pairs of sample and probe droplets, depending on the RH at which the measurements are taken) as shown in Figure 6.1 and the magnitude of these fluctuations is typically smaller or comparable to the uncertainty associated with the RH determination (<0.2-0.3% above 80% RH with water as a probe, <0.5-0.6% below 80% RH with NaCl as a probe).

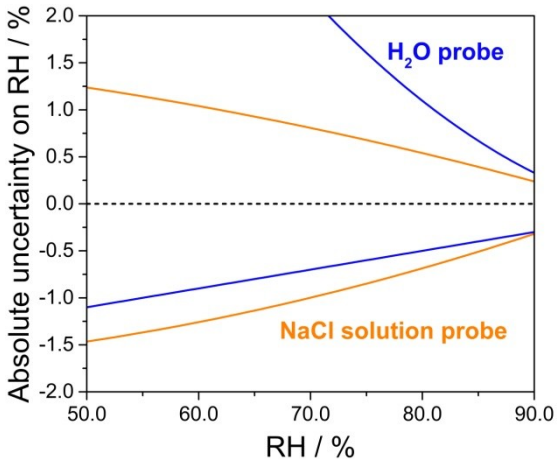

Figure 6.3: Absolute error on RH calculated from Eq. 6.4 and 6.5 for water (blue) and an NaCl solution (orange) used as a probe.

6.1.2 Calculating Hygroscopic Growth Curves for Sample Aerosol Droplets

Once the gas phase RH is known, the evaporation kinetics model by Kulmala and co-workers (1993)[145] (Eq. 6.3) can be applied for the interpretation of the evaporation profiles of sample droplets and used to calculate the variation of water activity within

the droplets solution, as follows. All the operations needed for the retrieval of hygroscopic growth curves from evaporation profiles collected in comparative kinetics experiments are summarized in Figure 6.4 and described below.

For the calculation of mass flux (J), the radii data need to be converted to particle mass values and the density of the droplet is thus needed. In order to perform this conversion, a polynomial parameterization of density as a function of square-rooted mass fraction of solute is used, as discussed in Section 5.2.3. The initial solute *mfs* at $t = 0$ s is known from the prepared solution and the initial droplet density can be determined. Therefore, considering the measured variation in volume due to the evaporation of water, the *mfs* and density for every measured point during evaporation can be calculated. Knowing how the mass of the droplet varies in time, the mass flux ($J=dm/dt$) can be calculated as the slope of the mass versus time calculated curve and Eq. 6.3 can be used to determine how the a_w varies in the droplet with time. Over each time-step, the droplet is considered homogeneous in composition with the diffusional mixing time estimated to be 0.01 s for a droplet with a radius of 15 µm, assuming a water diffusion coefficient of $2 \cdot 10^{-9}$ m^2 s^{-1}.

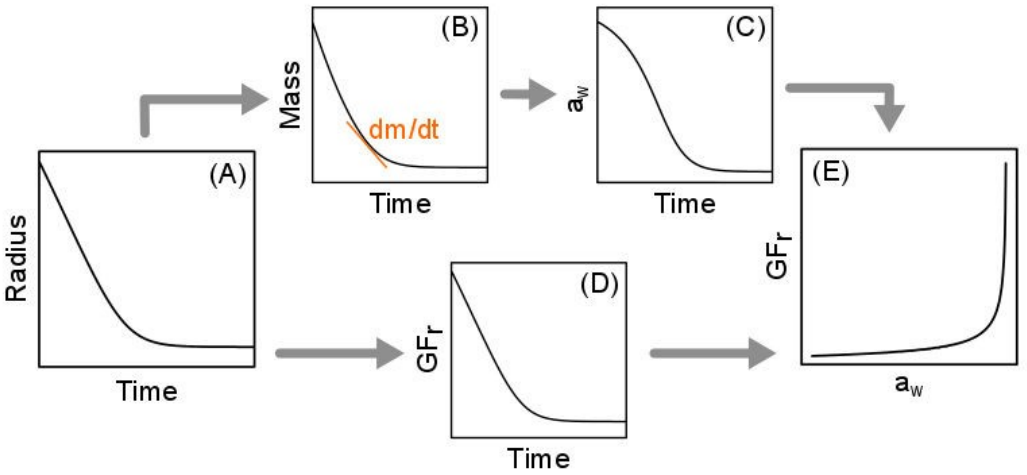

Figure 6.4: Retrieval of hygroscopic growth curves from evaporation profiles. The radius vs. time curve (A), corrected for the variable solution m, is converted to mass (B), thanks to a parameterisation of density. The mass flux can be calculated as dm/dt and it is used with Eq. 6.3 to calculate the variation of the aw in the evaporating droplet (C). From the radii data, GF_r vs. time can also be calculated (D) and coupled with plot (C) to calculate the final growth

In addition, from the measured radii data and knowing the density of the droplet at each instant, radial growth factors (GF_r) can be calculated; the radius of the reference dry state is estimated from the initial solution concentration, the initial radius of the droplet

(a_0) and considering the dry density of the solute. In addition, the moles and mass of water and solute can be calculated for each measured radii during the evaporation of the sample droplet. Coupling these quantities with the information about the solution water activity, hygroscopicity curves for the sample compounds can be plotted as GF_r vs. a_u, n_{water}/n_{solute} vs. a_w, mfs vs. a_w and osmotic coefficients (Section 2.1.5).

6.1.3 Experimental Uncertainties, Reproducibility and Averaging Data from Multiple Droplets

For a rigorous determination of hygroscopic properties from comparative kinetics experiments in a C-EDB, all the experimental uncertainties associated to each of the computed quantities need to be taken into account. These arise mainly from the uncertainty in the determination of a_0 and of the droplets radius during the evaporation (Section 5.2.2), of the RH determined from the probe droplets (Section 6.1.1) and in the concentration of the initial solution. They are all summarised in Table 6.1 and, whenever one of these quantities is plotted in the following Sections in this work, the error bars were calculated by propagating all these experimental uncertainties.

Note that no uncertainties on the density and refractive index parameterisations (Section 5.2.3) used for the data treatment are taken into account in the routine calculation of the experimental uncertainties of the measured hygroscopic properties. They are assumed to be reliable for the common inorganic compounds used for the determination of the method accuracy in this Chapter and in Section 7.1.5 they are discussed separately for the class of aminium sulphates.

The reproducibility of comparative kinetics experiments is very good. Figure 6.5 shows the reproducibility of the hygroscopic growth curves expressed in terms of n_{water}/n_{solute} vs. a_w obtained from the evaporation of ten different NaCl droplets belonging to a single dataset like the one in Figure 6.1 (initial solute mass fraction of 0.005, RH=88.7%), compared to calculations from E-AIM Model (grey line). Pure water droplets were used as a probe for the retrieval of NaCl hygroscopic properties in Figure 6.5. The reproducibility of the obtained growth curves is very good and the agreement of the results with the model prediction is extremely satisfactory, as well. If the inset in Figure 6.5 is observed, the maximum discrepancy between growth curves resulting from different droplets is smaller than 0.002 in water activity at a_u~0.993, which is smaller than the uncertainties resulting from the calculation of the uncertainty on RH from Eq. 6.4 ($88.7\,^{+0.4}_{-0.3}\%$).

Because of this, the averaging of data obtained from multiple droplets is legit in order to obtain more robust hygroscopicity data from these comparative kinetics measurements. To average the growth curves calculated from the evaporation of multiple droplets, all the obtained GF_r, n_{water}/n_{solute} and mfs values from at least 10 sample droplets within a dataset are separated into a_w bins (0.03-0.005 a_w intervals, depending on the RH at which the measurements are taken) and the data points attributed to each bin are then averaged. The final averaged curves for each compound will be presented in the following Sections, unless otherwise specified.

Quantity	**Formula**	**Uncertainties**
Radial GF	$GF_r = \frac{a}{a_{dry}}$	- a: ±100 nm[144], <1% for droplets bigger than 10 µm (with Geometrical Optics Approximation, Section 5.2.2.1). - a_{dry}: uncertainty on the initial radius extrapolation at t$_0$ ($a_{dry}{}^{+150\ nm}_{-100\ nm}$); uncertainty on the initial solution concentration.
Mass fraction	$mfs = \frac{m_{solute}}{m_{tot}}$	- m_{solute} (dry mass from the concentration at t$_0$): $a_{dry}{}^{+150\ nm}_{-100\ nm}$; uncertainty on the initial solution concentration. - m_{tot}: uncertainty from radius determination.
Mole curves	$\frac{n_{water}}{n_{solute}}$	- n_{water}, calculated from $m_{water} = m_{tot} - m_{solute}$ (see uncertainties indicated for mfs).
Osmotic coefficient	$\phi_{st} = \frac{-\ln(a_w)}{(m_{st} \cdot M_w/1000)}$	- a_w: uncertainty from RH determination in the EDB measurements[96] - RH>80% (water used as a probe): Eq. 6.4 - RH<80% (NaCl used as a probe): Eq. 6.5 - m_{st} (stoichiometric molality): uncertainties on n_{solute} and m_{water} (see uncertainties indicated for mfs and for n_{water}/n_{solute}).

Table 6.1: List of all the uncertainties taken into account for the calculation of the most relevant quantities retrieved from comparative kinetics measurements.

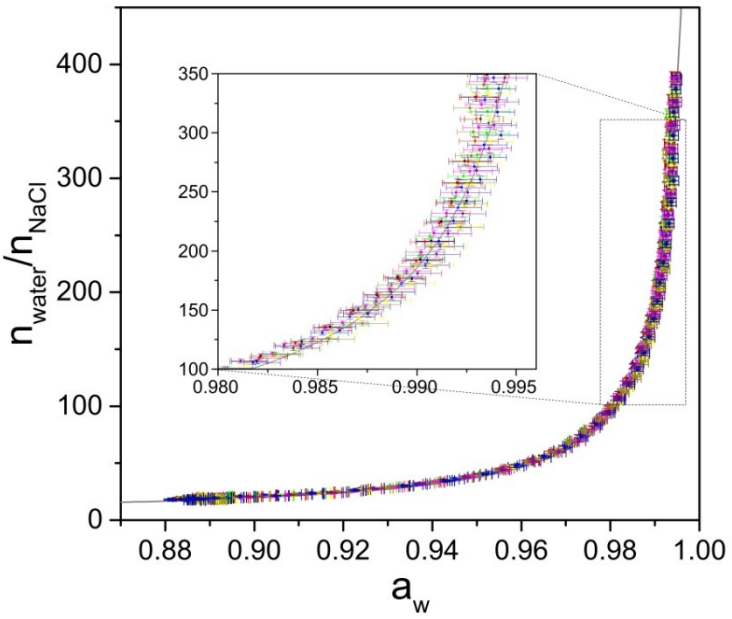

Figure 6.5: Reproducibility of n_{water}/n_{solute} growth curves obtained for NaCl from the evaporation of 10 different droplets (initial *mfs* of 0.005, RH=88.7%), each represented with a different colour.

In order to take into account the uncertainty (σ_i) of each experimental data point (k_i), calculated as described in Section 6.1.3, the average value ($\bar{k}$), the internal and external standard deviations (σ_{int} and σ_{ext}) for each of the quantity of interest were calculated as follows[249]:

$$\bar{k} = \frac{\sum_i (k_i/\sigma_i^2)}{\sum_i (1/\sigma_i^2)} \quad 6.6$$

$$\sigma_{int} = \sqrt{\frac{1}{\sum_i (\sigma_i^{-2})}} \quad 6.7$$

$$\sigma_{ext} = \sqrt{\frac{\sum_i (\sigma_{int}/\sigma_i)^2 \cdot (k_i - \bar{k})^2}{(n-1)\sum_i (\sigma_{int}/\sigma_i)^2}} \quad 6.8$$

The final average data are then reported according to Eq. 6.9:

$$k = \bar{k} \pm t_{0.99} \cdot \sigma \quad 6.9$$

where σ is the highest value between σ_{int} and σ_{ext} and $t_{0.99}$ is the t-student test value at 99% probability.

6.2 Effect of the Temperature Depression of Droplets during Evaporation

A series of seven $(NH_4)_2SO_4$ solution droplets evaporating into different RHs at 20°C are shown in Figure 6.6-A over the range from 50% to 85% RH. The initial mass fraction of the starting solution was 0.05 and the initial radii of the seven different droplets varied from 23.0 µm to 23.3 µm. The total amount of water that evaporates from each droplet depends on the gas phase RH and the final equilibrated radius is such that the a_w in the droplet matches the RH in the surrounding gas phase. The evaporation rate increases with decreasing RH since the mass flux is proportional to the difference between the solution water activity and the RH (Eq. 6.2). As shown in Figure 6.6-B, the mass flux is at its highest value for every droplet at the beginning of the evaporation, because $S_\infty - a_w$ is at its maximum. Over time, the evaporation slows down and the mass flux decreases until the droplet is in equilibrium with the gas phase and I is zero. The evaporation time to reach equilibrium extends from 5 s at 50% RH to about 25 s at 85% RH.

The mass transport of water from the droplet to the gas phase during evaporation is coupled to heat transfer, with the latent heat of vaporisation associated with this phase change removed from the droplet. The heat flux from the droplet is greatest when the evaporation rate of water is fastest and, when it is not balanced by the heat flux from the surrounding environment to the droplet, the condensed phase cools down. This temperature depression of the droplet has to be taken into account because the vapour pressure of water at the surface of the droplet is temperature dependent and directly influences the evaporation rate. In the derivation of the kinetics model of Kulmala and co-workers[145] (Eq. 6.3), the dependence of the vapour pressure of the evaporating species at the droplet surface (p_a) on temperature is calculated from the Clausius-Clapeyron equation. The exponential term in this expression is approximated with the first order term in a Taylor series expansion:

$$p_a = a_w p^0(T_{gas}) \exp\left(\frac{LM\left(T_{droplet} - T_{gas}\right)}{RT_{droplet}T_{gas}}\right) \approx a_w p^0(T_{gas})\left(1 + \frac{LM\left(T_{droplet} - T_{gas}\right)}{RT_{droplet}T_{gas}}\right) \quad 6.10$$

where $p^0(T_{gas})$ is the saturation vapour pressure at the temperature of the gas phase (T_{gas}) and $T_{droplet}$ is the temperature at the droplet surface.

This approximated expression for the temperature dependence of the vapour pressure of water is only accurate when the difference between the droplet and gas phase temperatures is less than ~3°C; beyond this threshold value the approximation with the

Taylor series expansion results in an underestimation of the value of the exponential bigger than 1% at 25°C[145], with a subsequent underestimation of p_a. Consequently, when the droplet temperature depression is large the vapour pressure of water at the surface of the droplet is increasingly underestimated. Therefore, the only measured points that can be used to reliably calculate the water activity in the evaporating sample droplet are those that satisfy this condition. $T_{droplet} - T_{gas}$ can be estimated according to Eq. 6.11[145]:

$$T_{droplet} - T_{gas} = -\frac{IL}{4\pi\beta_T Ka} \qquad 6.11$$

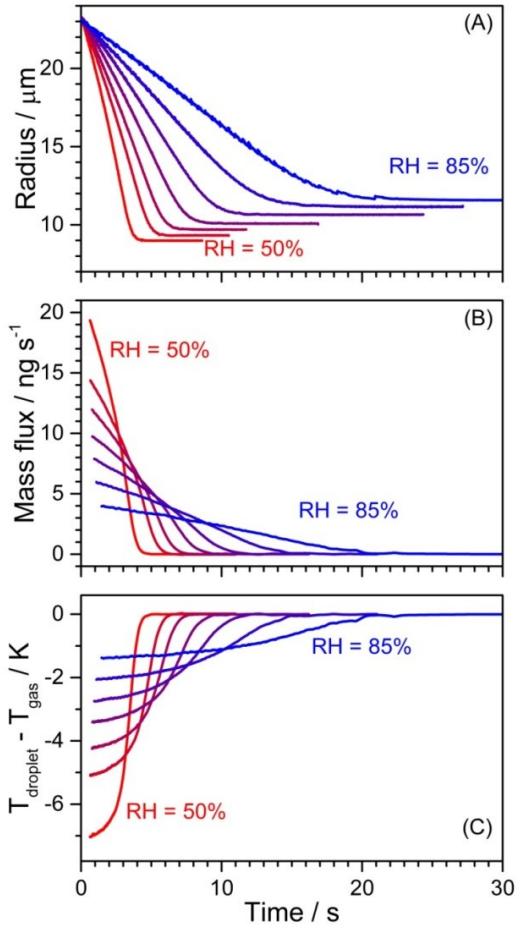

Figure 6.6: (A) Measured radii (µm) of seven $(NH_4)_2SO_4$ solution droplets (initial *mfs* of 0.05) evaporating into different RHs (increasing from 50% to 85%, from red to blue) at 20°C. (B) Calculated mass flux (ng s^{-1}) vs. time, for the same droplets. (C) Variation in time of $T_{droplet} - T_{gas}$, calculated according to Eq. 6.11.

Figure 6.6-C shows the time dependence of the calculated $T_{droplet} - T_{gas}$ for the same seven $(NH_4)_2SO_4$ droplets as in the two previous panels. The initial temperature depression can reach -7 K in correspondence to the fastest evaporation rates (at 50% RH), while for the three droplets evaporating into a higher RH (about 78%, 81% and 85%, respectively) the calculated temperature depression is always less than 3 K. The measured and modelled evaporation profiles and mass flux variation in time are compared in Figure 6.7 for two of the droplets analysed in Figure 6.6. For the droplet evaporating into RH=85%, Eq. 6.3 is able to accurately model the evaporation kinetics of water from the ammonium sulphate solution because the 3 K threshold is not exceeded, and the agreement between the modelled and measured curves is excellent (Panels A-B). In the case of the second considered droplet, which is evaporating at RH=55%, the modelled mass flux is highly overestimated by the kinetics model at the beginning of the evaporation (Figure 6.7-D), because the estimated p_a is underestimated because of the approximation introduced in Eq. 6.10. Consequently, also the modelled evaporation profile in Figure 6.7-C does not match the measured curve.

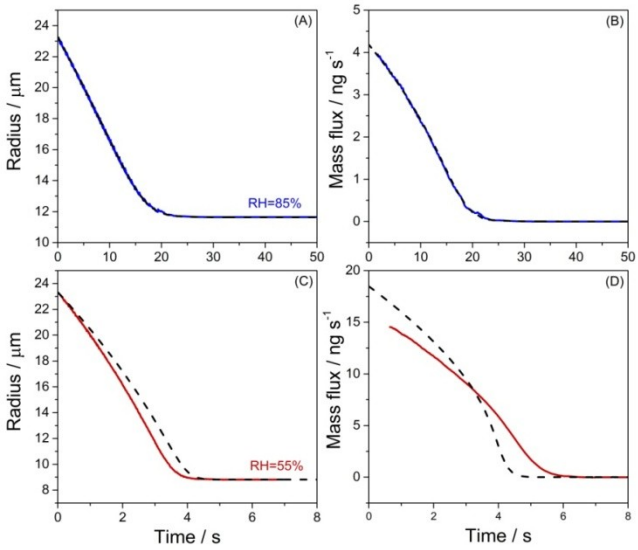

Figure 6.7: Comparison of the experimental (solid lines) and modelled (dashed lines) of the radius vs. time evaporation profiles and of the mass flux time-dependency for two of the $(NH_4)_2SO_4$ droplets in Figure 6.6, at RH=85% (Panels A-B) and RH=55% (Panels C-D).

The effect of the droplet temperature depression on the estimated hygroscopic behaviour of a sample compound retrieved from the measurements is shown in Figure 6.8. Panel A presents the *mfs* versus a_w relation obtained from a dataset of ten $(NH_4)_2SO_4$ droplets evaporating at 58% RH. A very good agreement with the E-AIM Model prediction can be observed for low a_w values, both for the averaged curve

and for all the ten single droplets. For higher a_w values, which are derived from the measurements of fluxes at early evaporation times, the water activity calculated with Eq. 6.3 is overestimated and even leads to unrealistic values beyond 1. This issue arises because the corresponding droplet temperature depression (Figure 6.8-B) is larger in magnitude than the -3 K threshold, which is satisfied only below a calculated a_w of 0.73. The absolute error on the calculation of a_w is shown in Figure 6.8-C. This a_w error was calculated as the difference between the experimental a_w calculated with Eq. 6.3 and the water activity calculated with the E-AIM Model at a certain *mfs* value. For the averaged data, the absolute errors on the calculated a_w are very close to 0 at a_w values below 0.73, while they reach values up to about 0.06 when $T_{droplet} - T_{gas}$ is of the order of -5 to -6 K.

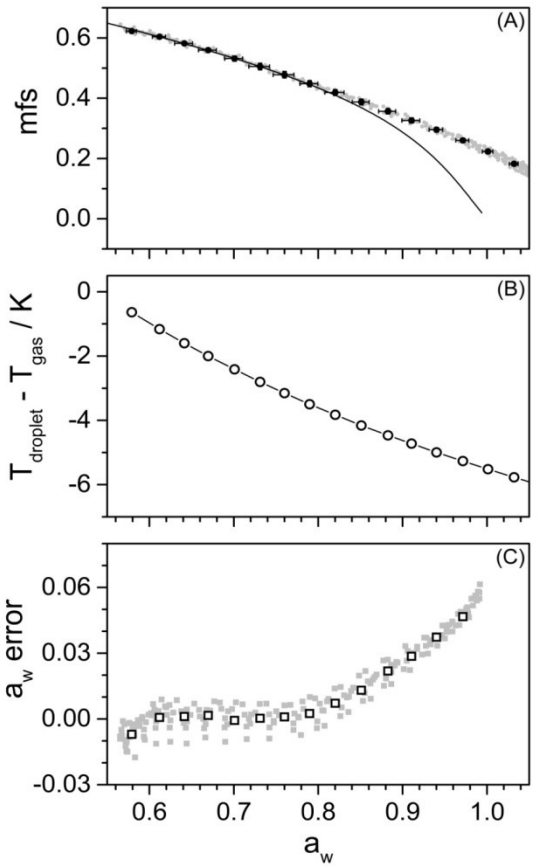

Figure 6.8: (A) *mfs* vs. a_w from the evaporation kinetics of 10 $(NH_4)_2SO_4$ droplets (RH=58%). Symbols: grey dots –data from individual droplets; black dots – averaged curve; solid black line – calculation from E-AIM Model. (B) Variation of $T_{droplet} - T_{gas}$, calculated according to Eq. 6.11, as a function of a_w. (C) Absolute error between the experimental and modelled a_w. Symbols: grey squares – single droplets; open squares –averaged curve.

6.3 Full Hygroscopicity Curves from Droplets Evaporating into Different RHs

As a consequence of the limitation of the kinetics model when used to interpret the evaporation of sample droplets in the EDB discussed in Section 6.2, only a portion of about 20% RH of the *mfs* curve of a sample compound can be retrieved when measurements are taken into an RH at 50%. As a consequence, evaporation measurements into at least three different RHs need to be performed in order to measure a full curve from 0.5 to >0.99 a_w. An example of this procedure is shown in Figure 6.9 for the determination of the relation between a_w and *mfs* for $(NH_4)_2SO_4$, in which C-EDB results are compared to the E-AIM Model prediction (solid black line).

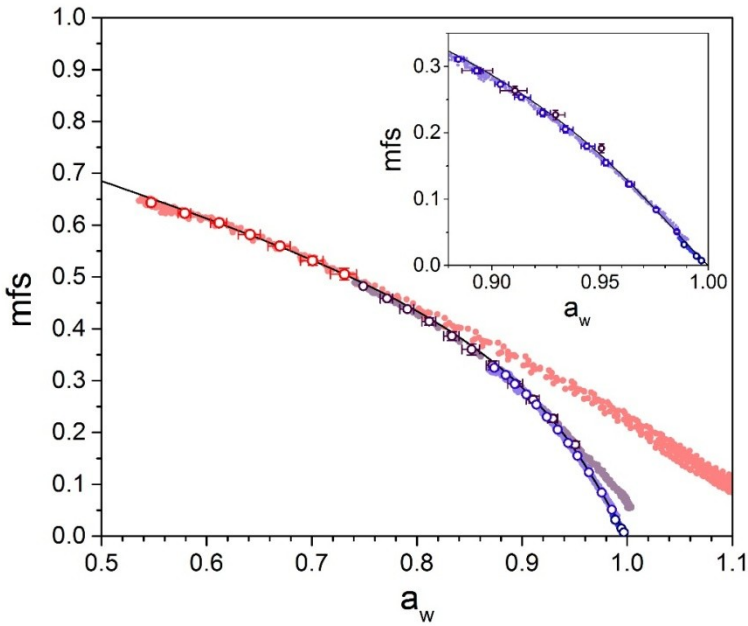

Figure 6.9: full *mfs* vs. a_w curve of ammonium sulphate from measurements into different RHs. Symbols: black line – calculation from E-AIM Model; solid circles – individual data from all 10 droplets in each data set; open circles – averaged data for which the maximum 3 K droplet temperature depression condition is satisfied. Colours: red, purple and light blue – 0.05 *mfs* starting solution, gas phase 54%, 74% and 87.3% RH, respectively; dark blue – 0.005 *mfs* starting solution, gas phase 90% RH. Note: error bars are smaller than the data point when not shown.

Evaporation measurements with a starting solution of ~0.05 *mfs* were made into three different RHs (54%, 74% and 87.3%). A fourth dataset was collected at high RH (90%,

more clearly visible in the inset in Figure 6.9) using a solution with lower starting concentration (*mfs* of 0.005) and therefore with a higher starting a_w (0.997). In this latter case, just a very small section of the *mfs* curve can be calculated: since the droplet had a very low initial concentration, it was not possible to keep it trapped until its a_w equilibrated with the surrounding RH, as it undergoes an exceptionally large size change. The open circles represent data points averaged over ten droplets and have been considered acceptable only if the difference in temperature between the droplet and the gas phase is estimated to be smaller than the 3 K limit. In the background, data for all the ten droplets in the same four datasets are shown. All the data points can be accepted for the two datasets measured at high RH, with the evaporation sufficiently slow to maintain a low droplet temperature depression, while just small portions of the data measured at 54% and 74% RH can be accepted. The agreement with the a_w vs *mfs* curve calculated with the E-AIM Model is very good for the points that lie within the 3 K threshold for the droplet temperature depression.

One of the interesting features of the comparative kinetics measurements in the C-EDB is that hygroscopic growth curves can be measured up to very high a_w values (>0.99). In Figure 6.10, the very high end for the measured GF_r, n_{water}/n_{solute} and *mfs* versus water activity plots are shown for $(NH_4)_2SO_4$, and are compared with simulations from the E-AIM Model (grey solid lines). In this case, the highest a_w reached with this averaged dataset is 0.997, corresponding to a GF_r value of 6.22 (Figure 6.10-A). For the calculation of the radial growth curve, the dry radius of the droplets is calculated from the wet size at $t = 0$, the concentration of the starting solution and the density of crystalline ammonium sulphate (1.77 g cm^{-3})[246]. In Figure 6.10-B, at $a_w = 0.997$ the number of absorbed moles of water per moles of $(NH_4)_2SO_4$ inferred from the measurements is close to 1000 and the agreement between the measured value and the E-AIM Model prediction is quantitative. If the *mfs* vs. a_w plot is considered (Figure 6.10-C), the lowest measured ammonium sulphate mass fraction is 0.005 at $a_w = 0.997$. It is also worth noting that with this technique not only is it possible to measure growth curves up to very high water activity values, but also that the accuracy on the calculated a_w is highest when the RH at which measurements are taken is high (>90%), according to Eq. 6.4 and 6.5 and as shown in Figure 6.3. It should also be stressed that the growth curve is retrieved in a matter of seconds, potentially allowing accurate hygroscopic growth measurements for droplets containing semi-volatile components, provided their vapour pressure is less than that of water.

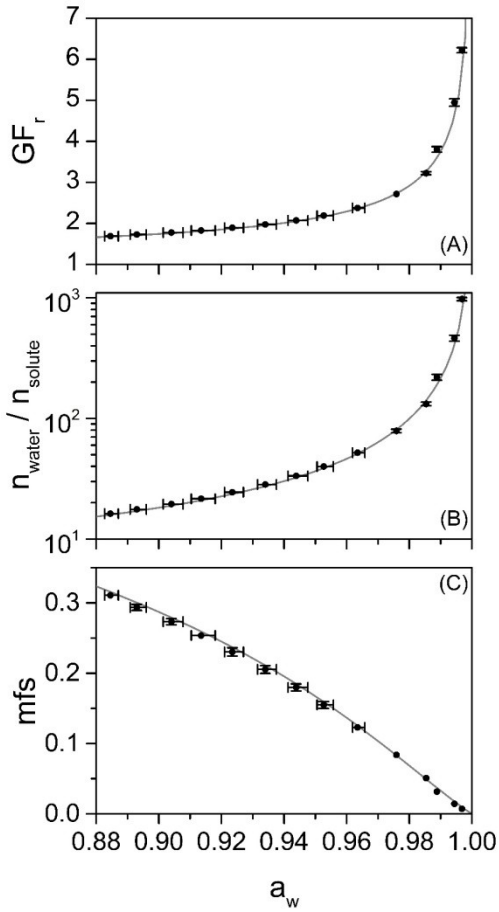

Figure 6.10: GF_r, n_{water}/n_{solute} and mfs for a_w values between 0.88 and 1 are shown for $(NH_4)_2SO_4$. Symbols: black circles – experimental data points averaged over a minimum of 10 droplets; solid grey lines – calculated curves from the E-AIM Model. Note: error bars are smaller than the data point when not shown.

6.4 Testing the Experimental Method with Well Characterised Aerosol Systems

The experimental technique proposed in Sections 6.1 and 6.3 is tested with binary mixtures of four well-characterised inorganic compounds (NaCl, Na_2SO_4, $NaNO_3$ and $(NH_4)_2SO_4$, Section 6.4.1) and water. The hygroscopic properties obtained for these compounds over the 0.5 to 0.99 a_w range have been compared to predictions from E-AIM Model, in order to demonstrate the effectiveness of the C-EDB comparative kinetics

method in accurately representing the hygroscopicity of well-known inorganic aerosol systems. In addition, the same comparison was performed for ternary mixtures of sodium chloride and ammonium sulphate with different mass ratio between the two salts (Section 6.4.2). This also allowed the determination of the sensitivity of the proposed technique to small changes in the chemical composition of the analysed NaCl-$(NH_4)_2SO_4$-H_2O systems. This represents an interesting test because it gives an indication of what kind of mixtures could be characterised in the future with comparative kinetics experiments in a C-EDB.

6.4.1 Binary Mixtures of Inorganics

Sodium chloride, ammonium sulphate (both ≥99.5%, Sigma-Aldrich) sodium nitrate and sodium sulphate (≥99.5% and ≥99% respectively, Fisher Scientific) solutions were prepared with an initial known mass fraction of solute of ~0.05 for all compounds. In order to reach higher initial a_w values, solutions with an initial known *mfs* of ~0.005 was also prepared. Multiple datasets of at least 10 droplets evaporating into different RHs were collected and combined according to the procedure at the beginning of Section 6.3. The dependence of *mfs* on a_w for each solute is shown in Figure 6.11, compared with the corresponding prediction from the E-AIM Model. The agreement obtained for the measured mass fractions with the E-AIM Model is good for all the systems studied. Na_2SO_4 was observed to crystallize during measurements at $a_w = 0.57$ and therefore it was not possible to reach lower water activity values during the experiments on this compound.

The same datasets are also plotted in Figure 6.12 in terms of molar osmotic coefficients (ϕ_{sl}, Eq. 2.16) as a function of the square-rooted molality of solute. This quantity is the most sensitive expression of the a_w and solute concentration relation and for this reason some more scatter in the data can be observed in the plots in Figure 6.12, especially in the low molality range (high water activity). In addition, the data points in that region are characterized by higher error bars on the y axis, because in the osmotic coefficient expression the molality appears in the denominator and therefore even very slight uncertainties on its value can produce important uncertainties on the calculated osmotic coefficient. Anyway, the agreement with the E-AIM Model simulations (grey lines) is in general very good. Some minor discrepancies can be observed for Na_2SO_4, which could be attributed to the uncertain parameterisation included in the model for this compound (Figure 3 in the work of Clegg et al. (1997)[72]), and for $NaNO_3$ in the high concentration region.

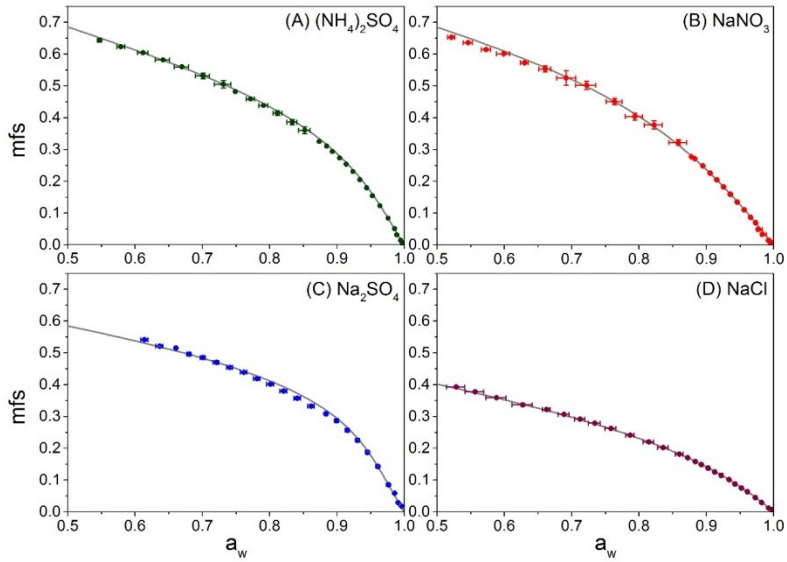

Figure 6.11: Measured *mfs* vs. a_w plots for $(NH_4)_2SO_4$, $NaNO_3$, Na_2SO_4 and NaCl (panels A-D). Symbols: circles – experimental data; solid grey lines – calculation from the E-AIM Model. Note: error bars are smaller than the data point when not shown.

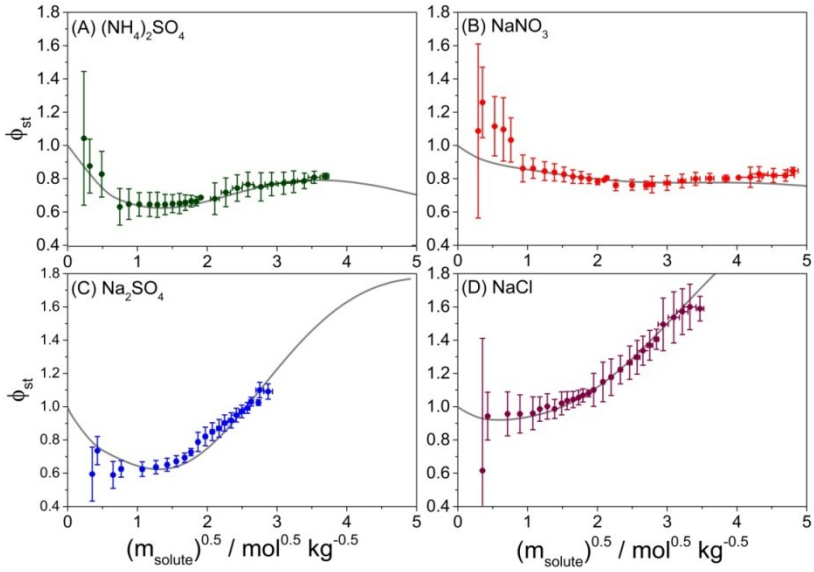

Figure 6.12: Measured molar osmotic coefficients (ϕ_{st}) vs. square-rooted solute molality plots for $(NH_4)_2SO_4$, $NaNO_3$, Na_2SO_4 and NaCl (panels A-D). Symbols: circles – experimental data; solid grey lines – calculation from the E-AIM Model. Note: error bars are smaller than the data point when not shown.

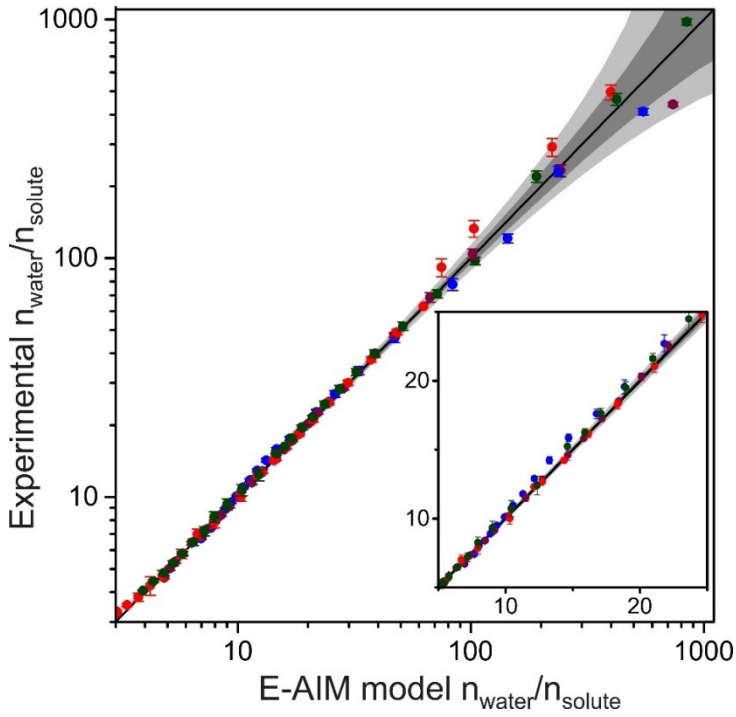

Figure 6.13: Correlation of the experimentally measured and E-AIM predicted values for n_{water}/n_{solute} (logarithmic scale in the main graph, linear scale in the inset). Symbols: green - $(NH_4)_2SO_4$; red – $NaNO_3$; blue – Na_2SO_4; purple – NaCl; black solid line – 1:1 line; grey envelopes: uncertainty on n_{water}/n_{solute} for $(NH_4)_2SO_4$ corresponding to an error in a_w of ±0.001 (dark grey) and 0.002 (light grey).

In addition, to better show the agreement between the experimental results and simulations from the E-AIM Model a correlation plot for the n_{water}/n_{solute} curves of NaCl, Na_2SO_4, $NaNO_3$ and $(NH_4)_2SO_4$ is shown in Figure 6.13 spanning the range from just 3 water molecules per ion pair (or per each three ions in the case of sulphate salts) up to 1000. For each point in the plot, n_{water}/n_{solute} was calculated with the E-AIM Model at the a_w value of the experimental data point. For n_{water}/n_{solute} values up to about 100 (corresponding to a_w of about 0.98, depending on the salt), all the points lie close to the 1:1 line, thus revealing a very good agreement of the experimental results with the E-AIM Model calculations. For $n_{water}/n_{solute} > 100$, the points appear a little more scattered. This is due to the fact that at very high a_w values, just a slight variation in water activity results in a significant variation in the calculated water moles values, with the hygroscopic growth curve extremely steep in this region. As an example, the highest measured data point for $(NH_4)_2SO_4$ can be considered: the measured a_w is 0.997 and it corresponds to 799 n_{water}/n_{solute} calculated with the E-AIM Model; if an uncertainty of ±0.001 in a_w is considered, the calculated n_{water}/n_{solute} values are 585 and 1236 for water

activity values of 0.996 and 0.998, respectively. In order to show the effect of such a small uncertainty on water activity, in Figure 6.13 the uncertainty on the calculated n_{water}/n_{solute} for ammonium sulphate is represented with dark and light grey envelopes if an error of ± 0.001 and ± 0.002 in a_w is supposed, respectively. These envelopes become increasingly large when the amount of absorbed water increases because of the steepness of the hygroscopic growth curve in that region.

6.4.2 Ternary Inorganic Mixtures

Hygroscopic growth measurements on mixtures of NaCl and $(NH_4)_2SO_4$ were also taken in order to further evaluate the performance of the technique with well-characterised aerosol systems and to evaluate the sensitivity of the experimental method to small changes in the chemical composition of the aerosol droplets. Three different $(NH_4)_2SO_4$/NaCl mass ratios were considered (50/50, 90/10 and 95/5) and the *mfs* and GF_r vs. a_w experimental curves (circles) are compared with simulations from the E-AIM Model (dashed lines) in Figure 6.14. For the calculation of growth factors of these mixtures, the reference dry state is considered to be a solid particle made of non-mixed crystalline ammonium sulphate and sodium chloride. The dry density is calculated estimating the dry volumes separately for NaCl and $(NH_4)_2SO_4$ and calculating the ratio between the total mass and the total volume of the two dry salts.

The experimental results show an overall good agreement with the curves predicted by the E-AIM Model for all three mixtures considered, both for the *mfs* and for the GF_r curves. The obtained *mfs* vs. a_w plot (Figure 6.14-A) shows that it is possible to successfully characterise the different hygroscopic behaviours of the 90/10 and 95/5 mixtures up to about $a_w = 0.93$. Above this value, the trends for the 90/10 and 95/5 mixtures become very similar: the difference between the two curves is less than 0.01 *mfs* and discriminating between them is not possible. When the experimental results are plotted as GF_r vs. a_w (Figure 6.14-B), the predicted curves for the same two mass ratios differ by 0.021 in GF_r at $a_w = 0.65$ and by 0.058 in GF_r at $a_w = 0.95$ and in this range it was possible to discriminate between their GF_r trends with the EDB measurements. Again, for higher water activity values, the hygroscopic growth curve becomes steep and the two trends are not discernible.

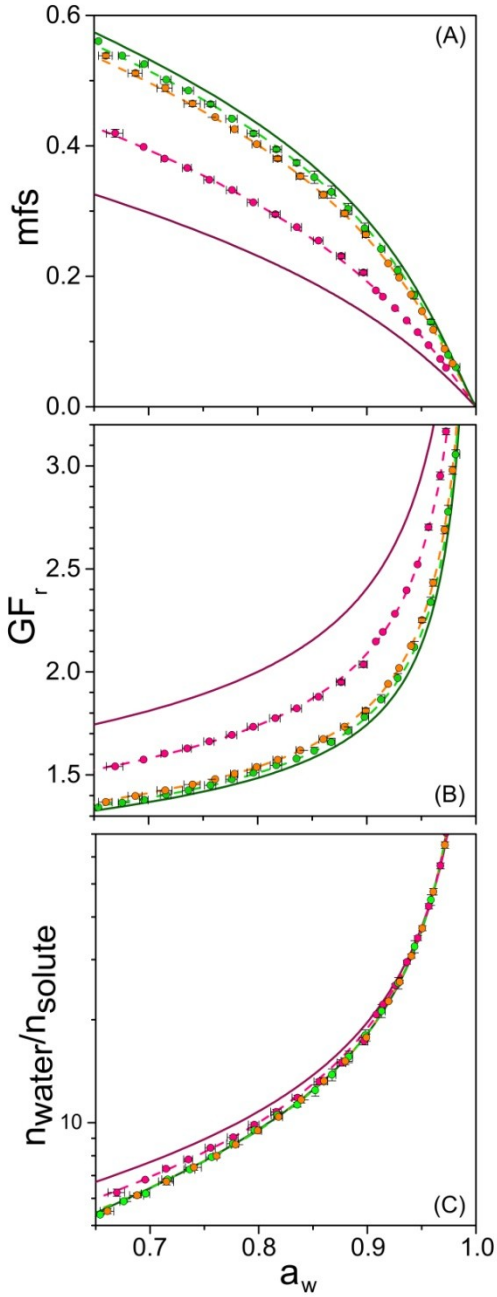

Figure 6.14: *mfs* vs. a_w (Panel A), GF_r vs. a_w (Panel B) and n_{water}/n_{solute} vs. a_w (Panel C) plots for mixtures with different $(NH_4)_2SO_4$/NaCl mass ratios. Colours: violet – pure NaCl; pink – 50/50 ratio; orange 90/10 ratio; light green – 95/5 ratio; dark green – pure $(NH_4)_2SO4$. Symbols: circles – experimental data; solid lines – calculations from the E-AIM Model for pure $(NH_4)_2SO_4$ and NaCl; dashed lines – calculations from the E-AIM Model for the mixtures.

However, the same comparison cannot be carried out for the ratio n_{water}/n_{solute} (Figure 6.14-C), because the curves predicted by the E-AIM Model for the 90/10 and 95/5 mixtures are both essentially indistinguishable from that of ammonium sulphate. Some differences are present below a_w~0.8 with the 50/50 mass ratio mixture and it if possible to discriminate different hygroscopic behaviours that correspond to a difference in n_{water}/n_{solute} of at least of 0.5 at a_w=0.8.

These results show that with this technique it is possible to detect variations in the hygroscopicity of solutions with only slight differences in chemical compositions, down to a 5% difference on a mass basis for mixtures of NaCl and $(NH_4)_2SO_4$. In the case of different mixtures, the minimum detectable variation would depend on the nature of their components: it could potentially be lower than found for this particular ternary system if the individual pure components have very dissimilar hygroscopic properties. On the other hand, a larger difference in chemical composition would probably be needed to detect similar variations in the case of mixture components exhibiting more similar hygroscopic properties.

6.5 Sensitivity to the Value of the Mass Accommodation Coefficient

The sensitivity of the hygroscopicity measurements presented in this Chapter to variations in the mass accommodation coefficient (α_M, Section 2.3) was also investigated. In the literature, measurements of the mass accommodation coefficient have been performed with a number of different techniques and resulting in a considerable range of different α_M values[143,148,250]. Up to this point in this Chapter, it was assumed that it has a value equal to 1, in agreement with previous studies which have reported the value of α_M for water accommodating/evaporation from a water surface[132,143,147]. Note that, the thermal accommodation coefficient (α_T) was maintained constant at 1, in agreement with literature studies on aqueous solution droplets[148,149], and the possible effects of its variation have not been investigated, both for all the results presented in the previous Sections and for the analysis discussed below.

In previous work[17], the influence of the uncertainty in α_M on the evaporation kinetics profiles of aqueous solutions was examined. The evaporation kinetics measurements for droplets with radii larger than 5 μm was shown to be insensitive to variations in α_M when >0.05, when the uncertainties resulting from the remaining thermophysical parameters and the experimental conditions are considered. Here the influence of α_M on the obtained hygroscopic growth curve of NaCl expressed in terms of n_{water}/n_{solute} for NaCl

is shown over the entire range of RH investigated in this work (from 50% to above 99% RH, Figure 6.15). The black circles represent the original growth curve calculated with $\alpha_M = 1$, while the grey open circles represent the n_{water}/n_{solute} for the same evaporating droplets datasets but with the analysis performed assuming $\alpha_M = 0.1$. A slight shift in the water activity calculated with Eq. 6.3 can be observed when varying the value of the mass accommodation coefficient, especially for a_w values above 0.95 where the growth curve gets really steep. Nevertheless, the two curves can be considered to be very similar within the experimental errors. However, the superior agreement of the curve calculated with $\alpha_M = 1$ (black circles) and the prediction from the E-AIM Model (black solid line) at very high a_w, together with the very good results obtained for all the aerosol systems presented in Sections 6.4.1 and 6.4.2, suggests that assuming a value of $\alpha_M = 1$ most accurately characterises the mass transport behaviour observed in the evaporating droplets.

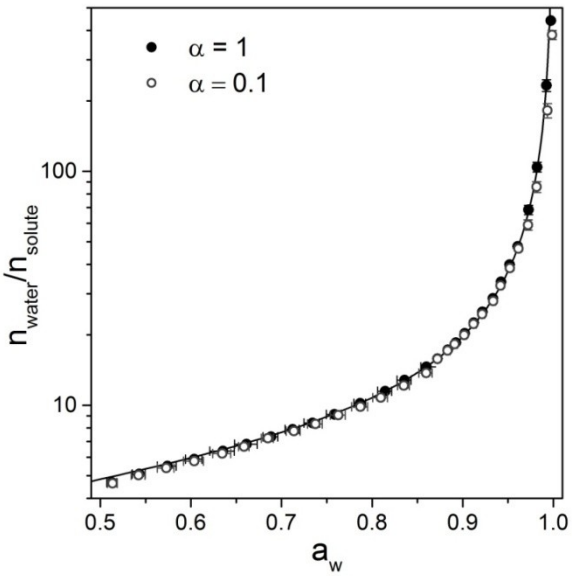

Figure 6.15: n_{water}/n_{solute} vs. a_w growth curve on a logarithmic scale for NaCl obtained when two different values for the mass accommodation coefficient were used in data processing (Eq. 6.3). Symbols: black circles – experimental obtained with $\alpha_M = 1$; open grey circles – experimental obtained with $\alpha_M = 0.1$; black solid line – prediction from the E-AIM Model.

6.6 Summary and Conclusions

The experimental approach for the determination of hygroscopic properties of aerosols with comparative kinetics measurements of probe and sample droplets individually confined in a C-EDB has been described and validated. In order to apply an existing technique down to RH=50%, the limitations of the used literature kinetics model had to be investigated, with particular reference to the approximate representation of the vapour pressure of water over a droplet surface. In order for the model to be applied, a 3 K threshold for the difference of the gas phase temperature and that of an evaporating droplet needs to be respected, so that the vapour pressure of water on the droplet surface is accurately modelled within the Kulmala at al. (1993)[145] model framework. It was shown that for that portion of the evaporation profiles for which this threshold is not exceeded, the retrieved hygroscopic properties are reliable and accurate. The proposed technique was successfully validated by comparing the hygroscopic growth curves measured for four well-characterised inorganic compounds with calculations from the E-AIM Model. Ternary mixtures of water, sodium chloride and ammonium sulphate with variable content of each salt were also considered; they provided a further confirmation of the validity of the comparative kinetics approach and also provided some information on the sensitivity of the method to small changes in chemical composition.

Data on the hygroscopicity of atmospherically-relevant compounds (organic compounds, expecially SOA, and their mixtures with inorganics) are very important for the reduction of the uncertainties relating to many effects of atmospheric aerosols, as discussed in Section 2.2. Comparative kinetics measurements in a C-EDB represent a powerful tool for the characterisation of the hygroscopic properties of aerosol systems with increasing chemical complexity. With the experimental approach proposed in this Chapter, growth curves can be determined rapidly and accurately, potentially opening up the possibility of mapping hygroscopic response for a large number of organic components of SOA and, indeed, complex mixtures and possibly SOA samples directly.

Chapter 7 Hygroscopic Properties of Aminium Sulphates

The comparative kinetics experimental technique in the C-EDB described and validated in Chapters 5 and 6 is applied in this Chapter for the determination of the hygroscopic properties of aminium sulphates. These compounds are organic salts formed from the neutralisation reaction between short-chained amines and sulphuric acid; their physicochemical behaviour is less well characterised than their inorganic equivalent, ammonium sulphate, even though they can have a relevant role in atmospheric processes such as the nucleation and growth of new particles and cloud droplet formation. In this Chapter, the procedure for the preparation of the aminium sulphate solutions is described and the measured densities, refractive indices and hygroscopic properties are presented. They are also compared with some other literature works that applied different experimental approaches. Reproducibility tests and effects of the density parameterisation used for the C-EDB data treatment are shown, too. Finally, long trapping measurements were performed for the determination of the vapour pressure of amines over these solutions and they are discussed at the end of this Chapter.

7.1 Aminium Sulphates

Low molecular weight amines are mostly emitted in to the atmosphere as gaseous compounds by a number of different sources, both anthropogenic (animal husbandry, food processing and cooking, combustion, pesticides) and natural (oceans, biomass burning, vegetation)[251]. These chemical species are basic, highly water-soluble and have high pure liquid vapour pressures (see physical properties of the six amines considered in this work in Table 7.1). Their ambient concentrations in the gas phase can span over wide ranges, depending on the sampling location (for example, up to 140 mg m^{-3} close to a city market[252], 110-300 ng m^{-3} in the exhaust gas of a waste disposal[253], in the order of tens of µg m^{-3} inside livestock buildings[253]) and on the season[254,255]. Contrasting data can be found in literature about the gas/particle partitioning of amines in the atmosphere,

e.g. Kallinger and Niessner[253] found that a fraction of about 20% of the amines measured in some livestock buildings partitioned to the condensed phase, while Akyuz[254] found a higher relative content in $PM_{2.5}$ and in PM_{10} if compared to amines in the gas phase measured during both Summer and Winter sampling campaigns in Turkey (Zonguldak province, high coal use for heating purposes, detected amines concentrations in the order of ng m^{-3}). This kind of variability is likely due to variable primary emission sources in different sampling locations and to a spatial dependence of the amines partitioning depending on how far from emission source the sampling is performed (i.e. the closer to the source the more these compounds are mostly present in their original gas phase). In the condensed phase, amines can account for up to hundreds of pg m^{-3} or a few ng m^{-3}; an extensive review of the measured concentrations of a large number of amines both in the gas and in the condensed phases is given in the work of Ge et al.[251,256].

	M_w / g mol^{-1}	Solubility / mol kg^{-1} (T=298.15 K)	Vapour pressure / kPa	pK_a
NH_3	17.031	/	1956[(b)]	9.25[(b)]
MMA	31.06	17.9[(a)]	336[(a)]	10.66[(b)]
DMA	45.08	17.9[(a)]	193[(a)]	10.73[(b)]
TMA	59.11	4.9[(a)]	231[(a)]	9.80[(b)]
MEA	45.08	5.3[(a)]	133[(a)]	10.65[(b)]
DEA	73.14	2.0[(a)]	31.5[(a)]	10.84[(b)]
TEA	101.19	0.7[(a)]	9.03[(a)]	10.75[(b)]

Table 7.1: Physical properties of ammonia, methylamine (MMA), dimethylamine (DMA), trimethylamine (TMA), monoethylamine (MEA), diethylamine (DEA) and triethylamine (TEA). Data from Ge et al.[256] (a) and from CRC Handbook[246] (b).

As a matter of fact, despite the volatility of short-chained alkylamines, these compounds can undergo gas-to-particle partitioning thanks to different chemical processes[251]: direct solubilisation, oxidation reactions that lead to the formation of SOA, acid-base reactions similar to those of ammonia[3] with both inorganic (sulphuric, nitric and hydrochloric acids) and organic acids[257,258], displacement reactions of ammonium cations with aminium cations[259,260]. With respect to these last two types of chemical reactions, aminium sulphates are the products of the neutralisation of sulphuric acid and short-chained alkylamines:

$$H_2SO_4 + 2R_3N \rightleftarrows (R_3NH)_2SO_4 \qquad 7.1$$

where R can be either $–CH_3$, $-CH_2CH_3$ or –H. The formation of aminium sulphates and other similar aminium salts is believed to be one of the main factors responsible for the lowering of the vapour pressure of aliphatic amines, thus favouring their partitioning

from the gas to the aerosol phase[261,262]. Because of this and because of their relative abundance in the atmosphere, aminium sulphates can play a relevant role in the nucleation and growth of new particles[263–265] and in cloud formation[266]. However, their physicochemical properties are less well characterised than their inorganic corresponding compound, $(NH_4)_2SO_4$. Some work has been recently done in order to fill this gap and the densities[81,104,266], CCN activity and optical properties[266], hygroscopicity and phase transitions of aminium sulphates[73,81,104,228,266] have been investigated with different experimental approaches for the series of the six methyl and ethyl aminium sulphates (or subsets of these six compounds). In this work, the hygroscopic behaviour of these six aminium sulphates shown in Figure 7.1 was characterised by means of evaporation kinetics experiments in a C-EDB (Section 6.1), together with the measurement of densities and refractive indices of their solutions. The results of this study are reported in the following Sections; some discrepancies with previous works were found and will also be discussed, in the light of the different experimental procedures applied.

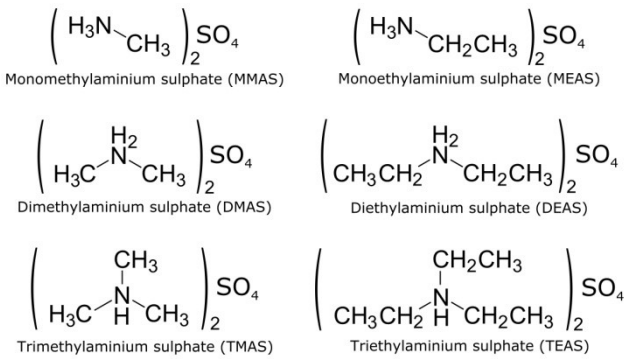

Figure 7.1: Chemical formulas of the six studied aminium sulphates.

7.1.1 Preparation of the Solutions

Aminium sulphates stock solutions were prepared from the neutralization reaction of sulphuric acid and each of the six considered amines. The commercial amines stock solutions (Sigma Aldrich, MMA, ~ 40 wt%; DMA, ~ 40 wt%; TMA, ~ 45 wt%; MEA, ~ 66.0-72.0 wt%; DEA ≥ 99.5 wt%; TEA ≥ 99 wt%) were titrated with standardised HCl (1 M, SLS). Three repetitions were performed for each titration and during their whole duration the pH was measured by means of a pH-meter (HI 8314, Hanna Instruments), which was calibrated with standard pH 7 and pH 4 solutions. Before the titration, the amine stock solution was always diluted down to 1-5 wt% in order to minimize the heat generated by the neutralisation reaction. In addition, both the H_2SO_4 and the HCl used for the standardisation of the amines commercial solutions were

titrated with Na_2CO_3 (≥ 99.5%, Alfa Aesar), which was dried at 225°C for 3 h before weighing to make sure that no water was adsorbed on it. Three repetitions were performed in these cases, too.

For the preparation of the aminium sulphates stock solutions, stoichiometric amounts of the standardised H_2SO_4 and of one of the standardised amines were mixed, with an initial concentration of both solutions around 40 wt%. The pH of the solution was monitored for the whole duration of the reaction as well, to make sure that all the amine in solution reacted. The obtained concentrated stock solutions of the salts were subsequently diluted down to a mass fraction of ~0.05, in order to obtain a suitable concentration for the C-EDB comparative kinetics measurements.

During both the amines titration with HCl and the preparation of the aminium sulphates solutions with H_2SO_4, the amine solution was always kept in an ice bath and the addition of the acid was done slowly and dropwise, in order to disperse the heat generated by the neutralisation reaction and to avoid any possible amine volatilization.

Phase separation was observed when titrating the triethylamine commercial solution and its concentration was determined to be 81.6 wt% (0.52 wt% standard deviation over 3 repetitions), which is considerably lower than the ≥ 99 wt% concentration value given by the manufacturer. This is possibly due to the fact that TEA is the least soluble of the six considered amines (Table 7.1), which results in an incomplete solvation of the amine in water and in a consequently distorted measurement of pH during the titration. For this reason, a 99 wt% concentration for the commercial TEA solution was assumed; this probably represents a better estimate of the actual TEA concentration since the density measurements obtained using this value for the concentration of the TEAS solutions are more in line with literature data (Section 7.1.2).

This experimental procedure assured that the concentrations of the reagents were well known and consequently that the concentrations of the stock solutions prepared for aminium sulphates were well known, as well. The uncertainty on the commercial solution concentrations of the reagents determined with the titrations was taken into account for the calculation of the uncertainties of the quantities determined from C-EDB experiments (GF_r, mfs, n_{water}/n_{solute}, osmotic coefficients) as discussed in Section 6.1.3.

In addition, in order to show the effectiveness of the proposed procedure, all the steps discussed above were also carried out for the preparation of $(NH_4)_2SO_4$ from the reaction of ammonia and sulphuric acid; the obtained solution was used in comparative kinetics measurements and the hygroscopicity of the ammonium sulphate from reaction was compared with calculations from the E-AIM Model, similar to what is shown in Section 6.4 (but in that case, the initial ammonium sulphate solutions were prepared from

commercial crystalline solid). Figure 7.2 shows the hygroscopic properties of $(NH_4)_2SO_4$ obtained from direct reaction of ammonia and sulphuric acid, in terms of n_{water}/n_{solute}, vs. a_w (Panel A) and osmotic coefficients vs. $m(SO_4^{2-})^{0.5}$ (Panel B). The graphs show averaged data obtained from two datasets of ten droplets each (black circles: *mfs* of $(NH_4)_2SO_4$ in the initial solution 0.03, gas phase RH of 88.5%; open circles: *mfs* of $(NH_4)_2SO_4$ in the initial solution 0.004, gas phase RH of 90%). The agreement with the E-AIM Model calculations (grey lines) is extremely satisfactory and it indicates that the volatility of ammonia (which is even higher than that of the six considered amines, see vapour pressure values in Table 7.1) is not an issue when the neutralisation reaction with H_2SO_4 is performed. This result is extremely important because it confirms that the concentration of the prepared $(NH_4)_2SO_4$ solution is well known and that the preparation method of the solutions employed for both $(NH_4)_2SO_4$ and all the six aminium sulphates is efficient and reliable.

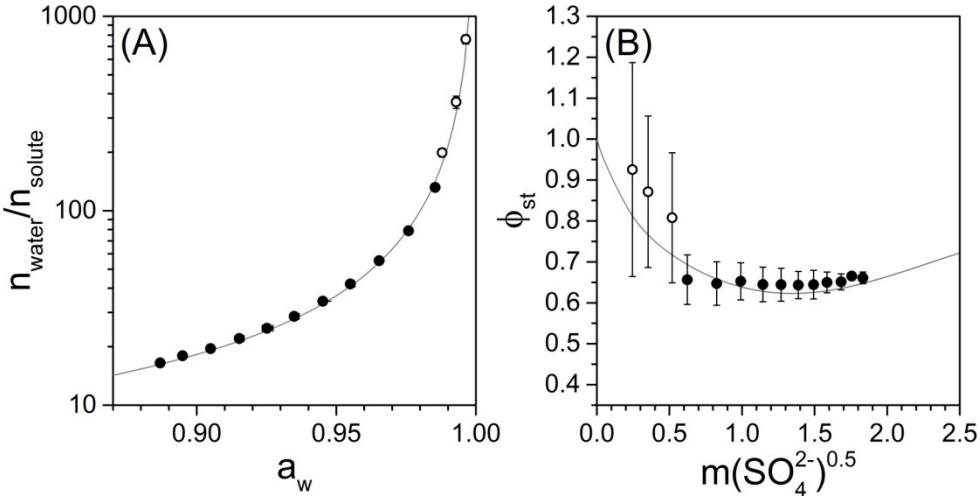

Figure 7.2: Measured n_{water}/n_{solute} vs. a_w (Panel A) and osmotic coefficients vs. $m(SO_4^{2-})^{0.5}$ of ammonium sulphate obtained from the reaction between NH_3 and H_2SO_4.

7.1.2 Density and Refractive Index of Aminium Sulphates

As discussed in Section 6.1.2, in order to retrieve the hygroscopic properties of a compound (GF_r, *mfs*, n_{water}/n_{solute}, etc. vs. a_w) from evaporation profiles (radius vs. time)

measured at different RHs in the C-EDB, density and refractive index parameterisations as a function of solute concentration are needed.

The densities of at least ten solutions with different concentrations for each aminium sulphate were measured with a density meter (Densito 30PX, Mettler Toledo, accuracy of ±0.001 g cm^{-3}), which was calibrated with pure water before each use. Densities were measured at ambient temperature, which oscillates in the laboratory between 293 K and 295 K; temperatures were always registered together with the measured density values, as well. Refractive indices of the same solutions were measured at 589 nm by means of a refractometer (Palm Abbe II, Misco, precision of ±0.0001), which was calibrated with pure water before each use, too. The optical measurements in the C-EDB for the measurements of the size of levitated droplets are taken at a wavelength of 532 nm (Section 5.2.2), but the wavelength dependence of refractive index was considered negligible (i.e. for pure water m=1.333 at 589 nm and m=1.335 at 532 nm), if compared to the other experimental uncertainties that need to be accounted for in C-EDB experiments (Section 6.1.3). As described in Section 5.2.3, the density data are fitted with a 3rd order polynomial and the melt density is determined at mf_S=1; this value is then used in the molar refraction mixing rule (Eq. 5.6) and it allows the determination of the melt refractive index for each compound. m_{melt} and ρ_{melt} are needed in order to apply the molar refraction mixing rule to the correction of the varying refractive index of the evaporating aminium sulphate solution droplets in the C-EDB (Section 5.2.3). The measured density and m values for each aminium sulphate are shown in Figure 7.3 together with the 3rd order polynomial fit and the molar refraction mixing rule fit for each compound, respectively. The coefficients of each fitted polynomial curve, m_{melt} and ρ_{melt} are also reported in Table 7.3.

A trend of decreasing density with increasing molecular weight is observed (Figure 7.3, Panel A): each methylaminium sulphate is denser than its equivalent in the ethylaminium sulphates series. Within the methyl and the ethyl compounds series, the following trends are individuated: MMAS>DMAS>TMAS and MEAS>TEAS>DEAS. The measured refractive indices do not show such evident trends (Figure 7.3, Panel B); TMAS and TEAS have a slightly stronger dependence of m on the solution concentration and the extrapolated m_{melt} values increase in the ethylaminium sulphate series (MEAS<DEAS<TEAS) but not in the methylaminium one (DMAS<MMAS<TMAS).

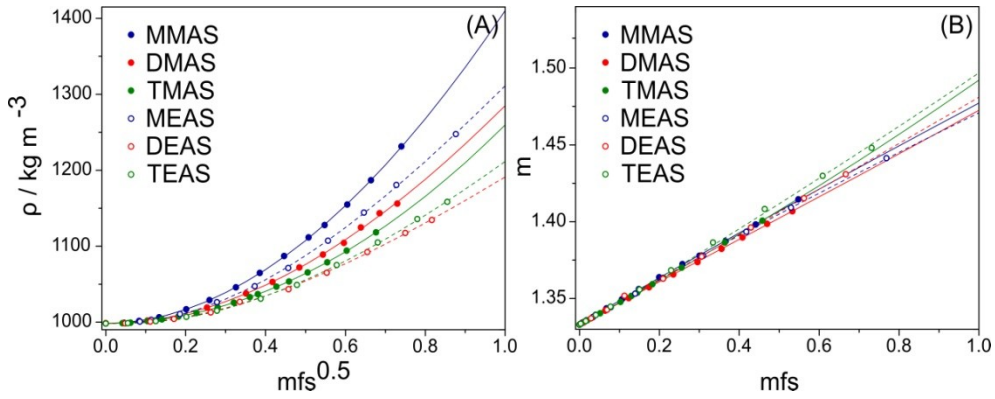

Figure 7.3: ρ (kg m^{-3}) vs. $mfs^{0.5}$ (Panel A) and refractive indices vs. *mfs*. Symbols: circles – measured values; lines – parameterisations for methyl (solid) and ethyl (dashed) aminium sulphates.

	a_0	a_1	a_2	a_3	ρ_{melt} $(kg\ m^{-3})$	m_{melt}
MMAS	998.10	5.12	447.11	-40.19	1410.1	1.4771
DMAS	998.47	-2.55	341.03	-51.91	1285.0	1.4725
TMAS	998.03	4.64	252.17	4.82	1259.7	1.4921
MEAS	998.17	-19.25	459.22	-127.00	1311.1	1.4708
DEAS	998.10	-10.09	285.60	-82.47	1191.1	1.4810
TEAS	998.50	-25.09	378.58	-100.86	1251.1	1.5357

Table 7.2: Parameters of the 3rd order polynomial fit of density measurements and of the molar refraction mixing rule fitting for aminium sulphates solutions.

The obtained m_{melt} and ρ_{melt} were compared to some available literature data. With respect to the densities (Figure 7.4), Qiu and Zhang (2012)[81] obtained values for the solid compounds (grey circles in Figure 7.4) by plotting mass against volume of particles heated up to 80°C and measured with a DMA-APM-CPC system (coupled differential mobility analyzer, aerosol particle mass analyzer and condensation particle counter) and assuming spherical particles; they also proposed a semiempirical model (solid line in Figure 7.4) to predict the densities of aminium sulphates as a function of the number of carbon atoms in the compound (n):

$$\rho = \rho_{AS}(1 + An)/(1 + Bn) \qquad 7.2$$

where ρ_{AS} is the crystalline density of $(NH_4)_2SO_4$, A is a relative increase in mass when a $-CH_2-$ is added to ammonium sulphate (0.016) and B is the equivalent to A but on a volume basis (0.210 from Qiu and Zhang (2012)[81] DMA measurements). In another

paper, Clegg et al. (2013)[104] fitted some density values measured at various solution concentrations for each aminium suphate converted to apparent molar volumes with polynomial curves of variable orders and extrapolated a melt density value at *mfs*=1. Both these literature works did not consider MEAS. The comparison of these two datasets with the ρ_{melt} values obtained in this work is shown in Figure 7.4; as suggested by Clegg et al.(2013)[104], a theoretical extrapolated ρ_{melt} is expected to be lower than the solid density values and that can be observed for both the extrapolated ρ_{melt} datasets (black diamonds – this work; light grey squares – Clegg et al.(2013)[104]) if compared to the solid values estimated by Qiu and Zhang (2012)[81] (grey circles). A clear decrease of the pure component density was found as the number of carbon atoms in the cation ($n_{C\ atoms}$) increases and can be seen in all the three datasets, except for TEAS. The overall agreement with ρ_{melt} values from Clegg et al.[104] is good and the percentage difference in the extrapolated ρ_{melt} is lower than 3% for all compounds except for TEAS (4.8%). The effect of the uncertainties of ρ_{melt} on the hygroscopic properties determined with evaporation kinetics measurements is discussed in more detail in Section 7.1.5.

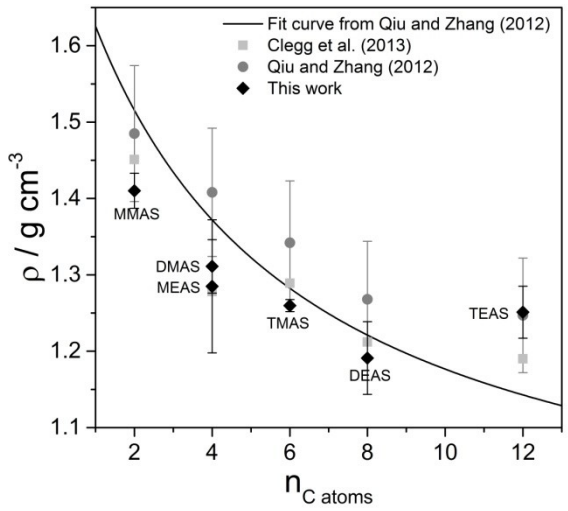

Figure 7.4: ρ_{melt} of the six aminium sulphates from this work (black diamonds) and from Clegg et al. (2013)[104] together with the solid ρ values from Qiu and Zhang (2012)[81] and their prediction model (Eq. 7.1, black line).

With respect to the refractive indices of aminium sulphates, Lavi et al.(2013)[266] measured them for four solid aminium sulphates (MMAS, DMAS, MEAS, DEAS) using Broadband Cavity Enhanced Spectroscopy, in the wavelength range of 360-420 nm. Briefly, this technique allows the measurement of the extinction cross section of an aerosol ensemble and the refractive index of a compound is inferred by fitting a Mie curve to the measured

cross sections. In Figure 7.5, data reported in Figure 7 of Lavi et al. (2013)[266] (grey circles and grey dashed line, which represents a linear fit of their data) are compared with the results obtained in this work (black circles), in terms of refractive index versus density for each compound. The poor agreement between the two datasets can be attributed to the fact that Lavi et al. (2013)[266] consider solid compounds and used the solid densities reported by Qiu and Zhang (2012)[81], while in this work melt densities and refractive indices were considered (see in particular the discrepancies for ammonium sulphate, AS); in addition, the wavelength at which measurements were taken is different, since they averaged the refractive indices calculated between 360-420 nm, while in this work m was measured at 589 nm. Anyway, since the work of Lavi et al.[266] is the only one found in the literature that measured the optical properties of aminium sulphates, this comparison is shown for the sake of completeness.

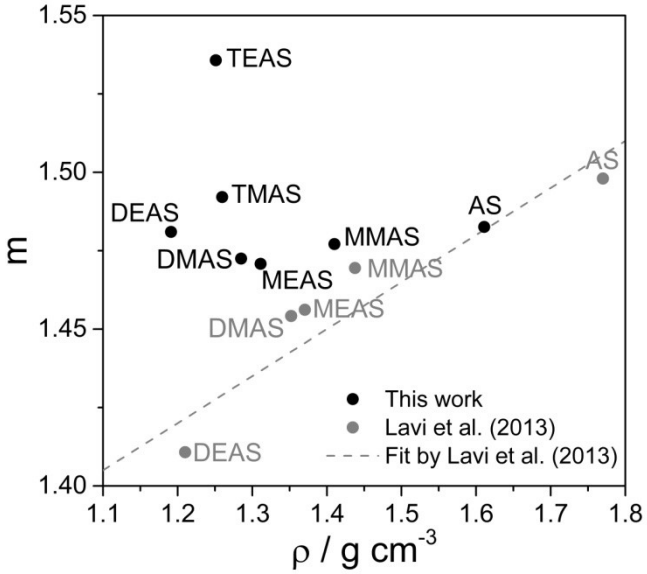

Figure 7.5: Comparison of refractive indices from the work of Lavi et al.[266] (grey circles, solid compounds) and this work (black circles, melt) as a function of density.

7.1.3 Hygroscopic Properties of Aminium Sulphates

The hygroscopic properties of the series of the six aminium sulphates were characterised by means of comparative kinetics measurements, as described in Section 6.1 and using the density and refractive index parameterisations shown in Table 7.2 for the C-EDB data treatment. First, the obtained radial growth curves are shown in Figure 7.6. Considering the compound with the lowest molecular weight first, the hygroscopic

behaviour of MMAS (◖) is the most similar to ammonium sulphate (grey line, calculation from the E-AIM Model), in terms of GF_r. Continuing in the methylaminium sulphates series, a slight decrease in GF_r is observed in the high water activity region (a_w>0.8) for DMAS (■) and TMAS (◆), while in the lower part of the investigated a_w region the hygroscopic properties of these compounds tend to be more similar to $(NH_4)_2SO_4$, too. With respect to the ethylaminium sulphates series, a more evident decreasing trend in the radial growth curve is observed with increasing number of C atoms in the cation (MEAS(○)>DEAS(□)>TEAS(◇)), once again especially in the upper part of the curves. If the mono-, di- and tri- pairs of the two different series are compared, the methyl compound always presents higher values of radial growth factor than its equivalent in the ethylaminium sulphates series.

Note that for the calculation of the reference state radius in the denominator of GF_r (Eq. 2.1), the theoretical pure melt density was used (Table 7.2); if the pure crystalline density values were known and used, one could expect that the calculated radial growth curve would be slightly higher, because the crystalline density is expected to be higher than the melt density[104] (Section 7.1.2) and consequently it would result in $a_{melt}>a_{dry}$ if a constant mass was considered. Anyway, for example, if a hypothetical increase of 5% from ρ_{melt} to ρ_{dry} as a rough estimate is supposed for DMAS, the obtained GF_r curve would increase by less than 1% (less than 0.01 in GF_r); this would not affect the trends shown in Figure 7.6, it would just slightly change the relative position of the aminium sulphates curves to that of ammonium sulphate.

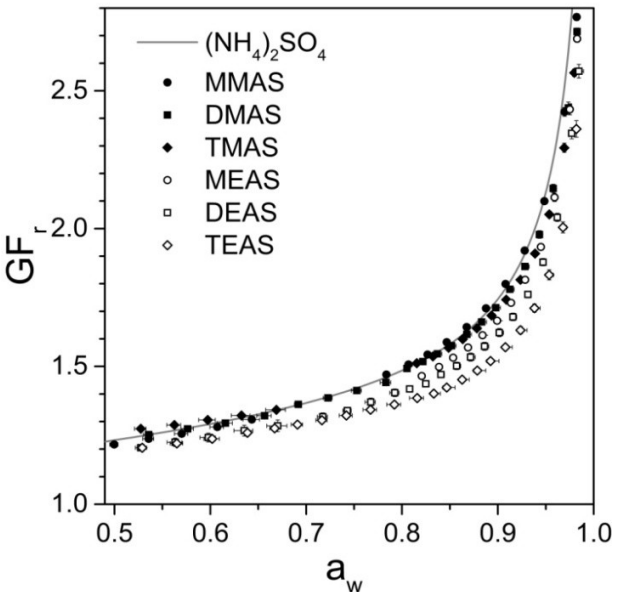

Figure 7.6: GF_r vs a_w hygroscopic growth plot from C-EDB comparative kinetics measurements compared with $(NH_4)_2SO_4$ calculation from the E-AIM Model (grey solid line).

The same datasets shown in Figure 7.6 have been converted to n_{water}/n_{solute} vs. a_w and plotted in Figure 7.7, where the symbols previously used for each compound are maintained. Note that the y axis is displayed on a logarithmic scale for clarity. Different trends can be individuated in this case: the main factor influencing how many moles of water are absorbed per moles of solute is the number of alkyl groups in the cation and not the length of the carbon chains in it. In fact, conversely to the hygroscopic behaviour observed with the GF_r plot, more significant differences are found within the methyl- and ethyl- series rather than between two analogous compounds belonging to different series, even if the ethylaminium sulphate in a pair always presents slightly higher values of n_{water}/n_{solute} (MMAS(●)≈MEAS(○)<DMAS(■)≈DEAS(□)<TMAS(◆)≈TEAS(◇)). In addition, in the case of these moles of water per moles of solute curves, a higher number of carbon atoms in the cation results in an increasing trend of n_{water}/n_{solute}, which is exactly the opposite trend to that found when the hygroscopic properties of aminium sulphates were represented in terms of GF_r (Figure 7.6).

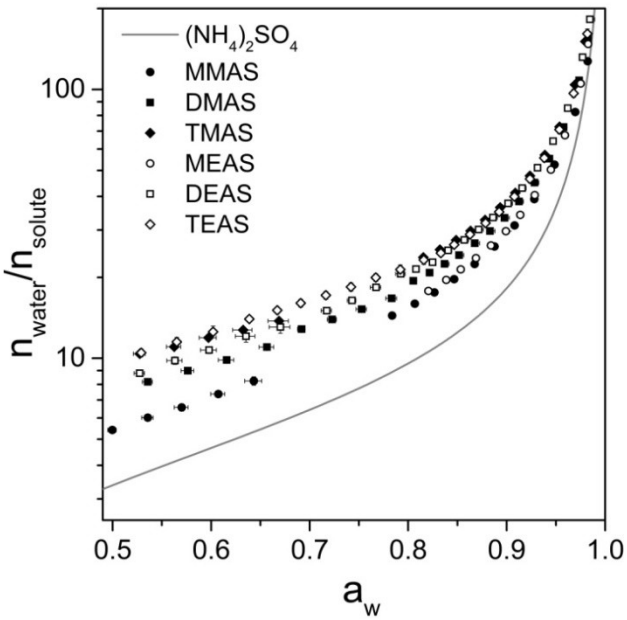

Figure 7.7: n_{water}/n_{solute} vs a_w hygroscopic growth plot from C-EDB comparative kinetics measurements compared with $(NH_4)_2SO_4$ calculation from the E-AIM Model (grey solid line).

These different trends found for the hygroscopic properties of these compounds when considered either in terms of GF_r or n_{water}/n_{solute} as a function of a_w originate in the different physicochemical properties that each quantity is able to represent. When GF_r is calculated, the density and molecular weight of each analysed compound have a relevant role in its determination. For example, if particles with a dry radius of 1 μm for each of

the six aminium sulphates are considered, the moles of salt in each droplet is going to be smaller the higher its molecular weight and the lower its density, as shown in Figure 7.8. Therefore, if hygroscopicity is represented with a size growth factor, this is going to be determined not only by the ability of a compound to absorb water at a certain relative humidity, but also by the number of molecules present in the droplet itself. For this reason, a decreasing hygroscopic growth trend with increasing molecular weight of the aminium sulphates was found in Figure 7.6 for GF_r.

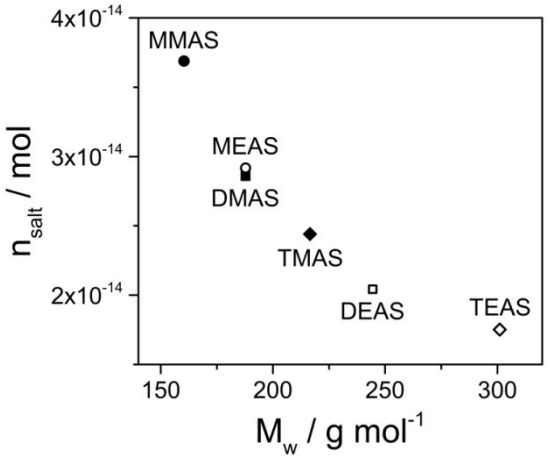

Figure 7.8: Moles of salt (n_{salt}) in a 1 μm radius particle as a function of the molecular weight (M_u) of each aminium sulphate.

As discussed in Section 2.1.5, size growth curves are widely used in the aerosol science community, especially when the optical properties, the radiative forcing or the climatic effects of atmospheric aerosols are investigated, since they largely depend on the size of particles (Sections 1.1.3 and 1.2.1). For this reason, the quantification of the hygroscopic properties of a compound in terms of GF_r is useful for such applications and it was done in this work, as well. Nevertheless, n_{water}/n_{solute} vs. a_w curves allow the characterisation of the water uptake of a substance on a molecular level and the decoupling of its hygroscopic properties from its density and molecular weight, because the water uptake is 'normalised' on the molar amount of solute in the particle. This kind of representation is mostly used in works focusing on chemical reactivity or on thermodynamic properties of compounds in the aerosol phase, as discussed in Section 2.1.5. The increasing trend individuated in Figure 7.7 for n_{water}/n_{solute} curves with the increasing number of carbon atoms in the cation is related to the size of the cation itself: the bigger the cation, the higher the number of water molecules absorbed per mole of salt.

7.1.3.1 Comparison with Literature Data

As stated at the beginning of Section 7.1, some literature works investigated the physicochemical properties of aminium sulphates in recent years because of the increasing understanding of their role in atmospheric processes[251,257–260]. With respect to the determination of their hygroscopic properties, the approach presented here differs from them in both the preparation method of the solutions and in the experimental measurement technique; the results obtained with comparative kinetics measurements in a C-EDB are here compared with those shown by other authors in the light of the different experimental approaches that were used.

Qiu and Zhang (2012)[81] were the first who measured size growth curves for these compounds (MEAS excluded) by means of an H-TDMA (Section 1.3). They calculated size hygroscopic growth factors as the ratio of mobility diameters measured at variable RH (up to 90%) and at an RH of ~12%. A monotonic increase in the particle size for each compound was observed and no deliquescent behaviour was found. If their growth curves are compared with the GF_r shown in Figure 7.6, a systematic underestimation results from the H-TDMA measurements; it is the highest for TEAS (-16% on average in the a_w range where the two datasets overlap) and for TMAS (-13%), it is about -10% for DEAS and DMAS and it is the smallest for MMAS (-7%). These discrepancies are most likely due to the presence of some residual water at the conditions at which the reference diameter was measured in the H-TDMA experiments (RH ~12%); this would result in an overestimated reference 'dry' size and in underestimated growth factor values. This first explanation is supported by the studies of Chan and Chan (2012)[267], who found that for some aminium sulphates water was still present in the particle phase at RH~3%. In addition, a possible volatilisation of the amine during the drying step in the H-TDMA could affect the chemical composition of the particles[233,267], shifting it towards an aminium bisulphate composition (1:1 molar ratio of sulphuric acid to amine), which was shown to be less hygroscopic than its sulphate counterpart[73]. In this respect, interestingly the two compounds that presented the biggest GF_r underestimation (TMAS and TEAS) are those that were found to be the most volatile in long trapping measurements performed in this work (see Section 7.1.6). This is also in line with the findings in the work by Chan and Chan (2012)[267], who studied ammonium displacement reactions by alkylamines by levitating single droplets in an EDB and evaluating the changes in the recorded Raman Spectra during experiments. After TEAS solution droplets were levitated at RH<3% for more than 5 h, TEAS was found to have converted to TEA bisulphate almost completely, indicating that half of the amine in the initial solution had evaporated. A similar behaviour was observed for TMAS, while DMAS and DEAS showed smaller evaporation of the amine (~25% and ~5%, respectively); MMAS and MEAS did not show any relevant evaporation in the observed timescales. These results

support the hypothesis of a possible evaporation of the amine in solution during H-TDMA experiments, and at the same time represents an interesting comparison to evaluate the timescales over which this kind of evaporation occurs. Each droplet evaporation for comparative kinetics measurements in the C-EDB covers just up to 30 s: this allows the decoupling of the fast water evaporation and the slow amine evaporation, since these two processes occur over different timescales. In addition, the evaporation experiments in the present work were carried out at RH>50% and for this reason the evaporation rates in this case have to be smaller than those measured by Chan and Chan[267] (droplets levitated at RH<3%).

At a later stage, Clegg et al. (2013)[104] converted the size growth curves measured by Qiu and Zhang (2012)[81] to n_{water}/n_{solute} vs. a_w, thanks to density measurements (discussed in more detail in Section 7.1.5). The obtained growth curves did not allow the discernment of any significant trend in the hygroscopicity of aminium sulphates; they resulted to be essentially similar to that of ammonium sulphate in the lower a_w range and the scatter of the data do not give any certain trends for a_w above 0.7, even if it seems that the methylaminium sulphates absorb less moles of water per moles of solute than the compounds in the ethyl series.

Because of the uncertainties associated with the H-TDMA measured GF_r, the comparison with another study from Sauerwein et al. (2015)[73] revealed interesting. Bulk water activity measurements for four different amine-to-sulphate ratios and over a concentration range of salt up to 9 mol kg^{-1} were performed at 25°C with an activity meter. Using a bulk measurement technique for the determination of hygroscopic properties of aminium sulphates has the advantage of minimizing possible evaporative losses of amine during the measurements, if compared to measurements in the aerosol phase with a H-TDMA or in classical EDB humidification and dehumidification experiments. Note that TEAS was not considered in their study. As a first comparison, the hygroscopic growth curves previously shown in Figure 7.7 in terms of n_{water}/n_{solute} vs. a_w are plotted separately for each compound with results from Sauerwein et al. (2015)[73] (Figure 6a in their paper) in Figure 7.9 (note that again the y axis is shown with a logarithmic scale). The hygroscopic growth curves determined with the two different experimental methods slightly differ one from the other, but these discrepancies are less significant than what was found for the comparison with H-TDMA data from Qiu and Zhang (2012)[81]. The comparison of the two datasets in terms of osmotic coefficients (Eq. 2.16) can provide a further insight into these discrepancies. Similarly to Figure 7.9, the osmotic coefficients as a function of $m(SO_4^{2-})^{0.5}$ are plotted individually for each compound in Figure 7.10; the discrepancies previously observed are obviously present in these plots as well, but a few more considerations can be done. First, if the errors associated with each dataset are considered, they overlap over some $m(SO_4^{2-})^{0.5}$ ranges especially in the low molality end (high water activity region) for MMAS, TMAS, MEAS

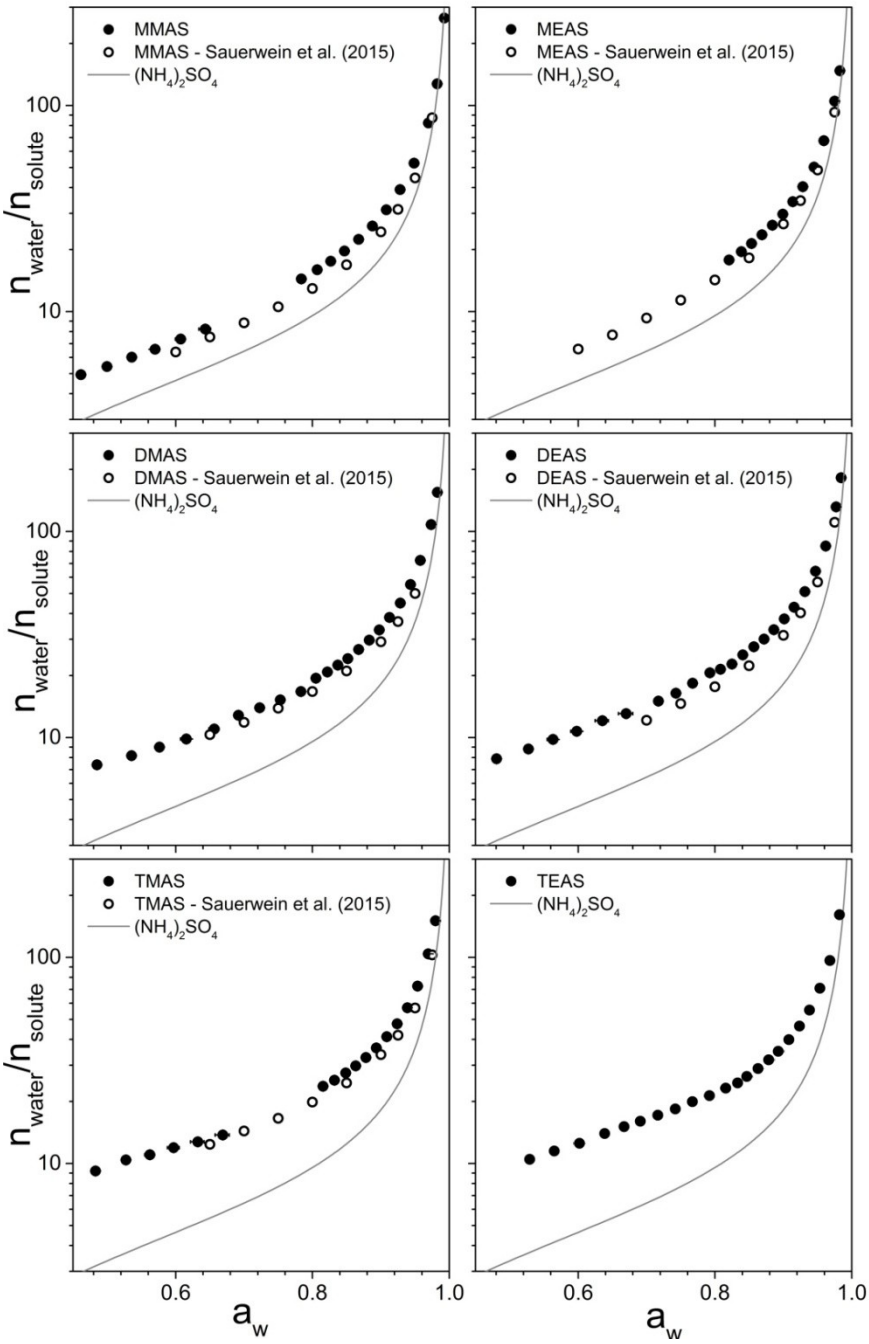

Figure 7.9: n_{water}/n_{solute} vs a_w from C-EDB comparative kinetics measurements (solid circles) compared with data from Sauerwein et al. (2015)[73] (open circles) and $(NH_4)_2SO_4$ calculation from the E-AIM Model (grey solid line).

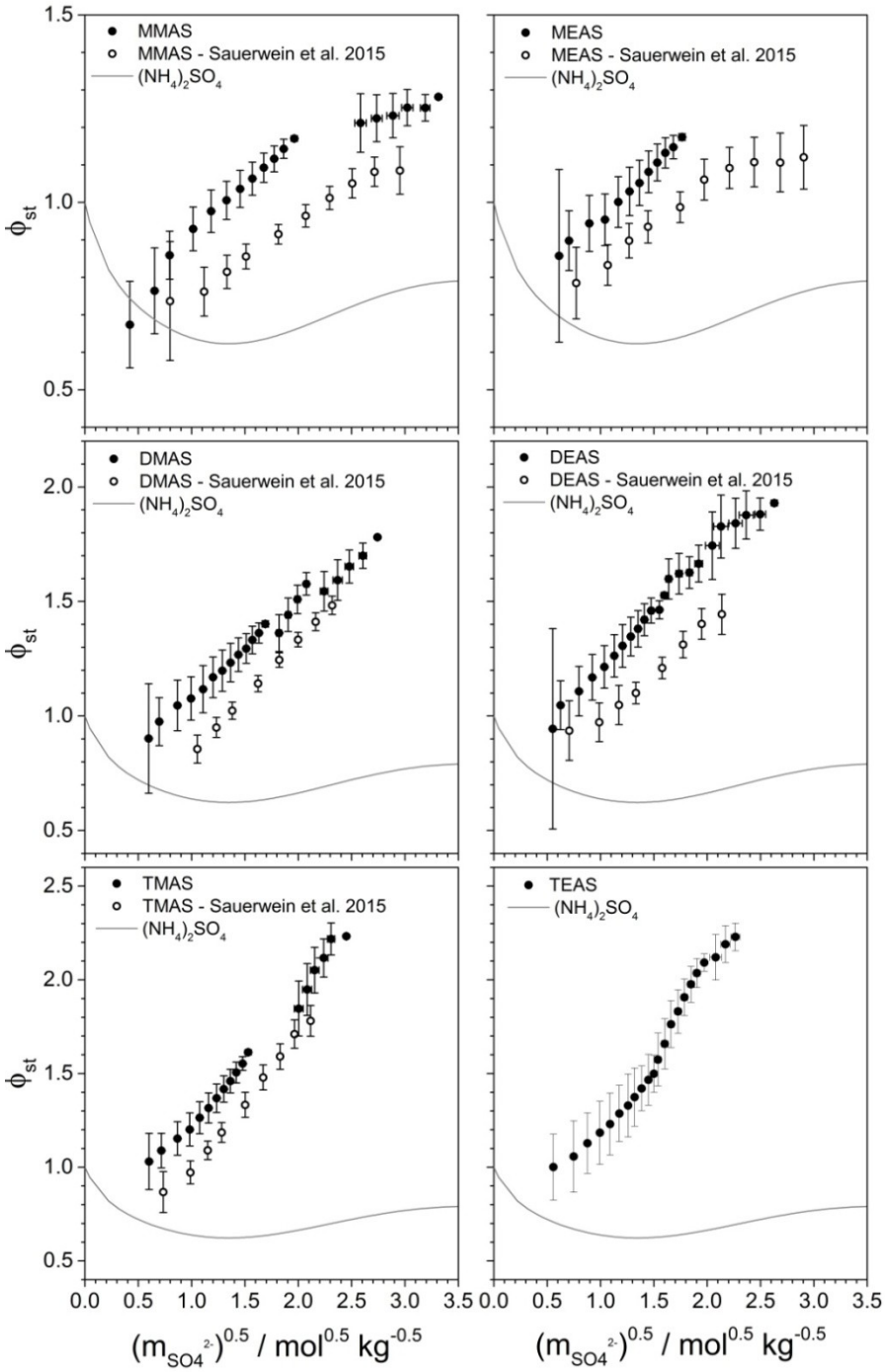

Figure 7.10: osmotic coefficients vs. $m(SO_4^{2-})^{0.5}$ from C-EDB comparative kinetics measurements (solid circles) compared with data from Sauerwein et al. (2015)[73] (open circles) and $(NH_4)_2SO_4$ calculation from the E-AIM Model (grey solid line).

and DEAS ($m(SO_4^{2-})^{0.5}$ <1, approximately), but also in the region $m(SO_4^{2-})^{0.5}$ >2 for DMAS and TMAS. Despite these discrepancies, results from the two different experimental methods show the same hygroscopicity trends over the methyl and ethylaminium sulphates series, conversely to results from the H-TDMA measurements[81] that did not allow the discrimination of different hygroscopic behaviour among the considered compounds.

Some work was done in order to understand these discrepancies. The evaporation kinetics measurements technique in the C-EDB was validated by means of the determination of the hygroscopic properties of well-characterised inorganic compounds and their mixtures (Chapter 6). In addition, sensitivity tests were performed to evaluate possible effects of random experimental errors associated with the proposed experimental method. The reproducibility of the measurements and the uncertainty associated with the density parameterisations used are presented in Sections 7.1.4 and 7.1.5, where it is shown that they do not affect significantly the determined hygroscopic properties of a compound. Thus, other possible sources of error related to the physicochemical features of these particular aerosol systems were investigated. If these discrepancies were due to a partial volatilisation of the amine in the droplets evaporating in the C-EDB, the observed bias between the two datasets should be opposite, i.e. an underestimation of n_{water}/n_{solute} and of osmotic coefficients would be expected, similarly to what was discussed in the case of the H-TDMA size-based measurements from Qiu and Zhang (2012)[81] and converted to a molar basis by Clegg et al. (2013)[104]. Another potential source of error could be an inaccurate knowledge of the concentrations of the aminium sulphates initial solutions. In this respect, the solution preparation method described in Section 7.1.1 was validated through the reaction of ammonia and sulphuric acid and the measurements of the hygroscopic properties of the obtained $(NH_4)_2SO_4$. The results of this test proved the validity of the proposed method and if the volatilisation of NH_3 during the neutralisation reaction was not an issue it cannot have represented a problem for the considered alkylamines, since they are characterised by lower vapour pressures than ammonia (Table 7.1). Furthermore, in order to achieve complete agreement with the data from Sauerwein et al. (2015)[73] the aminium sulphates solutions should be 5-10% more concentrated than what was calculated from the titration of the commercial stock solutions and from the amount of the reagents. Not only does this percentage seem unrealistically high, but also if any volatilisation of the amine occurred during the preparation of the solutions the solute concentrations would be overestimated and not underestimated.

Therefore, in order to understand these differences, the data treatment of the bulk measurement results in Sauerwein et al. (2015)[73] needs to be described more in detail. First of all, a linear interpolation of the experimentally determined water activities was necessary, since measurements were taken at different molality values and this

interpolation is needed so that data for the different aminium compounds can be compared at fixed a_w values (note that this operation was done on the C-EDB data as well, but just to allow the comparison in Figure 7.11). Subsequently, these interpolated datapoints at fixed water activities were fitted with the Zdanovskii-Stokes-Robinson (ZSR) model[106,268], in the simplified form[119] shown in Eq. 7.3:

$$W_{tot} = w_a^0 + w_{salt}^0 + (n_a + n_{salt}) x_a x_{salt} A^0 \qquad 7.3$$

where W_{tot} is the total mass of water in the mixture, w^0 is the mass of water associated with the acid (a) or to the aminium sulphate ($salt$), x_a and x_{salt} are the mole fractions of the two dry solutes (calculated as: $x_a = n_a/(n_a+n_{salt})$ and $x_{salt} = n_{salt}/(n_a+n_{salt})$, n_a and n_{salt} being molar amounts of acid and of salt, respectively) and A^0 is an empirical parameter obtained by fitting the experimental datapoints.

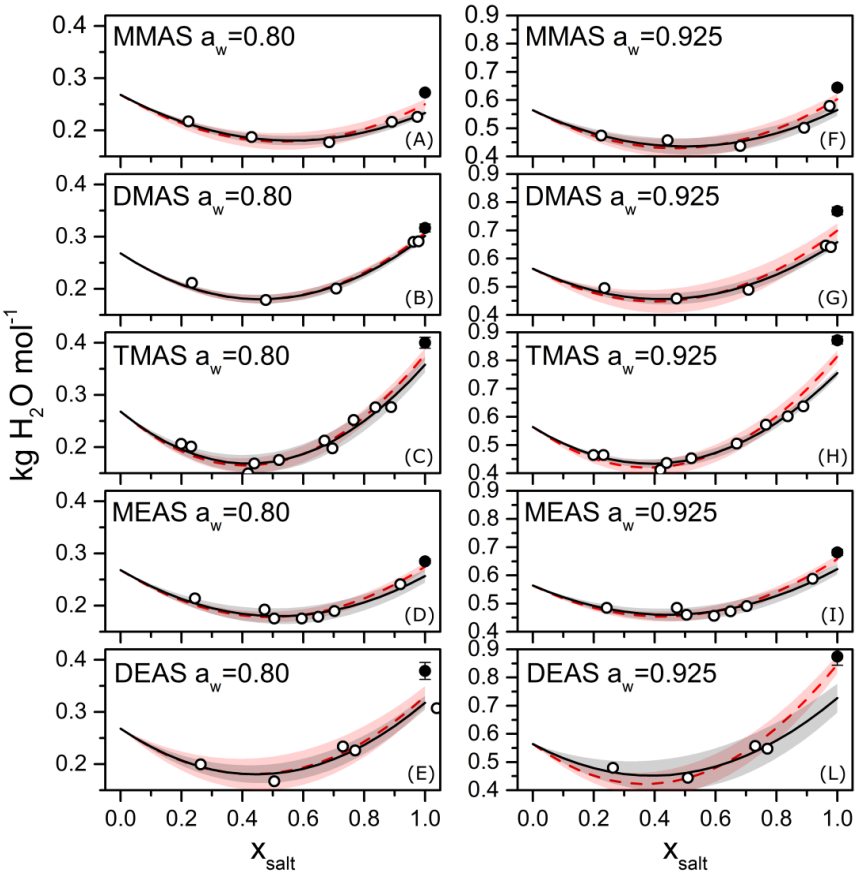

Figure 7.11: kg of H_2O per mole of solute as a function of the degree of neutralisation of sulphuric acid by amine (x_{salt}). Symbols: solid cirles – data from this work; open circles – data from Sauerwein et al. (2015)[73]. Lines: black – fitting of the data in Sauerwein et al. (2015)[73] with Eq. 7.3; red dashed – same fitting but including the C-EDB datapoint

This model provides a framework for the estimation of the water content in mixtures (in this case ternary mixtures of H_2O-H_2SO_4-aminium sulphate) with different molar ratios between the solutes. This allowed the authors to calculate the water content (in terms of kg of water per mole of solute, or molality) and the stoichiometric osmotic coefficients (Eq. 2.16) for the relevant aminium:sulphate ratio of 1:1 (bisulphate) and 2:1 (sulphate). Examples of these fittings are reported in Figure 7.11, where the water content (kg mol^{-1}) as a function of x_{salt} is shown. x_{salt} can be considered as the degree of neutralisation of sulphuric acid: x_{salt}=0 corresponds to pure H_2SO_4 and the water content in this case is well-known[269] (the ZSR fit is therefore constrained to this value), while x_{salt}=1 corresponds to the completely neutralised aminium sulphate. In Figure 7.11, the open circles are data at fixed a_w from Sauerwein et al. (2015)[73], the black line represents the ZSR fitted curve from parameters in Table 1 of their paper together with its uncertainty (grey envelope, both from parameters in Table 1 of their paper) and the black solid circles represent C-EDB data that have been linearly interpolated at the same fixed a_w for comparison (0.8 in Panels A-E, 0.925 in Panels F-L); as in Sauerwein et al. (2015)[73], the uncertainty of these points is set as the biggest uncertainty among the experimental points used for the interpolation.

The discrepancies between the estimations from bulk and C-EDB measurements shown in Figure 7.9 are present in this case too: at x_{salt}=1, the amount of water associated with each aminium sulphate determined with the comparative kinetics measurements at the two different a_w values is systematically higher than the ZSR fitted value from a_w bulk measurements. The ZSR fittings of these data in Sauerwein et al. (2015)[73] are good and the authors demonstrated that with this approach the performance of the model in estimating the amount of water (and the osmotic coefficients) at arbitrary aminium:sulphate ratios is satisfactory within the uncertainties of the model, which are due to some scatter in the data (TMAS, MEAS, Panels C-D and H-I in Figure 7.11) and to the fewer number of data points available for different x_{salt} values in the case of MMAS, DMAS and DEAS (Panels A-B-E and F-G-L). In the light of these uncertainties and comparing the kg H_2O mol^{-1} determined with C-EDB experiments with the bulk a_w measurements, despite the discrepancies with the extrapolated data from the ZSR fitting at x_{salt}=1, they are in good agreement if the trends of data with increasing x_{salt} are considered.

In order to show this agreement more quantitatively, another ZSR fit of Sauerwein et al. (2015)[73] data was performed including the datapoint from C-EDB comparative kinetics measurements (red dashed line with light red uncertainty envelope in Figure 7.11). In most cases, this second fitted ZSR curve doesn't introduce significant variations for x_{salt}<0.6 while it predicts higher values in the higher end of the curve. In addition, the uncertainty of the fitting is comparable between the two cases, except for DEAS (both fixed a_w, Panels E and L) and for DMAS at a_w=0.925 (Panel G), for which the scatter of

the datapoints and their number result in a bigger error envelope than for the other compounds. Consequently, the discrepancies seen in terms of n_{water}/n_{solute} (Figure 7.9), osmotic coefficients (Figure 7.10) and kg of water per mole of solute in Figure 7.11 can be attributed to the uncertainty in the ZSR fittings and to the errors associated to the two different experimental techniques. Sauerwein et al. (2015)[73] state that there is no physical reason why a simple relation such as the one in the applied ZSR approach (Eq. 7.3) should exactly represent the relationships that connects the water activity with the variable chemical composition of such systems, even if it is able to describe it satisfactorily when including the C-EDB datapoints in the fitting (red dashed curve in Figure 7.11). In addition, the measurements of the hygroscopic properties of aminium sulphates discussed in this Chapter are directly carried out on solutions characterised by 2:1 amine-to-sulphate ratios, whereas data from Sauerwein et al. (2015)[73] are derived by means of a ZSR fitting (Eq. 7.3) of experimental data of solutions with other amine-to-sulphate ratios.

As a final remark, it is worth noting that with the C-EDB experimental technique applied in this work the characterization of the hygroscopic properties of aminium sulphates up to a_w of 0.99 was possible. The other literature approaches that were discussed in this Section were able to cover larger a_w ranges (down to 0.1) but none of them could be applied to obtain any data for a_w>0.9. Thus, the comparative kinetics measurements in a C-EDB provide a powerful tool for investigating a water activity region that is otherwise hard to characterise with such accuracy but which is of great importance for the understanding of the activity of aerosol particles as cloud condensation nuclei (Section 2.1.4).

7.1.4 Reproducibility of Measurements

In Section 6.1.3 (Figure Figure 6.5), the reproducibilty of the hygroscopic growth curves for NaCl retrieved from the evaporation kinetics of 10 different droplets whithin a single dataset was shown, in order to uphold the averaging of the hygroscopic properties over multiple droplets within a dataset. Here, in order to evaluate the reproducibility of the solution preparation method (Section 7.1.1) and of the retrieval of hygroscopic properties of a compound from comparative evaporation kinetics measurement, data obtained from three different datasets of evaporating DMAS solution droplets are compared in Figure 7.12. The n_{water}/n_{solute} vs. a_w curve (Panel A) and the osmotic coefficient vs. square root of sulphate mass fraction (Panel B) for DMAS are calculated from three different data sets of 10 droplets each, measured on different days (22/05/2014, 16/10/2014 and 24/03/2015) from different starting stock solution of diethylaminium sulphate. Data from

Sauerwein et al. (2015)[73] (open circles) and calculations for ammonium sulphate (E-AIM Model, grey line) are plotted for comparison as well. Measurements were taken at RH ~ 80%. The reproducibility of the obtained curves is very satisfcatory, giving further proof that the proposed experimental method is valid and reliable. In addition, this satisfactory experimental reprodubility proves that the discrepancies with Sauerwein et al. (2015)[73] discussed in Section 7.1.3.1 cannot originate from random errors associated with the C-EDB experiments.

Observing the error bars in Figure 7.12, a brief consideration on their variable amplitude within a dataset and among different datasets is necessary. If the three different datasets are compared, they are characterized by small differences in the amplitude of their error bars and these are due to the internal reproducibility of measurements from the ten different droplets that compose a single dataset (Section 6.1.3). If the variability of the uncertainties within an individual dataset is considered, that is related to the variability of the uncertainty of the sulphate molality, because it changes during the evaporation of a droplet (see the calculation of uncertainties in Table 6.1); all these aspects reflect in the overall calculation of the uncertainties of osmotic coefficients.

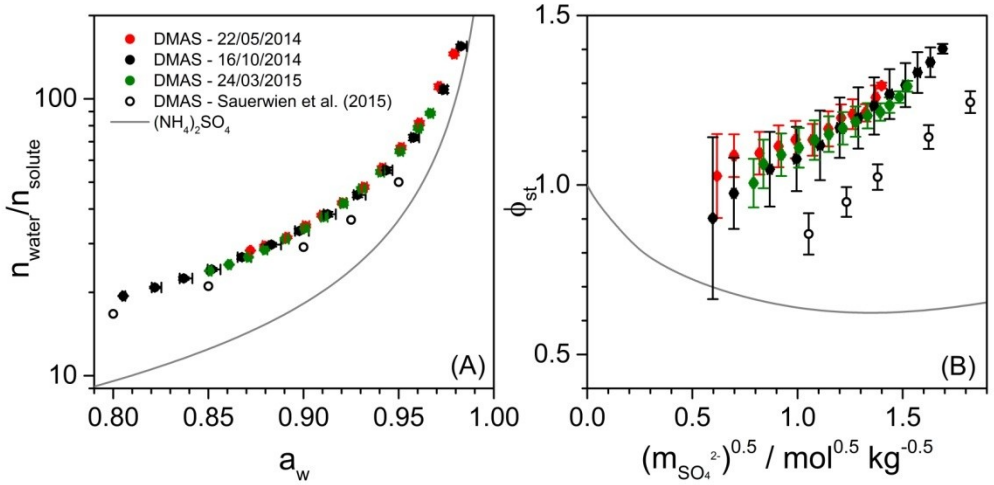

Figure 7.12: Evaluation of the reproducibility of measurements of the hygroscopic properties of DMAS. Lines: $(NH_4)_2SO_4$ calculations from the E-AIM Model. Symbols: solid circles – C-EDB experimental measurements from three different solutions; open circles: data from water activity measurements in Sauerwein et al. (2015)[73].

7.1.5 Sensitivity to Density Parameterization

A parameterisation of density as a function of solute concentration is needed for the processing of C-EDB evaporation radius profiles (Section 5.2.3). The effect of uncertainties on the density parameterization used was evaluated for DMAS, in order to estimate how potential errors in the density measurements and uncertainties in the extrapolation of ρ_{melt} at mfs=1 could affect the hygroscopicity data calculated from comparative kinetics measurements. In Figure 7.13, the densities of DMAS solutions measured in this work are shown (black squares) together with their 3rd order polynomial fit (black line), which is the parameterization used in all the calculations for this compound (Table 7.2). A ±2% error was set on the melt density (mfs=1) and for the rest of the curve the error is linearly decreased with $mfs^{0.5}$ (grey envelope in Figure 7.13). The two obtained 3rd order polynomials (called 'Error+' and 'Error-' in Table 7.3, respectively) were applied together with the molar refraction mixing rule for the data treatment of the DMAS original evaporation kinetics datasets.

Density data from Clegg et al. (2013)[104] are also shown in Figure 7.13 for comparison (red dots); a little discrepancy between their measurements and the data presented in this work is observed, not only for DMAS but also for the other 5 aminium sulphates they considered; no clear pattern can be observed from these differences. However, they can probably be attributed to the different preparation procedures of the aminium sulphates solutions and to the different experimental techniques for the measurement of densities. Clegg and co-workers[104] removed water under vacuum from the solution obtained from the reaction of each amine and H_2SO_4, obtaining a 'solid' aminium sulphate, which was then dissolved in a small amount of water; successive dilutions of the same solutions were then performed and at each dilution step the diluted solution was weighted in a volumetric flask to calculate its density. The same approach was at first tested in this work too with DMAS: after removing the water under vacuum as indicated by Clegg et al. (2013)[104], an amorphous gel-like solid was formed and in the moment that the flask was removed from the vacuum pump and the solid was exposed to the laboratory air water adsorption by the solid could be seen to the naked eye, since its surface appeared 'wet'. Therefore, this approach was no longer followed, because the presence of unaccounted water when weighing the 'dry' solid could result in a wrong determination of the actual concentration of aminium sulphates in solution. The densities of at least ten solutions obtained by non-successive dilutions of a concentrated stock solution prepared as described in Section 7.1.1 were measured with a density meter (Section 7.1.2) for each aminium sulphate, which represents another difference with the experimental procedure of Clegg and co-workers[104]. In addition, densities in this work were measured at ambient temperature (293-295 K, Section 7.1.2), while in their work they operated at 297 K.

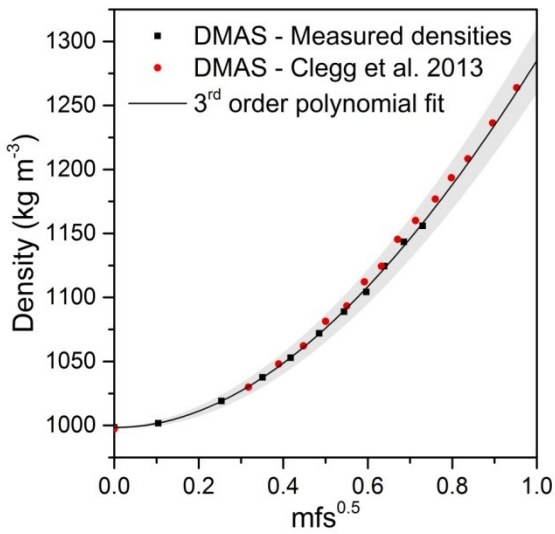

Figure 7.13: DMAS density measurements (black squares) and their 3rd order polynomial fit as a function of $mfs^{0.5}$ of solute. Data from Clegg et al. (2013)[104] are also shown for comparison (red circles).

	3rd order polynomial density coefficients				Melt	Melt ρ /
	a	***b***	***c***	***d***	**R.I.**	g cm^{-3}
DMAS	0.99847	$-2.55 \cdot 10^{-3}$	0.34103	-0.05191	1.4725	1.2850
Error+	0.99847	0.017256	0.342053	-0.04702	1.4665	1.3108
Error-	0.99847	-0.02231	0.339909	-0.05675	1.4783	1.2593

Table 7.3: Parameters of the 3rd order polynomial parameterisation for density and for the molar mixing rule (Section 5.2.3). DMAS is the original fitting of experimental data (black circles in Figure 7.13), while 'Error+' and 'Error-' are calculated supposing a ±2% error on the extrapolated ρ_{melt}, as described in the text.

The hygroscopic properties of DMAS obtained from the treatment of the evaporation kinetics data with the 'original' density parameterization (black squares), with the 'Error+' (purple triangles) and the 'Error-' (light blue diamonds) parameterisations are shown in Figure 7.14. Data from Sauerwein et al. (2015)[73] (open circles) and calculations for ammonium sulphate (E-AIM Model, grey line) are plotted for comparison as well. When the hygroscopic properties of DMAS are represented either in terms of n_{water}/n_{solute} or GF_r vs. a_w (Panels A and B), the three curves deriving from the three different data treatments are virtually undistinguishable and a possible uncertainty in the applied density parameterisation does not seem to be significant because they are comparable to the other experimental uncertainties of the C-EDB measurements. In the case of the osmotic coefficients plot (Panel C) some very slight deviations within the three curves

can be distinguished at the two extremes of the plot. With respect to the low sulphate molality region, these small differences are due to the fact that a small variation in the sulphate molality results in more relevant variations in the osmotic coefficients, because m_{st} appears in the denominator in the osmotic coefficient expression (Eq. 2.16). If the high sulphate molality region is considered, the variations among the three curves are a bit more significant because the simulated error on the density parameterisation is bigger for more concentrated solutions (grey envelope in Figure 7.13).

Therefore, the hygroscopic properties of aminium sulphates determined by means of comparative kinetics measurements in a C-EDB are relatively insensitive to reasonable variations in the extrapolated ρ_{melt} value ($\pm 2\%$) and to the applied density parameterisation. In addition, if the variations introduced by different density parameterisations are compared to the discrepancies found with the data from Sauerwein et al. (2015)[73], it is clear that their differences with the C-EDB datasets cannot be caused by inaccurately accounted for variations of the density of the evaporating droplets.

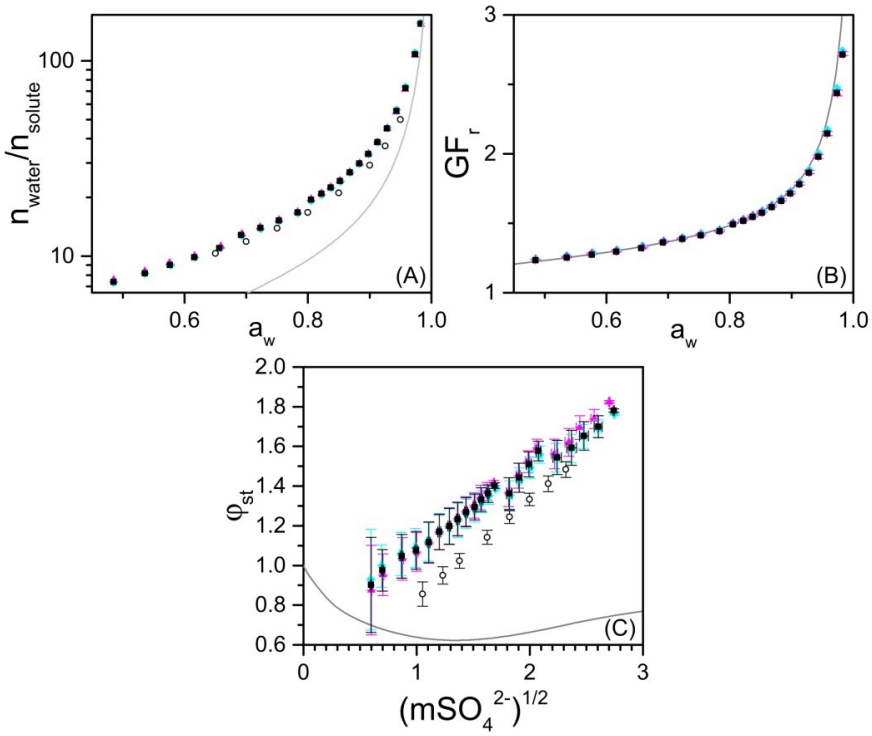

Figure 7.14: Hygroscopic properties of DMAS obtained from the treatment of the C-EDB kinetics evaporation data with the three different set of parameters in Table 7.3. Symbols: black circles – original data; pink triangles – obtained with 'error+' parameters; light blue diamonds – obtained with 'error-' parameters; open circles – Sauerwein et al. (2015) Line – E-AIM Model for $(NH_4)_2SO_4$.

More generally, note that aminium sulphates are very soluble compounds and it was possible to directly measure the density of their bulk solutions over a wide range of solute mass fractions (up to $mfs^{0.5}$ values of 0.67-0.85, depending on the compound); consequently, the $mfs^{0.5}$ range over which the extrapolation for the calculation of ρ_{melt} is needed is quite small and an uncertainty of ±2% (Figure 7.13) seems reasonably large for the evaluation of its effects. This could be different for less soluble organic compounds and, if density extrapolations over wider ranges are needed, the uncertainties associated to such extrapolations should be evaluated, too.

7.1.6 Vapour Pressures of Amines over Aminium Sulphate Solutions

The determination of the vapour pressures of semi-volatile compounds is important for the understanding of their impact on cloud droplet activation and other physicochemical properties of atmospheric aerosol particles (Section 2.1). The C-EDB is suitable for the estimation of vapour pressures down to ~10^{-6} Pa[144] since they can be estimated from the evaporation kinetics of aerosol particles.

As discussed in Section 2.3, water evaporation from a droplet occurs until when the water activity in the solution is equal to the RH in the gas phase and an equilibrium between the liquid and the gas phases is established. If, besides water, non-volatile compounds are present in solution, when the equilibrium radius is reached by a droplet it is going to be constant, if the RH is kept constant. If a semi-volatile compound is present in the considered aerosol system, it will partition between the droplet and the surrounding gas phase, as well. With respect to aminium sulphates, the equilibrium that is estabilished within the liquid phase and with the surrounding gas phase is shown as a schematic in Figure 7.15, taking as an example methylamine.

The cations in solution are in equilibrium with the neutral form of the amine and this equilibrium is characterised by a certain pK_a for each compound (Table 7.1). In addition, an equilibrium between the amine in the gas and in the aerosol phase is present too and the amount of $CH_3NH_{2(gas)}$ depends on the pure component vapour pressure of the compound (p^0). The partitioning of water is going to be affected by possible evaporative losses of the amine in to the gas phase and, in order to keep the water activity in the solution constant, some water will evaporate together with the semi-volatile.

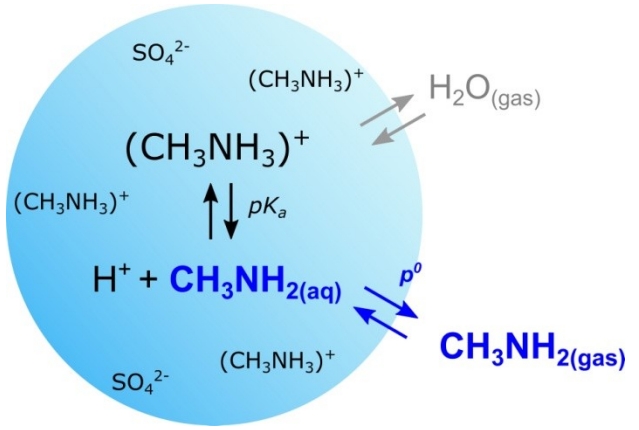

Figure 7.15: Equilibria established between a methyaminium sulphate solution droplet and the gas phase.

The partial vapour pressure of a semi-volatile substance over a multi-component droplet can be experimentally determined by measuring the mass flux from the droplet to the gas phase, at constant RH conditions[3]. If the mass loss from the droplet is expressed in terms of the change in particle radius squared with time (da^2/dt), the single component vapour pressure of the amine partitioning from an aminium sulphate solution droplet to the gas phase ($p_{amine,a}$) can be written as follows[270]:

$$\left(p_{amine,\infty} - p_{amine,a}\right) = \frac{mfs_{amine}\rho RT}{2M_{amine}D_{amine}x_{amine}f_{amine}}\frac{da^2}{dt} \qquad 7.4$$

where $p_{amine,\infty}$ is the partial pressure of the amine at infinite distance from the droplet (in C-EDB experiments single droplets sit in a continuous nitrogen flow (Section 5.2.4), thus $p_{amine,\infty}$=0), mfs_{amine}, x_{amine} and f_{amine} are the mass fraction, the mole fraction and the activity coefficient of the neutral form of the amine in solution, ρ is the solution density, R is the universal gas constant (8.314472 J K^{-1} mol^{-1}), T is the gas phase temperature in Kelvin (steady evaporation and $T_{droplet} \approx T_{gas}$ are assumed, all measurements at 293.15 K), M_{amine} is the molar mass of the considered amine and D_{amine} is the diffusion coefficient of the amine in the gas phase.

ρ, mfs_{amine} and x_{amine} were calculated from the radius of the evaporating droplet after the evaporation of water has completed, from its initial radius and initial concentration and with the density parameterisations shown in Section 7.1.2. f_{amine} was estimated with the E-AIM Model, instead; for this calculation, the parameterisations from Peng et al.[97] were used, and the amount of water, amine and sulphuric acid in solution calculated from EDB measurements were given as an input for the model simulation at 293.15 K. Experimental data for the diffusion coefficients of semi-volatile compounds in the gas phase are difficult to find, but they can be estimated with the Chapman-Enskog theory,

that models the transport properties of binary gaseous mixtures (amine + nitrogen, in this case) calculating intermolecular potential energies from Lennard-Jones potentials[271,272]:

$$D = 0.0018583\sqrt{T^3\left[\frac{1}{M_{amine}}+\frac{1}{M_{N_2}}\right]}\frac{1}{p\sigma^2_{amine,N_2}\Omega_{amine,N_2}} \qquad 7.5$$

where M_{amine} and M_{N2} are the molar masses of the amine and of nitrogen, respectively, p is the pressure of the gas phase (in atm), $\sigma_{amine,N2}$ is the binary collision diameter, which is calculated according to Eq. 7.6 (V_c is the molar volume) and represents the average diameter of the two colliding chemical species, $\Omega^2_{amine,N2}$ is the collision integral for diffusivity, which is calculated according to Eq. 7.7[272]. Even if water is also present in the gas phase, this was not taken into account for the calculation of the diffusion coefficient of the amines in the gas phase, since the H_2O molar fraction is negligible.

$$\sigma^2_{amine,N_2} = 0.5\left(\sigma_{amine}+\sigma_{N_2}\right);\ \sigma_i = 0.841{V_c}^{1/3} \qquad 7.6$$

$$\Omega = \frac{1.06036}{T^{*0.15610}}+\frac{0.19300}{exp\ (0.47635T^*)}+\frac{1.03587}{exp\ (1.52996T^*)}+\frac{1.76474}{exp\ (3.89411T^*)} \qquad 7.7$$

In Eq. 7.7, T^* is the reduced temperature, expressed as $T^*=k_BT/\epsilon_{amine,N2}$, where k_B is the Boltzmann constant and $\epsilon_{amine,N2}$ represents the Lennard-Jones parameter describing the intermolecular interaction ($\epsilon_{amine,N2}=(\epsilon_{amine}\cdot\epsilon_{N2})^{1/2}$ and $\epsilon/k_B=1.92T_m$ (T_m is the melting point temperature, values from CRC Handbook[246]). All the parameters used for the calculation of the relevant D_{amine} diffusion coefficient are summarised in Table 7.4.

Compound	σ / cm mol^{-1}	ϵ/k_B	$\Omega_{amine,N2}$	D / cm^2 s^{-1}
N_2	3.798	71.4	-	-
TMA	3.784	299.616	1.07456	0.1385
TEA	4.358	304.224	1.07742	0.1111

Table 7.4: Parameters used for the calculations of D_{TMA} and D_{TEA}, as described in the text. The diffusion coefficient values obtained are reported as well.

In order to estimate $p_{amine,a}$ for the six aminium sulphates characterised in this study, da^2/dt in Eq. 7.4 were measured at different RH values by means of long trapping measurements. In Figure 7.16, an example of the outcome of such experiments is given for a droplet of TEAS solution evaporating at RH=49%. After the first rapid evaporation of water from the droplet (~ 5 s, radius decreasing from about 25 to 12 μm), a further slow mass loss is observed for the following 200 s: the a_w in solution is constant, because the gas phase RH is kept constant, and the change in radius is due to the evaporative

loss of some amine from the solution. da^2/dt is calculated by linearly fitting this second portion of the evaporation profile (converted to radius squared). Note that the one shown in Figure 7.16 is the case where the biggest mass loss was observed (see the measured gradient values in Table 7.5). Considering the minimum radius variations that can be measuread with the C-EDB (Section 5.2.2) and the fitting of light scattering patterns with Mie-theory simulation (Section 5.2.2.2), vapour pressures down to ~10^{-6} P can be measured with this approach, assuming a minimum necessary size change of 100 nm[144] for an accurate fit of da^2/dt.

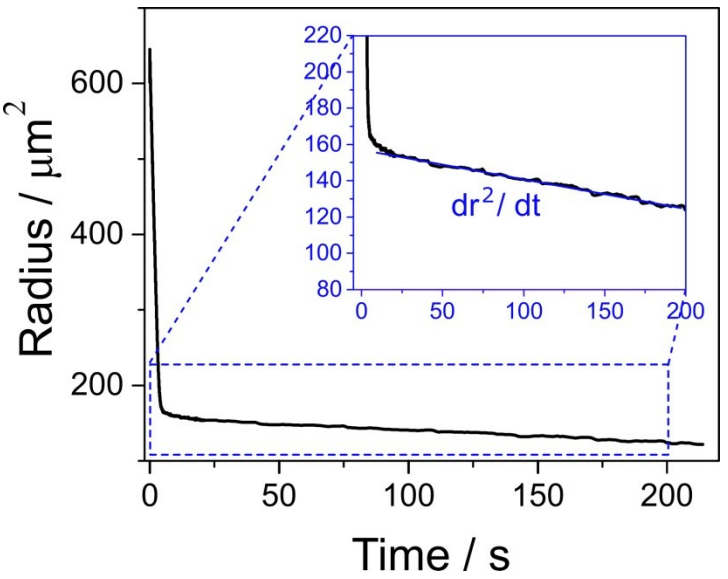

Figure 7.16: Example of a long trapping measurement in a C-EDB for the determination of the vapour pressure of semi-volatile compounds. The squared radius profile refers to a TEAS droplet evaporated at RH=49%.

The gas phase RH was checked before and after the long trapping of a single test droplet with either water or NaCl droplets used as a probe (Section 6.1.1) and only experiments for which the measured RH was constant were considered. Because of the comparative method used in the C-EDB for the determination of the gas phase RH, it was not possible to keep track of possible RH fluctuations during these long trapping experiments, but the linearity of the evaporation profiles after water evaporation has completely occurred is a good indication that no RH fluctuations affected the measured radius of the droplets.

In the case of long trapping measurements, the sizing of droplets was performed by collecting the intensity of the angularly resolved scattered light (every 0.01 s during water evaporation and every second in the second part of the curve) and by fitting the

obtained phase functions with simulations from Mie theory, as described in Section 5.2.2.2. The geometric optics approximation was not applied in this case, because the variations in radius that are observed in these experiments (on the order of hundreds of nm) are small and a higher accuracy in sizing is preferable.

Interestingly, it was not possible to measure p_{amine} from evaporation profiles of MMAS, DMAS, MEAS and DEAS, because on the timescales of these long trapping measurements (up to 500 s) the part of the curve after water evaporation had completed was flat and no significant evaporation of amine could be observed over the gas phase RH range considered (~50-80% RH). This means that the evaporative loss of amine for these compounds is too slow to be observed by means of this experimental technique. It also implies that the volatilisation of MMAS, DMAS, MEAS and DEAS from evaporating droplets during comparative kinetics experiments is not an issue, because this phenomenon cannot be observed over much longer timescales than those covered by the water evaporation in comparative kinetics experiments (less than 30 s).

The only two compounds for which this evaporative loss of amine could be observed were TMAS and TEAS. Table 7.5 shows the average calculated p_{TMA} and p_{TEA} values for the corresponding amines are p_{TMA}=6.6·10^{-2}±3.0·10^{-2} Pa (average over 5 measurements at different RH) and p_{TEA}=4.6·10^{-1}±2.9·10^{-1} Pa (average over 4 measurements at different RH), respectively.

TMAS solutions

RH	$\mathbf{d(a^2)/dt}$ ($m^2\ s^{-1}$)	$\boldsymbol{p_{TMA}}$ (Pa)
48.2%	$-4.57 \cdot 10^{-14}$	$1.1 \cdot 10^{-1}$
62.8%	$-2.15 \cdot 10^{-14}$	$7.2 \cdot 10^{-2}$
63.3%	$-1.78 \cdot 10^{-14}$	$4.9 \cdot 10^{-2}$
71.4%	$-2.02 \cdot 10^{-14}$	$6.2 \cdot 10^{-2}$
88.0%	$-8.94 \cdot 10^{-15}$	$3.5 \cdot 10^{-2}$
	Average	$6.7 \cdot 10^{-2}$
	s	$3.0 \cdot 10^{-2}$

TEAS solutions

RH	$\mathbf{d(a^2)/dt}$ ($m^2\ s^{-1}$)	$\boldsymbol{p_{TEA}}$ (Pa)
49.0%	$-1.24 \cdot 10^{-13}$	$3.3 \cdot 10^{-1}$
53.0%	$-1.95 \cdot 10^{-13}$	$8.7 \cdot 10^{-1}$
71.2%	$-9.35 \cdot 10^{-14}$	$3.5 \cdot 10^{-1}$
79.9%	$-4.66 \cdot 10^{-14}$	$2.0 \cdot 10^{-1}$
	Average	$4.4 \cdot 10^{-1}$
	s	$2.9 \cdot 10^{-1}$

Table 7.5: Measured radii gradient after complete water evaporation (da^2/dt) of TMAS and TEAS solutions at variable RH, together with the corresponding p_{TMA} and p_{TEA}, calculated using Eq. 7.4.

The single component vapour pressures calculated over trimethyl and triethylaminium sulphate solutions are seven and four orders of magnitude lower than the pure component vapour pressures of TMA and TEA indicated in Table 7.1, respectively (231

and 9.03 kPa). This is due to the acid-base equilibrium established by the presence of sulphuric acid in solution (Figure 7.15), which significantly lowers the vapour pressure of the amines, as anticipated in Section 7.1, since the amount of the volatile form of the neutral amine in solution is very small. In fact, if the mass fractions of the neutral amines (mfs_{TMA} and mfs_{TEA}) in the considered TMAS and TEAS are calculated using the pKa values in Table 7.1, they result in the order of 10^{-6}, whereas mfs_{TEAS} and mfs_{TMAS} span from ~0.2 to ~0.6 at after the first fast evaporation of water, depending on the gas phase RH.

In addition, thanks to the calculation of p_{TMA} and p_{TEA}, it is possible to calculate the amount of amine loss from TMAS and TEAS evaporating droplets over significant timescales for comparative kinetics experiments in the C-EDB.

7.2 Summary and Conclusions

In this Chapter, the hygroscopic properties of aminium sulphates were investigated. These are organic salts that result from the neutralisation reaction of sulphuric acid by amines. Such compounds have been found in atmospheric aerosols, because short-chained amines can convert from the gas to the particle phase following different pathways. Hence, the understanding of the hygroscopic properties of aminium sulphates is important for an accurate understanding and modelling of some atmospheric processes they can be involved in (e.g. formation and growth of new particles, activation of cloud droplets). In order to measure their hygroscopic properties with comparative kinetics measurements in a C-EDB, the dependence of aminium sulphates solution densities and refractive indices on mass fraction of solute were measured. Different hygroscopicity trends were observed when the obtained growth curves were plotted either in terms of radial growth factors or of moles of water per moles of solute. This result allowed some considerations on how different parameters used to represent the hygroscopicity of an aerosol system can give different perspectives on the hygroscopic properties of a compound, because each parameter is able to reflect a different aspect of the same complex property. All the experimental results were also compared with the few studies available in the literature and the observed discrepancies were discussed in the light of the different experimental approaches.

Long trapping experiments were carried out to quantify the single component vapour pressures of amines over aminium sulphate solutions. After the first fast evaporation of water, no significant mass loss was observed for MMAS, DMAS, MEAS and DEAS solutions, indicating that their pure component vapour pressures are too high to be

observed by means of long trapping measurement in the C-EDB, over the considered timescales (up to 500 s). On the contrary, it was possible to measure the single component vapour pressures of TMA and TEA over TMAS and TEAS solutions. The measured values resulted several orders of magnitude less than the vapour pressures of the pure compounds. These results indicate that the acid-base reaction with sulphuric acid significantly lowers the volatility of the six considered amines.

Aminium sulphates represented the first class of more complex aerosol systems to be investigated by means of the C-EDB comparative kinetics technique over a wide range of water activities. Therefore, besides their atmospheric relevance, this study was also fundamental for a deeper understanding of all the possible effects caused by eventual random errors in the experimental procedure, potential uncertainties on the representation of the density of a compound and possible issues caused by evaporative losses of semi-volatile compounds. For these reasons, reproducibility tests, evaluation of different density parameterisations and the measurement of the amines pure component vapour pressures were performed.

Chapter 8 Summary and conclusions

The hygroscopic properties of atmospheric aerosols determine their interaction with water molecules in the gas phase and they strictly depend on the heterogeneous chemical composition of particles, which includes both inorganic and organic species. The phase transitions relative humidity and the hygroscopic properties of atmospheric aerosols determine the physical state and the water content of particles in the atmosphere. The size distribution of particles and their optical properties are strictly dependent on their hygroscopic properties. The interplay of all these interdependent chemico-physical properties of atmospheric aerosol particles influences their climate and health effects and also the potential risk that deposited particles on surfaces represent for sensitive materials. For a better understanding of the impact of atmospheric aerosols in these field of research, their hygroscopic properties need to be better understood and constrained in aerosol thermodynamic models.

Within this context, in this thesis two complementary approaches for improving the understanding of the hygroscopic properties of aerosols were employed. First, the characterisation of the deliquescence and crystallisation relative humidity of $PM_{2.5}$ atmospheric aerosol samples was performed by means of an electrical conductance method. Successively, with a change of perspective, an experimental technique for the measurement of the hygroscopic properties of single confined aerosol particles was proposed, validated and applied for the characterisation of the hygroscopicity of a first class of atmospherically-relevant mixtures.

These two approaches partially reflect the current research themes on atmospheric aerosols in the literature. First, accurate laboratory measurements over a wide relative humidity range and up to values close to saturation are needed to provide the necessary data for an improvement of the current aerosol thermodynamics models. On the other side, the observation and rationalisation of the hygroscopic properties of atmospheric aerosol particles as they are found in the atmosphere are essential to understand their role in atmospheric processes and their effects on substrates they may deposit on, but also to validate the prediction of aerosol models.

In the first part of this work, an experimental approach that combines standardised $PM_{2.5}$ sampling of atmospheric aerosol particles, conductance measurements in an Aerosol Exposure Chamber for the investigation of phase transitions during humidity cycles and ion chromatography analysis for the characterisation of the chemical composition of the ionic fraction of samples was proposed. This experimental approach was presented in Chapter 3, together with the description of its development and improvement and with the tests that were carried out to prove the validity of the conductance method.

The results of DRH and CRH measurements on $PM_{2.5}$ aerosol samples were presented in Chapter 4. One of the most relevant findings was represented by the correlation of the seasonal trends of the deliquescence and crystallisation RHs frequency distributions with the seasonally-modulated chemical composition of samples, typical of atmospheric aerosols in the Po valley. This aspect is relevant because it has implications in various fields of applications, such as the safe operation of DFC Data Centers, the risk assessment on stone cultural heritage artefacts associated to the contamination with deposited particles and the determination of ground-level particles concentrations with remote sensing techniques. These three applications of the electrical conductance measurements were discussed in Chapter 4 and it is worth highlighting what all three of them evidenced. First of all, it was shown how simplified approaches that do not consider the hysteresis behaviour of the hydration state of aerosols can lead to bias and to a partially incomplete characterisation of the effects of atmospheric aerosols. In addition, the direct characterisation of DRH and CRH values and of their characteristic seasonal trends evidenced that the temporal and spatial heterogeneity of the chemical composition of particles results in different effects of particles at different times of the year and in different sampling sites.

A future development of this part of the work is represented by the direct observation of deliquescence and crystallisation processes of aerosol particles deposited on materials of interest (e.g. stone porous materials, printed circuit boards assemblies). The aim would be that of observing the effects triggered by the phase changes and by the water absorption of aerosol particles directly on surfaces of interest. The work of by D'Angelo (2016)[161] and Casati (2016)[162] lays the foundations for this future applications by proposing standardised aerosol sampling techniques on non-filtering substrate.

A comparison of the measured deliquescence relative humidity with simulations from E-AIM Model was performed, giving the ionic fraction and the carboxylic acids quantified compositions as an input to the model. It was interesting that the overall seasonal trends experimentally individuated were reproduced by the calculated DRH values from E-AIM Model, even though the ionic fraction given as an input to the model represents only up to ~40% of the overall $PM_{2.5}$ aerosols mass. However, a bias of 5% RH in the DRH frequency distribution plots and a very limited point-to-point agreement between

modelled and experimental data were evidenced. These results indicated that the driving force of deliquescence are the ionic components but also that the individuated discrepancies are most likely due to the unaccounted hygroscopic properties of other organic species in the analysed aerosol samples.

In the second part of this work, a single particle technique was proposed for the quantification of the equilibrium hygroscopic properties of atmospherically-relevant aerosol components. Generally speaking, single particle techniques present the advantage of observing an isolated confined particle within a controlled environment, so that its behaviour can be decoupled from the particle-particle interactions that complicate ensemble measurements. In addition, measurements in the aerosol phase allow to evaluate the properties of particles in superasaturated conditions that cannot be investigated with bulk measurement techniques.

The concentric cylindrical electrodynamic balance (C-EDB) experimental setup and the comparative kinetics approach presented in Chapters 5 and 6 lay their foundation in the work of Davies et al.[96,144]. Electrodynamic trapping allows single charged droplets to be confined within an electrical field and the concentric cylindrical electrodes setup assures that the confinement of droplets is fast and tight. The equilibrium hygroscopic properties of droplets were retrieved from comparative evaporation kinetics experiments of probe and sample droplets. The evaporation rate of a pure water or of a NaCl solution droplet is measured and interpreted by means of a literature evaporation kinetics model by Kulmala et al. (1993)[145] for the estimation of the gas phase RH within the trapping chamber. The same model is then applied to sample droplets evaporation profiles to retrieve their equilibrium hygroscopic properties using the gas phase RH determined from probe droplets.

This previously developed technique was widened and validated for its application to a wider RH range, from 50% RH up to values close to saturation (>99%). With this respect, the limitations of the applied literature kinetics model needed to be taken into account and, in order to retrieve the hygroscopic properties over the desired RH range and overcome these limitations, evaporation kinetics measurements on binary and ternary mixtures were performed at multiple RHs. The proposed approach was successfully validated by means of measurements on well-characterised inorganic compounds (Na_2SO_4, $(NH_4)_2SO_4$, $NaNO_3$, NaCl) and ternary mixtures of ammonium sulphate and sodium chloride, which were compared with E-AIM Model simulations. One of the key features of the comparative evaporation kinetics approach for the determination of the equilibrium hygrosfcopic properties of single particles is that water activity values close to saturation can easily and accurately be characterised. This aspect is of great importance for a better constraint of the hygroscopic properties of aerosols in the estimation of their activation as cloud condensation nuclei.

In Chapter 7, the comparative kinetics technique on single particles levitated in the C-EDB was used for the characterisation of the hygroscopic properties of a first class of mixed inorganic-organic aerosol systems, aminium sulphates. These organic salts are the products of the reaction between sulphuric acid and methyl and ethyl amines and have been detected in atmospheric aerosols. Variable trends in the hygroscopic properties of the six analysed aminium sulphates were individuated depending on the used representation of their water uptake. This result evidenced that the different ways of representing the hygroscopicity of aerosols (on a size or molar basis, in this case) provide different points of view on the water uptake of aerosols. In addition, the obtained data on the hygroscopic properties of aminium sulphates were compared to different literature studies that investigated this class of compounds and the found discrepancies were discussed with reference to the different applied experimental approaches. This comparison also represented a further test for the proposed analytical technique, since all the possible artefacts deriving from potential uncertainties in the applied density and refractive indices parameterisations and possible evaporative losses of other chemical species besides water were investigated.

The extended comparative kinetics approach in a C-EDB proposed in this work represents a promising tool for the accurate characterisation of the hygroscopic properties of atmospheric aerosol components and their mixtures. In the future, this technique can be applied for the investigation of aerosol systems of atmospheric interest (such as multifunctional organic compounds and mixtures of organic and inorganic species), in order to provide accurate data for the improvement of the hygroscopicity parameterisations in current aerosol thermodynamics models.

Bibliography

(1) IPCC (Intergovernmental Panel On Climate Change). *Fifth Assessment Report*; 2013.

(2) Poschl, U. Atmospheric Aerosols: Composition, Transformation, Climate and Health Effects. *Angew. Chemie - Int. Ed.* **2005**, *44* (46), 7520–7540.

(3) Seinfeld, J. H.; Pandis, S. N. *Atmospheric Chemistry and Physics: From Air Pollution to Climate Change*; Wiley, 2006.

(4) Pope, C. A.; Thun, M. J.; Namboodiri, M. M.; Dockery, D. W.; Evans, J. S.; Speizer, F. E.; Heath, C. W. Particulate Air Pollution as a Predictor of Mortality in a Prospective Study of U.S. Adults. *Am. J. Respir. Crit. Care Med.* **1995**, *151* (3_pt_1), 669–674.

(5) Pope, C. A.; Ezzati, M.; Dockery, D. W.; Pope III, C. A.; Ezzati, M.; Dockery, D. W. Fine-Particulate Air Pollution and Life Expectancy in the United States. *N. Engl. J. Med.* **2009**, *360* (4), 376–386.

(6) Schwartz, J.; Laden, F.; Zanobetti, A. The Concentration-Response Relation between PM2.5 and Daily Deaths. *Environ. Health Perspect.* **2002**, *110* (10), 1025–1029.

(7) Malm, C.; Sisler, J. F.; Cahill, A. Spatial and Seasonal Trends in Particle Concentration and Optical Extinction in the United States. *J. Geophys. Res.* **1994**, *99*, 1347–1370.

(8) Perrone, M. G.; Gualtieri, M.; Consonni, V.; Ferrero, L.; Sangiorgi, G.; Longhin, E.; Ballabio, D.; Bolzacchini, E.; Camatini, M. Particle Size, Chemical Composition, Seasons of the Year and Urban, Rural or Remote Site Origins as Determinants of Biological Effects of Particulate Matter on Pulmonary Cells. *Environ. Pollut.* **2013**, *176*, 215–227.

(9) Ferrero, L.; Castelli, M.; Ferrini, B. S.; Moscatelli, M.; Perrone, M. G.; Sangiorgi, G.; Rovelli, G.; D'Angelo, L.; Moroni, B.; Scardazza, F.; et al. Impact of Black Carbon Aerosol over Italian Basin Valleys: High Resolution Measurements along Vertical Profiles, Radiative Forcing and Heating Rate. *Atmos. Chem. Phys. Discuss.* **2014**, *14* (1), 541–591.

(10) Morgan, W. T.; Allan, J. D.; Bower, K. N.; Capes, G.; Crosier, J.; Williams, P. I.; Coe, H. Vertical Distribution of Sub-Micron Aerosol Chemical Composition from North-Western Europe and the North-East Atlantic. *Atmos. Chem. Phys. Discuss.* **2009**, *9*, 9117–9150.

(11) Pant, P.; Harrison, R. M. Critical Review of Receptor Modelling for Particulate Matter: A Case Study of India. *Atmos. Environ.* **2012**, *49*, 1–12.

(12) Andreae, M. O.; Gelencser, A. Black Carbon or Brown Carbon ? The Nature of Light-Absorbing Carbonaceous Aerosols. **2006**, No. 1985.

(13) Jacobson, M. C.; Hansson, H. Organic Atmospheric Aerosols: Review and State of the Science. *Rev. Geophys.* **2000**, No. 1998, 267–294.

(14) Rogge, W. F.; Mazurek, M. A.; Hildemann, L. M.; Cass, G. R.; Simoneit, B. R. T. Quantification of Urban Organic Aerosols at a Molecular Level: Identification, Abundance and Seasonal Variation. *Atmos. Environ. Part A, Gen. Top.* **1993**, *27* (8), 1309–1330.

(15) Srogi, K. Monitoring of Environmental Exposure to Polycyclic Aromatic Hydrocarbons: A Review. *Environ. Chem. Lett.* **2007**, *5* (4), 169–195.

(16) Fuzzi, S.; Baltensperger, U.; Carslaw, K.; Decesari, S.; Denier Van Der Gon, H.; Facchini, M. C.;

Fowler, D.; Koren, I.; Langford, B.; Lohmann, U.; et al. Particulate Matter, Air Quality and Climate: Lessons Learned and Future Needs. *Atmos. Chem. Phys.* **2015**, *15* (14), 8217–8299.

(17) Davies, J. F.; Haddrell, A. E.; Miles, R. E. H.; Bull, C. R.; Reid, J. P. Bulk, Surface, and Gas-Phase Limited Water Transport in Aerosol. *J. Phys. Chem. A* **2012**, *116* (45), 10987–10998.

(18) Shulman, M. L.; Charlson, R. J.; Davis, E. J. The Effects of Atmospheric Organics on Aqueous Droplet Evaporation. *J. Aerosol Sci.* **1997**, *28* (5), 737–752.

(19) Lienhard, D. M.; Huisman, A. J.; Bones, D. L.; Te, Y.-F.; Luo, B. P.; Krieger, U. K.; Reid, J. P. Retrieving the Translational Diffusion Coefficient of Water from Experiments on Single Levitated Aerosol Droplets. *Phys. Chem. Chem. Phys.* **2014**, *16* (31), 16677.

(20) Zobrist, B.; Soonsin, V.; Luo, B. P.; Krieger, U. K.; Marcolli, C.; Peter, T.; Koop, T. Ultra-Slow Water Diffusion in Aqueous Sucrose Glasses. *Phys. Chem. Chem. Phys.* **2011**, *13* (8), 3514–3526.

(21) Krieger, U. K.; Marcolli, C.; Reid, J. P. Exploring the Complexity of Aerosol Particle Properties and Processes Using Single Particle Techniques. *Chem. Soc. Rev.* **2012**, *41* (19), 6631.

(22) You, Y.; Smith, M. L.; Song, M.; Martin, S. T.; Bertram, A. K. Liquid–liquid Phase Separation in Atmospherically Relevant Particles Consisting of Organic Species and Inorganic Salts. *Int. Rev. Phys. Chem.* **2014**, No. October 2015, 1–35.

(23) Hodas, N.; Zuend, a.; Mui, W.; Flagan, R. C.; Seinfeld, J. H. Influence of Particle-Phase State on the Hygroscopic Behavior of Mixed Organic–inorganic Aerosols. *Atmos. Chem. Phys.* **2015**, *15* (9), 5027–5045.

(24) McFiggans, G.; Artaxo, P.; Baltensperger, U.; Coe, H.; Facchini, M. C.; Feingold, G.; Fuzzi, S.; Gysel, M.; Laaksonen, A.; Lohmann, U.; et al. The Effect of Physical and Chemical Aerosol Properties on Warm Cloud Droplet Activation. *Atmos. Chem. Phys. Discuss.* **2005**, *5*, 8507–8646.

(25) Topping, D.; Connolly, P.; McFiggans, G. Cloud Droplet Number Enhanced by Co-Condensation of Organic Vapours. *Nat. Geosci.* **2013**, *6*, 443–446.

(26) Dusek, U.; Frank, G. P.; Hildebrandt, L.; Curtius, J.; Schneider, J.; Walter, S.; Chand, D.; Drewnick, F.; Hings, S.; Jung, D.; et al. Size Matters More than Chemistry for Cloud-Nucleating Ability of Aerosol Particles. *Science* **2006**, *312* (5778), 1375–1378.

(27) Haddrell, A. E.; Davies, J. F.; Reid, J. P. Dynamics of Particle Size on Inhalation of Environmental Aerosol and Impact on Deposition Fraction. *Environ. Sci. Technol.* **2015**, *49* (24), 14512–14521.

(28) Bohren, C. F.; Huffman, D. R. *Absorption and Scattering of Light by Small Particles*; Wiley-Interscience, 1987.

(29) Mie, G. Articles on the Optical Characteristics of Turbid Tubes, Especially Colloidal Metal Solutions. *Ann. Phys. (N. Y).* **1908**, *25 (3)*, 377–445.

(30) *Aerosol Measurement: Principles, Techniques, and Applications*; Pramod Kulkarni, Paul A. Baron, K. W., Ed.; John Wiley & Sons, 2011.

(31) Davis, E. J. A History of Single Aerosol Particle Levitation. *Aerosol Sci. Technol.* **1997**, *26* (3), 212–254.

(32) Reid, J. P. Particle Levitation and Laboratory Scattering. *J. Quant. Spectrosc. Radiat. Transf.* **2009**, *110* (14-16), 1293–1306.

(33) IPCC (Intergovernmental Panel On Climate Change). *Climate Change 2007 Synthesis Report*; 2008.

(34) Boucher, O. Estimates of the Direct and Indirect Radiative Forcing Due to Tropospheric Aerosols: A Review. **2000**, No. 1999, 513–543.

(35) IPCC (Intergovernmental Panel On Climate Change). *Second Assessment Report*; 1995.

(36) IPCC (Intergovernmental Panel On Climate Change). *Third Assessment Report*; (Keine Angabe); Cambridge University Press, 2001.

(37) IPCC (Intergovernmental Panel On Climate Change). *Fourth Assessment Report*; 2007.

(38) Bernstein, J. A.; Alexis, N.; Barnes, C.; Bernstein, I. L.; Bernstein, J. A.; Nel, A.; Peden, D.; Diaz-Sanchez, D.; Tarlo, S. M.; Williams, P. B. Health Effects of Air Pollution. *J. Allergy Clin. Immunol.* **2004**, *114* (5), 1116–1123.

(39) Brunekreef, B.; Holgate, S. T. Air Pollution and Health. *Lancet* **2002**, *360* (9341), 1233–1242.

(40) European Committee for Standardization (CEN). *Workplace Atmospheres-Size Fraction Definitions for Measurement of Airborne Particles*; 1993.

(41) Burnett, R. T.; Brook, J.; Dann, T.; Delocla, C.; Philips, O.; Cakmak, S.; Vincent, R.; Goldberg, M. S.; Krewski, D.; Brook, J.; et al. Association Between Particulate- and Gas-Phase Components of Urban Air Pollution and Daily Mortality in Eight Canadian Cities. *Inhal. Toxicol.* **2000**, *12* (s4), 15–39.

(42) Ostro, B.; Feng, W. Y.; Broadwin, R.; Green, S.; Lipsett, M. The Effects of Components of Fine Particulate Air Pollution on Mortality in California: Results from CALFINE. *Environ. Health Perspect.* **2007**, *115* (1), 13–19.

(43) Mühlfeld, C.; Rothen-Rutishauser, B.; Blank, F.; Vanhecke, D.; Ochs, M.; Gehr, P. Interactions of Nanoparticles with Pulmonary Structures and Cellular Responses. *Am. J. Physiol. Lung Cell. Mol. Physiol.* **2008**, *294* (5), L817–L829.

(44) Smyth, H. D. C.; Hickey, A. J. *Controlled Pulmonary Drug Delivery*; 2011.

(45) Haddrell, A. E.; Hargreaves, G.; Davies, J. F.; Reid, J. P. Control over Hygroscopic Growth of Saline Aqueous Aerosol Using Pluronic Polymer Additives. *Int. J. Pharm.* **2013**, *443* (1-2), 183–192.

(46) Doehne, E. Salt Weathering: A Selective Review. *Geol. Soc. London, Spec. Publ.* **2002**, *205* (1), 51–64.

(47) Urosevic, M.; Yebra-Rodríguez, A.; Sebastián-Pardo, E.; Cardell, C. Black Soiling of an Architectural Limestone during Two-Year Term Exposure to Urban Air in the City of Granada (S Spain). *Sci. Total Environ.* **2012**, *414*, 564–575.

(48) Syed, S. Atmospheric Corrosion of Materials. *Emirates J. Eng. Res.* **2006**, *11* (1), 1–24.

(49) Leygraf, C. Atmospheric Corrosion. In *Encyclopedia of Electrochemistry vol. 4*; Wiley, 2003; pp 191–215.

(50) Chen, Z. Y. The Role of Particles on Initial Atmospheric Corrosion of Copper and Zinc, Royal Institute of Technology, Stockholm, 2005.

(51) Casati, M.; Rovelli, G.; D'Angelo, L.; Perrone, M. G.; Sangiorgi, G.; Bolzacchini, E.; Ferrero, L. Experimental Measurements of Particulate Matter Deliquescence and Crystallization Relative Humidity: Application in Heritage Climatology. *Aerosol Air Qual. Res.* **2015**, *15*, 399–409.

(52) Ghedini, N.; Ozga, I.; Bonazza, A.; Dilillo, M.; Cachier, H.; Sabbioni, C. Atmospheric Aerosol Monitoring as a Strategy for the Preventive Conservation of Urban Monumental Heritage: The Florence Baptistery. *Atmos. Environ.* **2011**, *45* (33), 5979–5987.

(53) Brimblecombe, P. Heritage Climatology. In *Climate Change and Cultural Heritage*; Lefevre R.A., Sabbioni, C., Eds.; Edipuglia, 2010; pp 54–57.

(54) Tencer, M. Deposition of Aerosol ("hygroscopic Dust") on Electronics - Mechanism and Risk. *Microelectron. Reliab.* **2008**, *48* (4), 584–593.

(55) Stock, M.; Cheng, Y. F.; Birmili, W.; Massling, a.; Wehner, B.; Müller, T.; Leinert, S.; Kalivitis, N.; Mihalopoulos, N.; Wiedensohler, a. Hygroscopic Properties of Atmospheric Aerosol Particles over the Eastern Mediterranean: Implications for Regional Direct Radiative Forcing under Clean and Polluted Conditions. *Atmos. Chem. Phys.* **2011**, *11* (9), 4251–4271.

(56) Comizzoli, R. B.; Frankentahal, R. P.; Milner, P. C.; Sinclair, J. D. Corrosion of Electronic Materials and Devices. *Science (86-.).* **1986**, *234*, 340–345.

(57) Sinclair, J. D. Corrosion of Electronics: The Role of Ionic Substances. *J. Electrochem. Soc.* **1988**, *135*, 89C – 95C .

(58) Shehabi, A. Energy Demands and Efficiency Strategies in Data Center Buildings, Lawrence Berkeley National Laboratory, 2009.

(59) Shehabi, A.; Horvath, A.; Tschudi, W.; Gadgil, A. J.; Nazaroff, W. W. Particle Concentrations in Data Centers. *Atmos. Environ.* **2008**, *42* (24), 5978–5990.

(60) Shields, H. C.; Weschler, C. J. Are Indoor Air Pollutants Threatening the Reliability of Your Electronic Equipment? *Heating, Pip. air Cond.* **1998**, *70* (5), 46–54.

(61) Song, B.; Azarian, M. H.; Pecht, M. G. Effect of Temperature and Relative Humidity on the Impedance Degradation of Dust-Contaminated Electronics. *J. Electrochem. Soc.* **2013**, *160* (3), C97–C105.

(62) Dai, J.; Das, D.; Pecht, M. A Multiple Stage Approach to Mitigate the Risks of Telecommunication Equipment under Free Air Cooling Conditions. *Energy Convers. Manag.* **2012**, *64*, 424–432.

(63) Lobnig, R. E.; Frankenthal, R. P.; Siconolfi, D. J.; Sinclair, J. D.; Stratmann, M. Mechanism of Atmospheric Corrosion of Copper in the Presence of Submicron Ammonium Sulfate Particles at 300 and 373 K. *J. Electrochem. Soc.* **1994**, *141* (11), 2935–2941.

(64) Lau, N. T.; Chan, C. K.; Chan, L. I.; Fang, M. A Microscopic Study of the Effects of Particle Size and Composition of Atmospheric Aerosols on the Corrosion of Mild Steel. *Corros. Sci.* **2008**, *50* (10), 2927–2933.

(65) Ferrero, L.; Sangiorgi, G.; Ferrini, B. S.; Perrone, M. G.; Moscatelli, M.; D'Angelo, L.; Rovelli, G.; Ariatta, A.; Truccolo, R.; Bolzacchini, E. Aerosol Corrosion Prevention and Energy-Saving Strategies in the Design of Green Data Centers. *Environ. Sci. Technol.* **2013**, *47* (8), 3856–3864.

(66) Singh, P.; Ruch, P.; Saliba, S.; Muller, C. Characterization , Prevention and Removal of Particulate Matter on Printed Circuit Boards. In *IPC APEX EXPO Conference Proceedings*; 2015.

(67) Camuffo, D. Physical Weathering of Stones. *Sci. Total Environ.* **1995**, *167* (1-3), 1–14.

(68) Cardell-Fernández, C.; Vleugels, G.; Torfs, K.; Van Grieken, R. The Processes Dominating Ca Dissolution of Limestone When Exposed to Ambient Atmospheric Conditions as Determined by Comparing Dissolution Models. *Environ. Geol.* **2002**, *43* (1/2), 160–171.

(69) Brimblecombe, P.; Grossi, C. M.; Harris, I. The Effect of Long-Term Trends in Dampness on Historic Buildings. *Weather* **2006**, *61* (10), 278–281.

(70) Bonazza, A.; Messina, P.; Sabbioni, C.; Grossi, C. M.; Brimblecombe, P. Mapping the Impact of Climate Change on Surface Recession of Carbonate Buildings in Europe. *Sci. Total Environ.* **2009**, *407* (6), 2039–2050.

(71) Grossi, C. M.; Brimblecombe, P.; Menéndez, B.; Benavente, D.; Harris, I.; Déqué, M. Climatology of Salt Transitions and Implications for Stone Weathering. *Sci. Total Environ.* **2011**, *409* (13), 2577–2585.

(72) Clegg, S. L.; Brimblecombe, P.; Liang, Z.; Chan, C. K. Thermodynamic Properties of Aqueous Aerosols to High Supersaturation: II—A Model of the System Na^+—Cl^-—NO^-_3—SO^{2-}_4—H_2O at 298.15 K. *Aerosol Sci. Technol.* **1997**, *27* (3), 345–366.

(73) Sauerwein, M.; Clegg, S. L.; Chan, C. K. Water Activities and Osmotic Coefficients of Aqueous Solutions of Five Alkylaminium Sulfates and Their Mixtures with H_2SO_4 at 25 °C. *Aerosol Sci. Technol.* **2015**, *49* (8), 566–579.

(74) Petters, M. D.; Kreidenweis, S. M. A Single Parameter Representation of Hygroscopic Growth and Cloud Condensation Nucleus Activity – Part 3: Including Surfactant Partitioning. *Atmos. Chem. Phys.* **2013**, *13* (2), 1081–1091.

(75) Good, N.; Topping, D. O.; Duplissy, J.; Gysel, M.; Meyer, N. K.; Metzger, a.; Turner, S. F.; Baltensperger, U.; Ristovski, Z.; Weingartner, E.; et al. Widening the Gap between Measurement and Modelling of Secondary Organic Aerosol Properties? *Atmos. Chem. Phys.* **2010**, *10*, 2577–2593.

(76) Martin, S. T.; Rosenoern, T.; Chen, Q.; Collins, D. R. Phase Changes of Ambient Particles in the

Southern Great Plains of Oklahoma. *Geophys. Res. Lett.* **2008**, *35* (22), 1–5.

(77) Santarpia, J. L.; Li, R.; Collins, D. R. Direct Measurement of the Hydration State of Ambient Aerosol Populations. *J. Geophys. Res. Atmos.* **2004**, *109* (18), 1–16.

(78) Swietlicki, E.; Hansson, H. C.; H??meri, K.; Svenningsson, B.; Massling, A.; Mcfiggans, G.; Mcmurry, P. H.; Pet??j??, T.; Tunved, P.; Gysel, M.; et al. Hygroscopic Properties of Submicrometer Atmospheric Aerosol Particles Measured with H-TDMA Instruments in Various Environments - A Review. *Tellus, Ser. B Chem. Phys. Meteorol.* **2008**, *60 B* (3), 432–469.

(79) Duplissy, J.; DeCarlo, P. F.; Dommen, J.; Alfarra, M. R.; Metzger, a.; Barmpadimos, I.; Prevot, a. S. H.; Weingartner, E.; Tritscher, T.; Gysel, M.; et al. Relating Hygroscopicity and Composition of Organic Aerosol Particulate Matter. *Atmos. Chem. Phys.* **2011**, *11* (3), 1155–1165.

(80) Hu, D.; Chen, J.; Ye, X.; Li, L.; Yang, X. Hygroscopicity and Evaporation of Ammonium Chloride and Ammonium Nitrate: Relative Humidity and Size Effects on the Growth Factor. *Atmos. Environ.* **2011**, *45* (14), 2349–2355.

(81) Qiu, C.; Zhang, R. Physiochemical Properties of Alkylaminium Sulfates: Hygroscopicity, Thermostability, and Density. *Environ. Sci. Technol.* **2012**, *46* (8), 4474–4480.

(82) Dougle, P. G.; Veefkind, J. P.; Ten Brink, H. M. Crystallisation of Mixtures of Ammonium Nitrate, Ammonium Sulphate and Soot. *J. Aerosol Sci.* **1998**, *29* (3), 375–386.

(83) Ten Brink, H. M.; Veefkind, J. P.; Waijers-Ijpelaan, A.; Van Der Hage, J. C. Aerosol Light-Scattering in the Netherlands. *Atmos. Environ.* **1996**, *30* (24), 4251–4261.

(84) Canepari, S.; Farao, C.; Marconi, E.; Giovannelli, C.; Perrino, C. Qualitative and Quantitative Determination of Water in Airborne Particulate Matter. *Atmos. Chem. Phys.* **2013**, *13* (3), 1193–1202.

(85) Khlystov, A.; Stanier, C. O.; Takahama, S.; Pandis, S. N. Water Content of Ambient Aerosol during the Pittsburgh Air Quality Study. *J. Geophys. Res. Atmos.* **2005**, *110*, 1–10.

(86) Pilinis, C.; Seinfeld, J.; Grosjean, D. Water Content of Atmospheric Aerosols. *Atmos. Environ.* **1989**, *23*, 1601–1606.

(87) Martin, S. T. Phase Transitions of Aqueous Atmospheric Particles. *Chem. Rev.* **2000**, *100* (9), 3403–3454.

(88) Shi, G.; Seinfeld, J. H. Transient Kinetics of Nucleation and Crystallization: Part II. Crystallization. *J. Mater. Res.* **1991**, *6* (10), 2097–2102.

(89) Wexler, A. S.; Seinfeld, J. H. Second-Generation Inorganic Aerosol Model. *Atmos. Environ. Part A, Gen. Top.* **1991**, *25* (12), 2731–2748.

(90) Badger, C. L.; George, I.; Griffiths, P. T.; Braban, C. F.; Cox, R. a.; Abbatt, J. P. D. Phase Transitions and Hygroscopic Growth of Aerosol Particles Containing Humic Acid and Mixtures of Humic Acid and Ammonium Sulphate. *Atmos. Chem. Phys. Discuss.* **2005**, *5* (5), 9581–9620.

(91) Choi, M. Y.; Chan, C. K. The Effects of Organic Species on the Hygroscopic Behaviors of Inorganic Aerosols. *Environ. Sci. Technol.* **2002**, *36* (11), 2422–2428.

(92) Marcolli, C.; Krieger, U. K. Phase Changes during Hygroscopic Cycles of Mixed Organic/inorganic Model Systems of Tropospheric Aerosols. *J. Phys. Chem. A* **2006**, *110* (5), 1881–1893.

(93) Pope, F. D.; Dennis-Smither, B. J.; Griffiths, P. T.; Clegg, S. L.; Cox, R. A. Studies of Single Aerosol Particles Containing Malonic Acid, Glutaric Acid, and Their Mixtures with Sodium Chloride. I. Hygroscopic Growth. *J. Phys. Chem. A* **2010**, *114* (16), 5335–5341.

(94) Svenningsson, B.; Rissler, J.; Swietlicki, E.; Mircea, M.; Bilde, M.; Facchini, M. C.; Decesari, S.; Fuzzi, S.; Zhou, J.; Mønster, J.; et al. Hygroscopic Growth and Critical Supersaturations for Mixed Aerosol Particles of Inorganic and Organic Compounds of Atmospheric Relevance. *Atmos. Chem. Phys. Discuss.* **2005**, *5* (3), 2833–2877.

(95) Kohler, H. The Nucleus in and the Growth of Hygroscopic Droplets. *Trans. Faraday Soc.* **1936**, *32*,

1152–1161.

(96) Davies, J. F.; Haddrell, A. E.; Rickards, A. M. J.; Reid, J. P. Simultaneous Analysis of the Equilibrium Hygroscopicity and Water Transport Kinetics of Liquid Aerosol. *Anal. Chem.* **2013**, *85* (12), 5819–5826.

(97) Peng, C.; Chan, M. N.; Chan, C. K. The Hygroscopic Properties of Dicarboxylic and Multifunctional Acids: Measurements and UNIFAC Predictions. *Environ. Sci. Technol.* **2001**, *35* (22), 4495–4501.

(98) Suda, S. R.; Petters, M. D. Accurate Determination of Aerosol Activity Coefficients at Relative Humidities up to 99% Using the Hygroscopicity Tandem Differential Mobility Analyzer Technique. *Aerosol Sci. Technol.* **2013**, *47* (9), 991–1000.

(99) Zardini, a. a.; Sjogren, S.; Marcolli, C.; Krieger, U. K.; Gysel, M.; Weingartner, E.; Baltensperger, U.; Peter, T. A Combined Particle trap/HTDMA Hygroscopicity Study of Mixed Inorganic/organic Aerosol Particles. *Atmos. Chem. Phys. Discuss.* **2008**, *8* (2), 5235–5268.

(100) Clegg, S. L.; Seinfeld, J. H.; Edney, E. O. Thermodynamic Modelling of Aqueous Aerosols Containing Electrolytes and Dissolved Organic Compounds. II. An Extended Zdanovskii–Stokes–Robinson Approach. *J. Aerosol Sci.* **2003**, *34* (6), 667–690.

(101) Hargreaves, G.; Kwamena, N. O. A.; Zhang, Y. H.; Butler, J. R.; Rushworth, S.; Clegg, S. L.; Reid, J. P. Measurements of the Equilibrium Size of Supersaturated Aqueous Sodium Chloride Droplets at Low Relative Humidity Using Aerosol Optical Tweezers and an Electrodynamic Balance. *J. Phys. Chem. A* **2010**, *114* (4), 1806–1815.

(102) Cai, C.; Stewart, D. J.; Reid, J. P.; Zhang, Y. H.; Ohm, P.; Dutcher, C. S.; Clegg, S. L. Organic Component Vapor Pressures and Hygroscopicities of Aqueous Aerosol Measured by Optical Tweezers. *J. Phys. Chem. A* **2015**, *119* (4), 704–718.

(103) Clegg, S. L.; Wexler, a S. Densities and Apparent Molar Volumes of Atmospherically Important Electrolyte Solutions. 2. The Systems H(+)-HSO4(-)-SO4(2-)-H2O from 0 to 3 Mol Kg(-1) as a Function of Temperature and H(+)-NH4(+)-HSO4(-)-SO4)2-)-H2O from 0 to 6 Mol Kg(-1) at 25 °C Using . *J. Phys. Chem. A* **2011**, *115* (15), 3461–3474.

(104) Clegg, S. L.; Qiu, C.; Zhang, R. The Deliquescence Behaviour, Solubilities, and Densities of Aqueous Solutions of Five Methyl- and Ethyl-Aminium Sulphate Salts. *Atmos. Environ.* **2013**, *75*, 145–158.

(105) Brimblecombe, P.; Clegg, S. L.; Pitzer, K. S. Thermodynamics of Multicomponent, Mlsclble, Ionlc Solutions. 2. Mlxtures Includlng Unsymmetrical Electrolytes. *J. Phys. Chem.* **1992**, *96* (23), 9470–9479.

(106) Stokes, R. H.; Robinson, R. A. Interactions in Aqueous Nonelectrolyte Solutions. I. Solute-Solvent Equilibria. *J. Phys. Chem.* **1966**, *70* (7), 2126–2131.

(107) Ervens, B. Influence of Water-Soluble Organic Carbon on Cloud Drop Number Concentration. *J. Geophys. Res.* **2005**, *110* (D18), D18211.

(108) Tang, I. N. Chemical and Size Effects of Hygroscopic Aerosols on Light Scattering Coefficients. *J. Geophys. Res.* **1996**, *101* (D14), 19245.

(109) Albrecht, B. a. Aerosols, Cloud Microphysics, and Fractional Cloudiness. *Science (80-.).* **1989**, *245*, 1227–1230.

(110) Kolb, C. E.; Cox, R. A.; Abbatt, J. P. D.; Ammann, M.; Davis, E. J.; Donaldson, D. J.; Garrett, B. C.; George, C.; Griffiths, P. T.; Hanson, D. R.; et al. An Overview of Current Issues in the Uptake of Atmospheric Trace Gases by Aerosols and Clouds. *Atmos. Chem. Phys.* **2010**, *10* (21), 10561–10605.

(111) Kanakidou, M.; Seinfeld, J. H.; Pandis, S. N.; Barnes, I.; Dentener, F. J.; Facchini, M. C.; Van Dingenen, R.; Ervens, B.; Nenes, A.; Nielsen, C. J.; et al. Organic Aerosol and Global Climate Modelling: A Review. *Atmos. Chem. Phys.* **2005**, *5*, 1053–1123.

(112) Ferrero, L.; D'Angelo, L.; Rovelli, G.; Sangiorgi, G.; Perrone, M. G.; Moscatelli, M.; Casati, M.; Rozzoni, V.; Bolzacchini, E. Determination of Aerosol Deliquescence and Crystallization Relative

Humidity for Energy Saving in Free-Cooled Data Centers. *Int. J. Environ. Sci. Technol.* **2014**, *12* (9), 2777–2790.

(113) Clegg, S. L.; Brimblecombe, P.; Wexler, A. S. Thermodynamic Model of the System H + -NH 4 + -SO 42- -NO 3 - -H 2 O at Tropospheric Temperatures. *J. Geophys. Res.* **1998**, *102* (12), 2137–2154.

(114) Wexler, A. S.; Clegg, S. L. Atmospheric Aerosol Models for Systems Including the Ions H+, NH4+, Na+, SO42−, NO3−, Cl−, Br−, and H2O. *J. Geophys. Res. Atmos.* **2002**, *107* (D14), ACH – 14–1 – ACH 14–14.

(115) Topping, D. O.; McFiggans, G. B.; Coe, H. A Curved Multi-Component Aerosol Hygroscopicity Model Framework: 2 – Including Organics. *Atmos. Chem. Phys. Discuss.* **2004**, *4* (6), 8677–8726.

(116) Topping, D. O.; Mcfiggans, G. B.; Coe, H. And Physics A Curved Multi-Component Aerosol Hygroscopicity Model Framework : Part 1 – Inorganic Compounds. *Atmos. Chem. Phys.* **2005**, *5*, 1205–1222.

(117) Nenes, A. ISORROPIA : A New Thermodynamic Equilibrium Model for Multiphase Multicomponent Inorganic Aerosols. *Aquat. Geochemistry* **1998**, *4*, 123–152.

(118) Fountoukis, C.; Nenes, A. ISORROPIA II : A Computationally Efficient Thermodynamic Equilibrium Model for K+–Ca2+–Mg2+–NH+ 4 –Na+–SO2−4 –NO− 3 –Cl−–H2O Aerosols. *Atmos. Chem. Phys.* **2007**, 4639–4659.

(119) Clegg, S. L.; Seinfeld, J. H.; Edney, E. O. Thermodynamic Modelling of Aqueous Aerosols Containing Electrolytes and Dissolved Organic Compounds. *J. Aerosol Sci.* **2001**, *32*, 713–738.

(120) Fredenslund, A.; Jones, R. L.; Prausnitz, J. M. Group-Contribution Estimation of Activity Coefficients in Nonideal Liquid Mixtures. *AIChE J.* **1975**, *21* (6), 1086–1099.

(121) Peng, C. G.; Chow, A. H. L.; Chan, C. K. Hygroscopic Study of Glucose, Citric Acid, and Sorbitol Using an Electrodynamic Balance: Comparison with UNIFAC Predictions. *Aerosol Sci. Tech.* **2001**, *35* (3), 753–758.

(122) Zuend, A.; Marcolli, C.; Booth, A. M.; Lienhard, D. M.; Soonsin, V.; Krieger, U. K.; Topping, D. O.; McFiggans, G.; Peter, T.; Seinfeld, J. H. New and Extended Parameterization of the Thermodynamic Model AIOMFAC: Calculation of Activity Coefficients for Organic-Inorganic Mixtures Containing Carboxyl, Hydroxyl, Carbonyl, Ether, Ester, Alkenyl, Alkyl, and Aromatic Functional Groups. *Atmos. Chem. Phys.* **2011**, *11* (17), 9155–9206.

(123) Zuend, a.; Marcolli, C.; Luo, B. P.; Peter, T. A Thermodynamic Model of Mixed Organic-Inorganic Aerosols to Predict Activity Coefficients. *Atmos. Chem. Phys. Discuss.* **2008**, *8* (2), 6069–6151.

(124) Kreidenweis, S. M.; Petters, M. D.; DeMott, P. J. Single-Parameter Estimates of Aerosol Water Content. *Environ. Res. Lett.* **2008**, *3*, 035002.

(125) Petters, M. D.; Kreidenweis, S. M. And Physics A Single Parameter Representation of Hygroscopic Growth and Cloud Condensation Nucleus Activity. *Atmos. Chem. Phys.* **2007**, *7*, 1961–1971.

(126) Chang, R. Y.-W.; Slowik, J. G.; Shantz, N. C.; Vlasenko, A.; Liggio, J.; Sjostedt, S. J.; Leaitch, W. R.; Abbatt, J. P. D. The Hygroscopicity Parameter (κ) of Ambient Organic Aerosol at a Field Site Subject to Biogenic and Anthropogenic Influences: Relationship to Degree of Aerosol Oxidation. *Atmos. Chem. Phys.* **2010**, *10* (11), 5047–5064.

(127) Rickards, A. M. J.; Miles, R. E. H.; Davies, J. F.; Marshall, F. H.; Reid, J. P. Measurements of the Sensitivity of Aerosol Hygroscopicity and the κ Parameter to the O/C Ratio. *J. Phys. Chem. A* **2013**, *117* (51), 14120–14131.

(128) Pajunoja, A.; Lambe, A. T.; Hakala, J.; Rastak, N.; Cummings, M. J.; Brogan, J. F.; Hao, L.; Paramonov, M.; Hong, J.; Prisle, N. L.; et al. Adsorptive Uptake of Water by Semisolid Secondary Organic Aerosols In the Atmosphere. *Nat. Geosci.* **2014**, 3063–3068.

(129) Topping, D.; Barley, M.; McFiggans, G. Including Phase Separation in a Unified Model to Calculate

Partitioning of Vapours to Mixed Inorganic–organic Aerosol Particles. *Faraday Discuss.* **2013**, *165*, 273.

(130) Nozière, B.; Baduel, C.; Jaffrezo, J.-L. The Dynamic Surface Tension of Atmospheric Aerosol Surfactants Reveals New Aspects of Cloud Activation. *Nat. Commun.* **2014**, *5*, 1–7.

(131) Cossio, M. L. T.; Giesen, L. F.; Araya, G.; Pérez-Cotapos, M. L. S.; VERGARA, R. L.; Manca, M.; Tohme, R. A.; Holmberg, S. D.; Bressmann, T.; Lirio, D. R.; et al. No Title No Title. *Uma ética para quantos?* **2012**, *XXXIII* (2), 81–87.

(132) Davies, J. F.; Miles, R. E. H.; Haddrell, A. E.; Reid, J. P. Temperature Dependence of the Vapor Pressure and Evaporation Coefficient of Supercooled Water. *J. Geophys. Res. Atmos.* **2014**, *119* (18), 10931–10940.

(133) Vehkamäki, H.; Riipinen, I. Thermodynamics and Kinetics of Atmospheric Aerosol Particle Formation and Growth. *Chem. Soc. Rev.* **2012**, *41*, 5160.

(134) Wex, H.; Petters, M. D.; Carrico, C. M.; Hallbauer, E.; Massling, A.; McMeeking, G. R.; Poulain, L.; Wu, Z.; Kreidenweis, S. M.; Stratmann, F. Towards Closing the Gap between Hygroscopic Growth and Activation for Secondary Organic Aerosol: Part 1 – Evidence from Measurements. *Atmos. Chem. Phys. Discuss.* **2009**, *9*, 3987–3997.

(135) Walker, J. S.; Wills, J. B.; Reid, J. P.; Wang, L.; Topping, D. O.; Butler, J. R.; Zhang, Y.-H. Direct Comparison of the Hygroscopic Properties of Ammonium Sulfate and Sodium Chloride Aerosol at Relative Humidities Approaching Saturation. *J. Phys. Chem. A* **2010**, *114* (48), 12682–12691.

(136) Martin, S. T. Crystallization of Atmospheric Sulfate-Nitrate-Ammonium Particles. *Geophys. Res. Lett.* **2003**, *30* (21), 2102.

(137) Han, J.; Martin, S. Heterogeneous Nucleation of the Efflorescence of (NH4) 2SO4 Particles Internally Mixed with Al2O3, TiO2, and ZrO2. *J. Geophys. Res. …* **1999**, *104*, 3543–3553.

(138) Tolman, R. . *Proceeding Natl. Acad. Sci.* **1925**, *11*, 436–439.

(139) Fowler, R.; Milne, E. . *Proceeding Natl. Acad. Sci.* **1925**, *11*, 400–402.

(140) Atkins, P.; De Paulo, J. *Physical Chemistry*; Oxford University Press, 2006.

(141) Miles, R. E. H.; Knox, K. J.; Reid, J. P.; Laurain, A. M. C.; Mitchem, L. Measurements of Mass and Heat Transfer at a Liquid Water Surface during Condensation or Evaporation of a Subnanometer Thickness Layer of Water. *Phys. Rev. Lett.* **2010**, *105* (11), 1–4.

(142) Davies, J. F.; Haddrell, A. E.; Reid, J. P. Time-Resolved Measurements of the Evaporation of Volatile Components from Single Aerosol Droplets. *Aerosol Sci. Technol.* **2012**, *46* (6), 666–677.

(143) Miles, R. E. H.; Reid, J. P.; Riipinen, I. Comparison of Approaches for Measuring the Mass Accommodation Coefficient for the Condensation of Water and Sensitivities to Uncertainties in Thermophysical Properties. *J. Phys. Chem. A* **2012**, *116* (44), 10810–10825.

(144) Davies, J. F. Characterising The Impact Of Bulk, Surface And Gas-Phase Limitations On Mass Transport In Aerosol, 2014.

(145) Kulmala, M.; Vesala, T.; Wagner, P. E. An Analytical Expression For the Rate of Binary Condensational Particle Growth. *Proc. R. Soc. A Math. Phys. Eng. Sci.* **1993**, *441* (1913), 589–605.

(146) Fuchs, N. A.; Sutugin, A. G. High-Dispersed Aerosols. In *Topics in Current Aerosol Research*; Hidy, G., Brock, J., Eds.; 1971; pp 1–60.

(147) Julin, J.; Shiraiwa, M.; Miles, R. E. H.; Reid, J. P.; Pöschl, U.; Riipinen, I. Mass Accommodation of Water: Bridging the Gap between Molecular Dynamics Simulations and Kinetic Condensation Models. *J. Phys. Chem. A* **2013**, *117* (2), 410–420.

(148) Winkler, P. M.; Vrtala, a.; Rudolf, R.; Wagner, P. E.; Riipinen, I.; Vesala, T.; Lehtinen, K. E. J.; Viisanen, Y.; Kulmala, M. Condensation of Water Vapor: Experimental Determination of Mass and Thermal Accommodation Coefficients. *J. Geophys. Res.* **2006**, *111* (D19), D19202.

(149) Li, Y. Q.; Davidovits, P.; Kolb, C. E.; Worsnop, D. R. Mass and Thermal Accommodation

Coefficients of H2O(g) on Liquid Water as a Function of Temperature. *J. Phys. Chem. A* **2001**, *105* (47), 10627–10634.

(150) Robinson, R. A.; Stokes., R. H. *Electrolyte Solutions*, Second Rev.; Dover Publications, I., Ed.; Wiley Subscription Services, Inc., A Wiley Company, 1960.

(151) Anderko, A.; Lencka, M. M. Computation of Electrical Conductivity of Multicomponent Aqueous Systems in Wide Concentration and Temperature Ranges. *Ind. Eng. Chem. Res.* **1997**, *36* (5), 1932–1943.

(152) Frankenthal, R. P. Accelerated Life Testing of Electronic Devices by Atmospheric Particles: Why and How. *J. Electrochem. Soc.* **1993**, *140* (11), 3129.

(153) Litvak, a; Gadgil, a J.; Fisk, W. J. Hygroscopic Fine Mode Particle Deposition on Electronic Circuits and Resulting Degradation of Circuit Performance: An Experimental Study. *Indoor Air* **2000**, *10* (1), 47–56.

(154) Sandroff, F. S.; Burnett, W. H. Reliability Qualification Test for Circuit Boards Exposed to Airborne Hygroscopic Dust. In *Electronic Components and Technology Conference, Proceedings., 42nd*; IEEE, Ed.; 1992; pp 384–389.

(155) Verdingovas, V.; Jellesen, M. S.; Ambat, R. Solder Flux Residues and Humidity-Related Failures in Electronics: Relative Effects of Weak Organic Acids Used in No-Clean Flux Systems. *J. Electron. Mater.* **2015**, *44* (4), 1116–1127.

(156) ASHRAE, T. C. *2011 Gaseous and Particulate Contamination Guidelines For Data Centers*; 2011.

(157) Ding, K.; Xiao, K.; Dong, C.; Zou, S.; Yi, P.; Li, X. Initial Corrosion Behavior and Mechanism of PCB–HASL in Typical Outdoor Environments in China. *J. Electron. Mater.* **2015**, *44* (11), 4405–4417.

(158) Schindelholz, E.; Tsui, L. K.; Kelly, R. G. Hygroscopic Particle Behavior Studied by Interdigitated Array Microelectrode Impedance Sensors. *J. Phys. Chem. A* **2014**, *118*, 167–177.

(159) Yang, L.; Pabalan, R. T.; Juckett, M. R. Deliquescence Relative Humidity Measurements Using an Electrical Conductivity Method. *J. Solution Chem.* **2006**, *35* (4), 583–604.

(160) D'Angelo, L.; Rovelli, G.; Casati, M.; Sangiorgi, G.; Perrone, M. G.; Bolzacchini, E.; Ferrero, L. Seasonal Behavior of PM2.5 Deliquescence, Crystallization and Hygroscopic Growth in the Po Valley (Milan): Implications for Remote Sensing Applications. *Atmos. Res.* **2016**, *(submitted*.

(161) D'Angelo, L. Atmospheric Aerosols Phase Transitions: Measurements and Applications, University of Milano-Bicocca, 2016.

(162) Casati, M. Interactions Between Atmospheric Particulate Matter and Stone Surfaces, 2016.

(163) Randriamiarisoa, H.; Chazette, P.; Couvert, P.; Sanak, J.; Mégie, G. Relative Humidity Impact on Aerosol Parameters in a Paris Suburban Area. *Atmos. Chem. Phys. Discuss.* **2005**, *5* (5), 8091–8147.

(164) Vecchi, R.; Marcazzan, G.; Valli, G.; Ceriani, M.; Antoniazzi, C. The Role of Atmospheric Dispersion in the Seasonal Variation of PM1 and PM2.5 Concentration and Composition in the Urban Area of Milan (Italy). *Atmos. Environ.* **2004**, *38* (27), 4437–4446.

(165) Rodríguez, S.; Van Dingenen, R.; Putaud, J.-P.; Dell'Acqua, a.; Pey, J.; Querol, X.; Alastuey, a.; Chenery, S.; Ho, K.-F.; Harrison, R. M.; et al. A Study on the Relationship between Mass Concentrations, Chemistry and Number Size Distribution of Urban Fine Aerosols in Milan, Barcelona and London. *Atmos. Chem. Phys. Discuss.* **2007**, *7* (1), 605–639.

(166) Carbone, C.; Decesari, S.; Mircea, M.; Giulianelli, L.; Finessi, E.; Rinaldi, M.; Fuzzi, S.; Marinoni, A.; Duchi, R.; Perrino, C.; et al. Size-Resolved Aerosol Chemical Composition over the Italian Peninsula during Typical Summer and Winter Conditions. *Atmos. Environ.* **2010**, *44* (39), 5269–5278.

(167) Ferrero, L.; Perrone, M. G.; Petraccone, S.; Sangiorgi, G.; Ferrini, B. S.; Lo Porto, C.; Lazzati, Z.; Cocchi, D.; Bruno, F.; Greco, F.; et al. Vertically-Resolved Particle Size Distribution within and above the Mixing Layer over the Milan Metropolitan Area. *Atmos. Chem. Phys.* **2010**, *10* (8), 3915–

3932.

(168) Ferrero, L.; Riccio, a.; Perrone, M. G.; Sangiorgi, G.; Ferrini, B. S.; Bolzacchini, E. Mixing Height Determination by Tethered Balloon-Based Particle Soundings and Modeling Simulations. *Atmos. Res.* **2011**, *102* (1-2), 145–156.

(169) Sangiorgi, G.; Ferrero, L.; Perrone, M. G.; Bolzacchini, E.; Duane, M.; Larsen, B. R. Vertical Distribution of Hydrocarbons in the Low Troposphere below and above the Mixing Height: Tethered Balloon Measurements in Milan, Italy. *Environ. Pollut.* **2011**, *159* (12), 3545–3552.

(170) Perrone, M. G.; Larsen, B. R.; Ferrero, L.; Sangiorgi, G.; De Gennaro, G.; Udisti, R.; Zangrando, R.; Gambaro, a.; Bolzacchini, E. Sources of High PM2.5 Concentrations in Milan, Northern Italy: Molecular Marker Data and CMB Modelling. *Sci. Total Environ.* **2012**, *414*, 343–355.

(171) Owoade, O. K.; Olise, F. S.; Obioh, I. B.; Olaniyi, H. B.; Bolzacchini, E.; Ferrero, L.; Perrone, G. PM10 Sampler Deposited Air Particulates: Ascertaining Uniformity of Sample on Filter through Rotated Exposure to Radiation. *Nucl. Instruments Methods Phys. Res. Sect. A Accel. Spectrometers, Detect. Assoc. Equip.* **2006**, *564* (1), 315–318.

(172) Gualtieri, M.; Mantecca, P.; Corvaja, V.; Longhin, E.; Perrone, M. G.; Bolzacchini, E.; Camatini, M. Winter Fine Particulate Matter from Milan Induces Morphological and Functional Alterations in Human Pulmonary Epithelial Cells (A549). *Toxicol. Lett.* **2009**, *188* (1), 52–62.

(173) Saathoff, H.; Blatt, N.; Gimmler, M.; Linke, C.; Schurath, U. Thermographic Characterisation of Different Soot Types. In *8th ETH Conference on Combustion Generated Particles, 14–16 September, 2004, Zurich, Switzerand.*; 1999.

(174) Chow, J.; Watson, J.; Fung, K. Climate Change – Characterization of Black Carbon and Organic Carbon Air Pollution Emissions and Evaluation of Measurement Methods. **2006**, *1*, 4–307.

(175) Watson, J.; Chow, J.; Lowenthal, D.; Motallebi, N. Measurement of Ultrafine and Fine Particle Black Carbon and Its Optical Properties. 684–688.

(176) Pietrogrande, M. C.; Mercuriali, M.; Perrone, M. G.; Ferrero, L.; Sangiorgi, G.; Bolzacchini, E. Distribution of N -Alkanes in the Northern Italy Aerosols: Data Handling of Gc-Ms Signals for Homologous Series Characterization. *Environ. Sci. Technol.* **2010**, *44* (11), 4232–4240.

(177) Popovicheva, O. B.; Persiantseva, N. M.; Kuznetsov, B. V.; Rakhmanova, T. a.; Shonija, N. K.; Suzanne, J.; Ferry, D. Microstructure and Water Adsorbability of Aircraft Combustor Soots and Kerosene Flame Soots: Toward an Aircraft-Generated Soot Laboratory Surrogate. *J. Phys. Chem. A* **2003**, *107* (47), 10046–10054.

(178) Potukuchi, S.; Wexler, A. S. Identifying Solid-Aqueous-Phase Transitions in Atmospheric Aerosols. II. Acidic Solutions. *Atmos. Environ.* **1995**, *29* (22), 3357–3364.

(179) Perrone, M. G.; Gualtieri, M.; Ferrero, L.; Lo Porto, C.; Udisti, R.; Bolzacchini, E.; Camatini, M. Seasonal Variations in Chemical Composition and in Vitro Biological Effects of Fine PM from Milan. *Chemosphere* **2010**, *78* (11), 1368–1377.

(180) Weschler, C. J. Predictions of Benefits and Costs Derived from Improving Indoor Air Quality in Telephone Switching Offices. *Indoor Air* **1991**, *1* (1), 65–78.

(181) Hoshen, J.; Kopelman, R. Percolation and Cluster Distribution. I. Cluster Multiple Labeling Technique and Critical Concentration Algorithm. *Phys. Rev. B* **1976**, *14* (8), 3438–3445.

(182) Hoshen, J.; Kopelman, R.; Monberg, E. M. Percolation and Cluster Distribution. II. Layers, Variable-Range Interactions, and Exciton Cluster Model. *J. Stat. Phys.* **1978**, *19* (3), 219–242.

(183) Baron, P. A.; Willeke, K. *Aerosol Measurement. Principles, Techniques and Applications.*; Wiley-interscience, Ed.; 2001.

(184) Search, H.; Journals, C.; Contact, A.; Iopscience, M.; Address, I. P. Water Vapour Adsorption and Surface Conductivity in Solids. **1972**, *1038*.

(185) Eom, H. J.; Gupta, D.; Li, X.; Jung, H. J.; Kim, H.; Ro, C. U. Influence of Collecting Substrates on

the Characterization of Hygroscopic Properties of Inorganic Aerosol Particles. *Anal. Chem.* **2014**, *86* (5), 2648–2656.

(186) Soles, C. L.; Yee, A. F. Discussion of the Molecular Mechanisms of Moisture Transport in Epoxy Resins. *J. Polym. Sci. Part B Polym. Phys.* **2000**, *38* (5), 792–802.

(187) Ferrero, L.; Sangiorgi, G.; Ferrini, B. S.; Perrone, M. G.; Moscatelli, M.; D'Angelo, L.; Rovelli, G.; Ariatta, A.; Truccolo, R.; Bolzacchini, E. Aerosol Corrosion Prevention and Energy-Saving Strategies in the Design of Green Data Centers. *Environ. Sci. Technol.* **2013**.

(188) Matta, E.; Facchini, M. C.; Decesari, S.; Mircea, M.; Cavalli, F.; Fuzzi, S.; Putaud, J.-P.; Dell'Acqua, a. Chemical Mass Balance of Size-Segregated Atmospheric Aerosol in an Urban Area of the Po Valley, Italy. *Atmos. Chem. Phys. Discuss.* **2002**, *2* (6), 2167–2208.

(189) Gysel, M.; Weingartner, E.; Nyeki, S.; Paulsen, D.; Baltensperger, U.; Galambos, I.; Kiss, G. Hygroscopic Properties of Water-Soluble Matter and Humic-like Organics in Atmospheric Fine Aerosol. *Atmos. Chem. Phys. Discuss.* **2003**, *3* (5), 4879–4925.

(190) Chebbi, a.; Carlier, P. Carboxylic Acids in the Troposphere, Occurrence, Sources, and Sinks: A Review. *Atmos. Environ.* **1996**, *30* (24), 4233–4249.

(191) Perrone, M. G.; Zhou, J.; Malandrino, M.; Sangiorgi, G.; Rizzi, C.; Ferrero, L.; Dommen, J.; Bolzacchini, E. PM Chemical Composition and Oxidative Potential of the Soluble Fraction of Particles at Two Sites in the Urban Area of Milan, Northern Italy. *Atmos. Environ.* **2016**, *128*, 104–113.

(192) Wang, J.; Hoffmann, A. a.; Park, R. J.; Jacob, D. J.; Martin, S. T. Global Distribution of Solid and Aqueous Sulfafte Aerosols: Effect of the Hysteresis of Particle Phase Transitions. *J. Geophys. Res. Atmos.* **2008**, *113* (11), D11206.

(193) Martin, S. T.; Han, J.-H.; Hung, H.-M. The Size Effect of Hematite and Corundum Inclusions on the Efflorescence Relative Humidities of Aqueous Ammonium Sulfate Particles. *Geophys. Res. Lett.* **2001**, *28* (13), 2601–2604.

(194) Clegg, S. L.; Brimblecombe, P.; Wexler, A. S. Thermodynamic Model of the System H+ - NH4+ - SO42- - NO3- - H2O at Tropospheric Temperatures. *J. Phys. Chem. A* **1998**, *102* (12), 2137–2154.

(195) Greenberg, S.; Mills, E.; Tschudi, B.; Rumsey, P.; Myatt, B. *Best Practices for Data Centers: Lessons Learned from Benchmarking 22 Data Centers 1*; 2006.

(196) Parolini, L.; Sinopoli, B. A Cyber–physical Systems Approach to Data Center Modeling and Control for Energy Efficiency. *Proc. …* **2012**, *100* (1).

(197) Tschudi, W.; Xu, T.; Sartor, D.; Nordman, B.; Koomey, J. *Energy Efficient Data Centers Prepared by*; 2004.

(198) Koomey, J. G. Worldwide Electricity Used in Data Centers. *Environ. Res. Lett.* **2008**, *3* (3), 034008.

(199) Masanet, E.; Shehabi, A.; Koomey, J. Characteristics of Low-Carbon Data Centres. *Nat. Clim. Chang.* **2013**, *3* (7), 627–630.

(200) Antler, M.; Gilbert, J. Electric Contacts. *J. Air Pollut. Control Assoc.* **1963**, *13* (9), 405–450.

(201) ASHRAE, T. C. *Particulate and Gaseous Contamination Guidelines for Data Centers*; 2009.

(202) ASHRAE, T. C. *2011 Thermal Guidelines for Data Processing Environments – Expanded Data Center Classes and Usage Guidance*; 2011.

(203) Nazaroff, W. W. Indoor Particle Dynamics. *Indoor Air* **2004**, *14* (Suppl 7), 175–183.

(204) Sangiorgi, G.; Ferrero, L.; Ferrini, B. S.; Lo Porto, C.; Perrone, M. G.; Zangrando, R.; Gambaro, A.; Lazzati, Z.; Bolzacchini, E. Indoor Airborne Particle Sources and Semi-Volatile Partitioning Effect of Outdoor Fine PM in Offices. *Atmos. Environ.* **2013**, *65*, 205–214.

(205) Saxena, P.; Hildemann, L. M.; McMurry, P. H.; Seinfeld, J. H. Organics Alter Hygroscopic Behavior of Atmospheric Particles. *J. Geophys. Res.* **1995**, *100* (D9), 18755.

(206) Conseil, H.; Verdingovas, V.; Jellesen, M. S.; Ambat, R. Decomposition of Nc-Clean Solder Flux Systems and Their Effects on the Corrosion Reliability of Electronics. *J. Mater. Sci. Mater. Electron.* **2015**.

(207) Anderson, J. E.; Markovac, V.; Troyk, P. R. Polymer Encapsulants for Microelectronics: Mechanisms for Protection and Failure. *IEEE Trans. components, hybrids, Manuf. Technol.* **1988**, *11* (I), 152–158.

(208) Andreae, M. O.; Gelencsér, a. Black Carbon or Brown Carbon? The Nature of Light-Absorbing Carbonaceous Aerosols. *Atmos. Chem. Phys. Discuss.* **2006**, *6* (3), 3419–3463.

(209) Akhter, M. S.; Chughtai, A. R.; Smith, D. M. The Structure of Hexane Soot I: Spectroscopic Studies. *Appl. Spectrosc.* **1985**, *39* (1), 143–153.

(210) Bond, T. C.; Bergstrom, R. W. Light Absorption by Carbonaceous Particles: An Investigative Review. *Aerosol Sci. Technol.* **2006**, *40* (1), 27–67.

(211) Brimblecombe, P. Temporal Humidity Variations in the Heritage Climate of South East England. *Herit. Sci.* **2013**, *3* (1), 1–11.

(212) Sabbioni, C. Contribution of Atmospheric Deposition to the Formation of Damage Layers. *Sci. Total Environ.* **1995**, *167* (1-3), 49–55.

(213) Grossi, C. .; Esbert, R. .; Díaz-Pache, F.; Alonso, F. . Soiling of Building Stones in Urban Environments. *Build. Environ.* **2003**, *38* (1), 147–159.

(214) Ferm, M.; Watt, J.; O'Hanlon, S.; De Santis, F.; Varotsos, C. Deposition Measurement of Particulate Matter in Connection with Corrosion Studies. *Anal. Bioanal. Chem.* **2006**, *384* (6), 1320–1330.

(215) Camuffo, D.; Del Monte, M.; Sabbioni, C.; Vittori, O. Wetting, Deterioration and Visual Features of Stone Surfaces in an Urban Area. *Atmos. Environ.* **1982**, *16* (9), 2253–2259.

(216) McAlister, J. J.; Smith, B. J.; Török, A. Transition Metals and Water-Soluble Ions in Deposits on a Building and Their Potential Catalysis of Stone Decay. *Atmos. Environ.* **2008**, *42* (33), 7657–7668.

(217) Steiger, M. Salts in Porous Materials: Thermodynamics of Phase Transitions, Modeling and Preventive Conservation. *Restor. Build. Monum.* **2005**, *11* (6), 419–432.

(218) Schowengerdt, R. A. *Remote Sensing: Models and Methods for Image Processing*; Academic Press, 2007; Vol. 3rd ed.

(219) King, M. D.; Kaufman, Y. J.; Tanré, D.; Nakajima, T. Remote Sensing of Tropospheric Aerosols from Space: Past, Present, and Future. *Bull. Am. Meteorol. Soc.* **1999**, *80* (11), 2229–2259.

(220) Snider, J. R.; Petters, M. D. Optical Particle Counter Measurement of Marine Aerosol Hygroscopic Growth. *Atmos. Chem. Phys. Discuss.* **2008**, *7*, 12381–12415.

(221) Boucher, O.; Anderson, T. L. General Circulation Model Assessment of the Sensitivity of Direct Climate Forcing by Anthropogenic Sulfate Aerosols to Aerosol Size and Chemistry. *J. Geophys. Res.* **1995**, *100* (D12), 26117.

(222) Martin, S. T.; Hung, H.-M.; Park, R. J.; Jacob, D. J.; Spurr, R. J. D.; Chance, K. V.; Chin, V. Effects of the Physical State of Tropospheric Ammonium-Sulfate-Nitrate Particles on Global Aerosol Direct Radiative Forcing. *Atmos. Chem. Phys.* **2004**, *4* (1), 183–214.

(223) Chu, D. A. Global Monitoring of Air Pollution over Land from the Earth Observing System-Terra Moderate Resolution Imaging Spectroradiometer (MODIS). *J. Geophys. Res.* **2003**, *108* (D21), 4661.

(224) Al-Saadi, J.; Szykman, J.; Pierce, R. B.; Kittaka, C.; Neil, D.; Chu, D. A.; Remer, L.; Gumley, L.; Prins, E.; Weinstock, L.; et al. Improving National Air Quality Forecasts with Satellite Aerosol Observations. *Bull. Am. Meteorol. Soc.* **2005**, *86* (9), 1249–1261.

(225) Levy, R. C.; Remer, L. A.; Dubovik, O. Global Aerosol Optical Properties and Application to Moderate Resolution Imaging Spectroradiometer Aerosol Retrieval over Land. *J. Geophys. Res.* **2007**, *11%*.

(226) Barnaba, F.; Putaud, J. P.; Gruening, C.; Dell'Acqua, a.; Dos Santos, S. Annual Cycle in Co-Located in Situ, Total-Column, and Height-Resolved Aerosol Observations in the Po Valley (Italy):

Implications for Ground-Level Particulate Matter Mass Concentration Estimation from Remote Sensing. *J. Geophys. Res. Atmos.* **2010**, *115* (19), 1–22.

(227) Barnes, M. D.; Lermer, N.; Whitten, W. B.; Ramsey, J. M. A CCD Based Approach to High-Precision Size and Refractive Index Determination of Levitated Microdroplets Using Fraunhofer Diffraction. *Rev. Sci. Instrum.* **1997**, *68* (6), 2287.

(228) Chu, Y.; Sauerwein, M.; Chan, C. K. Hygroscopic and Phase Transition Properties of Alkyl Aminium Sulfates at Low Relative Humidities. *Phys. Chem. Chem. Phys.* **2015**, *17* (30), 19789–19796.

(229) Peng, C. G.; Chow, A. H. L.; Chan, C. K. Study of the Hygroscopic Properties of Selected Pharmaceutical Aerosols Using Single Particle Levitation. *Pharm. Res.* **2000**, *17* (9), 1104–1109.

(230) Heinisch, C.; Wills, J. B.; Reid, J. P.; Tschudi, T.; Tropea, C. Temperature Measurement of Single Evaporating Water Droplets in a Nitrogen Flow Using Spontaneous Raman Scattering. *Phys. Chem. Chem. Phys.* **2009**, *11* (42), 9720–9728.

(231) Pope, F. D.; Gallimore, P. J.; Fuller, S. J.; Cox, R. A.; Kalberer, M. Ozonolysis of Maleic Acid Aerosols: Effect upon Aerosol Hygroscopicity, Phase and Mass. *Environ. Sci. Technol.* **2010**, *44* (17), 6656–6660.

(232) Gallimore, P. J.; Achakulwisut, P.; Pope, F. D.; Davies, J. F.; Spring, D. R.; Kalberer, M. Importance of Relative Humidity in the Oxidative Ageing of Organic Aerosols: Case Study of the Ozonolysis of Maleic Acid Aerosol. *Atmos. Chem. Phys.* **2011**, *11* (23), 12181–12195.

(233) Chan, L. P.; Chan, C. K. Role of the Aerosol Phase State in Ammonia/amines Exchange Reactions. *Environ. Sci. Technol.* **2013**, *47* (11), 5755–5762.

(234) Haddrell, A. E.; Davies, J. F.; Yabushita, A.; Reid, J. P. Accounting for Changes in Particle Charge, Dry Mass and Composition Occurring during Studies of Single Levitated Particles. *J. Phys. Chem. A* **2012**, *116* (40), 9941–9953.

(235) Wilson, H. A. A Determination of the Charge on the Ions Produced in Air by Röntgen Rays. *he London, Edinburgh, Dublin Philos. Mag. J. Sci.* **1903**, *5* (28), 429–441.

(236) Millikan, R. A. A New Modification of the Cloud Method of Determining the Elementary Electrical Charge and the Most Probable Value of That Charge. *London, Edinburgh, Dublin Philos. Mag. J. Sci.* **1910**, *19* (110), 209–228.

(237) Straubel, H. DIE DOSIERUNG VON SUBSTANZMENGEN UNTER 10-6G MITTELS ELEKTROSTATISCHER AUFLADUNG FUR ZWECKE DER MIKROANALYSE. *ZEITSCHRIFT FUR ELEKTROCHEMIE* **1956**, *60.9-10*, 1033–1036.

(238) Wuerker, R. F.; Shelton, H.; Langmuir, R. V. Electrodynamic Containment of Charged Particles. *J. Appl. Phys.* **1959**, *30* (3), 342–349.

(239) Ray, A. K.; Johnson, R.; Souyri, A. Dynamic Behavior of Single Glycerol Droplets in Humid Air Streams. *Langmuir* **1989**, *5* (10), 133–140.

(240) Draper, N. D.; Bakhoum, S. F.; Haddrell, A. E.; Agnes, G. R. Ion-Induced Nucleation in Solution: Promotion of Solute Nucleation in Charged Levitated Droplets. *J. Am. Chem. Soc.* **2007**, *129* (37), 11364–11377.

(241) Bogan, M. J.; Bakhoum, S. F. W.; Agnes, G. R. Promotion of Alpha-Cyano-4-Hydroxycinnamic Acid and Peptide Cocrystallization within Levitated Droplets with Net Charge. *J. Am. Soc. Mass Spectrom.* **2005**, *16* (2), 254–262.

(242) Glantschnig, W. J.; Chen, S. H. Light Scattering from Water Droplets in the Geometrical Optics Approximation. *Appl. Opt.* **1981**, *20* (14), 2499–2509.

(243) Preston, T. C.; Reid, J. P. Angular Scattering of Light by a Homogeneous Spherical Particle in a Zeroth-Order Bessel Beam and Its Relationship to Plane Wave Scattering. *J. Opt. Soc. Am. A* **2015**, *32* (6), 1053–1062.

(244) Cotterell, M.; Mason, B. J.; Preston, T. C.; Orr-Ewing, A.; Reid, J. P. Optical Extinction Efficiency

Measurements on Fine and Accumulation Mode Aerosol Using Single Particle Cavity Ring-Down Spectroscopy. *Phys. Chem. Chem. Phys.* **2015**, *17*, 15843–15856.

(245) Liu, Y.; Daum, P. H. Relationship of Refractive Index to Mass Density and Self-Consistency of Mixing Rules for Multicomponent Mixtures like Ambient Aerosols. *J. Aerosol Sci.* **2008**, *39* (11), 974–986.

(246) Lide, D. R. *CRC Handbook of Chemistry and Physics, 85th Ed.*; CRC Press, 2005.

(247) Nielsen, J. K.; Maus, C.; Rzesanke, D.; Leisner, T. Charge Induced Stability of Water Droplets in Subsaturated Environment. *Atmos. Chem. Phys.* **2011**, *11* (5), 2031–2037.

(248) Hopkins, R. J.; Reid, J. P. Evaporation of Ethanol/water Droplets: Examining the Temporal Evolution of Droplet Size, Composition and Temperature. *J. Phys. Chem. A* **2005**, *109* (35), 7923–7931.

(249) Reid, J. P. PhD Dissertation, 1997.

(250) Davidovits, P.; Kolb, C. E.; Williams, L. R.; Jayne, J. T.; Worsnop, D. R. Mass Accommodation and Chemical Reactions at Gas-Liquid Interfaces. *Chem. Rev.* **2006**, *106*, 1323–1354.

(251) Ge, X.; Wexler, A. S.; Clegg, S. L. Atmospheric Amines - Part I. A Review. *Atmos. Environ.* **2011**, *45* (3), 524–546.

(252) Namieśnik, J.; Jastrzębska, A.; Zygmunt, B. Determination of Volatile Aliphatic Amines in Air by Solid-Phase Microextraction Coupled with Gas Chromatography with Flame Ionization Detection. *J. Chromatogr. A* **2003**, *1016* (1), 1–9.

(253) Kallinger, G.; Niessner, R. Laboratory Investigation of Annular Denuders as Sampling System for the Determination of Aliphatic Primary and Secondary Amines in Stack Gas. *Mikrochim. Acta* **1999**, *130* (4), 309–316.

(254) Akyüz, M. Simultaneous Determination of Aliphatic and Aromatic Amines in Indoor and Outdoor Air Samples by Gas Chromatography-Mass Spectrometry. *Atmos. Environ.* **2008**, *42*, 3809–3819.

(255) Pratt, K. a.; Hatch, L. E.; Prather, K. a. Seasonal Volatility Dependence of Ambient Particle Phase Amines. *Environ. Sci. Technol.* **2009**, *43* (14), 5276–5281.

(256) Ge, X.; Wexler, A. S.; Clegg, S. L. Atmospheric Amines - Part II. Thermodynamic Properties and Gas/particle Partitioning. *Atmos. Environ.* **2011**, *45* (3), 561–577.

(257) Lavi, A.; Segre, E.; Gomez-Hernandez, M.; Zhang, R.; Rudich, Y. Volatility of Atmospherically Relevant Alkylaminium Carboxylate Salts. *J. Phys. Chem. A* **2015**, 150126161336007.

(258) Liu, Y.; Ma, Q.; He, H. Heterogeneous Uptake of Amines by Citric Acid and Humic Acid. *Environ. Sci. Technol.* **2012**, *46* (20), 11112–11118.

(259) Qiu, C.; Zhang, R. Multiphase Chemistry of Atmospheric Amines. *Phys. Chem. Chem. Phys. PCCP* **2013**, *15* (16), 5738–5752.

(260) Bzdek, B. R.; Ridge, D. P.; Johnston, M. V. Amine Exchange into Ammonium Bisulfate and Ammonium Nitrate Nuclei. *Atmos. Chem. Phys. Discuss.* **2010**, *10* (1), 45–68.

(261) Barsanti, K. C.; McMurry, P. H.; Smith, J. N. The Potential Contribution of Organic Salts to New Particle Growth. *Atmos. Chem. Phys.* **2009**, *9* (9), 2949–2957.

(262) Yli-Juuti, T.; Barsanti, K.; Hildebrandt Ruiz, L.; Kieloaho, a. J.; Makkonen, U.; Petäjä, T.; Ruuskanen, T.; Kulmala, M.; Riipinen, I. Model for Acid-Base Chemistry in Nanoparticle Growth (MABNAG). *Atmos. Chem. Phys.* **2013**, *13* (24), 12507–12524.

(263) Loukonen, V.; Kurtén, T.; Ortega, I. K.; Vehkamäki, H.; Pádua, a. a. H.; Sellegri, K.; Kulmala, M. Enhancing Effect of Dimethylamine in Sulfuric Acid Nucleation in the Presence of Water – a Computational Study. *Atmos. Chem. Phys. Discuss.* **2010**, *10* (2), 2321–2356.

(264) Wang, L.; Vinita, L.; Khalizov, A. F.; Zhang, R. Heterogeneous Chemistry of Alkylamines with Sulfuric Acid: Implications for Atmospheric Formation of Alkylaminium Sulfates. *Environ. Sci. Technol.* **2010**, *44* (7), 2461–2465.

(265) DePalma, J. W.; Bzdek, B. R.; Doren, D. J.; Johnston, M. V. Structure and Energetics of Nanometer Size Clusters of Sulfuric Acid with Ammonia and Dimethylamine. *J. Phys. Chem. A* **2012**, *116* (3), 1030–1040.

(266) Lavi, A.; Bluvshtein, N.; Segre, E.; Segev, L.; Flores, M.; Rudich, Y. Thermochemical, Cloud Condensation Nucleation Ability, and Optical Properties of Alkyl Aminium Sulfate Aerosols. *J. Phys. Chem. C* **2013**, *117* (43), 22412–22421.

(267) Chan, L. P.; Chan, C. K. Displacement of Ammonium from Aerosol Particles by Uptake of Triethylamine. *Aerosol Sci. Technol.* **2012**, *46* (2), 236–247.

(268) Zdanovskii, A. B. Zakonomernosti v Izmeneniyakh Svoistv Smeshannykh Rastvorov: Trudy Solyanoi Laboratorii (Fundamental Aspects of Variation of Properties of Mixed Solutions: Works of Salt Laboratory). *Tr. Solyanoi Lab. Akad. Nauk SSSR* **1936**, No. 6, 5–70.

(269) Clegg, S. L.; Brimblecombe, P. Application of a Multicomponent Thermodynamic Model to Activities and Thermal Properties of 0-40 Mol Kg^-1 Aqueous Sulfuric Acid from <200 to 328 K. *J. Chem. Eng. Data* **1995**, *40* (1), 43–64.

(270) Dennis-Smither, B. J.; Marshall, F. H.; Miles, R. E. H.; Preston, T. C.; Reid, J. P. Volatility and Oxidative Aging of Aqueous Maleic Acid Aerosol Droplets and the Dependence on Relative Humidity. *J. Phys. Chem. A* **2014**, *118* (30), 5680–5691.

(271) Chapman, S.; Cowling, T. G. *The Mathematical Theory of Non-Uniform Gases: An Account of the Kinetic Theory of Viscosity, Thermal Conduction and Diffusion in Gases*; Press, C. U., Ed.; 1970.

(272) Bird, R. B.; Stewart, W. E.; Lightfoot, E. N. *Transport Phenomena*; 2007.

Acknowledgments

I have been lucky enough to work with many great people in these three years! I would like to thank you all and let you know I am grateful for all the support and help you gave me throughout my PhD adventures.

Many thanks to my supervisor, Prof. Ezio Bolzacchini, who believed in me since my undergraduate studies and gave me the opportunity of working with his group for my PhD. Thank you for your guidance and support during these three years.

These three years would not have been the same without Luca D. and Marco, who shared all the fruitful, funny and desperate times during our PhDs. Luca D., thanks for sharing with me a lot of lab hours, but also your depression times and your 'I am almost happy' times. You helped me out so many times in these three years, I will always remember it. Marco, I learnt a lot of new things from you during these three years, thanks for all your advice and for sharing with me your theories about life. A special thank you to Luca F., for all the time you spent working with me and for all of your helpful advice. Thanks to all my colleagues at the University of Milano Bicocca, Giorgia, Grazia, Cristiana, both for your advice and your friendship.

I had the opportunity to spend part of my PhD at the University of Bristol and I want to thank Prof. Jonathan P. Reid for welcoming me in his research group and for always being supportive and helpful throughout my time in Bristol.

A special thanks to Rachael for giving me a lot of good advice, working with you has always been very easy and productive. Thanks to James, who helped me a lot in my first months working on the EDB, and to Al for his technical support in the lab and for teaching me how not to speak English. Many thanks to all the other people in the Bristol aerosol group: Aleks, Andy, Bernie, Bryan, Chen, Fran, Jim, Mara, Michael, Rory, Rose, Stephen, Young. You all made my time in Bristol special, thank you for your friendship.

Thanks to Prof. Simon L. Clegg, for your helpful collaboration and for giving me the opportunity to visit the Hong Kong University of Science and Technology.

Thanks to Prof. Giorgio Moro, coordinator of the PhD School in Chemical Science, for his support during these three years.

E infine, un grazie infinito alla mia famiglia. Se non avessi avuto il vostro supporto non sarei mai arrivata fino qui e non sarei la persona che sono ora. Grazie per aver sempre creduto in me e per essermi vicini in ogni situazione. Mi rendo conto che non sempre è facile, anche se sicuramente le gioie sono più dei dolori, per voi e per me. Questo lavoro è dedicato a voi.